ACTIVELY CONTROLLABLE HYDRODYNAMIC JOURNAL BEARING DESIGN USING MAGNETORHEOLOGICAL FLUIDS

A Dissertation

Presented to

The Graduate Faculty of The University of Akron

In Partial Fulfillment

of the Requirements for the Degree

Doctor of Philosophy

Nathaniel Moles

December, 2015

ACTIVELY CONTROLLABLE HYDRODYNAMIC JOURNAL

BEARING DESIGN USING MAGNETORHEOLOGICAL FLUIDS

Nathaniel Moles

Dissertation

Approved:

_____
Advisor
Dr. Minel J. Braun

_____
Committee Member
Dr. Alex Povitsky

_____
Committee Member
Dr. Abhilash J. Chandy

_____
Committee Member
Dr. Robert Veillette

_____
Committee Member
Dr. Kevin Kreider

Accepted:

_____
Department Chair
Dr. Sergio Felicelli

_____
Interim Dean of the College
Dr. Mario Ricardo Garzia

_____
Dean of the Graduate School
Dr. Chand Midha

_____
Date

ABSTRACT

This research comprised a multi-stage effort to create a hydrodynamic journal bearing design that had capability to be actively controlled through the use of magnetorheological fluids. An arrangement of electromagnets was designed and a modified Reynolds equation was derived to evaluate the performance of the bearing design. The fluid was modeled as a Bingham plastic, whose yield strength is proportional to the strength of the applied magnetic field.

Bench tests were then utilized to provide a proof of performance for the bearing design and to quantify the rheological properties of the magnetorheological fluids created for the study. The evaluation of the performance of the bearing design consisted of 15 steady state conditions with operational parameters of speed and applied magnetic field as the key variables. The bearing performance was analyzed by measuring eccentricity, torque and fluid pressure.

The results of the experimental testing indicated that a decrease of 15% in the eccentricity ratio was achievable relative to the baseline eccentricity ratio for all speeds. Given that the applied load remained constant, a decrease in eccentricity correlates to an increase in load capacity when a magnetic field is applied. The analysis also showed that an increase of up to 4.5% in the bearing torque, which represents reduction in operating efficiency when a magnetic field is applied. These results validated the advantages and disadvantages of this bearing design. This proves the bearing design gives the ability

to control the bearing performance with the expected consequence of increased heat generation and power consumption from the electromagnets as well as the bearing torque.

ACKNOWLEDGMENTS

I want to take this opportunity to thank all of the people who have helped me in getting this far in my career. First I would like to thank Dr. Minel Braun who gave me this great opportunity to work on this research project and who has helped me through every stage of this project and beyond. Also, I extend my thanks to the committee members Dr. Abhilash Chandy, Dr. Kevin Kreider, Dr. Alex Povitsky and Dr. Robert Veillette. I could not have successfully made it through without their professional expertise and direction. I also want to thank Bill Wenzel for his excellent work and expertise in machining the bearing assembly and operating the bench test.

I would also like to thank my former co-workers John Feltman, Keith Bandi and Greg Sturm who supported me during the long days of work, followed by evening classes and late nights studying; and Dr. Bill Hannon, for his mentorship and guidance throughout this process. Last, but certainly not least, I would like to thank Jackie Mach for her love and support during the last few years. Knowing she was in my corner helped me finally reach the finish line.

TABLE OF CONTENTS

Page

LIST OF TABLES

LIST OF FIGURES

ABBREVIATIONS

CIP	Carbonyl Iron Powder
EHD	Electro-Hydrodynamics
ER	Electrorheological
ERF	Electrorheological Fluids
FHD	Ferro-Hydrodynamics
MHD	Magneto-Hydrodynamics
MR	Magnetorheological
MRF	Magnetorheological Fluids
FEMM	Finite Element Method Magnetics

LIST OF SYMBOLS

Symbol	Description, (*units*)
$\vec{A}$	Vector Potential, (*N/A*)
A_e	Nodal Flux Constant for all Eastern Boundary Pressure Fields
A_f	Nodal Flux Constant for Lubrication Feed
A_n	Nodal Flux Constant for all Northern Boundary Pressure Fields
A_s	Nodal Flux Constant for all Southern Boundary Pressure Fields
A_w	Nodal Flux Constant for all Western Boundary Pressure Fields
A_{pole}	Area of Electromagnetic Pole, (m^2)
$\vec{B}$	Magnetic Field Vector, ($N/A{\cdot}m$)
$B_{xx}, B_{xz}, B_{zx}, B_{zz}$	Damping Coefficients
c	Bearing Clearance, (m)
d_o	Diameter of Lubrication Injection Orifice, (m)
$d\bar{l}$	Differential Length Along the Path of Current Flow, (m)
e	Bearing Eccentricity, (m)
F_{mag}	Electromagnetic Force Acting on the Journal, (N)
F_n	Bearing Force Acting Normal to Applied Load, (N)
F_t	Bearing Force Acting Tangent to Applied Load, (N)

g	Cavitation Switching Function
$\vec{H}$	Magnetic Field, (A/m)
$H\left(\lvert\dot{\gamma}\rvert\right)$	Shear Switching Function
H_n	Magnetic Field Normal to Bearing Surface, (A/m)
h	Film Thickness, (m)
I	Applied Current, (A)
$\vec{J}$	Current Density, (A/m^2)
K	Effective Anisotropy Constant, ($kg/m{\cdot}s$)
k_B	Boltzmann's Constant, ($m^{2}{\cdot}kg/s^{2}{\cdot}K$)
$K_{xx}, K_{xz}, K_{zx}, K_{zz}$	Stiffness Coefficients
L	Axial Length of Bearing, (m)
l_o	Length of Lubrication Injection Supply Tube, (m)
M	Mass Supported by Bearing, (kg)
M_c	Critical Mass Supported by Bearing, (kg)
P	Pressure, (N/m^2)
P_a	Atmospheric Pressure, (N/m^2)
P_c	Cavitation Pressure, (N/m^2)
P_{inj}	Lubrication Injection Pressure, (N/m^2)
P_{mag}	Polarization, (A/m)
R	Journal Radius, (m)

r	Position Vector in the Direction of an Evaluation Point, (m)
$\hat{r}$	Unit Vector in the Direction of a Magnetic Field Evaluation Point
$\overline{S}$	Source Term (Used for all Pressure Fields)
T	Temperature, (K)
t	Time, (s)
U	Journal Velocity in x-direction, (m/s)
u	Velocity in x-direction, (m/s)
v	Velocity in y-direction, (m/s)
V_{core}	Volume of Particle Magnetic Core, (m^3)
V_{eff}	Effective (Hydrodynamic) Particle Volume, (m^3)
v_i	Velocity Vector, (m/s)
V_{part}	Particle Volume, (m^3)
$W_{\tilde{x}}$	Applied Load in $\tilde{x}$ -direction, (N)
$W_{\tilde{z}}$	Applied Load in $\tilde{z}$ -direction, (N)
w	Velocity in z-direction, (m/s)
w_{inj}	Lubrication Injection Velocity, (m/s)
x	Cartesian Coordinate in the Direction of Rotation, (m)
x'	Complex Notation for Cartesian Coordinate in the x-direction, (m)
$\tilde{x}$	Cartesian Coordinate Parallel to the Load Line, (m)
$\dot{\tilde{x}}$	Change in $\tilde{x}$ with Respect to Time, (m/s)
x_i, x_j	Position Vector, (m)

x_{inj}	Center Point of Lubrication Injection in x-direction, (m)
y	Cartesian Coordinate in the Axial Direction, (m)
y_{inj}	Center Point of Lubrication Injection in y-direction, (m)
z	Cartesian Coordinate in the Radial Direction, (m)
z'	Complex Notation for Cartesian Coordinate in the z-direction, (m)
$\tilde{z}$	Cartesian Coordinate Perpendicular to the Load Line, (m)
$\dot{\tilde{z}}$	Change in $\tilde{z}$ with Respect to Time, (m/s)
Greek Symbol	Description, ($units$)
β	Bulk Modulus, (kg/m^2)
$\dot{\gamma}$	Strain Rate, ($1/s$)
$\Delta W_{\tilde{x}}$	Discrete Change in Applied Load in the $\tilde{x}$ -direction, (N)
$\Delta W_{\tilde{z}}$	Discrete Change in Applied Load in the $\tilde{z}$ -direction, (N)
Δx	Discrete Circumferential Length, (m)
$\Delta\tilde{x}$	Discrete Length in the $\tilde{x}$ -direction, (m)
$\Delta\dot{\tilde{x}}$	Change in $\Delta\tilde{x}$ with Respect to Time, (m/s)
$\Delta\ddot{\tilde{x}}$	Change in $\Delta\dot{\tilde{x}}$ with Respect to Time, (m/s^2)
Δy	Discrete Axial Length, (m)
$\Delta\tilde{z}$	Discrete Length in the $\tilde{z}$ -direction, (m)
$\Delta\dot{\tilde{z}}$	Change in $\Delta\tilde{z}$ with Respect to Time, (m/s)
$\Delta\ddot{\tilde{z}}$	Change in $\Delta\dot{\tilde{z}}$ with Respect to Time, (m/s^2)
$\Delta\Phi$	Discrete Change in Attitude Angle, (rad)

Θ	Density Ratio
θ	Azimuthal Angle, (*rad*)
λ	Energy Factor
μ	Dynamic Viscosity, ($kg/m \cdot s$)
$\mu_{apparent}$	Analytical Dynamic Viscosity of MR Fluid, (*cP*)
μ_o	Permeability of Free Space, (N/A^2)
$\mu_{measured}$	Measured Dynamic Viscosity with Magnetic Field Applied, (*cP*)
$\mu_{unmagnitized}$	Measured Dynamic Viscosity, No Magnetic Field Applied, (*cP*)
ρ	Density, (kg/m^3)
$\hat{\tau}$	Unit Vector Tangent to Path of Current Flow
τ_A	Attempt Period, (*s*)
τ_B	Brownian Relaxation Time, (*s*)
τ_{ji}	Shear Stress Tensor, (N/m^2)
τ_N	Neel Relaxation Time, (*s*)
τ_o	Yield Strength of MR Fluid, (N/m^2)
$\tau_{apparent}$	Analytical Yield Strength of MR Fluid, (N/m^2)
$\tau_{unmagnitized}$	Analytical Yield Strength, No Magnetic Field Applied, (N/m^2)
τ_{yield}	Analytical Yield Strength, With Magnetic Field Applied, (N/m^2)
Φ	Attitude Angle, (*rad*)
ω	Bearing Rotational Frequency, (*1/sec*)
ω_c	Critical Bearing Rotational Frequency, (*1/sec*)

$\mathfrak{I}$	Lubrication Injection Switching Function
Subscript Symbol	Description
E	Pertaining to the Eastern Face of the Control Volume
e	Pertaining to the Eastern Node of the Control Volume
inj	Pertaining to the Bearing Lubrication Injection
N	Pertaining to the Northern Face of the Control Volume
n	Pertaining to the Northern Node of the Control Volume
o	Steady State or Fixed Parameter
S	Pertaining to the Southern Face of the Control Volume
s	Pertaining to the Southern Node of the Control Volume
W	Pertaining to the Western Face of the Control Volume
w	Pertaining to the Western Node of the Control Volume
$\tilde{x}$	Component in the Direction of $\tilde{x}$ and/or on the Order of $\tilde{x}$
$\dot{\tilde{x}}$	Component on the Order of $\dot{\tilde{x}}$
$\tilde{z}$	Component in the Direction of $\tilde{z}$ and/or on the Order of $\tilde{z}$
$\dot{\tilde{z}}$	Component on the Order of $\dot{\tilde{z}}$

CHAPTER I

INTRODUCTION

Progress in mechanical systems continues to trend towards more power dense and intricate designs, which requires advancements in tribological performance between the numerous mechanical contacting surfaces. In order to keep pace with the progress in specialized applications, passive tribological fluids have given way to active fluids that can interact with electric and magnetic fields. Three main categories of fluid/field interactions are: electro-hydrodynamics (EHD), which involves interactions pertaining to the effects of electrical forces; magneto-hydrodynamics (MHD), which involves the interactions between electrical conductors and magnetic fields; and the focus of this work, ferro-hydrodynamics (FHD), which involves magnetic fluids in the presence of magnetic fields [1]. There are several types of field responsive fluids which include: electrorheological (ER) fluids, magnetorheological (MR) and ferrofluids. All of which can be generally described as colloidal mixtures; where, a colloid is a suspension of dispersed particles in a continuous medium.

Electrorheological fluids are colloidal systems typically comprised of fine dielectric particles suspended in a dielectric liquid. The most significant characteristic of ERFs is their ability to reversibly transition from a liquid state to a viscoelastic or solid

state within milliseconds, in the presence of an electric field. The magnitude of rheological changes of the fluid varies with the applied electric field providing the potential for actively controlled systems. Electrorheological fluids' rheological properties were discovered by Willis Winslow in the early 1940's [2]. Winslow found that a substantially dielectric or non-conducting fluid containing a dispersion of dielectric particles separating two plates will cause the two plates to mechanically act as one, when an electric potential difference exists between them. Winslow theorized that the apparent yield strength developed from the applied electric field resulted from the formation of chainlike structures by the suspended particles in the fluid. These chainlike structures have been observed by several researchers for a wide variety of electrorheological fluids, and are the accepted rationalization for the increase in yield strength [2, 3, 4, 5, 6].

Two theories have been proposed to explain the mechanism of the increase in strength of electrorheological fluids, water bridging and polarization of the particles. The water bridging theory proposes that water molecules are located in the pores of the particles, which move to the end of the particle when the electric field is applied, and forms a "bridge" with an adjacent particle [7, 8]. Polarization of the dispersed particles proposes that when the electric field is applied, the particles are polarized and create a dipole-dipole or multiple pole interactions between adjacent particles [5].

The strength of electrorheological fluids generally varies with: volume fraction of particles, temperature, shear rate and the magnitude of the applied electric field. The strength of electrorheological fluids generally increases with the volume fraction of the particles until a saturation point is reached [5]. The strength of the fluid also increases with increasing temperatures at lower temperature ranges (below approximately 100^{o}C),

then decrease as the temperature is increased further [5]. Electrorheological fluids also exhibit shear thinning behavior, where the apparent viscosity decreases as the shear rate increases, while an electric field is applied. This behavior has been attributed to the breaking of the chainlike structures by hydrodynamic shearing forces [9, 10]. The most significant advantage of using electrorheological fluids is the change in apparent viscosity of the fluid depending on the magnitude of the applied electric field [4, 10, 1]. This change can occur on the order of a few milliseconds and is completely reversible. Despite this desirable effect, electrorheological fluids have not seen much success in commercial devices. This has been generally attributed to electrorheological fluids' relatively lower yield strength (compared to magnetic field responsive fluids), and the requirement of high voltage supplies, as well as, their temperature dependence and sensitivity to impurities [12, 13].

At nearly the same time Winslow was working on electrorheological fluids, Jacob Rabinov discovered magnetorheological fluid effects at the United States National Bureau of Standards to be utilized in a clutch device [14]. Magnetic fluids typically consist of multi-domain magnetic particles suspended in a non-magnetic carrier liquid such as kerosene, water or oil. Similar to ERFs, the most significant characteristic of magnetic fluids is their ability to reversibly transition from a liquid state to a viscoelastic or solid state within milliseconds, in response to an applied magnetic field rather than an electric field. Magnetic fluids can be broken down into two categories depending on their particle diameters: ferrofluids and magnetorheological fluids. Where ferrofluid particles are on the order of nanometers and magnetorheological fluid particles are on the order of micrometers.

Early in the development of magnetic and ER fluids, more research work was carried out on ERFs than magnetic fluids due to the difficulties with thickening, sedimentation and abrasiveness of magnetic fluids during usage [13]. However, in recent years, interests in using magnetic fluids have increased and efforts to address these issues have resulted in their commercial use in rotary shaft seals, loudspeakers, actuators, dampers, clutches and polishing devices to list a few examples. Magnetorheological fluids have several technological advantages over equivalent ERF fluids including lower power requirements, better stability and higher control effect [16]. Table 1-1 below provides an overview of key features of MR and ER fluids for comparison.

Table 1-1 Representative Features of MRF and ERF [15]

	MRF	**ERF**
Maximum Yield Strength	50 - 100 *kPa*	2 - 5 *kPa*
Maximum Field	~250 *kA/m* (limited by saturation)	~4 *kV/m* (limited by saturation)
Viscosity	0.1 - 1.0 *Pa-s*	0.1 - 1.0 *Pa-s*
Operable Temperature Range	-40 to +150 *°C* (limited by carrier fluids)	+10 to +90 *°C* (ionic, DC) -25 to +125 *°C* (non-ionic, AC)
Stability	Unaffected by most impurities	Cannot tolerate impurities
Response Time	<milliseconds	<milliseconds
Density	3 - 4 *g/cm³*	1 - 2 *g/cm³*
Maximum Energy Density	0.1 *J/cm³*	0.001 *J/cm³*
Power Supply (Typical)	2 - 25 *V* @ 1 - 2 *A* (2 - 50 *W)*	2 - 5 *kV* @ 1 - 10 *mA* (2 - 50 *W*)

The magnetorheological response of a magnetic fluid results from the polarization induced in the magnetic particles in the presence of a magnetic field. The resulting induced dipoles can interact and align to form chainlike structures parallel to the applied magnetic field lines. This change is reversible and varies equivalently with the magnetic

field strength until a saturation point is reached [17, 18]. The rheological properties of the magnetic fluid depend on the type, size, shape and concentration of the particles; as well as, the properties of the carrier fluid, additives, rate of shear and the applied magnetic field [12, 19, 20, 21, 23]. When no magnetic field is applied to the magnetic fluid, its rheological behavior is similar to that of the carrier fluid with the exception of slightly higher viscosity due to the suspended particles, as first estimated by Albert Einstein in 1906 [24].

Ferrofluids and magnetorheological fluids both fall in the category of ferro-hydrodynamics and the terms are sometimes used interchangeably; however, there are significant differences between the two, not only in the composition of the fluids, but also in their functionality. The following paragraphs will attempt to explain and differentiate both types of magnetic fluids. Table 1-2 below provides an overview of key features of MRFs and ferrofluids.

Table 1-2 Representative Features of MRF and Ferrofluid [21]

	MRF	Ferrofluid
Energy Factor λ	>1	<1
Maximum Yield Strength	100 *kPa*	10 *kPa*
Particle Size	micrometers	nanometers
Particle material	carbonyl iron	iron oxide
Fraction by Volume	up to 50%	up to 10%
Stability	medium	good
Functionality	controllable shear stress	controllable liquid flow

Ferrofluids contain nano-sized, single domain, magnetic particles usually made of magnetite (Fe_3O_4), suspended in non-magnetic carrier liquids like oil or water. Typical mean diameters of the particles are on the order of 10 nm with the fraction by volume up

to approximately 10%. The size of the particles allows Brownian Motion to prevent them from settling under gravitational force. The particles are usually covered with an oleic acid or a polymer coating to prevent agglomeration due to van der Waal interactions as depicted in Figure 1-1. This surfactant layer allows the ferrofluid to be stable for years and also allows it to maintain fluidity in high magnetic field gradients [1, 20, 24, 25, 26].

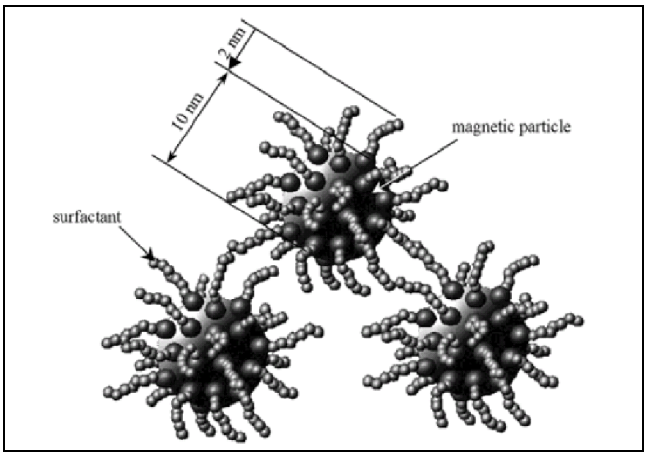

Figure 1-1 Schematic of Ferrofluid Magnetic Particle with Surfactant [25]

The rheological changes in ferrofluids are significant with typical increase in yield strength of 10 kPa, however they do not solidify. Therefore, the key functionality of a ferrofluid is to control the flow of the fluid by the magnetic field gradient and direction [21, 22]. This effect has allowed ferrofluids to have commercial success in several applications such as sealing and dampening of spindle shafts in hard drives [27, 28], cooling in loudspeakers [25], and magnetic drug targeting [29].

Magnetorheological fluids contain micro-sized, multi domain, magnetic particles usually made of high purity iron (carbonyl iron) or iron-cobalt alloys, which are suspended in non-magnetic carrier liquids. Typical mean diameters of the particles are on the order of 10 μm with the fraction by volume up to approximately 50%.

Magnetorheological fluid particles tend to settle under gravitational forces because they are too large for Brownian Motion to keep them suspended, and so additives such as grease or metal soaps are used to control the settling rate [12, 17, 21, 23, 30].

The suspended particles in an MR fluid become magnetized and form chain like structures, as shown in Figure 1-2 below, that align with the applied magnetic field lines. The particle chains restrict the movement of the fluid producing an apparent increase in yield strength up to 100 kPa [12, 21]. Thus, the main functional use of magnetorheological fluids is controllable shear stress. Utilizing the high strength of MR fluids has found commercial success in several areas including brakes, clutches and dampers [14, 31, 32].

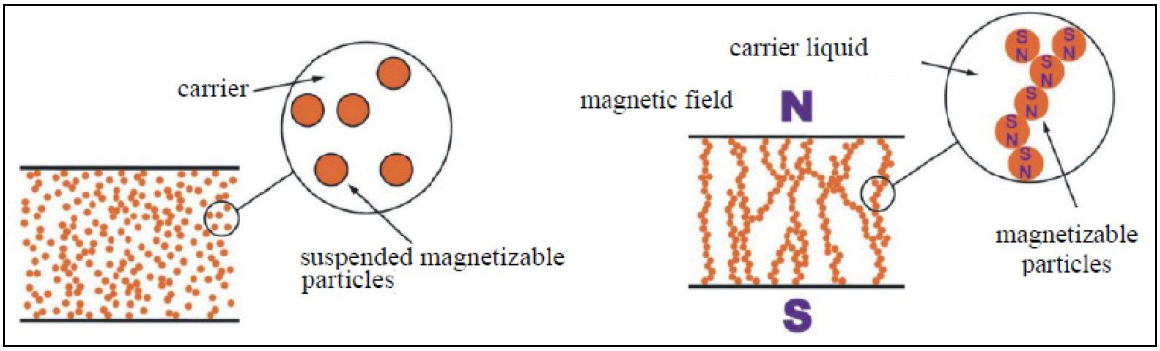

Figure 1-2 Magnetorheological Fluid Particles Chain Structure Formation [17]

The preceding paragraphs described some of the differences between ferrofluids and magnetorheological fluids in terms of function and composition. There is also a more fundamental difference between the two fluid types in terms of an energy or interaction parameter for the particles called the energy factor.

$$\lambda = \frac{\mu_o \cdot P_{mag}^2 \cdot V_{part}}{12 \cdot k \cdot T} \qquad \text{Equation 1-1}$$

When the energy factor is greater than 1, the magnetization energy is greater than the thermal energy and the inter particle interaction will lead the formation of chain structures. If the energy factor is below 1, the thermal energy dominates and the magnetic force flows the particles according to the magnetic field gradients [20, 21].

For particles with fixed magnetic moments that are not interacting with each other, a shear flow will cause the particles to rotate to align with the direction of vorticity, as shown on the left hand side of Figure 1-3. When a magnetic field is applied, the magnetic moments will try to align with the magnetic field lines. If the vorticity of the fluid is aligned with the magnetic field, the hydrodynamic force is in parallel with the magnetic moment. However, if there is a misalignment of the fluid vorticity and the magnetic field, as shown on the right hand side of Figure 1-3, the viscous friction opposes the alignment of the particles magnetic moment producing a so called magnetic torque or rotational viscosity [1, 25, 33, 34, 35].

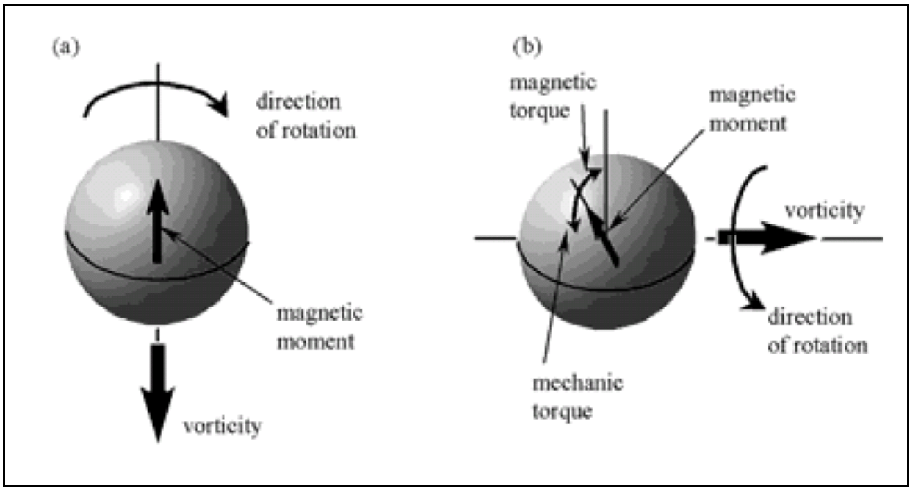

Figure 1-3 Schematic on the Origination of the Magnetoviscous Effect [25]

How the particles react to the magnetic field depends on the magnetic relaxation behavior, which depends on the shape and size of the particles. The mechanisms for relaxation are Brownian relaxation, where the whole particle rotates, and Neel relaxation, where the core's magnetic moment rotates within the particle. The respective relaxation times are given by:

$$\tau_B = \frac{3 \cdot \mu \cdot V_{eff}}{k_B \cdot T} \qquad \text{Equation 1-2}$$

$$\tau_N = \tau_A \cdot \exp\left(\frac{K \cdot V_{core}}{k_B \cdot T} \right) \qquad \text{Equation 1-3}$$

where the Brownian relaxation time is dependent on the volume of the particle including the surfactant layer and the fluid viscosity and the Neel relaxation time depends on the volume of the magnetic core and the effective anisotropy constant. The magnetic relaxation process the particle follows is determined by the shortest relaxation time. Thus, smaller particles will follow the Neel relaxation process while larger particles follow Brownian relaxation [1, 36].

The critical particle diameter to transition between Neel and Brownian relaxation is approximately 13nm. Particles below this diameter are called magnetically weak and those that follow Brownian relaxation are called magnetically hard [1, 20, 21, 36]. Obviously, only magnetically hard particles contribute to magnetic torque; however, this mechanism does not account for the observed increase in viscosity since there is particle interaction observed in the chain structures they form while a magnetic field is applied [1, 12, 20, 21, 36].

A new term, magnetoviscous effect, was introduced to identify and separate the effects of particle interaction on the viscosity of MR fluids from the magnetic torque effect [20]. For particles with diameters above the critical diameter or with an energy factor above 1, the magnetic dipole interaction is stronger than the Brownian thermal energy and the particles are able to form chain structures. A pressure difference or shear stress is required to deform or break these structures that give the fluid its apparent increase in yield strength [1, 12, 20, 21, 36]. The hydrodynamic contributions of the these structures provides an increase in viscosity with magnetic field strength, while breaking of the chain structures under increasing shear stress causes a shear thinning effect in the fluid [30, 37].

There are two general methods for producing magnetic fluids; size reduction and precipitation. Size reduction starts with larger particles mixed with a carrier liquid and a surfactant dispersing agent which are ground into smaller particles typically by adding ball grinders and centrifuging on the order of 1,000 hours [1]. Creating particles by precipitation involves, as the name implies, a chemical precipitation process. One precipitation method for producing ferrofluids is where magnetite precipitates from a chemical reaction of iron chlorides and sodium hydroxide [1]. For magnetorheological fluid particles, high purity iron particles are derived from the chemical vapor decomposition of iron penta-carbonyl [12]. A peptization step may be included to prevent the precipitated particles from agglomeration, followed by magnetic separation and filtration to separate the magnetic particles from the residual solution. Finally, a solvent is added to achieve desired concentration levels [1]. Chemical precipitation methods are much faster (on the order of hours rather than weeks) and sometimes less expensive than

the mechanical size reduction methods; however, they are limited in their possible material compounds [1].

In the absence of an applied magnetic field, MR fluids behave similar to Newtonian fluids with properties close to those of the carrier fluid [13, 23]. When a magnetic field is applied the apparent yield strength of the fluid increases with increasing field intensity until the fluid is magnetically saturated [17]. A Bingham plastic model is widely considered valid for describing the rheological behavior of MR fluids when a magnetic field is present [13, 23, 26, 38, 39]. The Bingham plastic model is a two parameter model with a yield shear stress and a viscosity. When the magnitude of the local shear stress is less than the yield strength the material behaves as a rigid body; when the yield strength is exceeded, the material flows in a Newtonian-like manner [40].

Actual MR fluid departs from both Newtonian behavior, in the absence of a magnetic field, and Bingham plastics behavior for an applied magnetic field. For example, actual MR fluids, with a magnetic field applied, behave viscoelastically with a complex modulus that has been observed to be dependent on the field intensity [30]. MR fluids also exhibit significant shear thinning where the viscosity decreases with increasing shear rate above the yield strength [30, 37]. A Herschel-Bulkley fluid model has been suggested as an alternative approach to the Bingham plastic model which utilizes a power shear rate law for the post-yield flow, while the pre-yield flow remains identical to the Bingham plastic model [26, 41, 42]. However, the deviations from the simple Bingham plastic model are considered small enough to predict macro-scale fluid behavior for MR fluids [13, 23, 30, 39].

The following research comprised of several stages in an effort to create a hydrodynamic journal bearing design that had capability to be actively controlled through the use of magnetorheological fluids. The initial stage was to design an arrangement of electromagnets such that the magnetic field lines generated by those magnets were perpendicular to the shearing forces across the fluid filled gap of the bearing. This required the magnetic field to be applied in the radial direction around the circumference of the bearing. The final design was accomplished by placing eight electromagnetic dipoles circumferentially around the bearing. The eight dipoles covered the entire circumference of the bearing and directed the field perpendicular to the fluid filled gap such that the normal magnetic field strength was nearly uniform within the fluid at the pole locations.

The next stage in this research was to create a numerical model to evaluate the performance of a hydrodynamic journal bearing using a fluid that had variable rheological properties relative to the magnetic field strength. To accomplish this, a modified Reynolds equation was derived where the fluid was modeled as a Bingham plastic, whose yield strength is proportional to the strength of the applied magnetic field. The results of the numerical model indicated that, for most speed and eccentricity ratio combinations, an increase of 20% in the load capacity was achievable relative to the baseline load capacity. The analysis also showed that an increase of 30% in the critical mass, which represents the mass the bearing can support and maintain stable operation, was achievable relative to the baseline with no magnetic field applied.

The final stage in this research was to create a bench test to provide a proof of performance for the bearing design. First, seven different samples of MR fluid were

created, which consisted of a range solid content by mass of carbonyl iron powder from approximately 2% to 75%. The samples were then analyzed in an effort to create a more complete quantification of the rheological properties of magnetorheological fluids. Next, the bearing assembly components were machined and assembled on a test bench. The evaluation of the performance of the bearing design consisted of 15 steady state conditions with operational parameters of speed and applied magnetic field as the key variables, while the bearing performance was analyzed by measuring eccentricity, torque and fluid pressure.

The results of the experimental testing indicated that, a decrease of 15% in the eccentricity ratio was achievable relative to the baseline eccentricity ratio for all speeds. Given the applied load remained constant, a decrease in eccentricity correlates to an increase in load capacity with the application of the magnetic field. The analysis also showed that an increase of up to 4.5% in the bearing torque, which represents reduction in operating efficiency when a magnetic field is applied.

CHAPTER II

REVIEW OF LITERATURE

2.1 Introduction

The durability of machine components such as gears, bearings and seals rely on a lubricating film to separate the contacting surfaces. If the separating film fails, the contacting surface can have an increase in friction, wear and can even result in seizure. The contacting surfaces found in rolling element bearings and gears, are typically non-conformal contacts and operate in the elastohydrodynamic regime with fluid films on the order of less than one millimeter. In fluid film bearings, such as journal bearings, the contacting surfaces are typically conformal and operate in the hydrostatic or hydrodynamic lubrication regime. The load carrying capacity of these bearings generally comes from the pressure generated within the lubrication film. In hydrostatic fluid film bearings the pressure is generated from an external source; while in hydrodynamic fluid film bearings, pressure is generated by the relative movement of the surfaces. The main advantage of fluid film bearings over friction or rolling element bearings are their high rigidity and low friction and wear characteristics. In both hydrostatic and hydrodynamic cases, magnetic fluids can provide improvements in performance through improved load capacity, controllable film thickness and sealing capabilities.

2.2 Hydrostatic Bearings

The conventional hydrostatic bearing is an established fluid film type bearing used in the field of machine tools. Hydrostatic bearings get their load carrying capacity from lubrication between the surfaces of a kinematic pair by means of externally supplied hydrostatic pressure. Figure 2-1 depicts the operation of a conventional hydrostatic bearing, where the recess of the bearing pad (surface 2) is fed by an external pump through a restrictor until the pressure lifts the bearing runner (surface 1). After which, a lubricant film of thickness *h* separates the surfaces and is continuously fed by the flow *Q* [43, 44].

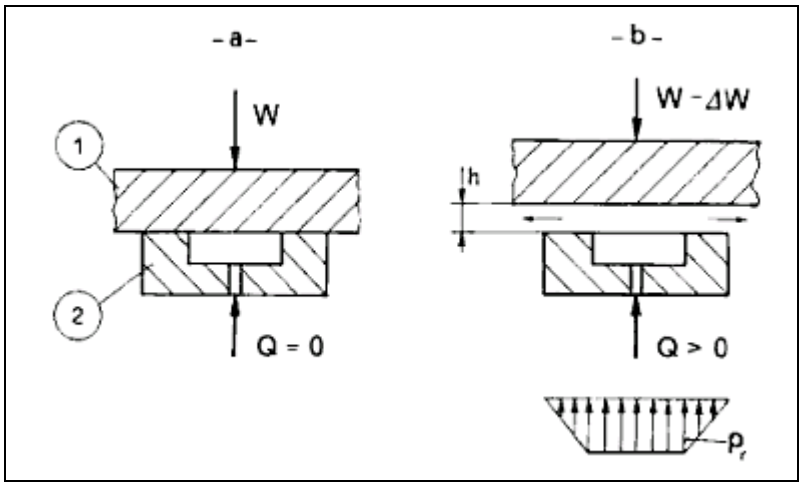

Figure 2-1 Schematic of a Axial Hydrostatic Single Pad Bearing [43]

The main advantage of hydrostatic bearings over friction or rolling element bearings are their high rigidity and low friction and wear characteristics. They can also be used when a hydrodynamic bearing cannot be used due to parallel mating surfaces or insufficient relative velocity between the separating surfaces. The key disadvantage for

the hydrostatic bearing design is the complexity of the lubrication supply circuits [43, 44].

Literature on the application of ferrofluids and MR fluids to hydrostatic bearings is scarce, perhaps in part due to the ability to control a conventional hydrostatic bearings performance without the use of such fluids [45]. However, in 2003 Hesslbach and Abel-Keilhack developed a "magnetohydrostatic" bearing, which is a hydrostatic bearing using MR fluid [46]. Hesslbach and Abel-Keilhack noted that in a conventional hydrostatic bearing, if the load changes the flow rate needs to change in order to maintain a constant gap. The time response for controlling the flow rate through external valves can be long, however; with MR fluids a magnetic field can be used to control the bearing gap from within and reduce the response time. In the study, Hesslbach and Abel-Keilhack used the Herschel-Bulkley model to show that with MR fluid inside the bearing gap, changing the applied magnetic field can be used to control the bearing gap. They then tested this theory by measuring the gap on a single pocket thrust bearing with a Lord Corporation MRF132-LD MR fluid while varying the applied thrust load and applied magnetic field. The results, which are provided in Figure 2-2 below, show that the bearing gap can be varied from 200-700μm with a small amount of power (approximately 1W). The data also showed that the bearing gap can be held constant for an increase in applied load by increasing the magnetic field as indicated by markers A and B on in the figure.

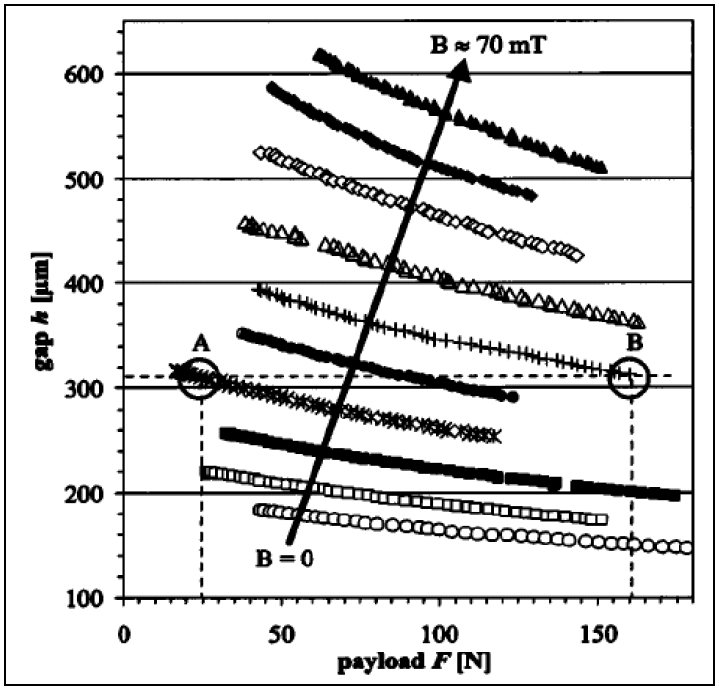

Figure 2-2 Bearing Gap Change with Load for Varying Magnetic Fields [46]

An extension of the Hesslbach and Abel-Keilhack study was completed by Guldbakke and Hesselbach in 2006 where a closed loop control was applied [47]. The bearing gap was controlled using a cascade control approach where the secondary loop controlled the magnetic field and the primary loop utilized a proportional integral derivative controller for the gap control. Figure 2-3 shows the system response with and without the controls applied. Increasing the load by 320N with the controlled system changed the gap 15µm, while increasing the load by 160N without the controls caused the gap to change by approximately 150µm. A control error of about one second was due to the necessary time to refill the decreased gap which could not be shortened. The results of this study show that nearly infinite stiffness can be achieved for hydrostatic bearings

lubricated with MR fluids, which is limited only by the resolution of the measuring system.

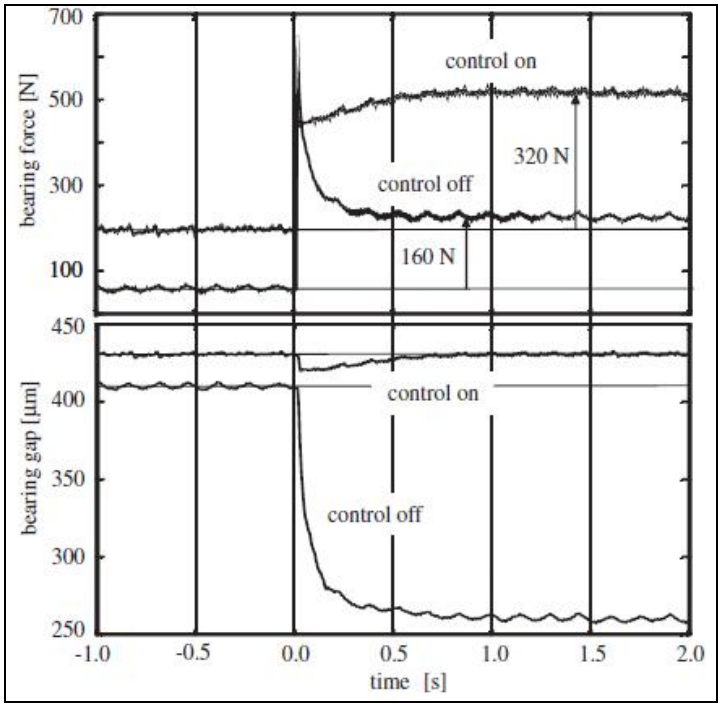

Figure 2-3 Control Characteristic of Hydrostatic Bearing with MR Fluid [47]

2.3 Hydrodynamic Bearings

Many different designs of hydrodynamic bearings exist, but in general a hydrodynamic bearing is a fluid film bearing which derives its load carrying capacity from hydrodynamic lubrication. Where hydrodynamic lubrication is the process in which two surfaces, with a relative velocity between them, are separated by a fluid film. The separating forces are generated from the pressure in the fluid film, by virtue of the surfaces relative motion [44]. The load capacity is primarily a function of the bearing geometry, the rotational speed and the properties of the working fluid [48]. Since the rotational speed is dictated by the operating conditions, the only way to actively control a

hydrodynamic bearing would be to change the bearing geometry or the fluid properties during operation. The ability to change the bearing geometry is very difficult and so there has been significant interest in the use of magnetic fluids for hydrodynamic bearings.

2.3.1 Squeeze Film Bearings with Magnetic Fluid Lubrication

Squeeze film bearings are hydrodynamic fluid film bearings where the load capacity is derived from hydrodynamic squeeze motion. In hydrodynamic squeeze motion, a positive pressure is generated in a fluid film separating two surfaces due to the relative normal velocity of the two surfaces. A load can be supported during the finite time required for the fluid to be squeezed out of the gap. A porous bearing surface is often used for a self-contained lubricant so that an external lubrication supply is not needed [49]. The advantage of using a magnetic fluid over a conventional lubricant is that the magnetic fluid can be retained on the bearing surface and increase the pressure and load capacity [50].

In 1995, Prajapti analyzed the use of ferrofluids in porous squeeze film bearings with various geometrical shapes including circular, annular, elliptical, infinitely long rectangular, conical, triangular and truncated conical [50]. The results of this study found that the load capacity and response time (the time to attain a specified film thickness) both increased with the externally applied magnetization. Prajapti also found that a bearing with magnetic fluid can support a load even when no flow is present. In 2003, Shah studied a two-step squeeze film bearing using ferrofluid lubrication [51]. The study found that with a magnetic field applied at an oblique angle, the load capacity of the bearing increased. Shah also found that the load capacity increased if the length of the

higher step was longer than the lower step with an optimum length of 80% of the total bearing length. In 2007, Patel and Deheri modeled magnetic fluids in a squeeze film bearing with porous conical plates [52]. The study found that the load capacity of the bearing decreased with increasing conical angle and porosity, while it increased with increasing magnetization. They concluded that by choosing the appropriate magnetization and conical angle combination, the system performance can be significantly improved.

Shah and Bhat, in 2000, studied magnetic fluid lubrication for curved porous squeeze film bearings with rotating circular plates [53]. This study was paired with a study in 1980, by Vora and Bhat, that analyzed the same bearing design without the use of magnetic fluids; which showed that the rotation of the circular plates reduced the load capacity of the bearing [54]. Shah and Bhat's paper also correlated to a study by Bhat and Deheria (1993) that investigated the same bearing design using magnetic fluids without rotation [55]. The analytical results of Shah and Bhat showed that the pressure and load capacity of the bearing increased with the magnetization, while the response time depended on magnetization and rotational speed. When the magnetization parameter was set to zero, the analytical results reduced to those found by Vora and Bhat. The results also matched Bhat and Deheria's study when both circular plates were not rotating. These studies, as well as many others, have shown that given the same bearing design, the use of magnetic fluids as a lubricant for squeeze film bearings, perform better than conventional lubricants by increasing load capacity and response time.

2.3.2 Slider Bearings with Magnetic Fluid Lubrication

Slider bearings are self-acting hydrodynamic fluid film bearings usually designed to support axial loads, where the load capacity is derived from linear hydrodynamic sliding motion. In linear hydrodynamic sliding motion, a positive pressure is generated in a fluid film separating two surfaces due to the relative parallel velocity of the two surfaces. In 1986, Agrawala used magnetic fluids to lubricate a porous inclined slider bearing [56]. By applying a magnetic field at an oblique angle to surface, such that the magnetic field vanished at the ends of the bearing, the magnetic fluid lubrication yielded a higher load capacity than with a conventional lubrication. Similarly, Shah and Bhat modeled a secant shaped slider bearing using the Jenkins flow behavior which also found that the load capacity increased with the magnetization without affecting the frictional force [57]. From 2003 to 2005, Shah and Bhat published a series of papers studying various geometric configurations of porous slider bearings with ferrofluid lubrication using the Jenkins model and adding a slip boundary condition at the porous surface, per a study by Beavers and Joseph on boundary conditions of a naturally permeable wall. The studies included convex surface, inclined surface, parallel surface and secant surface slider bearings [58, 59, 60, 61]. Each study found that magnetic fluid lubrication was more advantageous than conventional lubrication with load capacity and pressure increasing with magnetization. They also found that the load capacity decreases with increasing slip parameter at the porous boundary interface with the exception of the parallel slider which cannot support load with a conventional lubricant and thus the load was only dependent on the magnetization. A similar study was performed by Ahmad and Singh in 2006 for a porous pivoted slider bearing with slip velocity and magnetic fluid

lubrication [62]. The results of this study followed that of the studies by Shah and Bhat which found that load capacity and pressure increasing with magnetization and load capacity decreases with increasing slip parameter.

2.3.3 Hydrodynamic Journal Bearings with Ferrofluid Lubrication

Conventional hydrodynamic journal bearings are self-acting hydrodynamic fluid film bearings where the load capacity is derived from a rotating hydrodynamic motion. In rotating hydrodynamic motion, a positive pressure is generated in a fluid film separating a rotating inner shaft surface from a stationary outer housing due to the relative velocity of the two surfaces. Many bearing designs combine the use of ferrofluids with permanent magnets to take advantage of the fluids stiffness and damping characteristics, several of which are discussed in a paper by Ochonski [63]. Ferrofluid bearings are of particular interest for use in hard drive spindles as the increasing recording density requires smaller recording track widths and higher head positioning accuracy. Ferrofluids also have a self-sealing effect in a non-uniform magnetic field that can potentially eliminate the need for mechanical seals when used for lubrication [64].

In 1985, Huan *et al.* designed a ferrofluid lubricated journal bearing with self-sealing capabilities [65]. Flared ends were added to a conventional hydrodynamic journal bearing with a magnetic sleeve to produce a magnetic sealing effect. The flared ends generated a non-uniform magnetic field that retains the ferrofluid lubricant, as well as, serving as a reservoir for lubricant excursions. In 2000, Zhang *et al.* designed and tested a ferrofluid hydrodynamic bearing for a high speed spindle motor [28]. They determined that the shaft radius, bearing clearance and lubricant viscosity were the most significant

parameters to optimize their design. They also used a compound seal consisting of a magnetic seal and viscous pumping seal to prevent lubricant leakage. With this design they were able to lower the non-repeatable run out and eliminate side leakage. In 2002, Miwa *et al.* compared the performance of a ferrofluid hydrodynamic bearing with ball bearing and a conventional fluid bearing for a hard disk drive spindle [64]. They found that hydrodynamic bearings have lower non-repeatable run out, lower acoustic noise, higher stiffness and damping coefficients than an alternative ball bearing. Together these studies and several other studies demonstrate the key performance characteristics necessary for the continued growth of recording density that ferrofluids can offer to hard drive spindles.

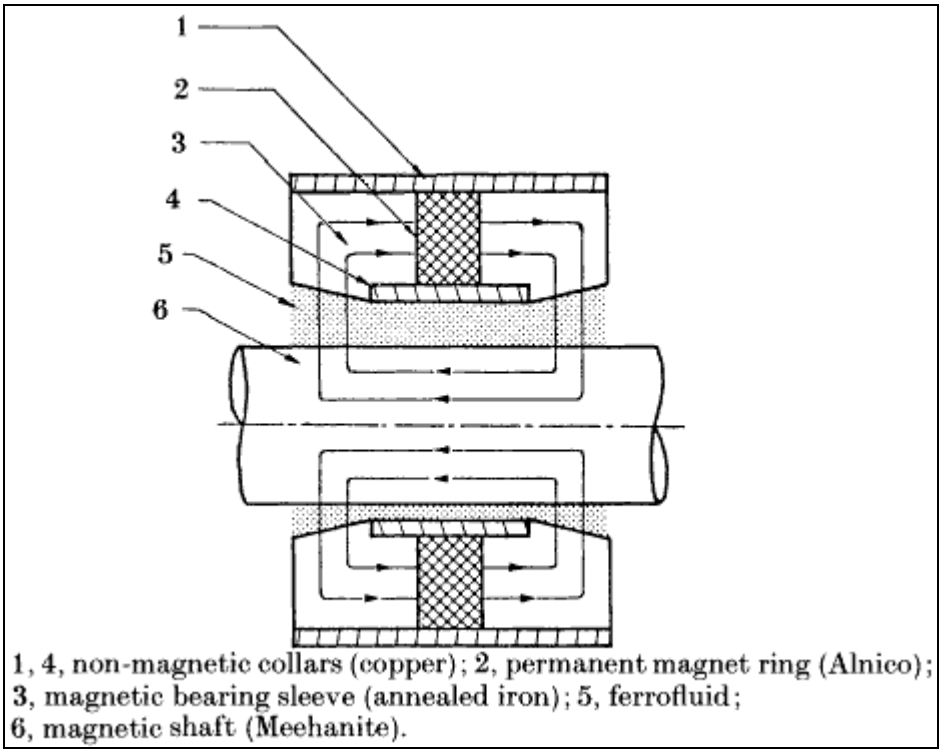

1, 4, non-magnetic collars (copper); 2, permanent magnet ring (Alnico); 3, magnetic bearing sleeve (annealed iron); 5, ferrofluid; 6, magnetic shaft (Meehanite).

Figure 2-4 Magnetic Sealing of a Ferrofluid Bearing [65]

In 2000, Osman *et al.* used a finite difference approach to solve modified Reynolds equation to analyze the performance of a hydrodynamic journal bearing lubricated with ferrofluid [66]. The study found that the use of ferrofluid lubrication increased the hydrodynamic pressure and magnetic pressure which increased the load capacity and reduced the cavitation region of the bearing. The most significant effect of the magnetic field on the load capacity was found at low eccentricity ratios. The same group of authors later published two more papers on the study of different magnetic field distribution models for hydrodynamic journal bearing lubricated with ferrofluid [67, 68]. The studies showed that bearing performance such as film pressure, load capacity and side leakage are impacted by the selection of the magnetic field distribution model used. They concluded that with the proper selection of the magnetic field model and design parameters, a significant increase in bearing performance can be achieved.

2.3.4 Hydrodynamic Journal Bearings with MR Fluid Lubrication

As previously mentioned in the introduction, magnetorheological fluids are often modeled as Bingham plastic flows when a magnetic field is applied. In 1965, Batra studied Bingham fluid lubrication in a hydrodynamic journal bearing and found that the load capacity and coefficient of friction was higher than that of a Newtonian fluid [69]. In 1991, Tichy investigated hydrodynamic lubrication theory for the Bingham plastic fluid flow model [70]. Tichy used modified Reynolds equations to study the development of floating rigid cores and rigid cores attached to the walls. Rigid cores were simply pockets of fluid that the yield strength of the Bingham fluid was not exceeded by the local shear stress. The calculation method divided the bearing into four sections based on the

velocity profile across the thickness of the fluid film, which dictates if and where a ridged core forms. If the strain rate exceeds the yield strength of the fluid across the film thickness, no core is formed. If at some point within the fluid film the strain rate does not exceed the yield strength of the fluid, a ridged core will form in one of three regions: floating in the free stream or attached to the wall of the bearing or the journal. The study found that these cores, both floating and attached, will occur in hydrodynamic journal bearings lubricated with Bingham plastic flow type fluids, specifically electrorheological fluids. Tichy concluded that control of such journal bearings was not promising due to the small effect of the fluids yield strength on the film pressure at low eccentricity ratios [70].

In 2008, Gertzos *et al.* compared the performance of Newtonian fluid to Bingham fluid lubrication in a hydrodynamic journal bearing using FLUENT, a three-dimensional computational fluid dynamics software [71]. The analysis assumed steady-state operation with laminar and isothermal flow. The half Sommerfeld boundary condition was used for the cavitation region and the software's Herschel-Bulkley model was linearized to model the Bingham fluid. The results of the analytical study were in agreement with previous theoretical and experimental work which showed that Bingham fluid lubrication increased the load capacity and film pressure of the bearing when compared to a Newtonian fluid. The study also showed the formation of rigid cores within the fluid film which were attached to the inlet surface for low eccentricity ratios and move towards the outlet side as the eccentricity was increased. They concluded that both ER and MR fluids which can be represented by the Bingham plastic flow model in their active state could be used for semi-active control of a hydrodynamic journal bearing [71].

In 2011, Bompos *et al.* expanded on Gertzos' investigation into Bingham fluid lubrication in a hydrodynamic journal bearing by simulating magnetorheological fluids (LORD Corporation MRF-132DG) using Flotran, the computational fluid dynamics suite for the ANSYS Multiphysics software [72]. The analysis assumed steady-state operation with laminar and isothermal flow. The half Sommerfeld boundary condition was used for the cavitation region and the software's bi-zone Bingham model was used to for the fluid viscosity. No inlet model was used due to the half Sommerfeld boundary condition. The ANSYS Multiphysics software was also used to solve the magnetic field which was applied using an MR fluid damper electromagnet configuration, shown in Figure 2-5, that was designed by Forte for rotor applications [73]. Several length to diameter ratios were evaluated ranging from ¼ to 2, with current intensities of 14A and 28A applied to the electromagnets. Applying the same current intensities, to varying length to diameter ratios designs, resulted in stronger magnetic fields being applied to the shorter length bearings. The most significant changes in performance were found in the lowest length to diameter ratio (strongest applied magnetic field) of ¼ and highest eccentricity ratio of 0.8, with an increase in bearing load of up to 36% and an increase in the friction coefficient of up to 22%. The study concluded that beneficial results can be found using MR fluids in journal bearings, although increased energy costs due to higher friction and electromagnets should be considered [72].

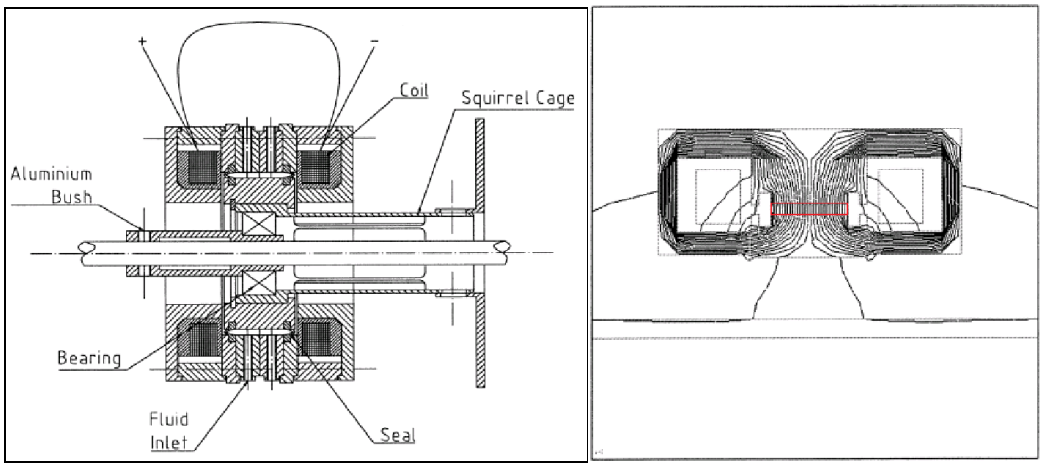

Figure 2-5 MR Fluid Damper Design and Two Dimensional Flux Lines [73]

In 2009, Urreta *et al.* investigated the use of both ferrofluids (FERROTEC APG s10n) and magnetorheological fluids (LORD Corporation MRF-122-2ED) in hydrodynamic journal bearings and demonstrated that magnetorheological fluids could be used to develop an actively controlled journal bearing with limitations to bearing speed and eccentricity [74, 75]. The results of both experimental and theoretical analysis of the ferrofluid lubrication showed there was minimal effect on the bearing load capacity when the magnetic field was applied. It can be observed in the results shown in Figure 2-6, the measured load capacity remained nearly unchanged and only a slight increase in the theoretical load capacity with the applied magnetic field. This is the result of the relatively limited rheological response of the ferrofluid lubrication.

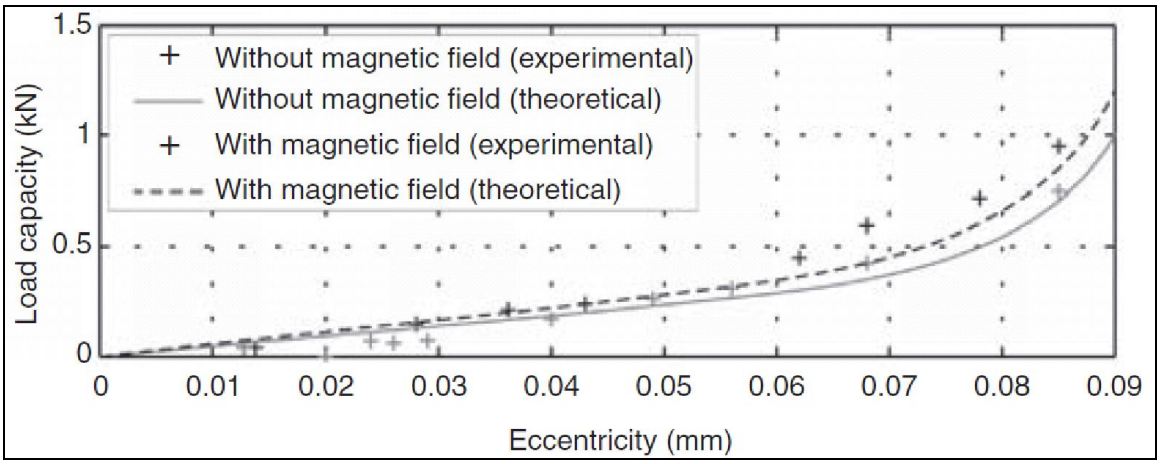

Figure 2-6 Capacity Verses Eccentricity Ratio at 100rpm with Ferrofluid Lubrication [75]

For the magnetorheological fluid portion of the study, Urreta *et al.* included a comparison of axial and radial magnetic fields applied across the fluid film by using a non-magnetic stainless steel shaft and a carbon steel shaft as shown in Figure 2-7. The non-magnetic stainless steel shaft inhibited the magnetic field when compared to the magnetic carbon steel shaft, resulting in the magnetic field being aligned in the axial direction within the fluid film. The results for the stainless steel shaft showed the application of the magnetic field had minimal effect on the bearing load capacity. The results for the carbon steel shaft, which permitted the magnetic field in the radial direction within the fluid film, showed measurable impact on both the load capacity and the displacement.

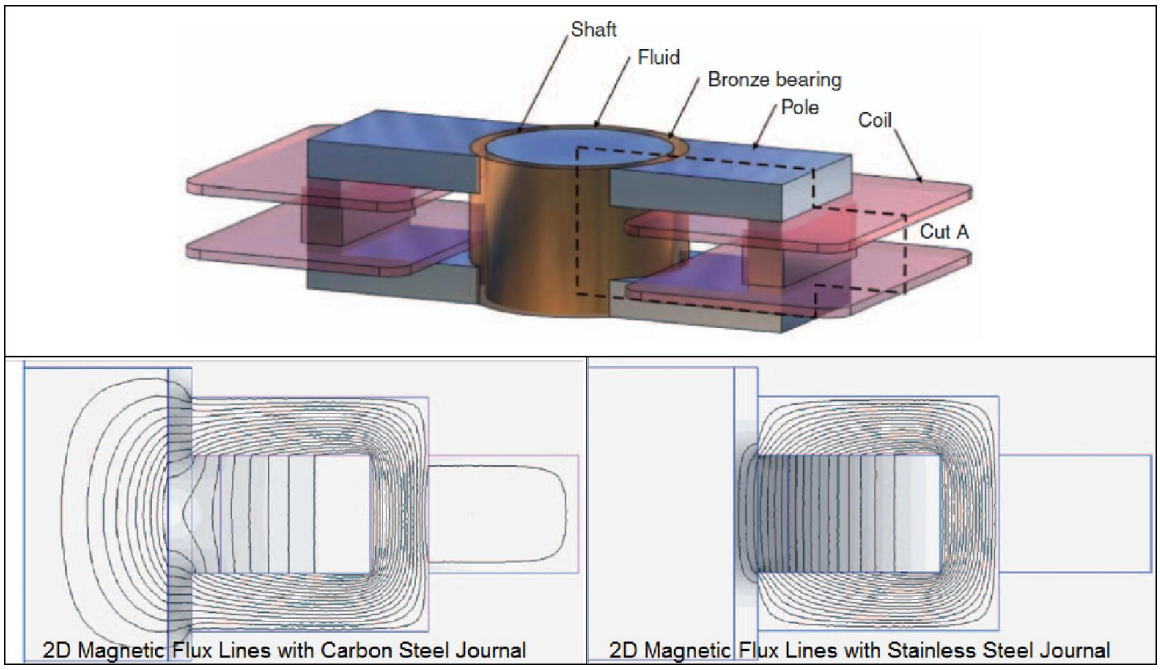

Figure 2-7 MR Fluid Journal Bearing and Two Dimensional Flux Lines [75]

Figure 2-8 shows the results of the load capacity for the magnetorheological fluid with the carbon steel shaft with respect to the bearing eccentricity. The results show that with the proper application of the magnetic field the load capacity increases, particularly at higher eccentricities. The theoretical results obtained followed Tichy's approach of calculating the pressure gradient according to the velocity distribution at different sections of the bearing [70]. As Figure 2-8 shows, the experimental load capacity results do not agree well with the analytical results for some higher eccentricities. The study concludes that magnetorheological fluids, with proper application of magnetic fields, can increase the operational range and achieve good performance for an actively controlled hydrodynamic journal bearing [74, 75].

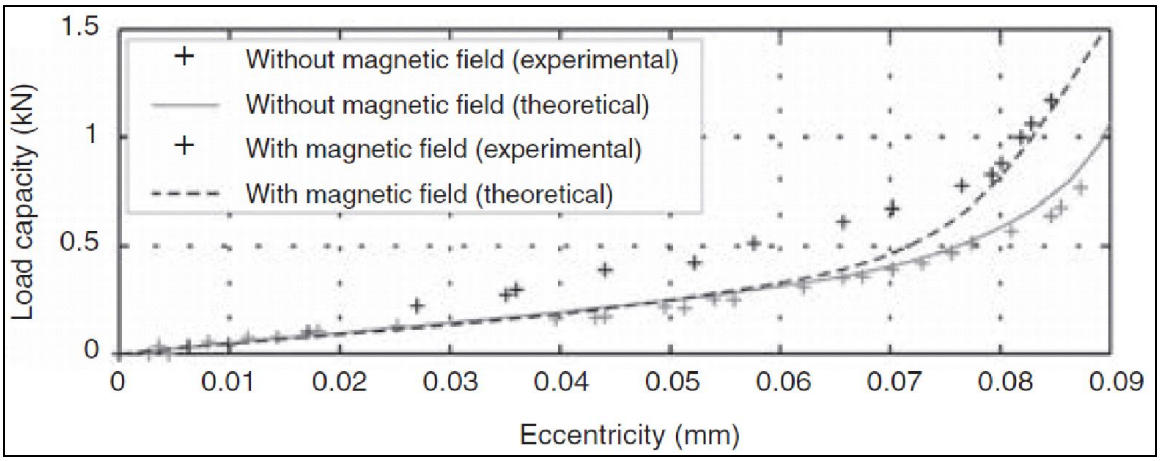

Figure 2-8 Capacity Verses Eccentricity Ratio at 200rpm with MR Fluid Lubrication [75]

CHAPTER III

NUMERICAL SETUP & PROCEDURES

3.1 Introduction

Many efforts have been presented to model fluid film lubrication, beginning in 1886, when Reynolds presented a mathematical model to represent the experimental results of Tower's study of a loaded hydrodynamic journal bearing [76, 77]. Reynolds developed a simplified version of the Navier-Stokes equations to solve the pressure gradient within a fluid film bearing which is referred to as the "Reynolds equation." Since that time, several individuals have improved upon the Reynolds equation; including Cope (1949) who accounted for the thermal wedge effect by coupling the Reynolds equation and the energy equation, and Dowson (1962) who developed the first generalized Reynolds equation which allowed the properties to vary across the fluid film [78, 79]. In this study, the "classical" Reynolds equation is augmented to include the effects of cavitation, in the form of the Elrod cavitation model, lubrication inlet feed and MR fluids for the limiting case of a hydrodynamic journal bearing.

The geometry of a journal bearing is shown in Figure 3-1. The end view on the right hand side of Figure 3-1 shows, the journal does not typically run concentric with the bearing. The eccentric position of the journal within the bearing clearance is determined by the load, rotational speed and the properties of the working fluid. The fixed coordinate

system shown in Figure 3-1 does not change, while the rotating coordinate system (not shown) is rotated by the attitude angle Φ and aligns with the line of centers. Where the attitude angle, is the angle which the load vector must be rotated in order to align it with the bearing and journal's center points (line of centers).

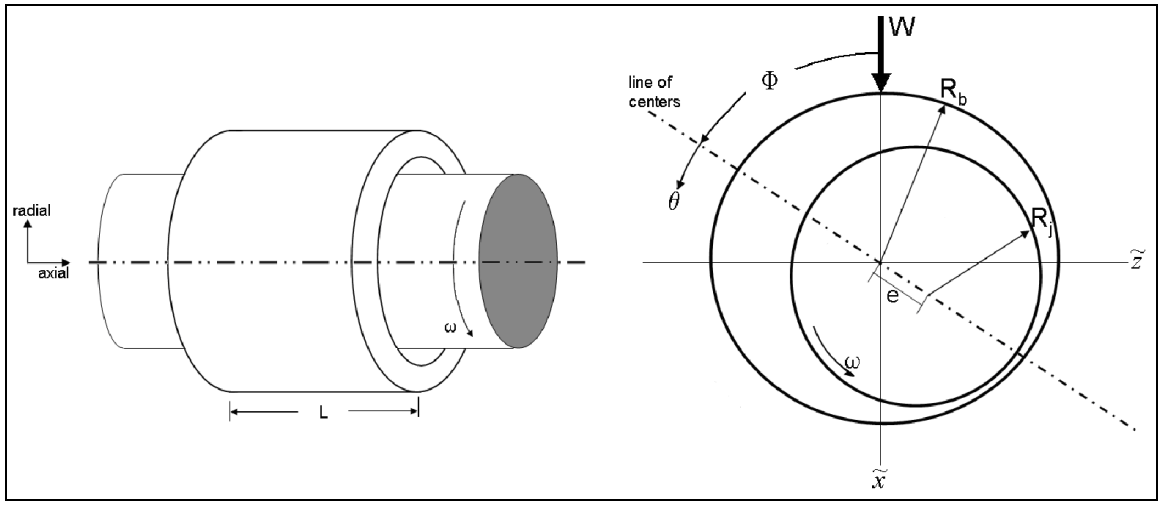

Figure 3-1 Hydrodynamic Journal Bearing Geometry

3.2 Derivation Reynolds Equation for Steady State Conditions

In 1886, Osborne Reynolds proposed the first mathematical model to solve the pressure within a journal bearing that respected the continuity of mass and momentum. The full Navier-Stokes equations are prohibitively complicated for analytical solutions to be found for most fluids problems. Thus, Reynolds used the dominating pressure and viscous terms to reduce the Navier-Stokes and mass continuity equations to the "classical" Reynolds equation. A more detailed summary of the analysis used to determine the validity of the Reynolds assumptions is provided in Appendix A. A review of Reynolds simplifying assumptions are listed below.

Reynolds' Assumptions [76]:

- The fluid flow is free of eddies or sinuosities (laminar flow).
- There is no slip on the boundary between the solid surfaces and the working fluid.
- The forces from weight and inertia are negligibly small compared to viscous forces.
- The working fluids density is constant (incompressible).
- The radius of curvature is large relative to the clearance which, allows curvature to be ignored and the use of Cartesian coordinates.
- The variation of velocity, pressure, and fluid properties across the clearance are small compared to the axial and circumferential directions and thus can be neglected.
- The viscosity of the working fluid is constant and the fluid is Newtonian, which originates from the Navier-Stoke assumptions.

Since the model is not coupled with the Energy equation, the fluid film is also assumed to be isothermal. The result of these assumptions being applied to the Navier-Stokes equations and the mass continuity equation yields the Reynolds equation shown below. The first two terms are the Poiseuille type terms and represent the pressure gradient in the circumferential and axial directions; the source term on the right hand side is the Couette type term and represents the fluid entrainment from the moving boundary [48, 76, 80].

$$\frac{\partial}{\partial x}\left(\frac{h^3}{\mu}\frac{\partial p}{\partial x}\right)+\frac{\partial}{\partial y}\left(\frac{h^3}{\mu}\frac{\partial p}{\partial y}\right)=6U\frac{\partial h}{\partial x} \qquad \text{Equation 3-1}$$

3.2.1 Modified Reynolds Equation for Bingham Plastic Fluids

The Reynolds equation can be derived by several approaches; however, in this section the modified Reynolds equation is derived directly from the Navier-Stokes and continuity equations. The full derivation of the final modified Reynolds equation can be found in Appendix B. Applying the simplifying Reynolds assumptions previously outlined and using the coordinate system shown in Figure 3-2, the Navier-Stokes equations reduce to:

$$\frac{\partial p}{\partial x_i} = \frac{\partial \tau_{ji}}{\partial x_j} \qquad \text{Equation 3-2}$$

To ensure the simplifying assumptions used to reduce the Navier-Stokes equations to the Reynolds equation are valid, an order of magnitude analysis should be performed. A summary of the order of magnitude analysis used to determine the validity of the Reynolds assumptions for the bearing design and operating conditions discussed in this paper, is provided in Appendix A.

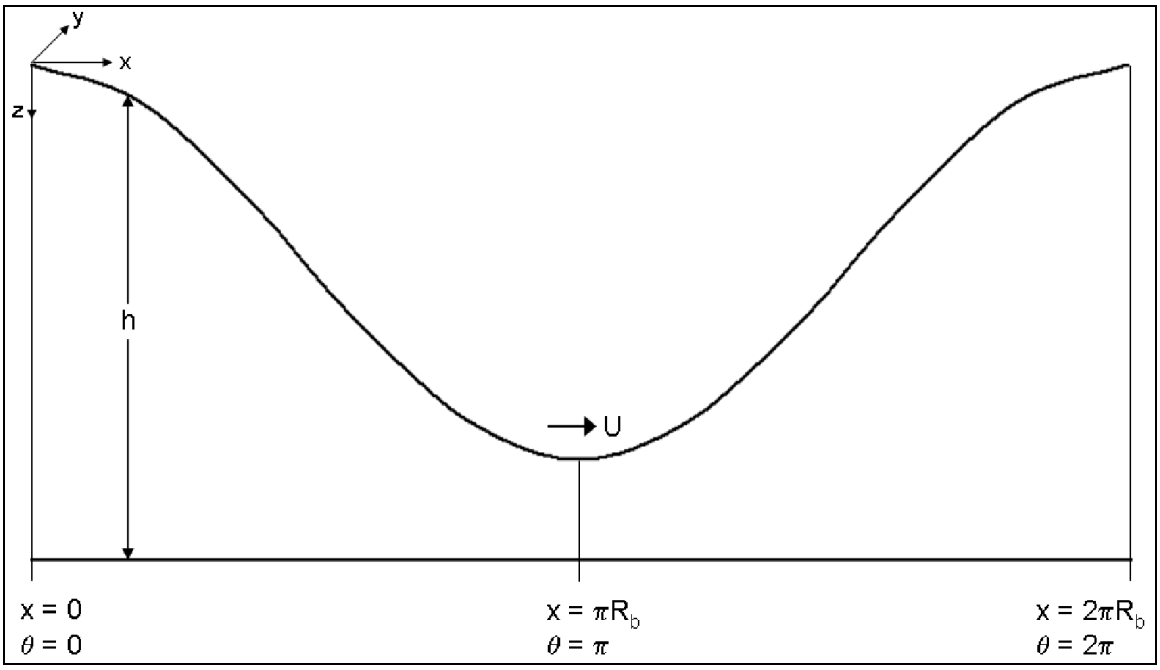

Figure 3-2 Unwrapped Fluid Film Cross Section

The addition of magnetorheological fluids to the operation of the hydrodynamic journal bearing requires modification of the Reynolds equation to account for the variable rheological properties. To account for this variability, the fluid was modeled as a Bingham plastic, whose yield strength is proportional to the strength of the applied magnetic field. A Bingham plastic is a viscoplastic that behaves as a ridged body at relatively small applied stresses, but flows as a viscous fluid at higher applied stresses. For the hydrodynamic journal bearing, the fluid behaves as a semi-sold anywhere the strain rate applied from the journal rotation is smaller than the yield strength of the fluid and flows as a viscous fluid anywhere the strain rate exceeds the yield strength. This requires the Newtonian shear stress terms, in the derivation of the Reynolds equation, to be replaced with a shear stress representative of a Bingham plastic as shown in the equation below.

$$\tau_{ji} = H(|\dot{\gamma}|)\left(\mu\frac{\partial v_i}{\partial x_j} + \mathrm{sgn}(\dot{\gamma})\cdot\tau_o\right) \qquad \text{Equation 3-3}$$

where H is a Heaviside step function called the shear switching function, dependent on the strain rate; and τ_o is the yield strength of the magnetorheological fluid, which is a function of the applied magnetic field, as shown in Figure 3-3.

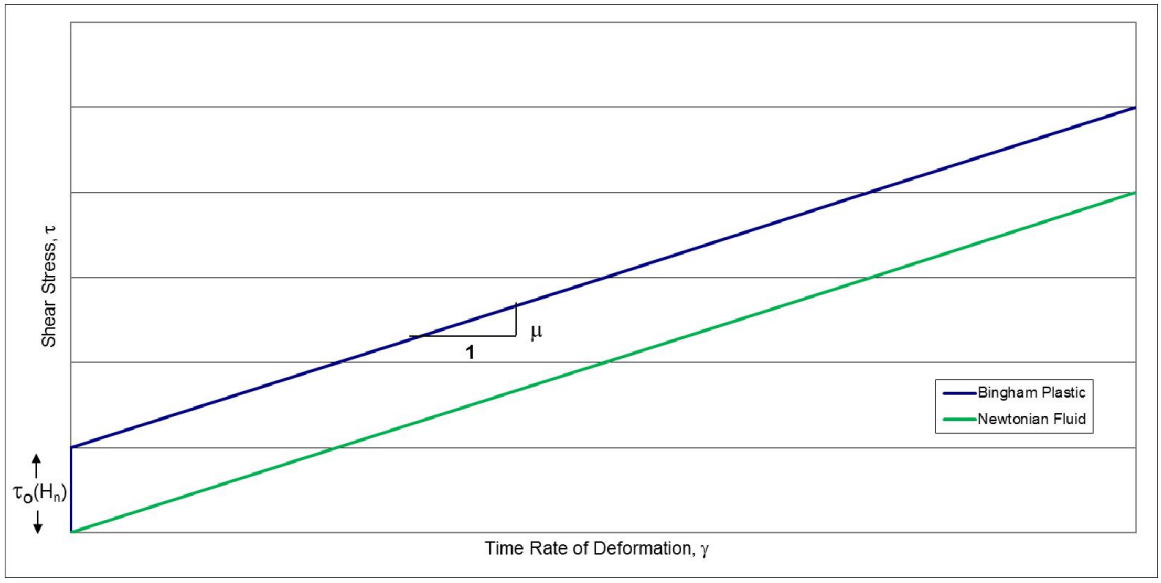

Figure 3-3 Newtonian Fluid Compared to a Bingham Plastic with Magnetic Field Dependent Yield Strength

Using the boundary conditions, the circumferential and axial velocities can be solved by integration of the simplified Navier-Stokes equations.

$$u = \frac{1}{2\mu\cdot H(|\dot{\gamma}|)}\frac{\partial p}{\partial x}\left(z^2 - hz\right) - \frac{z}{h}U + U \qquad \text{Equation 3-4}$$

$$v = \frac{1}{2\mu\cdot H(|\dot{\gamma}|)}\frac{\partial p}{\partial y}\left(z^2 - hz\right) \qquad \text{Equation 3-5}$$

where the boundary conditions, which can be observed in Figure 3-2, are as follows:

$$BC: \quad \begin{array}{lll} z = 0 & u = U & v = 0 \\ z = h & u = 0 & v = 0 \end{array}$$

The velocities are then inserted into the continuity equation which is then integrated using Leibniz rule to yield the modified Reynolds equation.

$$\frac{\partial}{\partial x}\left(\frac{h^3}{\mu \cdot H\left(|\dot{\gamma}|\right)}\frac{\partial p}{\partial x}\right)+\frac{\partial}{\partial y}\left(\frac{h^3}{\mu \cdot H\left(|\dot{\gamma}|\right)}\frac{\partial p}{\partial y}\right)=6U\frac{\partial h}{\partial x}-12\frac{\partial h}{\partial t} \qquad \text{Equation 3-6}$$

where the temporal term on the right hand side results from the integration of the radial velocity term in the continuity equation.

3.2.2 Modified Reynolds Equation with Lubrication Inlet Source Term

The lubrication within a journal bearing is forced in and out of the axial ends of the bearing in the diverging and converging sections respectively. Thus, there is a need to supply lubrication to the bearing; which is done through an inlet orifice located at the axial line of symmetry for the bearing considered in this paper. In 1997, Santos and Russo proposed a modeling method for radial oil injection for a tilting pad journal bearing. They modeled the oil injection by applying velocity boundary conditions at the oil injection locations and assuming the radial velocity profile was that of a fully developed laminar flow in an axis-symmetric pipe [81].

Santos and Russo assumed the differential pressure at the injection location was proportional to the difference of the injection pressure and the bearing pressure. By applying these assumptions to the derivation of the Reynolds equation, they developed a modified Reynolds equation with an additional pressure term that accounted for the

pressure variation at the oil injection inlets. The additional pressure terms in the Reynolds equation were activated by using the switching function described below [81].

$$\Im(x,y)=\begin{cases}\dfrac{d_o^2}{4}-(x-x_i)^2-(y-y_i)^2, & if\ (x-x_i)^2-(y-y_i)^2<\dfrac{d_o^2}{4}\\ 0, & if\ (x-x_i)^2-(y-y_i)^2\geq\dfrac{d_o^2}{4}\end{cases} \qquad \text{Equation 3-7}$$

where (x_i, y_i) are the coordinates of the oil injection inlets and d_o is the diameter of the oil injection orifice.

The same model used by Santos and Russo proposed for modeling radial oil injections for a tilting pad journal bearing can be similarly applied to a plain journal bearing. Using the new boundary conditions for the radial direction, the radial velocity can be solved by integration of the simplified Navier-Stokes equations.

$$w=\frac{h-z}{h}w+\frac{z}{h}w_{inj} \qquad \text{Equation 3-8}$$

$$BC:\quad \begin{aligned} z&=0 & w&=\frac{\partial h}{\partial t}=w\\ z&=h & w&=w_{inj}(x,y)\end{aligned}$$

where the injection velocity is:

$$w_{inj}(x,y)=\begin{cases}-\dfrac{1}{4\mu}\dfrac{\partial p}{\partial z}\left(\dfrac{d_o^2}{4}-(x-x_i)^2-(y-y_i)^2\right), & inside\ inlet\ orifice\ diameter\\ 0, & outside\ inlet\ orifice\ diameter\end{cases}$$

Equation 3-9

and the differential pressure is assumed to be:

$$\frac{\partial p}{\partial z} \approx \frac{p_{inj} - p}{l_o} \qquad \text{Equation 3-10}$$

The new radial velocity equation is then inserted into the continuity equation with the circumferential and axial velocities equations found in the previous section, which is integrated as before to yield the new modified Reynolds equation.

$$\frac{\partial}{\partial x}\left(\frac{h^3}{\mu \cdot H(|\dot{\gamma}|)}\frac{\partial p}{\partial x}\right) + \frac{\partial}{\partial y}\left(\frac{h^3}{\mu \cdot H(|\dot{\gamma}|)}\frac{\partial p}{\partial y}\right) - \frac{3}{\mu l_o} p \cdot \Im = 6U\frac{\partial h}{\partial x} - 12\frac{\partial h}{\partial t} - \frac{3}{\mu l_o} p_{inj} \cdot \Im$$

Equation 3-11

where the switching function for the lubrication inlet is the same as for the tilting pad journal bearing given in Equation 3-7.

The new modified Reynolds equation accounts for the variable rheological properties of the magnetorheological fluids and accounts for the pressure change at an arbitrary inlet location in a single equation. This allows one to solve for the pressure distribution within the journal bearing for varying applied magnetic fields and inlet pressures. The full derivation of the modified Reynolds equation in Equation 3-11, can be found in Appendix B.

3.3 Cavitation Model

The classical Reynolds equation from 1886, modeled a complete uninterrupted fluid film around the circumference of the bearing. This limiting case avoids the difficulties that arise when a rupture of the continuous fluid film, called cavitation, occurs

in the diverging low pressure region of the bearing; where the tensile stresses are higher than the tensile strength of the fluid [82]. The cavitation bubbles can originate from dissolved gasses within the fluid film or can be fed by the environment. Regardless of the origins of the cavitation bubbles, the discontinuity presents a problem for the solution of the Reynolds equation [83].

There are three types of cavitation: Pseudo-cavitation, gaseous cavitation and vaporous cavitation. Pseudo-cavitation occurs when the pressures in the low pressure divergent portion of the bearing decrease such that the microscopic gas bubbles, which exist independently within the working fluid, can grow and coalesce to form larger gas bubbles. Gaseous cavitation occurs if the pressure continues to decrease until one or several species of gases, such as oxygen or nitrogen, that are dissolved in the working fluid form gaseous bubbles as their respective partial pressures are reached. Finally, vaporous cavitation occurs if the pressure decreases further such that the vapor pressure of the working fluid is reached causing the working fluid to vaporize [83].

The first attempt to model the cavitation region of a hydrodynamic journal bearing was performed by Gumbel in 1914. Gumbel's approach was to set the pressure equal to a predetermined constant cavitation pressure for the entire divergent section of the bearing [84]. This model is also known as the half Sommerfeld condition because it only considers the positive pressure portion of the full Sommerfeld condition as shown in Figure 3-4 .

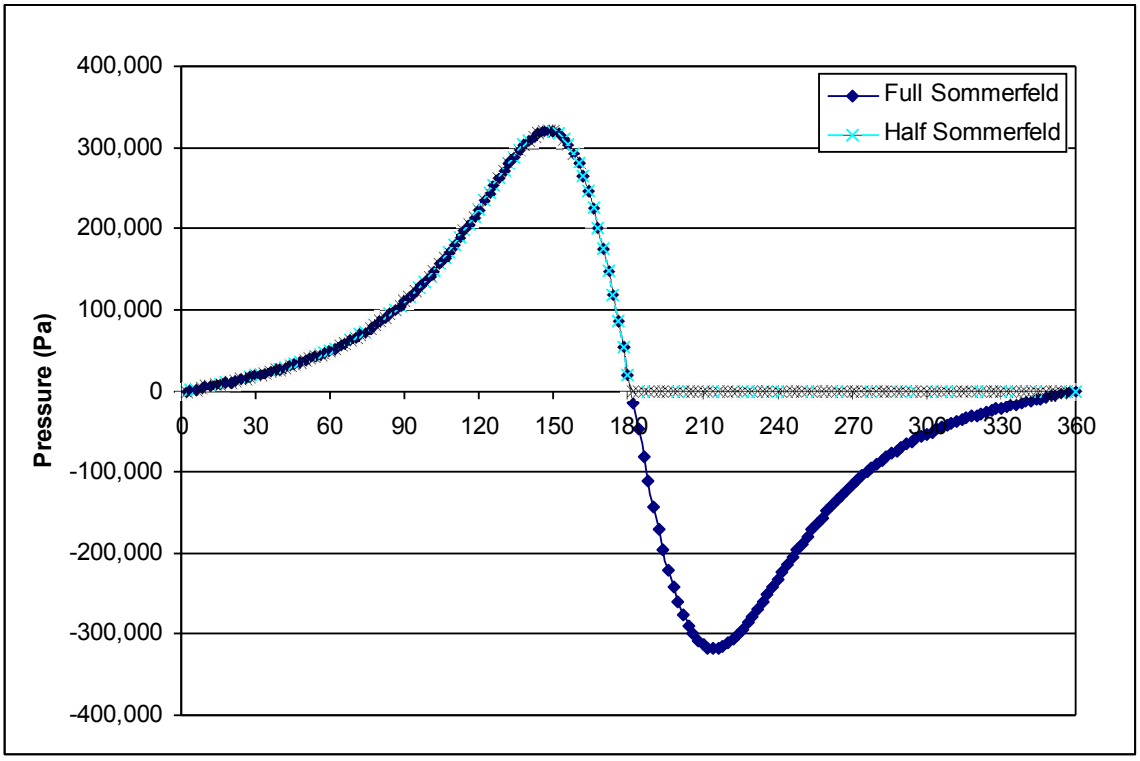

Figure 3-4 Two Dimensional Sommerfeld Curves Representative of the Circumferential Pressure Distribution at the Axial Line of Symmetry

In 1932, Swift provided an alternative model for the initiation of the cavitation region. Swift stated that the pressure derivative is zero at the start of cavitation in the divergent region [85]. Swift considered this a stability condition; however, it is actually a continuity condition for a continuous fluid film. Separately in 1933, Stieber also proposed that the zero pressure gradient marks the initiation of cavitation, but as a continuity condition [86]. The zero pressure gradient conditions, known as the Swift-Stieber conditions, work well in identifying the initiation of cavitation at lighter loads; however, it gives inaccurate results at heavier loads where the influence of sub-cavitational pressures are more significant [82]. They also do not predict the reformation of the fluid film or provide accurate results for dynamically loaded bearings [87].

Jakobsson, Floberg and Olsson developed a cavitation model, referred to as the JFO cavitation theory; this not only accounted for the initiation of cavitation, but also respects mass conservation and accounts for the reformation of the fluid film. Their theory assumed that the fluid was transported through the cavitated region in striations that extended across the clearance between the two surfaces. The JFO theory sets the pressure within the cavitated region to be constant which makes the mass flow a Couette flow [88, 89]. Although Etsion and Ludwig have experimentally found pressure variations within cavitated regions up 50kPa, the JFO theory is one of the best models available for journal bearings with cavitating fluid films [90].

3.3.1 The Elrod Cavitation Model

Unfortunately, the JFO theory is difficult to apply, however, Elrod and Adams developed a technique, called the Elrod algorithm, which numerically uses the JFO concept, but simplifies it to a single equation. It does so by making use of a switching function that removes the pressure gradient terms in the Reynolds equation at cavitated points. By using mass conserving boundary conditions from the JFO theory, the Elrod algorithm respects mass continuity, while using a single equation for both the full fluid film and cavitated regions [91, 92].

Other models have been developed for cavitation since Elrod, but most still follow in the same approach as the Elrod algorithm. The cavitation model used in this paper was developed in 1989 by Keith and Vijayaraghavan [93] which used the JFO theory and Elrod algorithm to further simplify the cavitation model, by coupling the bulk modulus with the switch function and density such that:

$$g\beta = \rho \frac{\partial p}{\partial \rho} \qquad \text{Equation 3-12}$$

where g is the switching function used in the Elrod algorithm:

$$g = \begin{cases} 1, \textit{ in the full film region} \\ 0, \textit{ in the cavitated region} \end{cases}$$

Equation 3-12 can be directly integrated to obtain an expression for pressure:

$$p = p_c + g \cdot \beta \cdot \ln(\Theta) \qquad \text{Equation 3-13}$$

where Θ is the dimensionless density ratio and p_c is the cavitation pressure. Applying this expression for pressure to the Reynolds equation yields:

$$g \cdot \frac{\partial}{\partial x}\left(\frac{\beta h^3}{\mu} \frac{\partial \Theta}{\partial x} \right) + g \cdot \frac{\partial}{\partial y}\left(\frac{\beta h^3}{\mu} \frac{\partial \Theta}{\partial y} \right) = 6U \frac{\partial \Theta h}{\partial x} - 12 \frac{\partial \Theta h}{\partial t} \qquad \text{Equation 3-14}$$

The density ratio warrants some further discussion as to how it is interpreted within the full film compared to the cavitation region. Within the full fluid film region, Θ is greater than one and represent the ratio of the density to the cavitation density. In the cavitation region, Θ is less than one; however, it does not represent the density below the cavitation density. Instead, within the cavitated region, Θ represents the fractional film content and 1- Θ represents the void fraction [93].

3.3.2 Coupling of the Cavitation Model and Modified Reynolds Equation

The Elrod algorithm is solved in terms of the density ratio and then finds pressure from the bulk modulus relation. However, it is more convenient to have pressure rather

than density ratio as the dependent variable. Applying the Elrod algorithm to the modified Reynolds equation in terms of pressure yields:

$$g \cdot \frac{\partial}{\partial x}\left(\frac{h^3}{\mu \cdot H\left(\left|\dot{\gamma}\right|\right)} \frac{\partial p}{\partial x} \right) + g \cdot \frac{\partial}{\partial y}\left(\frac{h^3}{\mu \cdot H\left(\left|\dot{\gamma}\right|\right)} \frac{\partial p}{\partial y} \right) - g \cdot \frac{3}{\mu l_o} p \cdot \Im = 6U \frac{\partial h}{\partial x} - 12 \frac{\partial h}{\partial t} - \frac{3}{\mu l_o} p_{inj} \cdot \Im$$

Equation 3-15

For the full film region the switch function is set to one; however, unlike the Elrod algorithm, the switch function is dependent on the pressure rather than the density ratio. If the local pressure drops below the predetermined cavitation pressure, the switch function is set to zero and the pressure is set equal to the cavitation pressure.

$$g = \begin{cases} 1, & \textit{full film region } \left(\textit{calculated } p > p_c\right) \\ 0 \;\&\; p = p_c, & \textit{cavitated region } \left(\textit{calculated } p \le p_c\right) \end{cases}$$

Equation 3-16

The application of the Elrod algorithm to the modified Reynolds equation in terms of pressure warrants some further discussion, as it is necessary to use a slightly different solution method.

1. Assume an initial pressure distribution
2. Solve the pressure distribution using Equation 3-15
3. Determine the cavitation switching function using Equation 3-16
4. Return to step 2 until the pressure solution has converged

This method is very similar to the Elrod algorithm with pressure as the dependent variable. Like the Elrod algorithm this method uses a single equation by making use of a switching function that removes the pressure gradient terms in the Reynolds equation at cavitated points. It also respects mass continuity without having to apply boundary

conditions to the fluid-gas interface. The full derivation of the modified Reynolds equation including the cavitation model can be found in Appendix B.

3.4 Electromagnetic Field Application

Magnetic induction, or a magnetic field, is a change in energy within a volume of space that is produced when there is an electrical charge in motion [94]. This motion can be produced by a current flowing through a conductor, as discovered by Hans Christian Oersted in 1820, or the orbital motions and spins of electrons in a permanent magnet of which Petrus Peregrinus de Maricourt is often credited for recording the first experiments in 1269 [94, 95, 96]. Magnetic fields are represented by a vector field having a magnitude and direction which can be detected by the acceleration of a charged particle, the force on a current carrying wire or the torque on a magnetic dipole. The magnetic induction (magnetic flux density, B) and the magnetic field (magnetizing field or magnetic field intensity, H) can be defined in terms of currents or poles; however, this paper will focus only in terms of the generation due to electrical current [94, 97].

Magnetic fields are visually represented by magnetic field lines. These lines are purely conceptual, but represent the magnitude and direction of the magnetic field for an area. The direction of these lines can also be experimentally observed using the needle of a compass or magnetic powders [94, 98]. Examples of magnetic field patterns detected by iron filings around a straight conductor, a single circular loop and a solenoid are shown in Figure 3-5 below.

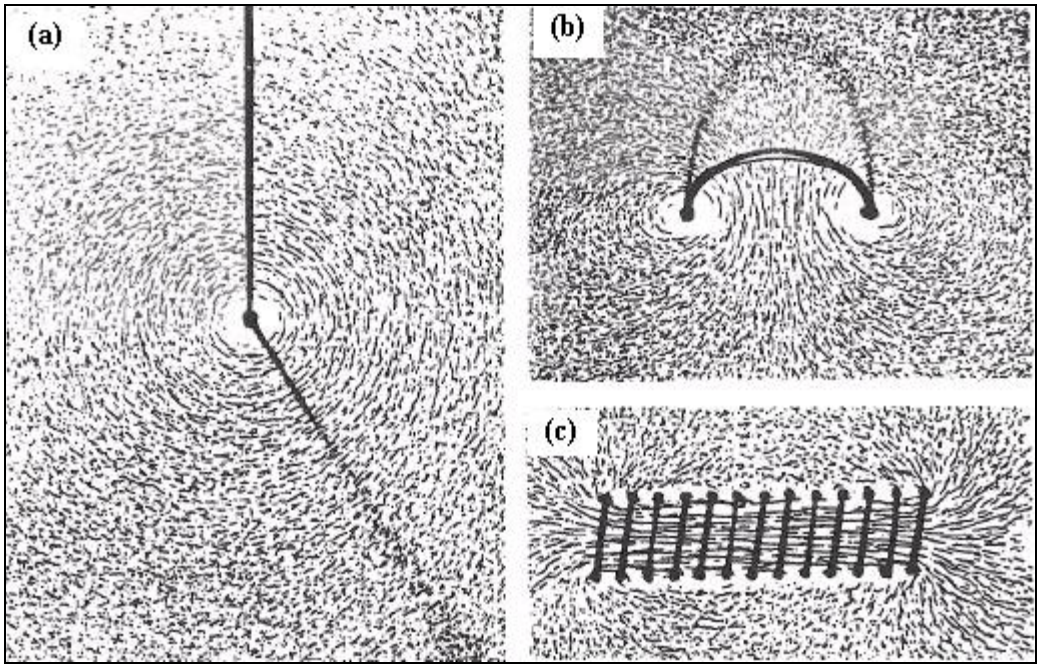

Figure 3-5 Various Magnetic Field Patterns Observed Using Iron Filings [94]

Although magnetic field lines are purely conceptual, they do provide a simple way to estimate the magnetic field at any point in the diagram. They also display important properties of magnetic fields for a particular situation and for magnetic fields in general. For example, one can observe that the magnetic field is always perpendicular to the flow of the current, which can be seen in the examples in Figure 3-5 above. One can also observe that magnetic field lines do not have end points, they either form a closed loop or extend infinitely outward. This is because the magnetic field is a solenoidal vector field [94, 98].

The geometries of current carrying conductors can be altered to achieve different magnetic fields. As shown on the left hand side of Figure 3-5 above, a long straight conductor produces a circular magnetic field pattern which decreases with the radial distance away from the conductor. That conductor can be bent into the shape of a loop, as

shown on the upper right hand side of Figure 3-5 above, and the opposing current directions work together to produce a straight magnetic field line along the axis. Then multiple loops can be linked together to form a solenoid, as shown on the lower right hand side of Figure 3-5 above, to produce a relatively uniform magnetic field within the middle 50% [94, 98]. The magnetic field outside of a solenoid is nearly zero because the opposing currents cancel out the magnetic field [99]. Another way to produce a uniform magnetic field is with two flat coaxial coils configured in a Helmholz pair. Both coils contain the same number of turns with the current flowing in the same direction as shown in Figure 3-6 below. The distance between the coils in a Helmholz pair is equal to their common radius [94].

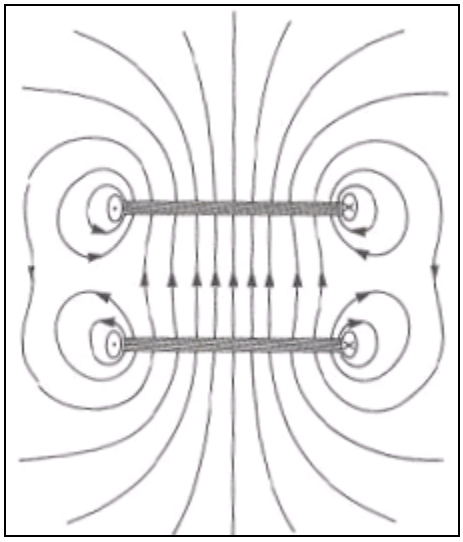

Figure 3-6 Magnetic Field Lines for a Helmholz Pair [94]

An electromagnet is a magnet where the magnetic field is produced by the flow of an electrical current through a conductor. This allows the magnetic field to be rapidly changed by controlling the electrical current. The magnetic field of an electromagnet can be increased if the electrical conductor is wound in a coil around a ferromagnetic material

as shown in Figure 3-7 below. The remainder of this section will primarily focus on ferromagnetic materials.

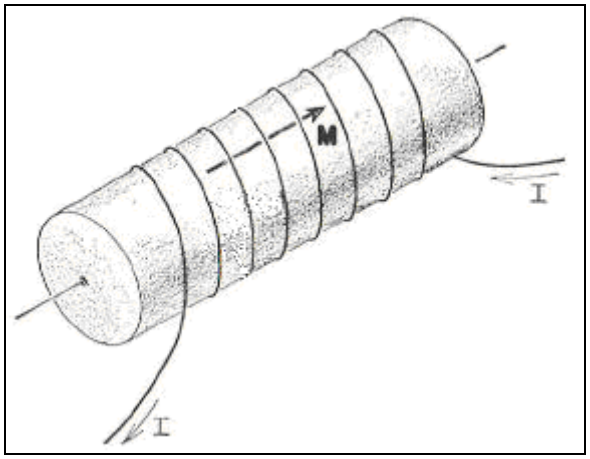

Figure 3-7 Coil Carrying an Electrical Current Polarizing a Core of Magnetic Material [98]

Electrons orbiting around a nucleus of an atom are similar to an atomically small current carrying loop. This would indicate that all materials would have magnetic effects; however, in most materials this effect is very weak. Materials are classified as diamagnetic, paramagnetic or ferromagnetic depending on their magnetic behavior. Diamagnetic materials have a weak magnetic effect that opposes the applied magnetic field. Paramagnetic materials have a weak magnetic effect in the same direction of the applied magnetic field. Ferromagnetic materials have a relatively strong magnetic effect which is in the same direction as the applied magnetic field [98, 100].

When a magnetic field is applied to a core material, such as a coil carrying an electrical current, the atoms magnetic dipoles begin to rotate and align with the applied field producing a resultant magnetic effect called magnetization. This magnetization has an additive effect to the applied field, thus the appropriate core material can magnify the

field by orders of magnitude. In a ferromagnetic material, such as iron, many atoms within a region, called a domain, tend to rotate and align with the applied field together. These domains act like small bar magnets and result in ferromagnetic materials relatively strong magnetic effect. As the applied field increases, more domains align with the applied field until magnetic saturation is reached [98, 100]. This progression is shown in Figure 3-8, for a non-isotropic polycrystalline material such as iron.

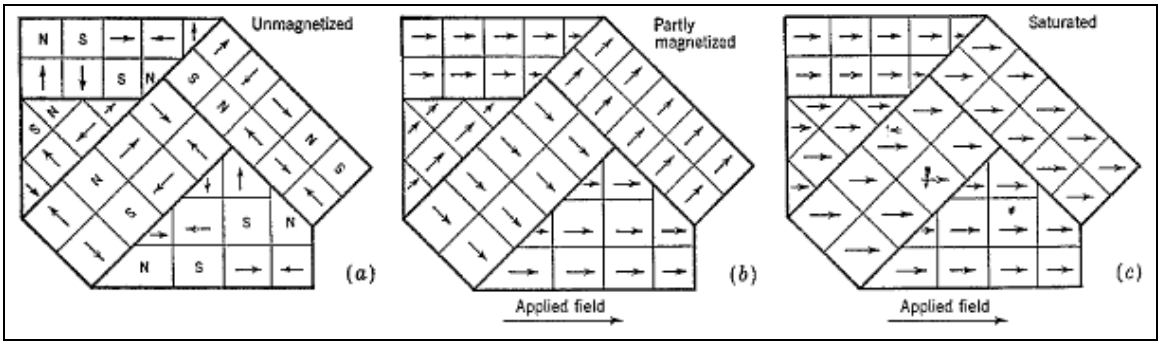

Figure 3-8 Successive Stages of Increasing Magnetization of a Polycrystalline Material [100]

It is convenient to define a dimensionless quantity, relative permeability, to compare magnetic materials. The relative permeability of a vacuum is defined as unity and diamagnetic materials are less than unity, while paramagnetic materials are slightly more than unity. The relative permeability of ferromagnetic materials is generally much greater than one; however, the relative permeability of ferromagnetic materials is not constant, but depends on the magnetic field intensity and hysteresis [100]. The relative permeability of several materials is listed in Table 3-1 below. The values given for ferromagnetic materials in Table 3-1 are the maximum relative permeability which is well defined for a particular material.

Table 3-1 Relative Permeability of Selected Materials [100]

Substance	Group Type	Relative Permeability μ_r
Silver	Diamagnetic	0.99998
Lead	Diamagnetic	0.999983
Copper	Diamagnetic	0.999991
Water	Diamagnetic	0.999991
Vacuum	Nonmagnetic	1 (by definition)
Air	Paramagnetic	1.0000004
Aluminum	Paramagnetic	1.00002
Palladium	Paramagnetic	1.0008
Cobalt	Ferromagnetic	250 max
Nickel	Ferromagnetic	600 max
Mild Steel (0.2 C)	Ferromagnetic	2,000 max
Iron (0.2 Impurity)	Ferromagnetic	5,000 max
Purified Iron (0.05 Impurity)	Ferromagnetic	200,000 max

3.4.1 Calculating Magnetic Fields Due to Electric Currents

Calculating the magnetic induction due to a current carrying conductor can be performed using Ampere's law or the more accurate Biot-Savart law shown in Equation 3-17 below. Ampere's law and Biot-Savart laws are equivalent where the assumptions for Ampere's law are satisfied and the simplest form may be used. However, the Biot-Savart law is the only approach where the current does not follow a simple path [101].

$$\vec{B} = \frac{\mu_o I}{4\pi} \oint \frac{\hat{\tau} \times \hat{r}}{r^2} d\vec{\ell} \qquad \text{Equation 3-17}$$

where μ_o is permeability of a vacuum, τ is the unit vector tangent to the path of the current, r is the position vector to point P where field is being calculated and $d\boldsymbol{\ell}$ is a differential element along current path. These variables are illustrated in Figure 3-9 below.

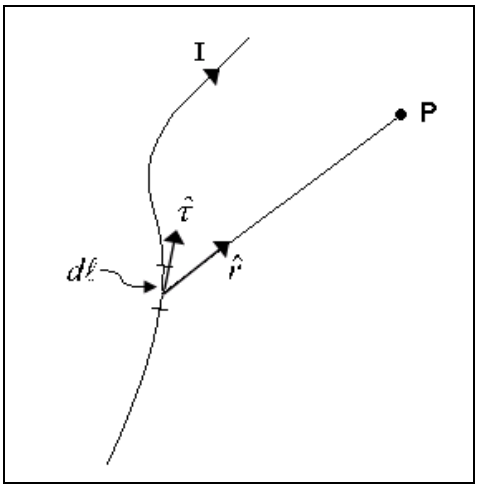

Figure 3-9 Arbitrary Current Carrying Conductor Illustrating Biot-Savart Law

The Biot-Savart law can be used to calculate the magnetic induction for a point in space due to a current following any geometric path. However, the integration can only be performed for very simple geometric paths and a closed form solution does not exist for most cases [94, 98, 101]. Therefore, numerical techniques must be used to solve more general cases such as finite element, boundary element and finite difference methods [94, 102].

The vector potential approach allows the magnetic induction and magnetic field strength to be found while combining all the conditions that need to be satisfied into a single equation. The vector potential of the magnetic induction can be found by taking the curl of a certain vector field such that:

$$\vec{B} = \nabla \times \vec{A} \qquad \text{Equation 3-18}$$

where

$$\vec{A} = \frac{\mu_o I}{4\pi} \oint \frac{d\vec{\ell}}{r} \qquad \text{Equation 3-19}$$

is the vector potential which can be found using the Biot-Savart law. Once the vector potential is known, the magnetic induction and magnetic field strength can be found by differentiating the vector potential and utilizing the Maxwell equations below [98, 100].

$$\nabla \cdot \vec{B} = 0 \qquad \text{Equation 3-20}$$

$$\nabla \times \vec{H} = \vec{J} \qquad \text{Equation 3-21}$$

3.4.2 Design of Magnetic Field Application

The main function of magnetorheological fluids is their controllable yield strength. In the presence of a magnetic field, the suspended magnetic particles in a magnetorheological fluid become magnetized and form chain like structures that align that are parallel to the applied magnetic field as shown in Figure 3-10. The particle chains restrict the movement of the fluid which produces an apparent increase in yield strength. Thus the key objective in applying a magnetic field to the journal bearing is to achieve a consistent field across the fluid film which is perpendicular to the shearing forces. This was accomplished by placing eight electromagnets around the circumference of the bearing directing the field radially inward as the symmetric cross section in Figure 3-10 shows.

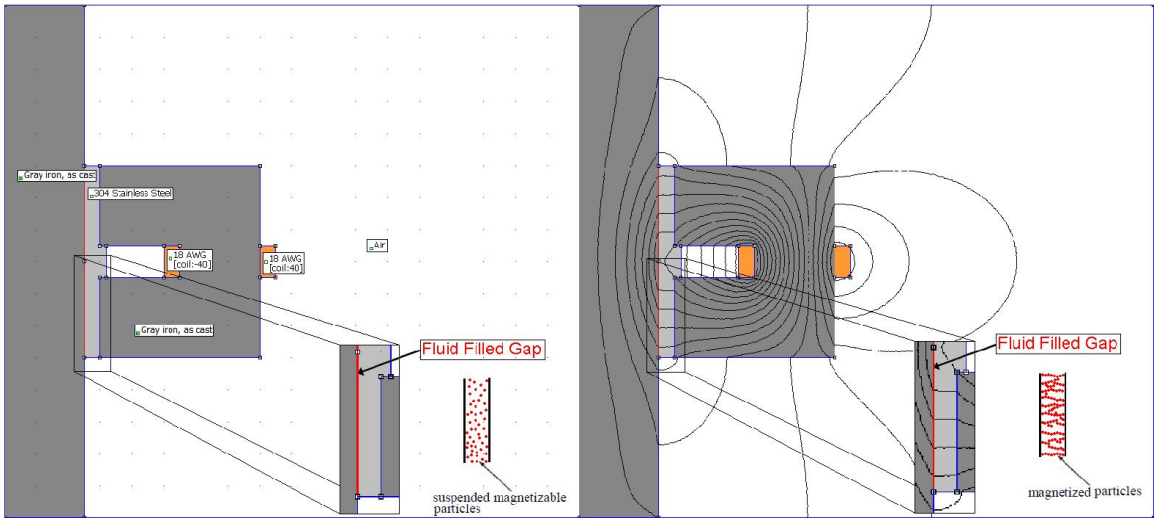

Figure 3-10 Bearing Cross Section With and Without Magnetic Field Applied

3.4.2.1 FEMM Magnetic Solver Approach [103]

Utilizing FEMM programs, the finite element method was used to evaluate the magnetic fields of the proposed experimental setup. The FEMM software uses finite element techniques to solve low frequency electromagnetic problems, where displacement currents can be neglected, for the limiting cases of planar and axis-symmetric two-dimensional domains [103].

The FEMM programs consist of a pre-processor and post-processor, a meshing program that breaks the solution region into a triangular mesh and a solver. The pre-processor contains a two-dimensional CAD interface to set up the solution domain and define material properties and boundary conditions. The pre-processor also contains a large database of magnetic properties for varying material types that was used to define the materials used in the experimental construction [103].

The solver program takes inputs from the pre-processor that describes the problem and solves the partial differential equations relevant to the problem type. For

magneto-static problems, where the temporal terms in the Maxwell equations are set to zero, the FEMM program uses a magnetic vector potential approach to solve the magnetic induction and magnetic field strength. The vector potential is a three component vector that for a two-dimensional planar or axis-symmetric case reduces to a single component normal to the plane. The advantage of using the vector potential approach is that a single equation satisfies the necessary Maxwell conditions and the magnetic induction and magnetic field strength can be found by differentiating the vector potential [98, 103].

3.4.2.2 Electromagnet Design Layout

The key objective to applying the magnetic field to the journal bearing was to achieve a consistent field across the fluid and perpendicular to the gap. As was shown by Urreta *et al.*, the MR fluid was designed to work with the magnetic field perpendicular to the direction of shear. A magnetic field applied parallel to the journal bearing's axis would align the magnetic particles parallel to the major shearing forces resulting in minimal impact on the bearing [75].

Several electromagnet designs and configurations were investigated in an attempt to apply the most uniform and controllable magnetic field across the fluid film. Initial designs attempted to apply the magnetic field across the fluid film by placing elongated solenoids outside the bearing and directing their magnetic field into the bearing. To strengthen the magnetic field across the fluid film, more solenoids were placed inside the journal leading to the design shown in Figure 3-11. The orientations of the electromagnets were arranged such that dipoles of the electromagnets outside of the

bearing as well as the dipoles of the internal electromagnets were all aligned in the same direction. This would allow opposing poles of the internal verses the external electromagnets to align and the magnetic field would travel across the fluid filled gap perpendicular to the primary shearing direction. Several iterations of this design were investigated; however, the magnetic field strength normal to the fluid motion for this configuration was relatively weak and extremely non-uniform.

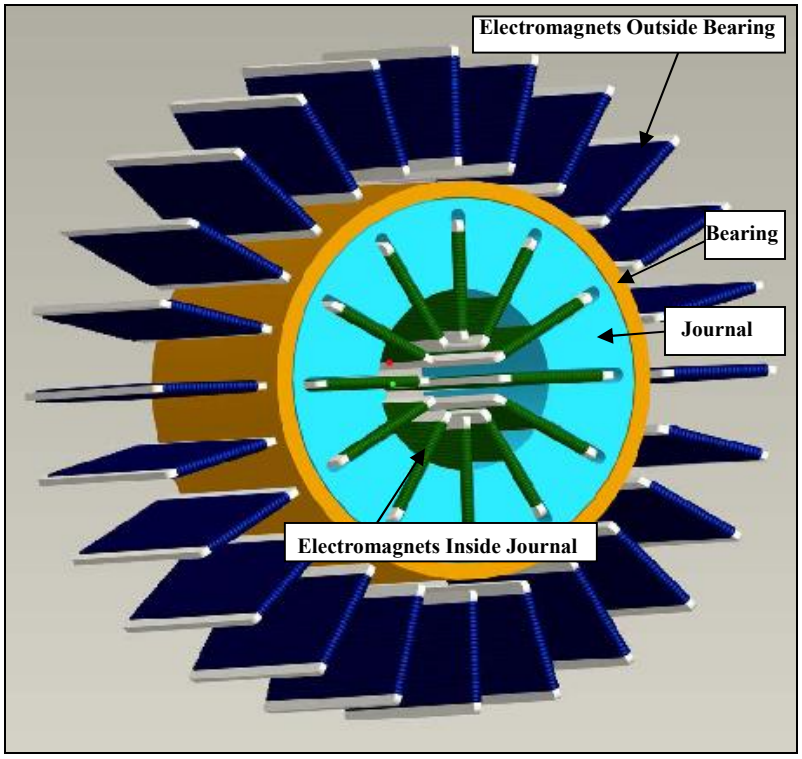

Figure 3-11 Three Dimensional Model of Initial Electromagnet Design

In the final design iteration, the magnetic field was applied by eight electromagnetic poles placed circumferentially around the bearing as shown in Figure 3-12 below. The eight poles covered the entire circumference of the bearing and directed the field perpendicular to the gap such that the normal magnetic field strength was nearly uniform within the fluid at the pole locations. Although the magnetic field strength

normal to the fluid drops to zero between the magnetic poles, this design provided a great improvement, over initial design, in the strength and uniformity of the magnetic field across the fluid film. The construction of the journal bearing consisted of a grey iron journal of high magnetic permeability and a 304 stainless steel bearing with low magnetic permeability. Each electromagnet was comprised of a 40 turn coil solenoid, of 18AWG copper wire, surrounding a grey iron U-shaped core. A small step in the center of the bearing aides in aligning the U-shaped electromagnet and two blind bore holes which are 180 degrees apart and on one axial end of the bearing were designed to accommodate two small key pins that fit into similar holes in two of the electromagnets. This prevents the complement of electromagnets from rotating along the outer circumference of the bearing. The eight electromagnets were then held in position by fixing a ring to each end of each electromagnet.

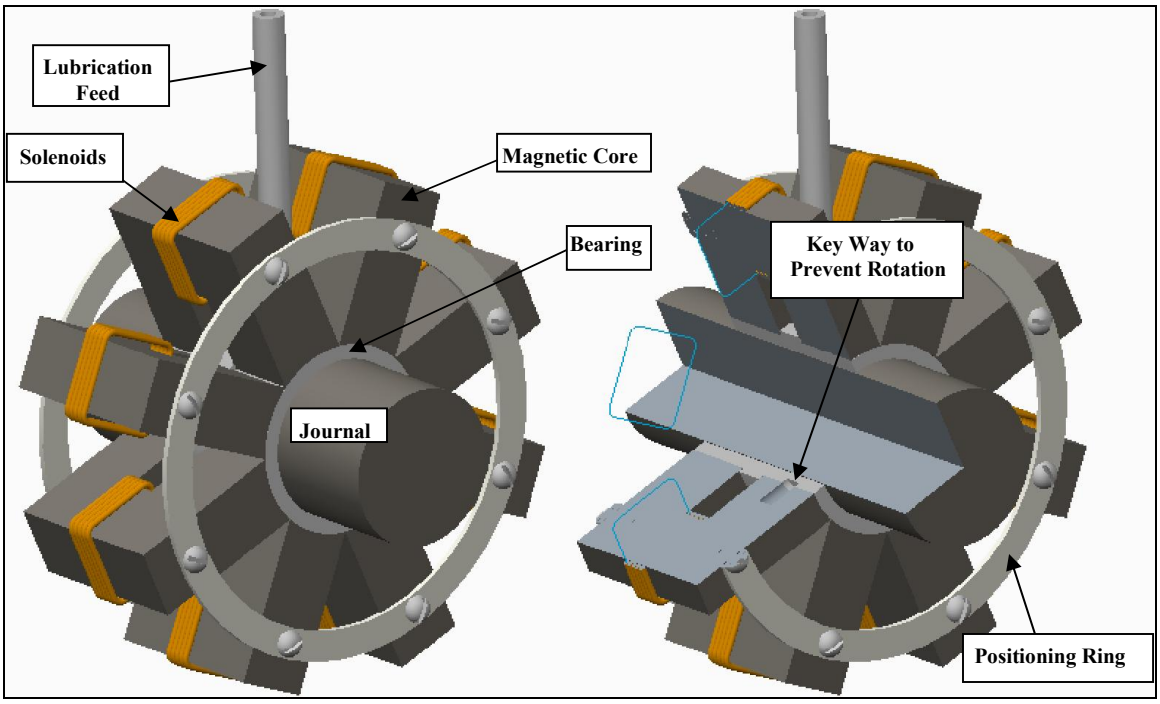

Figure 3-12 Three Dimensional Model of Electromagnet Design

Both poles of each electromagnet are aligned with the axial ends of the bearing such that the magnetic field travels from the pole through the bearing and across the fluid filled gap and into the shaft. The field then travels through the shaft and across the fluid filled gap and bearing back into to the opposing pole. This design is relatively symmetric about the journal axis allowing the two-dimensional FEMM software to be used. The magnetic field lines, generated by the FEMM software, can be seen in the cross section diagram in Figure 3-13 below. As can be seen on the right hand side of the figure, the magnetic field lines pass perpendicularly through the gap and into the shaft at each pole location.

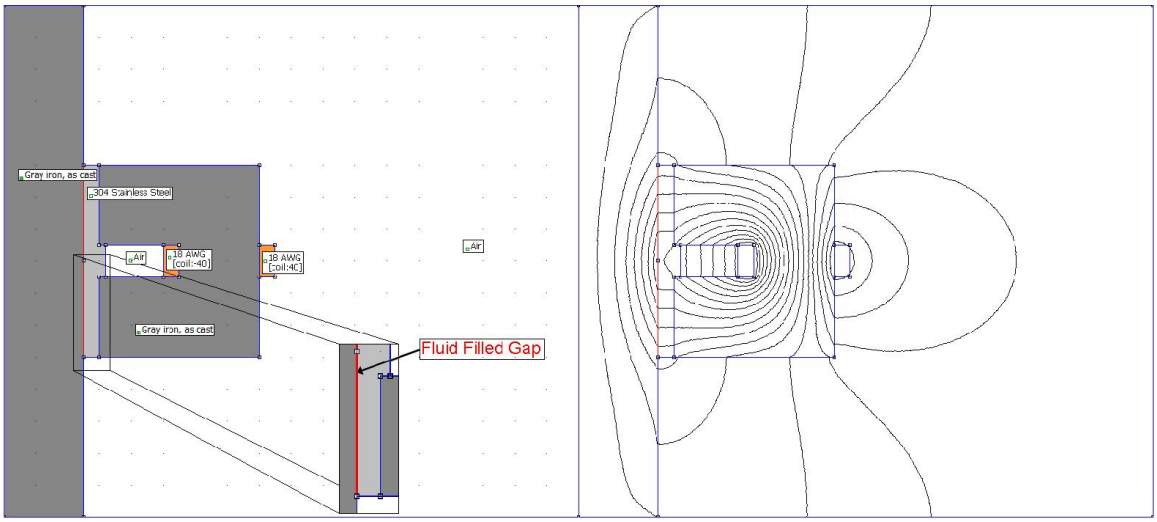

Figure 3-13 FEMM Model of a Quarter Cross Section with Magnetic Field Lines

The electromagnet configuration in Figure 3-12 produces a nearly constant magnetic field across the MR fluid in both the axial and circumferential directions at each pole location. This is true for the operable range of the electromagnets from an applied current of 0.1 to 20.0 amperes. The variation of magnetic field across the filled gap and normal to the primary shearing direction along the axial length of the journal bearing is

shown in Figure 3-14. As can be seen in Figure 3-14, the magnetic field strength tapers off between the electromagnet poles. This effect was minimized by moving the opposing poles close together.

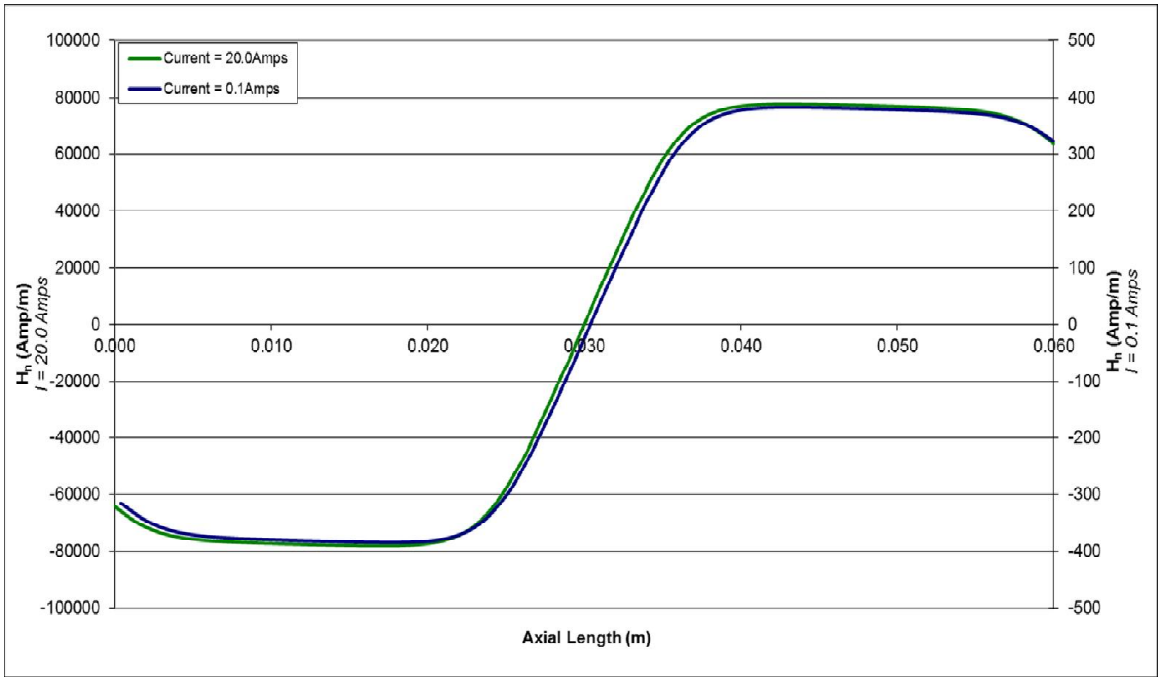

Figure 3-14 Magnetic Field Inside Fluid Film and Normal to the Primary Shearing Direction for Minimum and Maximum Applied Currents

The drop in magnetic field strength between the magnetic poles also has the advantage of allowing a lubrication inlet feed to remain functional when a strong magnetic field is applied. Although the current design does not utilize a lubrication groove, this common design feature, which is shown in Figure 3-15, could also be added and remain functional when a strong magnetic field is applied.

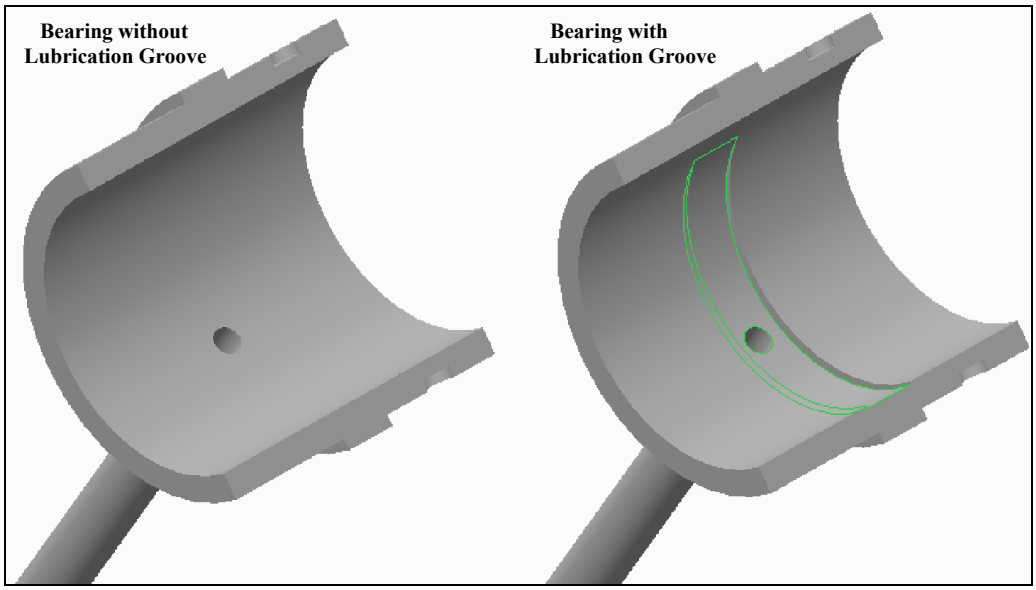

Figure 3-15 Bearing Design with and without Lubrication Groove

The magnetic field strength also changes signs between the two poles of the electromagnets as the field moves out of one dipole and into the opposing dipole. This was an inevitable result due to the configuration of the electromagnets and was minimized by moving the dipoles close together. It should be noted that the response of the magnetorheological fluid is the same regardless of the sign of the magnetic field strength. This simply reverses the dipole orientation of the individual suspended magnetic particles in the fluid when they form the chain like structures as shown in Figure 3-16.

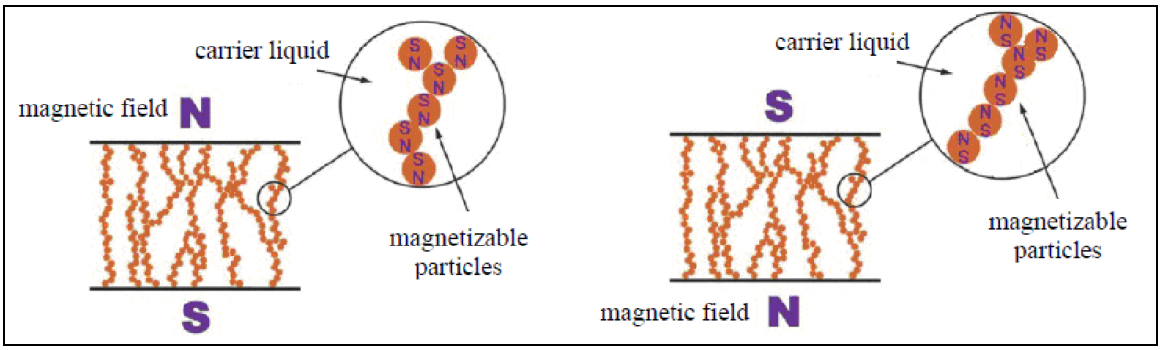

Figure 3-16 Magnetorheological Fluid Particles Chain Structure Formation at Opposing Pole Locations

Each electromagnet produces a force on the bearing journal in a radial direction towards the electromagnet. This force is proportional to the magnetic field strength squared and thus varies with the applied current to the solenoid. In general, the force distribution acting on the boundary of the electromagnet can be difficult to evaluate. However, if the forces are assumed to act only on the surface of the poles, the normal force acting on the bearing journal can be described by Equation 3-22 below. While Equation 3-22 does not describe the force distribution at the surface pole, it does provide the correct value for the total force [97].

$$F_{mag} = \frac{1}{2}\mu_o H_n^2 A_{pole} \qquad \text{Equation 3-22}$$

As can be seen in Figure 3-17 below, the radial force acting on the bearing journal from each electromagnet, through the range of applied currents, is very small relative to the hydrodynamic forces. Based on these results, the magnetic forces acting on the bearing journal are neglected in the numerical calculations discussed in the next section. By assuming the magnetic forces act only on the surface of one of the magnetic dipoles and neglecting the force from the opposing magnetic dipole on the opposite side of the

bearing, the maximum possible force on the journal was calculated. Thus, Equation 3-22 yielded a conservative result in calculating the effect of the magnetic force on the journal, relative to the expanded equation, for the current application.

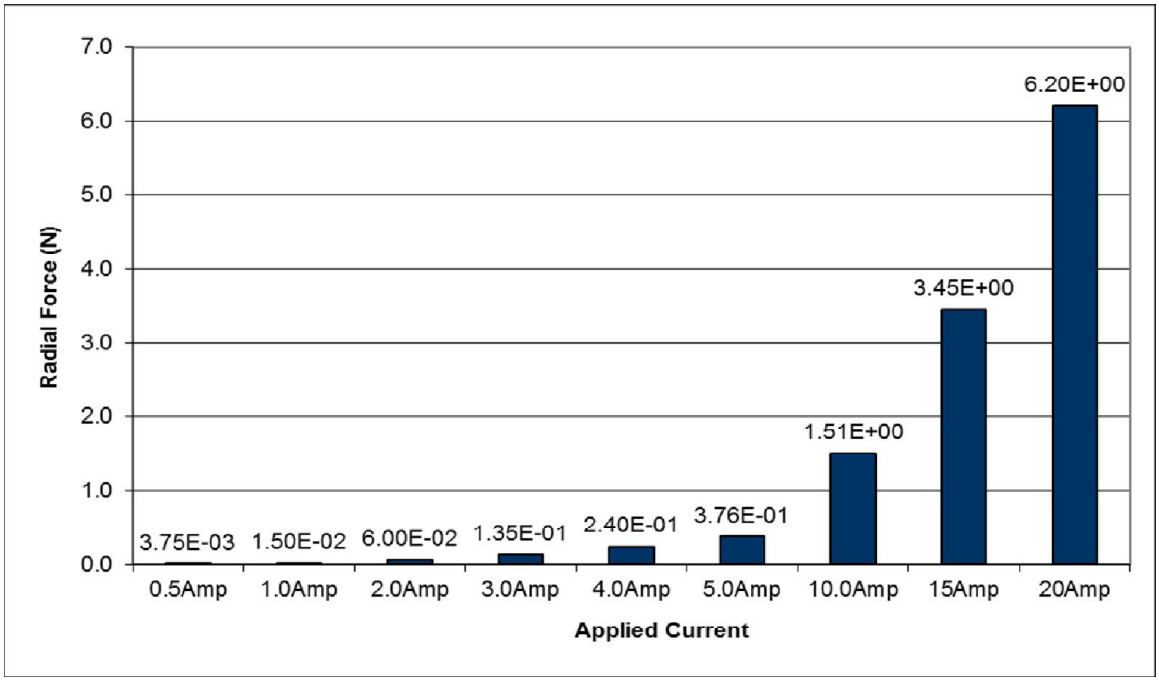

Figure 3-17 Magnetic Force on Journal for Varying Applied Solenoid Current

3.5 Numerical Implementation

The gathering of information about a physical process can be determined through actual measurements of an experimental investigation or by theoretical calculations of a mathematical model. Theoretical calculations can allow information to be gathered more efficiently and at a lower cost than most experimental methods. However, in some cases the mathematical description of a problem is not adequate to yield results that agree with reality. For problems which an adequate mathematical description exists, classical mathematical methods may not be sufficient to obtain closed form solutions. Fortunately,

many numerical methods have been developed which discretize complex equations into a series of solvable algebraic equations. The subdomain method or the control-volume formulation, which is second-order accurate, was utilized as the discretization method in this work.

3.5.1 Discretization of Modified Reynolds Equation

The subdomain method is a version of the method of weighted residuals, where the weighting function is equal to one. In the subdomain method, the domain under investigation is divided into a number of non-overlapping control volumes or subdomains. The control volumes are set up so that each grid point has a single control volume around it. The differential equation is then integrated over each control volume resulting in algebraic equations in terms of unknown variables for the adjacent grid points. Assumed piecewise profiles describing the variation of the dependent variable between the grid points are used to evaluate the integrals. The key advantage of using the subdomain method is that the solution satisfies conservation principles for the dependent variable for the individual control volumes and thus the entire calculation domain, even for a course grid [104, 105].

The implementation of the subdomain method for the journal bearing begins with dividing the fluid film region into non-overlapping control volumes around individual grid points. Figure 3-18 below shows how the fluid was broken into subdomains after "unwrapping" the bearing such that the x and y directions are the circumferential and axial directions respectively. This unwrapping of the bearing is possible by utilizing

Reynolds assumption that the radius of curvature is large relative to the clearance which allows the curvature to be ignored and the use of Cartesian coordinates.

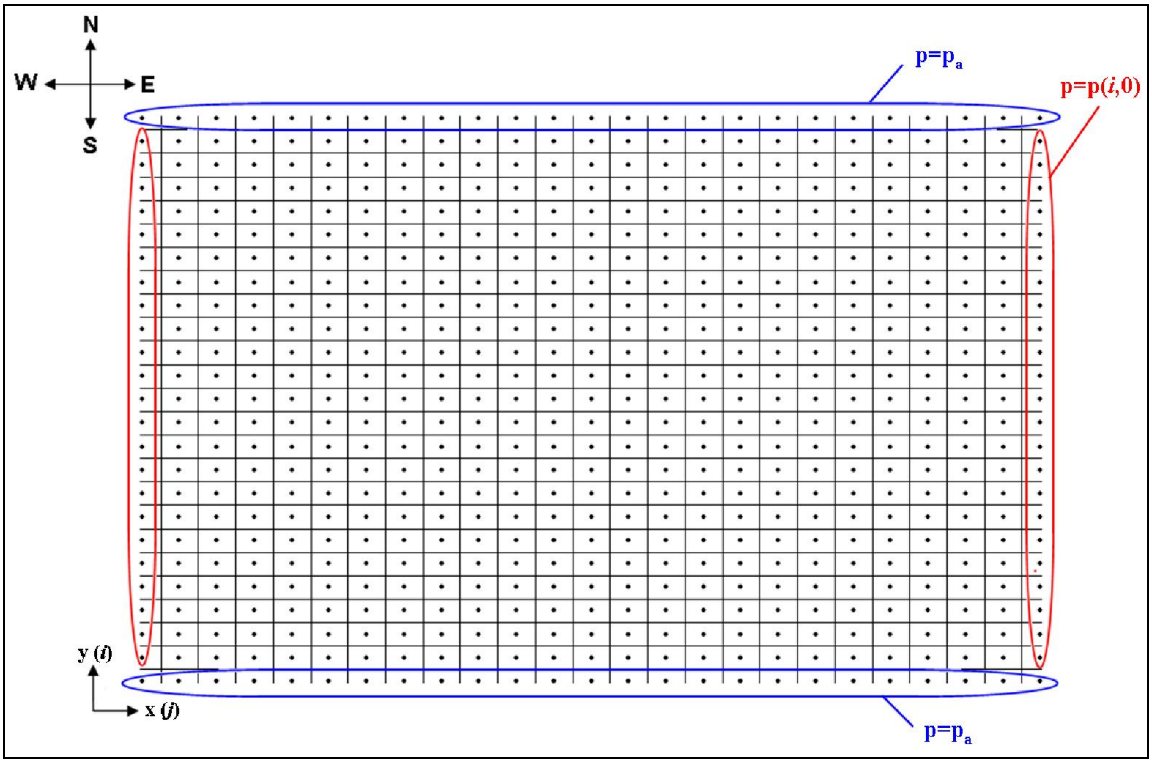

Figure 3-18 Fluid Subdomain Layout

The next step in the implementation of the subdomain method is to derive the discretization equation. Beginning with the grid point cluster shown in Figure 3-19, the discretization equation can be derived for the center node labeled P. The adjacent grid points are labeled N, S, E and W in accordance with the coordinate system defined in Figure 3-18. The box surrounding the center node shows the faces of the control volume with lower case letters n, s, e, and w denoting the faces.

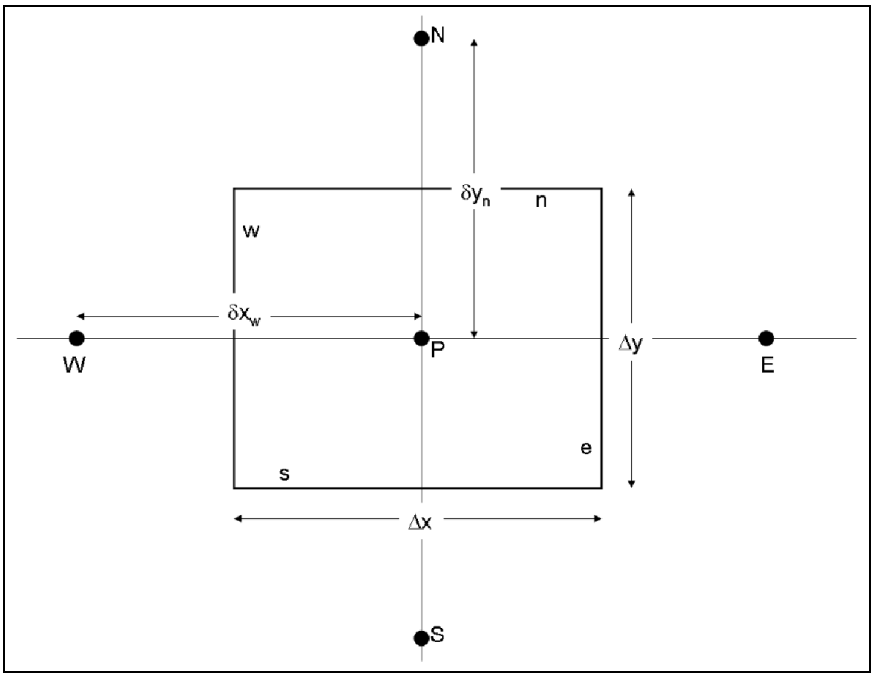

Figure 3-19 Two Dimensional Grid Point Cluster

By integrating the modified Reynolds equation over the control volume we get the following:

$$\int_s^n \int_w^e \left[g \cdot \frac{\partial}{\partial x}\left(\frac{h^3}{\mu \cdot H(|\dot{\gamma}|)} \frac{\partial p}{\partial x} \right) + g \cdot \frac{\partial}{\partial y}\left(\frac{h^3}{\mu \cdot H(|\dot{\gamma}|)} \frac{\partial p}{\partial y} \right) - g \cdot \frac{3}{\mu l_o} p \cdot \Im \right] dx \cdot dy =$$
$$= \int_s^n \int_w^e \left[6U \frac{\partial h}{\partial x} - 12 \frac{\partial h}{\partial t} - \frac{3}{\mu l_o} p_{inj} \cdot \Im \right] dx \cdot dy$$

Equation 3-23

Separating the three terms on the left hand side and integrating.

$$\int_s^n \int_w^e g \cdot \frac{\partial}{\partial x}\left(\frac{h^3}{\mu \cdot H(|\dot{\gamma}|)} \frac{\partial p}{\partial x} \right) dx \cdot dy = \left(\frac{g_e h_e^3}{\mu H_e} \frac{p_E - p_P}{\Delta x} - \frac{g_w h_w^3}{\mu H_w} \frac{p_P - p_W}{\Delta x} \right) \Delta y$$

Equation 3-24

$$\int_s^n \int_w^e g \cdot \frac{\partial}{\partial y}\left(\frac{h^3}{\mu \cdot H(|\dot{\gamma}|)}\frac{\partial p}{\partial y}\right) dx \cdot dy = \left(\frac{g_n h_n^3}{\mu H_n}\frac{p_N - p_P}{\Delta y} - \frac{g_s h_s^3}{\mu H_s}\frac{p_P - p_S}{\Delta y}\right)\Delta x \quad \text{Equation 3-25}$$

$$\int_s^n \int_w^e g \cdot \frac{3}{\mu l_o} p(\Im) dx \cdot dy = \frac{3\Im}{\mu l_o} p_{inj}\, \Delta x \cdot \Delta y \quad \text{Equation 3-26}$$

Gathering all independent variables, the left hand side simplifies to:

$$A_e p_E + A_w p_W - p_P(A_e + A_w) + A_n p_N + A_s p_S - p_P(A_n + A_s) - A_f p_P = RHS$$

Equation 3-27

where

$$A_e = \frac{g_e h_e^3}{\mu H_e}\frac{\Delta y}{\Delta x} \quad \text{Equation 3-28}$$

$$A_w = \frac{g_w h_w^3}{\mu H_w}\frac{\Delta y}{\Delta x} \quad \text{Equation 3-29}$$

$$A_n = \frac{g_n h_n^3}{\mu H_n}\frac{\Delta x}{\Delta y} \quad \text{Equation 3-30}$$

$$A_s = \frac{g_s h_s^3}{\mu H_s}\frac{\Delta x}{\Delta y} \quad \text{Equation 3-31}$$

$$A_f = \frac{3\Im}{\mu l_o}\Delta x \cdot \Delta y \quad \text{Equation 3-32}$$

Before integrating the source term, further discussion is warranted. The techniques used to solve the discretization equation are for linear algebraic equations and thus only linear dependence can be accounted for. Noting that the source term on the right hand side of

Equation 3-23 is not a function of the dependent variable, we can proceed with the integration.

$$\bar{S} = \int_s^n \int_w^e \left[6U \frac{\partial h}{\partial x} - 12 \frac{\partial h}{\partial t} - \frac{3}{\mu l_o} p_{inj} \cdot \Im \right] dx \cdot dy = 6U\Delta y\left(h_E - h_W\right) - 12\Delta x\Delta y \frac{\partial h}{\partial t} - \frac{3\Im}{\mu l_o} p_{inj} \Delta x\Delta y$$

Equation 3-33

where $\bar{S}$ is the average value of the source term over the control volume. Combining the simplified left and right hand sides of Equation 3-23 and solving for the dependent variable at node P, the discretization equation can be found.

$$p_p = \left(A_n p_N + A_s p_S + A_e p_E + A_w p_W - \bar{S}\right) / \left(A_f + A_n + A_s + A_e + A_w\right)$$

Equation 3-34

The pressure given in Equation 3-34 is the internal pressure for the journal bearing. There are three boundary conditions to be implemented, which were shown in Figure 3-18. Two boundary conditions account for the axial ends of the bearing where the pressure is set to be the ambient pressure. The third boundary condition ties the circumferential ends of the bearing together, where the nodes at 0 and 2π are equal. The three boundary conditions are summarized below.

$$\begin{aligned} p\left(y = 0,\ 0 \le x \le 2\pi R\right) &= p_a \\ p\left(y = L,\ 0 \le x \le 2\pi R\right) &= p_a \end{aligned}$$

Equation 3-35

$$p\left(0 \le y \le L,\ x = 0\right) = p\left(0 \le y \le L,\ x = 2\pi R\right)$$

Equation 3-36

3.5.2 Numerical Procedure for Steady State Pressure Distribution

The discretization equation developed in the previous section provides the necessary algebraic expressions to solve for the pressure distribution. Placing the discretization equation into a numerical format and coupling with the iterative method outlined in the flow chart shown in Figure 3-20, the solution converges to the pressure distribution for a self-acting journal bearing. The source code used to solve the steady state pressure distribution is given in Appendix C.

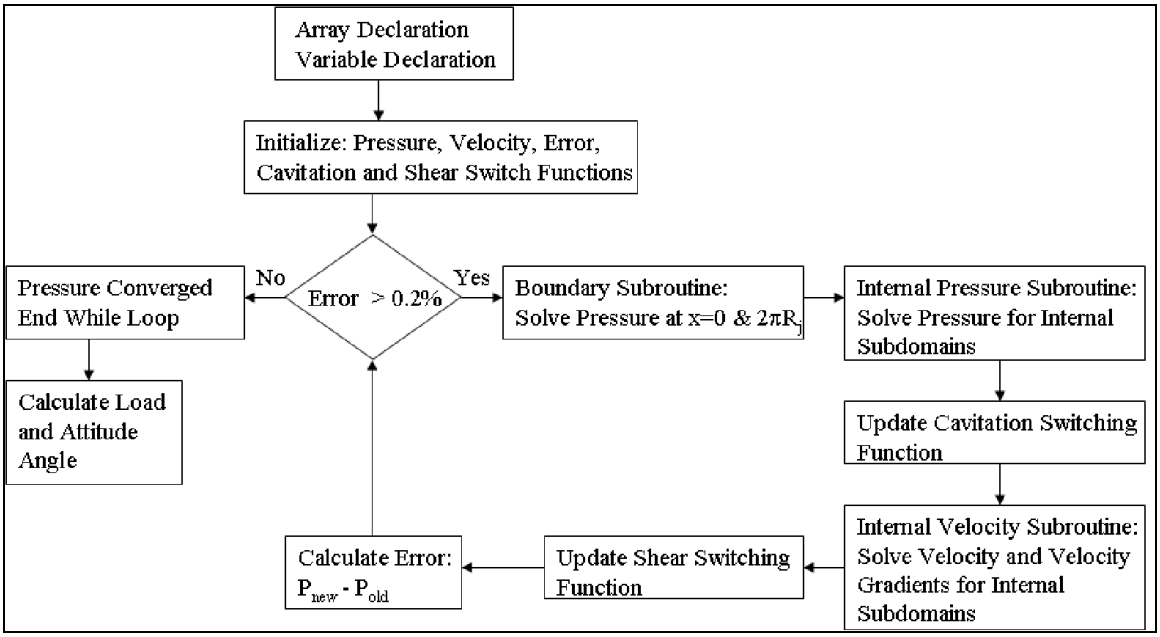

Figure 3-20 Flow Diagram Describing Complete Steady State Source Code

As the flow chart outlines, the procedure for solving the steady state pressure distribution involves several subroutines. The first two subroutines, listed in the flow diagram, solve the pressure distribution within the bearing using the modified Reynolds equation described earlier in this chapter. The third subroutine, listed as the internal velocity subroutine in the flow diagram, uses the current iteration of the calculated

pressure distribution to determine the local circumferential and axial velocities of the fluid using Equations 3-4 and 3-5 respectively. These velocity calculations are necessary to determine the local shear stress applied to the fluid film, which in turn is used to determine the shear switching function for each subdomain. The shear switching function values are then used in the solution of the pressure distribution for subsequent iterations.

3.5.3 Proof of Convergence

The entire source code was validated for the chosen convergence criteria. The convergence was first checked on each subroutine calculation and then final outputs of the resulting source code. A combination of doubling the number of subdomains and halving the maximum allowable error was used to verify that acceptable results were obtained.

A specific case study is provided in the table below for 500 rpm operating speed with a 0.5 eccentricity ratio. The chosen grid of 60 axial subdomains and 180 circumferential subdomains for a total of 10,800 subdomains was approximately doubled to a grid of 85 axial subdomains and 255 circumferential subdomains for a total of 21,675 subdomains. The chosen maximum allowable error of 0.2% was also reduced to half. The maximum allowable error refers to the difference in the new value of a variable relative to the same variable value calculated for the previous iteration step.

Table 3-2 Results Comparison of Grid and Acceptance Criteria Refinement

	Load Capacity (N)	Attitude Angle (deg)	Maximum Pressure (kPa)
60x180 Grid 0.2% Error	3,931	59.97	2,814
85x255 Grid 0.1% Error	3,921	60.01	2,807
% Difference	-0.25%	0.07%	-0.25%

The division of the axial and circumferential grid was specifically chosen for two reasons. The first reason was to achieve a reasonable resolution in the circumferential direction. For this reason, the number of subdomains in the circumferential direction was relatively large even though reasonable results could be obtained with a slightly courser grid. The second factor in the grid division selection was the number of axial divisions relative to the number of circumferential divisions, which was chosen such that the dimensions of the differential element in the axial and circumferential directions were nearly equal. This is important to ensure that contributions, in an equation, that are multiplied or divided by a differential length in either direction are equally weighted.

The results in Table 3-2 show that a significant refinement of the grid size, by increasing the number of subdomains, and a reduction in the acceptable error limits had a minimal impact on the critical calculated variables. Based on the results of the convergence study, it was determined that the minimal improvements given by the grid refinement and reduction in the acceptable error limits, did not justify the significant increase in computational efforts.

3.6 Dynamic Loading Model

The previous sections were focused on steady state operation, where the loads and speeds of the self-acting journal bearing were constant. However, many bearing applications are dynamically loaded such as cyclical loads in internal combustion engines or rotating loads due to centrifugal forces. Also, journal bearings are not inherently stable and under certain operating conditions, a self-exciting whirl orbit can increase until the journal comes in contact with the bearing [48, 80]. The purpose of the following section is to outline the steps used to determine the dynamic response of the bearing when the inertia forces produced by the journal movement are relatively significant. The details of the calculation of the bearing dynamic reactions can be found in Appendix D.

3.6.1 Dynamic Response to Small Perturbation

There are two simplified types of loading situations that can be analyzed for a journal bearing subjected to variable loads and speeds. The first case is when the motion of the journal due to the external loads is much larger than that of the inertia forces produced by the journal movement. For this case the inertia forces are determined independently of the journal motion and then included into the external forces, which then must be balanced by the resultant force from the internal bearing pressure. The second case, which this section is focused on, occurs when the inertia forces produced by the journal movement are relatively significant. For this case the journal motion is assumed to take place in the form of small perturbations around some steady state equilibrium position [80].

The hydrodynamic journal bearing displays a spring like resistance, however; the displacement of the journal relative to the bearing is not linearly related to the applied load as with a typical spring. The hydrodynamic fluid film separating the journal and bearing also exhibits damping effects which are important to the bearing stability [48, 80]. Figure 3-21 below depicts the reaction of bearing lubrication film, with bearing stiffness represented by springs and the bearing dampening represented by dashpots. The representative springs and dashpots span the gap between the bearing and journal at four locations. In 1966, Lund proposed a dynamic solution for a gas journal bearing by solving a set of spring and damping coefficients based on the load, speed and whirl motion of the journal [106, 107]. There are several other methods to solve for the dynamic response of a journal bearing; however, most follow the same approach used by Lund.

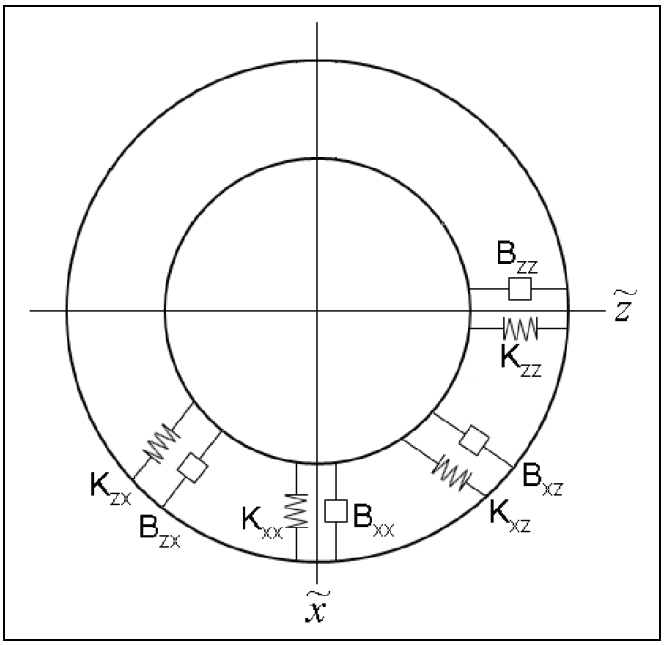

Figure 3-21 Journal Bearing Spring and Damping Coefficient Schematic

3.6.2 Implementation of the Small Perturbation Method

Figure 3-22 presents a diagram of a journal bearing with a dynamic coordinate system utilized in the small perturbationn method. The fixed coordinate systems are shown in black and the perturbed coordinate system is highlighted in red. The global coordinate system is located relative to the load line and remains unchanged. The local cooridate system is located relative to the line of centers and changes position following a small perturbation. The perturbation variables are indicated as such using a delta symbol or a tick mark.

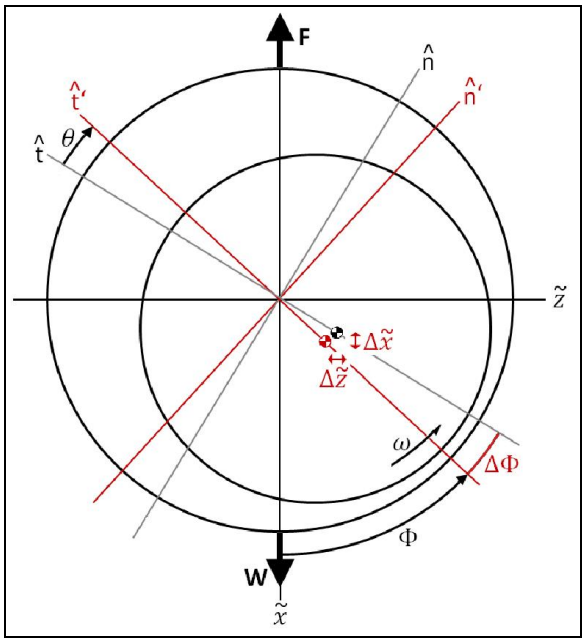

Figure 3-22 Journal Bearing Dynamic System of Coordinates

The perturbation method presented in this section follows the works of Hamrock, Constantinescu and Lund [48, 80, 106, 107]. Solving the bearings dynamic response to a small perturbation, the journal motion is assumed to take place in the form of small

perturbations around some steady state equilibrium position such that the instantaneous journal location can be given by:

$$\begin{aligned} \widetilde{x} &= \widetilde{x}_o + \Delta\widetilde{x} \\ \widetilde{z} &= \widetilde{z}_o + \Delta\widetilde{z} \end{aligned} \qquad \text{Equation 3-37}$$

where the subscript *o* indicates steady state variable and the delta prefix indicates a perturbation term, which represents a relatively small displacement of the journal from the steady state position.

By performing a first order Taylor series expansion on the pressure, letting p_o be the steady state pressure distribution, we get the following:

$$p = p_o + \left.\frac{\partial p}{\partial \widetilde{x}}\right|_o \Delta\widetilde{x} + \left.\frac{\partial p}{\partial \widetilde{z}}\right|_o \Delta\widetilde{z} + \left.\frac{\partial p}{\partial \dot{\widetilde{x}}}\right|_o \Delta\dot{\widetilde{x}} + \left.\frac{\partial p}{\partial \dot{\widetilde{z}}}\right|_o \Delta\dot{\widetilde{z}} \qquad \text{Equation 3-38}$$

To simplify the notation, Equation 3-38 can be written as:

$$p = p_o + p_{\widetilde{x}}\,\Delta\widetilde{x} + p_{\widetilde{z}}\,\Delta\widetilde{z} + p_{\dot{\widetilde{x}}}\,\Delta\dot{\widetilde{x}} + p_{\dot{\widetilde{z}}}\,\Delta\dot{\widetilde{z}} \qquad \text{Equation 3-39}$$

where the last four terms are small relative to the steady state pressure term. By using the pressure solution in Equation 3-15, the Taylor series expansion of the pressure can be used to obtain a system of differential equations, by retaining the terms of the same order of magnitude.

$$g\cdot\frac{\partial}{\partial x}\left(\frac{{h_o}^3}{\mu\cdot H\left(|\dot{\gamma}|\right)}\frac{\partial p_o}{\partial \widetilde{x}}\right) + g\cdot\frac{\partial}{\partial y}\left(\frac{{h_o}^3}{\mu\cdot H\left(|\dot{\gamma}|\right)}\frac{\partial p_o}{\partial \widetilde{y}}\right) - g\cdot\frac{3}{\mu l_o}p_o\cdot\Im = 6U\frac{\partial h_o}{\partial \widetilde{x}} - \frac{3}{\mu l_o}p_{inj}\cdot\Im$$

Equation 3-40

$$g\cdot\frac{\partial}{\partial x}\left(\frac{{h_o}^3}{\mu\cdot H\left(\left|\dot\gamma\right|\right)}\frac{\partial p_{\tilde x}}{\partial\tilde x}\right)+g\cdot\frac{\partial}{\partial y}\left(\frac{{h_o}^3}{\mu\cdot H\left(\left|\dot\gamma\right|\right)}\frac{\partial p_{\tilde x}}{\partial\tilde y}\right)-g\cdot\frac{3}{\mu l_o}p_{\tilde x}\cdot\Im=$$
$$=-6U\sin(\theta)-g\cdot\frac{\partial}{\partial\tilde x}\left(\frac{3{h_o}^2\cos(\theta)}{\mu\cdot H\left(\left|\dot\gamma\right|\right)}\frac{\partial p_o}{\partial\tilde x}\right)-g\cdot\frac{\partial}{\partial\tilde y}\left(\frac{3{h_o}^2\cos(\theta)}{\mu\cdot H\left(\left|\dot\gamma\right|\right)}\frac{\partial p_o}{\partial\tilde y}\right)$$

Equation 3-41

$$g\cdot\frac{\partial}{\partial\tilde x}\left(\frac{{h_o}^3}{\mu\cdot H\left(\left|\dot\gamma\right|\right)}\frac{\partial p_{\tilde z}}{\partial\tilde x}\right)+g\cdot\frac{\partial}{\partial y}\left(\frac{{h_o}^3}{\mu\cdot H\left(\left|\dot\gamma\right|\right)}\frac{\partial p_{\tilde z}}{\partial\tilde y}\right)-g\cdot\frac{3}{\mu l_o}p_{\tilde z}\cdot\Im=$$
$$=6U\cos(\theta)-g\cdot\frac{\partial}{\partial\tilde x}\left(\frac{3{h_o}^2\sin(\theta)}{\mu\cdot H\left(\left|\dot\gamma\right|\right)}\frac{\partial p_o}{\partial\tilde x}\right)-g\cdot\frac{\partial}{\partial y}\left(\frac{3{h_o}^2\sin(\theta)}{\mu\cdot H\left(\left|\dot\gamma\right|\right)}\frac{\partial p_o}{\partial\tilde y}\right)$$

Equation 3-42

$$g\cdot\frac{\partial}{\partial\tilde x}\left(\frac{{h_o}^3}{\mu\cdot H\left(\left|\dot\gamma\right|\right)}\frac{\partial p_{\dot{\tilde x}}}{\partial\tilde x}\right)+g\cdot\frac{\partial}{\partial\tilde y}\left(\frac{{h_o}^3}{\mu\cdot H\left(\left|\dot\gamma\right|\right)}\frac{\partial p_{\dot{\tilde x}}}{\partial\tilde y}\right)-g\cdot\frac{3}{\mu l_o}p_{\dot{\tilde x}}\cdot\Im=-12\cos(\theta)$$

Equation 3-43

$$g\cdot\frac{\partial}{\partial\tilde x}\left(\frac{{h_o}^3}{\mu\cdot H\left(\left|\dot\gamma\right|\right)}\frac{\partial p_{\dot{\tilde z}}}{\partial\tilde x}\right)+g\cdot\frac{\partial}{\partial\tilde y}\left(\frac{{h_o}^3}{\mu\cdot H\left(\left|\dot\gamma\right|\right)}\frac{\partial p_{\dot{\tilde z}}}{\partial\tilde y}\right)-g\cdot\frac{3}{\mu l_o}p_{\dot{\tilde z}}\cdot\Im=-12\sin(\theta)$$

Equation 3-44

The fluid film thickness can be written as:

$$h=c+e\cos(\theta-\Delta\Phi)\approx c+e_o\cos(\theta-\Delta\Phi)+\Delta\tilde x\cos(\theta)+\Delta\tilde z\sin(\theta)$$ Equation 3-45

such that,

$$h_0=c+e_o\cos(\theta-\Delta\Phi)$$ Equation 3-46

$$\frac{\partial h}{\partial t}=\Delta\dot{\tilde x}\cos(\theta)+\Delta\dot{\tilde z}\sin(\theta)$$ Equation 3-47

This system of differential equations can be solved by the same analytic methods that were used to solve the steady state pressure distribution. It can be seen that Equation

3-40 is the same as the steady state form of Equation 3-15, thus the solution for Equation 3-40, is the same as the steady state pressure distribution. It can also be seen that the left hand side of all five equations are of similar form and only the source terms on the right hand side differ. Clearly, once the solution for p_o is known, the other four differential equations can be solved by the same numerical methods.

Once the solutions to the system of differential equations are determined, the resultant reaction load can be calculated by integration of the pressure distribution. Performing a first order Taylor series expansion on the components of the resultant reaction loads gives:

$$W_{\tilde{x}} = W_{\tilde{x},o} + \left.\frac{\partial W_{\tilde{x}}}{\partial \tilde{x}}\right|_o \Delta\tilde{x} + \left.\frac{\partial W_{\tilde{x}}}{\partial \tilde{z}}\right|_o \Delta\tilde{z} + \left.\frac{\partial W_{\tilde{x}}}{\partial \dot{\tilde{x}}}\right|_o \Delta\dot{\tilde{x}} + \left.\frac{\partial W_{\tilde{x}}}{\partial \dot{\tilde{z}}}\right|_o \Delta\dot{\tilde{z}} \qquad \text{Equation 3-48}$$

$$W_{\tilde{z}} = W_{\tilde{z},o} + \left.\frac{\partial W_{\tilde{z}}}{\partial \tilde{x}}\right|_o \Delta\tilde{x} + \left.\frac{\partial W_{\tilde{z}}}{\partial \tilde{z}}\right|_o \Delta\tilde{z} + \left.\frac{\partial W_{\tilde{z}}}{\partial \dot{\tilde{x}}}\right|_o \Delta\dot{\tilde{x}} + \left.\frac{\partial W_{\tilde{z}}}{\partial \dot{\tilde{z}}}\right|_o \Delta\dot{\tilde{z}} \qquad \text{Equation 3-49}$$

The differential terms in Equations 3-48 and 3-49 can be written in terms of the spring and damping coefficients. Using the layout described in Figure 3-21 the coefficients are:

$$K_{\tilde{x}\tilde{x}} = -\left.\frac{\partial W_{\tilde{x}}}{\partial \tilde{x}}\right|_o \qquad K_{\tilde{x}\tilde{z}} = -\left.\frac{\partial W_{\tilde{x}}}{\partial \tilde{z}}\right|_o \qquad K_{\tilde{z}\tilde{x}} = -\left.\frac{\partial W_{\tilde{z}}}{\partial \tilde{x}}\right|_o \qquad K_{\tilde{z}\tilde{z}} = -\left.\frac{\partial W_{\tilde{z}}}{\partial \tilde{z}}\right|_o$$

$$B_{\tilde{x}\tilde{x}} = -\left.\frac{\partial W_{\tilde{x}}}{\partial \dot{\tilde{x}}}\right|_o \qquad B_{\tilde{x}\tilde{z}} = -\left.\frac{\partial W_{\tilde{x}}}{\partial \dot{\tilde{z}}}\right|_o \qquad B_{\tilde{z}\tilde{x}} = -\left.\frac{\partial W_{\tilde{z}}}{\partial \dot{\tilde{x}}}\right|_o \qquad B_{\tilde{z}\tilde{z}} = -\left.\frac{\partial W_{\tilde{z}}}{\partial \dot{\tilde{z}}}\right|_o$$

Equation 3-50

Using the Cartesian coordinates shown in Figure 3-22, the component loads are:

$$\begin{aligned} -W_{\tilde{x}} &= F_t \cos(\Phi) + F_n \sin(\Phi) \\ &= -W_{\tilde{x},o} + K_{\tilde{x}\tilde{x}} \cdot \tilde{x} + B_{\tilde{x}\tilde{x}} \cdot \dot{\tilde{x}} + K_{\tilde{x}\tilde{z}} \cdot + B_{\tilde{x}\tilde{z}} \cdot \dot{\tilde{z}} \end{aligned} \qquad \text{Equation 3-51}$$

$$
\begin{aligned}
-W_{\tilde{z}} &= F_t\cos(\Phi) - F_n\sin(\Phi) \\
&= -W_{\tilde{z},o} + K_{\tilde{z}\tilde{x}}\cdot\tilde{x} + B_{\tilde{z}\tilde{x}}\cdot\dot{\tilde{x}} + K_{\tilde{z}\tilde{z}}\cdot\tilde{z} + B_{\tilde{z}\tilde{z}}\cdot\dot{\tilde{z}}
\end{aligned}
$$

Equation 3-52

where the subscripts *n* and *t* denote the normal and tangential coordinates relative to the line of centers shown in Figure 3-22. The component forces in the normal and tangential direction can be found by integration of the pressure distribution. Details on the calculation of the bearing load capacity can be found in Appendix E.

Using the geometry shown in Figure 3-22, the spring and damping coefficients can be written in terms of the normal and tangential component forces calculated from the pressure distributions of the five differential equations given in Equations 3-40 through 3-44. The condensed form of the spring and damping coefficients can be written as:

$$
\begin{aligned}
c\cdot K_{\tilde{x}\tilde{x}} &= \left(F_{t,\Delta\tilde{x}}\cos(\Phi) + F_{n,\Delta\tilde{x}}\sin(\Phi)\right)\cos(\Phi) - \left(F_{t,\Delta\tilde{z}}\cos(\Phi) + F_{n,\Delta\tilde{z}}\sin(\Phi)\right)\sin(\Phi) \\
c\cdot K_{\tilde{x}\tilde{z}} &= \left(F_{t,\Delta\tilde{x}}\cos(\Phi) + F_{n,\Delta\tilde{x}}\sin(\Phi)\right)\sin(\Phi) + \left(F_{t,\Delta\tilde{z}}\cos(\Phi) + F_{n,\Delta\tilde{z}}\sin(\Phi)\right)\cos(\Phi) \\
c\cdot K_{\tilde{z}\tilde{x}} &= \left(F_{t,\Delta\tilde{x}}\sin(\Phi) - F_{n,\Delta\tilde{x}}\cos(\Phi)\right)\cos(\Phi) - \left(F_{t,\Delta\tilde{z}}\sin(\Phi) - F_{n,\Delta\tilde{z}}\cos(\Phi)\right)\sin(\Phi) \\
c\cdot K_{\tilde{z}\tilde{z}} &= \left(F_{t,\Delta\tilde{x}}\sin(\Phi) - F_{n,\Delta\tilde{x}}\cos(\Phi)\right)\sin(\Phi) + \left(F_{t,\Delta\tilde{z}}\sin(\Phi) - F_{n,\Delta\tilde{z}}\cos(\Phi)\right)\cos(\Phi) \\
c\cdot B_{\tilde{x}\tilde{x}} &= \left(F_{t,\Delta\dot{\tilde{x}}}\cos(\Phi) + F_{n,\Delta\dot{\tilde{x}}}\sin(\Phi)\right)\cos(\Phi) - \left(F_{t,\Delta\dot{\tilde{z}}}\cos(\Phi) + F_{n,\Delta\dot{\tilde{z}}}\sin(\Phi)\right)\sin(\Phi) \\
c\cdot B_{\tilde{x}\tilde{z}} &= \left(F_{t,\Delta\dot{\tilde{x}}}\cos(\Phi) + F_{n,\Delta\dot{\tilde{x}}}\sin(\Phi)\right)\sin(\Phi) + \left(F_{t,\Delta\dot{\tilde{z}}}\cos(\Phi) + F_{n,\Delta\dot{\tilde{z}}}\sin(\Phi)\right)\cos(\Phi) \\
c\cdot B_{\tilde{z}\tilde{x}} &= \left(F_{t,\Delta\dot{\tilde{x}}}\sin(\Phi) - F_{n,\Delta\dot{\tilde{x}}}\cos(\Phi)\right)\cos(\Phi) - \left(F_{t,\Delta\dot{\tilde{z}}}\sin(\Phi) - F_{n,\Delta\dot{\tilde{z}}}\cos(\Phi)\right)\sin(\Phi) \\
c\cdot B_{\tilde{z}\tilde{z}} &= \left(F_{t,\Delta\dot{\tilde{x}}}\sin(\Phi) - F_{n,\Delta\dot{\tilde{x}}}\cos(\Phi)\right)\sin(\Phi) + \left(F_{t,\Delta\dot{\tilde{z}}}\sin(\Phi) - F_{n,\Delta\dot{\tilde{z}}}\cos(\Phi)\right)\cos(\Phi)
\end{aligned}
$$

Equation 3-53

Once the steady state pressure is known, it can be used to obtain the perturbation pressures. The perturbation pressures can then be used to find the dynamic stiffness and damping coefficients. Substituting the dynamic coefficients into the equation of motion, the dynamic positioning (orbit) of the journal can be found. For the case of a rotor of

mass *2M*, supported by two identical and perfectly aligned journal bearings, the equation of motion can be written as:

$$\begin{bmatrix} M & 0 \\ 0 & M \end{bmatrix}\begin{bmatrix} \Delta\ddot{\tilde{x}} \\ \Delta\ddot{\tilde{z}} \end{bmatrix} = \begin{bmatrix} B_{\tilde{x}\tilde{x}} & B_{\tilde{x}\tilde{z}} \\ B_{\tilde{z}\tilde{x}} & B_{\tilde{z}\tilde{z}} \end{bmatrix}\begin{bmatrix} \Delta\dot{\tilde{x}} \\ \Delta\dot{\tilde{z}} \end{bmatrix} + \begin{bmatrix} K_{\tilde{x}\tilde{x}} & K_{\tilde{x}\tilde{z}} \\ K_{\tilde{z}\tilde{x}} & K_{\tilde{z}\tilde{z}} \end{bmatrix}\begin{bmatrix} \Delta\tilde{x} \\ \Delta\tilde{z} \end{bmatrix} + \begin{bmatrix} \Delta W_{\tilde{x}} \\ \Delta W_{\tilde{z}} \end{bmatrix}$$

Equation 3-54

Several methods can be used to solve the linear differential equation given Equation 3-54, to find the dynamic position of the journal for known perturbation values. However, this is still a simplified solution to a more complex dynamic response of the bearing. These results assume the journal motion occurs in one plane normal to the journal axis but, the journal may not be parallel to the bearing. Additional stiffness and damping coefficients are necessary to determine the potential conical motion of the journal relative to the bearing due to misalignment. For the present case only the translational displacements are considered.

The equation of motion given in the linear differential equation of Equation 3-54 is limited to small displacements from the initial steady state position. The linearization of the bearing reaction forces allows the decoupling of the rotor and the bearing, thus allowing the rotor equations to be solved independently of the lubrication equations. For larger displacements the nonlinear effects become more significant, requiring the rotor equations to be integrated simultaneously with the lubrication equations. For many practical applications, the solution of Equation 3-54 offers a good approximation for the dynamic response of a bearing.

The perturbation from a steady state equilibrium position was implemented by increasing the applied load by 2%, which correlated to a dimensional change in journal position of 0.3% - 0.5% of the total radial bearing clearance. It has been shown, when using linear stiffness coefficients, that the choice of the perturbation load must be made carefully due to the nonlinear characteristics of the bearing stiffness. Choy, Braun and Hu performed numerical experiments which showed that the nonlinear characteristics of the bearing decrease the accuracy of the linear stiffness coefficients near the equilibrium position for large perturbation loads, while the opposite is true for small perturbation loads [108, 109]. Their numerical experiments selected a change in the journal position in both radial coordinates equal to 0.2% of the total radial bearing clearance, which resulted in less than a 1% variation in the values of the linear stiffness coefficients. Thus, the applied perturbation load used for this study was limited to 2% to retain the same level of accuracy.

3.6.3 Journal Bearing Stability Analysis

For certain combinations of speeds and loads, bearing instability occurs and steady state operation is not possible. If the bearing operates in these unstable conditions, journal vibrations will continuously increase and are only restricted by contacting the inner bearing surface. A critical load and speed can be defined that marks the threshold of instability such that: below a certain value, deviations from steady state operation are dampened, and above the same value, deviations from steady state operation continuously increase. The following section outlines the solution method to solve for

these critical variables which follows the method presented in the works of Constantinescu [80].

By assuming the perturbation solution has the form:

$$\begin{bmatrix} \Delta\tilde{x} \\ \Delta\tilde{z} \end{bmatrix} = \begin{bmatrix} \mathrm{Re}\left\{x' e^{i\omega t}\right\} \\ \mathrm{Re}\left\{z' e^{i\omega t}\right\} \end{bmatrix} \qquad \text{Equation 3-55}$$

which can be written in matrix form as:

$$\begin{bmatrix} K_{\tilde{x}\tilde{x}} + i\omega B_{\tilde{x}\tilde{x}} - M\omega^2 & K_{\tilde{x}\tilde{z}} + i\omega B_{\tilde{x}\tilde{z}} \\ K_{\tilde{z}\tilde{x}} + i\omega B_{\tilde{z}\tilde{x}} & K_{\tilde{z}\tilde{z}} + i\omega B_{\tilde{z}\tilde{z}} - M\omega^2 \end{bmatrix} \begin{bmatrix} x' \\ z' \end{bmatrix} = 0$$

Equation 3-56

The system in Equation 3-56 is homogeneous, so the determinant must be zero allowing the critical mass and frequency to be found as:

$$M_c\omega_c^2 = \frac{K_{\tilde{x}\tilde{x}} B_{\tilde{z}\tilde{z}} + K_{\tilde{z}\tilde{z}} B_{\tilde{x}\tilde{x}} - K_{\tilde{x}\tilde{z}} B_{\tilde{z}\tilde{x}} - K_{\tilde{z}\tilde{x}} B_{\tilde{x}\tilde{z}}}{B_{\tilde{x}\tilde{x}} + B_{\tilde{z}\tilde{z}}} \qquad \text{Equation 3-57}$$

$$\omega_c^2 = \frac{\left(K_{\tilde{x}\tilde{x}} - M_c\omega_c^2\right)\left(K_{\tilde{z}\tilde{z}} - M_c\omega_c^2\right) - K_{\tilde{x}\tilde{z}} K_{\tilde{z}\tilde{x}}}{B_{\tilde{x}\tilde{x}} B_{\tilde{z}\tilde{z}} - B_{\tilde{z}\tilde{x}} B_{\tilde{x}\tilde{z}}} \qquad \text{Equation 3-58}$$

First, Equation 3-57 is solved for the product of the critical mass and frequency. Then Equation 3-58 can be solved for the critical frequency, which is then used in Equation 3-57 to find the critical mass. When $M_c>0$, the operating condition is stable if $M<M_c$ and unstable for $M>M_c$. If $M_c<0$, stability occurs for any condition.

From the definition of the stiffness and damping coefficients, a dimensionless can be defined as:

$$\overline{M}_c = \frac{M_c c \omega^2}{W} \qquad \text{Equation 3-59}$$

Since the critical mass is constant for a given set of steady state operating conditions, this dimensionless critical mass can be used to create a stability map for a range of rotational speeds [80].

3.6.4 Discretization of the Perturbation Equations

The discretization of the perturbation pressure equations uses the same subdomain method reviewed in Section 3.5. It can be seen that the left hand side of the perturbation equations are of similar form as the steady state pressure equation that was discretized in Section 3.5, and only the source terms on the right hand side differ. The fluid film region is divided into non-overlapping control volumes around individual grid points as was shown in Figure 3-18, with the same grid point cluster layout that was given in Figure 3-19.

By integrating the perturbation equations over the control volume we get the following:

$$\int_s^n \int_w^e \left[g \cdot \frac{\partial}{\partial x}\left(\frac{{h_o}^3}{\mu \cdot H\left(|\dot{\gamma}|\right)} \frac{\partial p_o}{\partial \tilde{x}} \right) + g \cdot \frac{\partial}{\partial y}\left(\frac{{h_o}^3}{\mu \cdot H\left(|\dot{\gamma}|\right)} \frac{\partial p_o}{\partial \tilde{y}} \right) - g \cdot \frac{3}{\mu l_o} p_o \cdot \Im \right] d\tilde{x} \cdot d\tilde{y} =$$
$$= \int_s^n \int_w^e \left[6U \frac{\partial h_o}{\partial \tilde{x}} - \frac{3}{\mu l_o} p_{inj} \cdot \Im \right] d\tilde{x} \cdot d\tilde{y}$$

Equation 3-60

$$\int_{s}^{n}\int_{w}^{e}\left[g\cdot\frac{\partial}{\partial\tilde{x}}\left(\frac{{h_o}^3}{\mu\cdot H\left(|\dot{\gamma}|\right)}\frac{\partial p_{\tilde{x}}}{\partial\tilde{x}}\right)+g\cdot\frac{\partial}{\partial\tilde{y}}\left(\frac{{h_o}^3}{\mu\cdot H\left(|\dot{\gamma}|\right)}\frac{\partial p_{\tilde{x}}}{\partial\tilde{y}}\right)-g\cdot\frac{3}{\mu l_o}p_{\tilde{x}}\cdot\Im\right]d\tilde{x}\cdot d\tilde{y}=$$

$$=\int_{s}^{n}\int_{w}^{e}\left[-6U\sin(\theta)-g\cdot\frac{\partial}{\partial\tilde{x}}\left(\frac{3{h_o}^2\cos(\theta)}{\mu\cdot H\left(|\dot{\gamma}|\right)}\frac{\partial p_o}{\partial\tilde{x}}\right)-g\cdot\frac{\partial}{\partial\tilde{y}}\left(\frac{3{h_o}^2\cos(\theta)}{\mu\cdot H\left(|\dot{\gamma}|\right)}\frac{\partial p_o}{\partial\tilde{y}}\right)\right]d\tilde{x}\cdot d\tilde{y}$$

Equation 3-61

$$\int_{s}^{n}\int_{w}^{e}\left[g\cdot\frac{\partial}{\partial\tilde{x}}\left(\frac{{h_o}^3}{\mu\cdot H\left(|\dot{\gamma}|\right)}\frac{\partial p_{\tilde{z}}}{\partial\tilde{x}}\right)+g\cdot\frac{\partial}{\partial\tilde{y}}\left(\frac{{h_o}^3}{\mu\cdot H\left(|\dot{\gamma}|\right)}\frac{\partial p_{\tilde{z}}}{\partial\tilde{y}}\right)-g\cdot\frac{3}{\mu l_o}p_{\tilde{z}}\cdot\Im\right]d\tilde{x}\cdot d\tilde{y}=$$

$$=\int_{s}^{n}\int_{w}^{e}\left[6U\cos(\theta)-g\cdot\frac{\partial}{\partial\tilde{x}}\left(\frac{3{h_o}^2\sin(\theta)}{\mu\cdot H\left(|\dot{\gamma}|\right)}\frac{\partial p_o}{\partial\tilde{x}}\right)-g\cdot\frac{\partial}{\partial\tilde{y}}\left(\frac{3{h_o}^2\sin(\theta)}{\mu\cdot H\left(|\dot{\gamma}|\right)}\frac{\partial p_o}{\partial\tilde{y}}\right)\right]d\tilde{x}\cdot d\tilde{y}$$

Equation 3-62

$$\int_{s}^{n}\int_{w}^{e}\left[g\cdot\frac{\partial}{\partial\tilde{x}}\left(\frac{{h_o}^3}{\mu\cdot H\left(|\dot{\gamma}|\right)}\frac{\partial p_{\dot{\tilde{x}}}}{\partial\tilde{x}}\right)+g\cdot\frac{\partial}{\partial\tilde{y}}\left(\frac{{h_o}^3}{\mu\cdot H\left(|\dot{\gamma}|\right)}\frac{\partial p_{\dot{\tilde{x}}}}{\partial\tilde{y}}\right)-g\cdot\frac{3}{\mu l_o}p_{\dot{\tilde{x}}}\cdot\Im\right]d\tilde{x}\cdot d\tilde{y}=$$

$$=\int_{s}^{n}\int_{w}^{e}\left[-12\cos(\theta)\right]d\tilde{x}\cdot d\tilde{y}$$

Equation 3-63

$$\int_{s}^{n}\int_{w}^{e}\left[g\cdot\frac{\partial}{\partial\tilde{x}}\left(\frac{{h_o}^3}{\mu\cdot H\left(|\dot{\gamma}|\right)}\frac{\partial p_{\dot{\tilde{z}}}}{\partial\tilde{x}}\right)+g\cdot\frac{\partial}{\partial\tilde{y}}\left(\frac{{h_o}^3}{\mu\cdot H\left(|\dot{\gamma}|\right)}\frac{\partial p_{\dot{\tilde{z}}}}{\partial\tilde{y}}\right)-g\cdot\frac{3}{\mu l_o}p_{\dot{\tilde{z}}}\cdot\Im\right]d\tilde{x}\cdot d\tilde{y}=$$

$$=\int_{s}^{n}\int_{w}^{e}\left[-12\sin(\theta)\right]d\tilde{x}\cdot d\tilde{y}$$

Equation 3-64

Integrating the left hand side of the perturbation equations and gathering all independent variables, the left hand side simplifies to:

$$A_e p_{(o,\tilde{x},\tilde{z},\dot{\tilde{x}},\dot{\tilde{z}}),E} + A_w p_{(o,\tilde{x},\tilde{z},\dot{\tilde{x}},\dot{\tilde{z}}),W} - p_{(o,\tilde{x},\tilde{z},\dot{\tilde{x}},\dot{\tilde{z}}),P}\left(A_e + A_w\right) + A_n p_{(o,\tilde{x},\tilde{z},\dot{\tilde{x}},\dot{\tilde{z}}),N} + A_s p_{(o,\tilde{x},\tilde{z},\dot{\tilde{x}},\dot{\tilde{z}}),S} - \\ - p_{(o,\tilde{x},\tilde{z},\dot{\tilde{x}},\dot{\tilde{z}}),P}\left(A_n + A_s\right) - A_f p_{(o,\tilde{x},\tilde{z},\dot{\tilde{x}},\dot{\tilde{z}}),P} = RHS$$

Equation 3-65

where

$$A_e = \frac{g_{(o,\tilde{x},\tilde{z},\dot{\tilde{x}},\dot{\tilde{z}}),e} h_{o,e}^3}{\mu H_{(o,\tilde{x},\tilde{z},\dot{\tilde{x}},\dot{\tilde{z}}),e}} \frac{\Delta\tilde{y}}{\Delta\tilde{x}}$$

Equation 3-66

$$A_w = \frac{g_{(o,\tilde{x},\tilde{z},\dot{\tilde{x}},\dot{\tilde{z}}),w} h_{o,w}^3}{\mu H_{(o,\tilde{x},\tilde{z},\dot{\tilde{x}},\dot{\tilde{z}}),w}} \frac{\Delta\tilde{y}}{\Delta\tilde{x}}$$

Equation 3-67

$$A_n = \frac{g_{(o,\tilde{x},\tilde{z},\dot{\tilde{x}},\dot{\tilde{z}}),n} h_{o,n}^3}{\mu H_{(o,\tilde{x},\tilde{z},\dot{\tilde{x}},\dot{\tilde{z}}),n}} \frac{\Delta\tilde{y}}{\Delta\tilde{x}}$$

Equation 3-68

$$A_s = \frac{g_{(o,\tilde{x},\tilde{z},\dot{\tilde{x}},\dot{\tilde{z}}),s} h_{o,s}^3}{\mu H_{(o,\tilde{x},\tilde{z},\dot{\tilde{x}},\dot{\tilde{z}}),s}} \frac{\Delta\tilde{y}}{\Delta\tilde{x}}$$

Equation 3-69

$$A_f = \frac{3\Im}{\mu l_o} \Delta\tilde{x} \cdot \Delta\tilde{y}$$

Equation 3-70

Integrating the source terms right hand side noting the source terms are not a functions of the dependent variables.

$$\overline{S}_o = \int_s^n \int_w^e \left[6U \frac{\partial h_o}{\partial \tilde{x}} - \frac{3}{\mu l_o} p_{inj}(\Im) \right] d\tilde{x} \cdot d\tilde{y} = 6U\left(h_{o,E} - h_{o,W}\right)\Delta\tilde{y} - \frac{3\Im}{\mu l_o} p_{inj} \cdot \Delta\tilde{y} \cdot \Delta\tilde{x}$$

Equation 3-71

$$\overline{S}_{\tilde{x}} = \int_s^n \int_w^e \left[-6U\sin(\theta) - g\cdot\frac{\partial}{\partial\tilde{x}}\left(\frac{3h_o{}^2\cos(\theta)}{\mu\cdot H(|\dot{\gamma}|)}\frac{\partial p_o}{\partial\tilde{x}}\right) - g\cdot\frac{\partial}{\partial\tilde{y}}\left(\frac{3h_o{}^2\cos(\theta)}{\mu\cdot H(|\dot{\gamma}|)}\frac{\partial p_o}{\partial\tilde{y}}\right)\right] d\tilde{x}\cdot d\tilde{y} =$$

$$= 6U(\cos(\theta_E) - \cos(\theta_W))\Delta\tilde{y} - \left[\frac{3g_e h_{o,e}^2\cos(\theta_e)}{\mu\cdot H_e}\frac{p_{o,E}-p_{o,P}}{\Delta\tilde{x}} - \frac{3g_w h_{o,w}^2\cos(\theta_w)}{\mu\cdot H_w}\frac{p_{o,P}-p_{o,W}}{\Delta\tilde{x}}\right]\Delta\tilde{y} -$$

$$-\left[\frac{3g_n h_{o,n}^2\cos(\theta_n)}{\mu\cdot H_n}\frac{p_{o,N}-p_{o,P}}{\Delta\tilde{y}} - \frac{3g_s h_{o,s}^2\cos(\theta_s)}{\mu\cdot H_s}\frac{p_{o,P}-p_{o,S}}{\Delta\tilde{y}}\right]\Delta\tilde{x}$$

Equation 3-72

$$\overline{S}_{\tilde{z}} = \int_s^n \int_w^e \left[6U\cos(\theta) - g\cdot\frac{\partial}{\partial\tilde{x}}\left(\frac{3h_o{}^2\sin(\theta)}{\mu\cdot H(|\dot{\gamma}|)}\frac{\partial p_o}{\partial\tilde{x}}\right) - g\cdot\frac{\partial}{\partial\tilde{y}}\left(\frac{3h_o{}^2\sin(\theta)}{\mu\cdot H(|\dot{\gamma}|)}\frac{\partial p_o}{\partial\tilde{y}}\right)\right] d\tilde{x}\cdot d\tilde{y} =$$

$$= 6U(\sin(\theta_E) - \sin(\theta_W))\Delta\tilde{y} - \left[\frac{3g_e h_{o,e}^2\sin(\theta_e)}{\mu\cdot H_e}\frac{p_{o,E}-p_{o,P}}{\Delta\tilde{x}} - \frac{3g_w h_{o,w}^2\sin(\theta_w)}{\mu\cdot H_w}\frac{p_{o,P}-p_{o,W}}{\Delta\tilde{x}}\right]\Delta\tilde{y} -$$

$$-\left[\frac{3g_n h_{o,n}^2\sin(\theta_n)}{\mu\cdot H_n}\frac{p_{o,N}-p_{o,P}}{\Delta\tilde{y}} - \frac{3g_s h_{o,s}^2\sin(\theta_s)}{\mu\cdot H_s}\frac{p_{o,P}-p_{o,S}}{\Delta\tilde{y}}\right]\Delta\tilde{x}$$

Equation 3-73

$$\overline{S}_{\tilde{x}} = \int_s^n \int_w^e \left[-12\cos(\theta)\right] d\tilde{x}\cdot d\tilde{y} = -12\Delta\tilde{y}(\sin(\theta_E) - \sin(\theta_W))$$ Equation 3-74

$$\overline{S}_{\tilde{z}} = \int_s^n \int_w^e \left[-12\sin(\theta)\right] d\tilde{x}\cdot d\tilde{y} = 12\Delta\tilde{y}(\cos(\theta_E) - \cos(\theta_W))$$ Equation 3-75

where $\overline{S}$ is the average value of the source term over the control volume. Combining the simplified left and right hand sides of the perturbation equations and solving for the dependent variables at node P, the discretization equations can be found.

$$p_{(o,\tilde{x},\tilde{z},\dot{\tilde{x}},\dot{\tilde{z}}),p} = \frac{\left(A_n p_{(o,\tilde{x},\tilde{z},\dot{\tilde{x}},\dot{\tilde{z}}),N} + A_s p_{(o,\tilde{x},\tilde{z},\dot{\tilde{x}},\dot{\tilde{z}}),S} + A_e p_{(o,\tilde{x},\tilde{z},\dot{\tilde{x}},\dot{\tilde{z}}),E} + A_w p_{(o,\tilde{x},\tilde{z},\dot{\tilde{x}},\dot{\tilde{z}}),W} - \overline{S}_{(o,\tilde{x},\tilde{z},\dot{\tilde{x}},\dot{\tilde{z}}),}\right)}{\left(A_f + A_n + A_s + A_e + A_w\right)}$$

Equation 3-76

The pressures given in Equation 3-76 are the internal perturbation pressures for the journal bearing. The boundary conditions are similar to those for the steady state pressure with the exception of the two boundary conditions account for the axial ends of the bearing where the perturbation pressures are set to zero rather than the ambient pressure. The boundary conditions for the dynamic loading model are summarized below.

$$\begin{aligned} p_o\left(y = 0,\, 0 \le x \le 2\pi R\right) &= p_a \\ p_o\left(y = L,\, 0 \le x \le 2\pi R\right) &= p_a \end{aligned}$$

Equation 3-77

$$\begin{aligned} p_{\tilde{x},\tilde{z},\dot{\tilde{x}},\dot{\tilde{z}}}\left(y = 0,\, 0 \le x \le 2\pi R\right) &= 0 \\ p_{\tilde{x},\tilde{z},\dot{\tilde{x}},\dot{\tilde{z}}}\left(y = L,\, 0 \le x \le 2\pi R\right) &= 0 \end{aligned}$$

Equation 3-78

$$p_{o,\tilde{x},\tilde{z},\dot{\tilde{x}},\dot{\tilde{z}}}\left(0 \le y \le L,\, x = 0\right) = p_{o,\tilde{x},\tilde{z},\dot{\tilde{x}},\dot{\tilde{z}}}\left(0 \le y \le L,\, x = 2\pi R\right)$$

Equation 3-79

3.6.5 Numerical Procedure for Dynamic Pressure Distribution

The discretization equations developed in the previous section provides the necessary algebraic expressions to solve for the pressure distribution for the dynamic loading; where the displacements from the initial steady state position are relatively small. Placing the discretization equation into a numerical format and coupling with the iterative method outlined in the flow chart shown in Figure 3-23 below, the solution

converges to describe the dynamic behavior of the journal bearing. The source code used to solve the dynamic pressure distribution is given in Appendix C.

As the flow chart outlines, the procedure for solving the dynamic pressure distribution involves several subroutines. There are five main subroutines outlined in the flow chart above which are used to solve the five differential equations given in Equations 3-40 to 3-44. Within each of the five subroutines, the same numerical procedure is used to solve for the pressure distribution as was outlined for the steady state pressure distribution described in Figure 3-20. This is possible since Equation 3-40 is the same form as the steady state equation in Equation 3-15; and the left hand side of all five equations (Equations 3-40 to 3-44) are of similar form, where only the source terms on the right hand side differ. Thus all five differential equations can be solved by the same numerical methods. Once the pressure distributions of all five differential equations are determined, the spring and damping coefficients can be found, as well as, the critical mass and frequency. The spring and damping coefficients can then be used to describe the path of the journal by solving the linear differential equation given Equation 3-54. A 4^{th} order Runge-Kutta method was used to find the dynamic position of the journal using the known perturbation values.

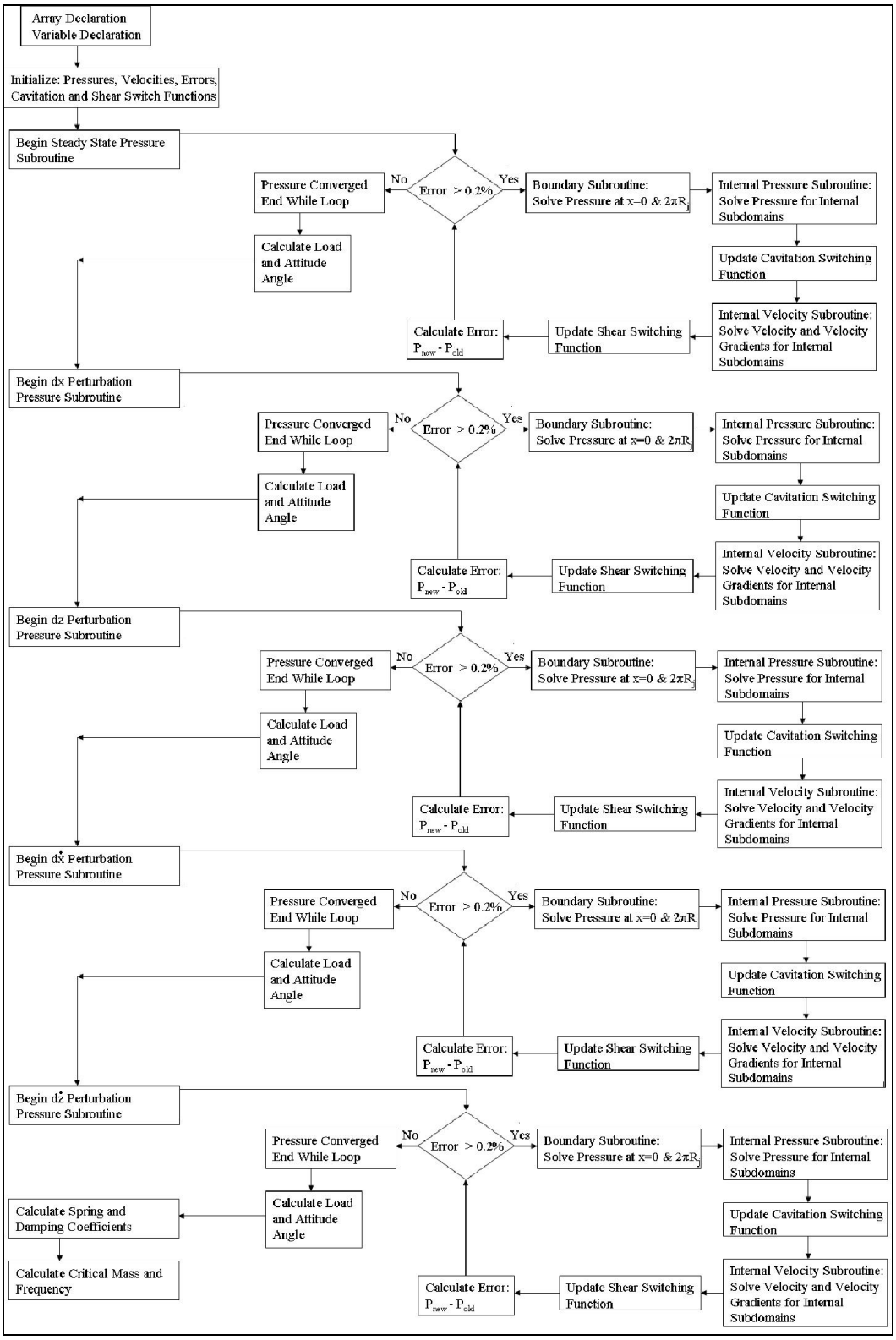

Figure 3-23 Flow Diagram Describing Dynamic Response Source Code

CHAPTER IV

EXPERIMENTAL SETUP & PROCEDURES

4.1 Introduction

A typical journal bearings load capacity is primarily a function of the bearing geometry, the rotational speed and the properties of the working fluid. For a given a set of operating conditions, the only way to actively control a hydrodynamic bearing would be to change the bearing geometry or the fluid properties during operation. The ability to change the bearing geometry is very difficult and so the variable rheology of magnetorheological fluids was used to construct a controllable hydrodynamic journal bearing.

As Urreta *et al.* [74, 75] have shown, magnetorheological fluids are most effective when the applied magnetic field is perpendicular to the primary direction of fluid motion. For a journal bearing, this can prove to be difficult as the fluid motion is primarily in the circumferential direction, requiring the magnetic field to be applied in the radial direction around the circumference of the bearing. To achieve this magnetic field, eight electromagnetic dipoles were placed circumferentially around the bearing as shown in Figure 4-1 below. The eight dipoles covered the entire circumference of the bearing and directed the field perpendicular to the fluid filled gap such that the normal magnetic field strength was nearly uniform within the fluid at the pole locations.

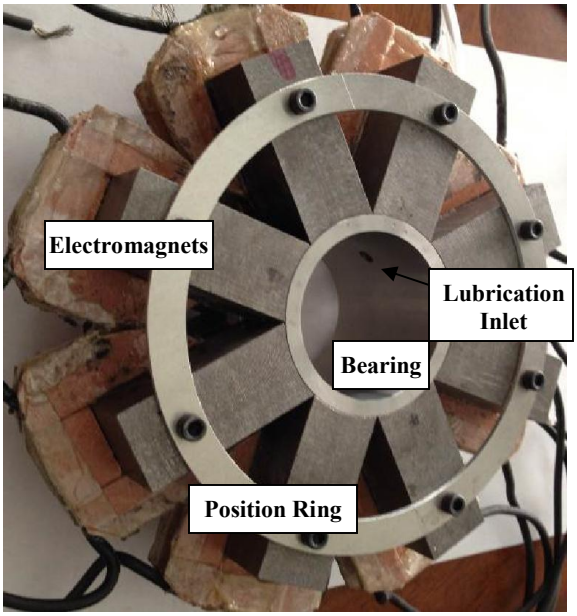

Figure 4-1 Hydrodynamic Journal Bearing and Electromagnet Design

The magnetorheological fluid created to lubricate the journal bearing contained suspended micro-sized, multi domain, magnetic carbonyl iron powder particles which were suspended in a non-magnetic ISO 32 viscosity grade carrier liquid. The suspended particles in the magnetorheological fluid become magnetized and form chain like structures that align with the applied magnetic field. The particle chains restrict the movement of the fluid which produces an apparent increase in the fluid yield strength which is proportional to the strength of the applied field. This allows control of the load capacity and damping properties of the journal bearing by using this reversible and nearly instantaneous change in the fluid rheological properties.

Using the test bench shown in Figure 4-2, a series of short experiments were performed to provide proof of performance for the bearing design and validate the numerical results. To evaluate the primary effect of the magnetorheological fluid on the bearing performance, the experiments attempted to verify load capacity increase by

recording the change in the bearing position, which correlates to the change in eccentricity ratio, with increasing magnetic field.

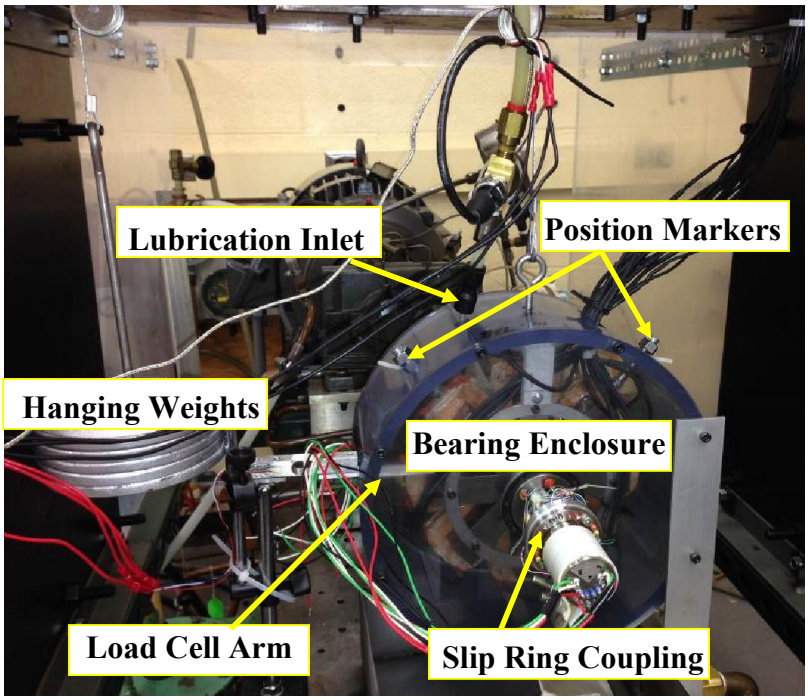

Figure 4-2 Picture of Test Bench Setup

4.2 Magnetorheological Fluid Production and Qualification

The magnetorheological fluid was created by adding carbonyl iron powder (CIP) to an ISO 32 viscosity grade hydraulic carrier fluid with white lithium grease mixed into the fluid to act as a surfactant dispersing agent. A total of seven different samples of approximately 400ml were initially evaluated which consisted of a range of solid content by mass of carbonyl iron powder from approximately 2% to 75%. The viscosity at 40 ^{o}C and 80 ^{o}C for a range of magnetic fields was measured as well as the specific gravity.

4.2.1 Magnetorheological Fluid Sample Compositions

Carbonyl iron was chosen to be used for the magnetic particles because: it can easily be magnetized and demagnetized, it has a high magnetic permeability and it is commercially available in the desired particle size range. The carbonyl iron powder was manufactured by BASF, using the thermally decomposing iron penta-carbonyl process outlined in Figure 4-3. The main properties of the CIP result from the decomposition conditions, while the individual grades are determined by the finishing processes [110]. The CN grade, whose properties are contained in Table 4-1, was chosen for its particle size distribution and high iron content.

Table 4-1 Carbonyl Iron Powder CN Properties (BASF Certified Analysis)

Property	Value	Test Method
Fe (g/100g)	99.8	Calculated
C (g/100g)	0.007	IRS (RCA/Q-C 296)
N (g/100g)	0.01 max.	TCD (RCA/Q 297)
O (g/100g)	0.18	IRS (RCA/Q-C 297)
Tap Density (g/cm^3)	4.1	ASTM B 527 (analog)
Particle Size Distribution:		
D_{10} (μm)	3.4	Beckman LS 13320 (RCA/Q-C-300)
D_{50} (μm)	7.1	
D_{90} (μm)	15.3	

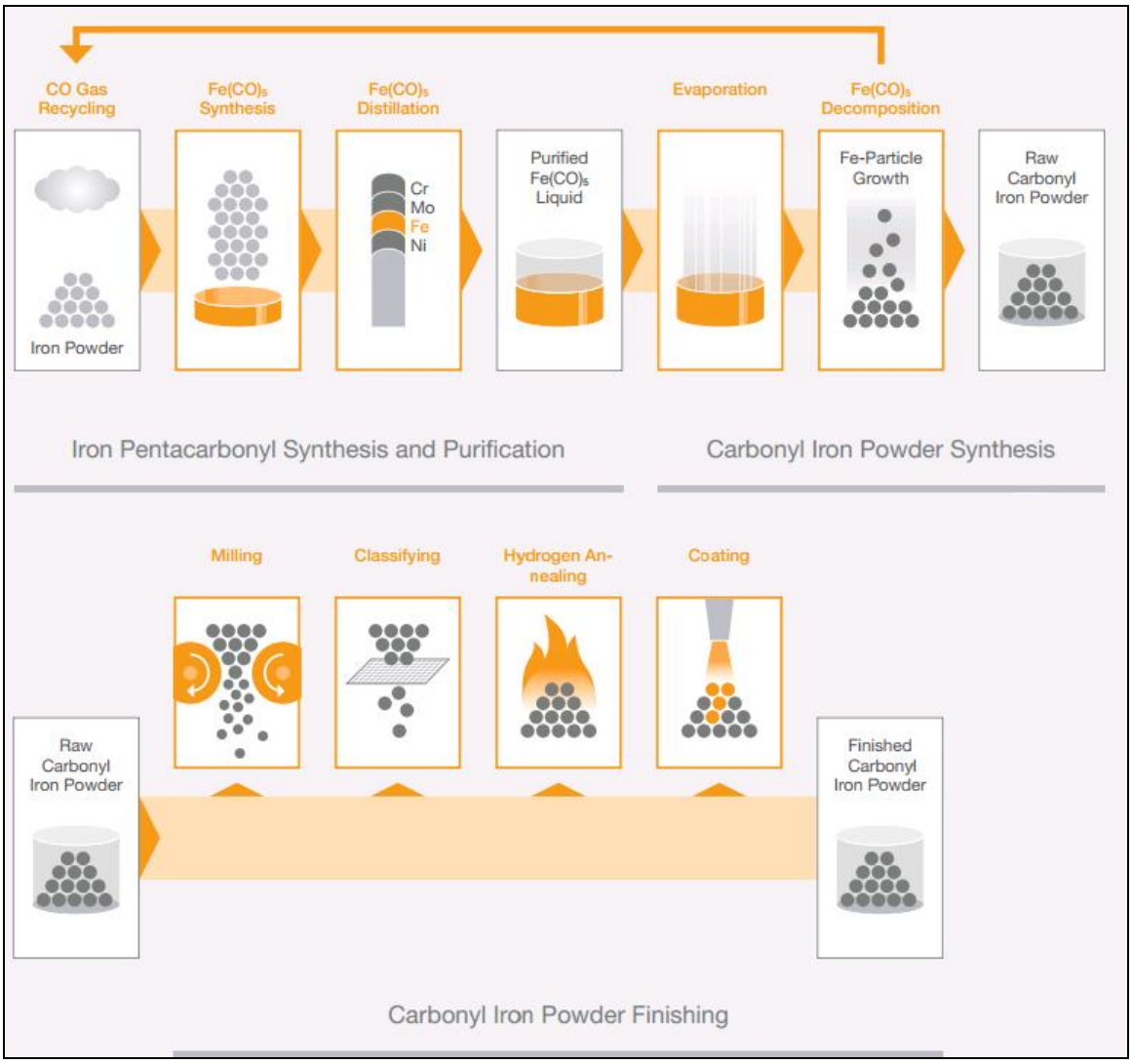

Figure 4-3 BASF Carbonyl Iron Powder Production Process [110]

The carrier fluid chosen was an ISO 32 viscosity grade fully formulated hydraulic fluid produced by Mag1. A lower viscosity grade carrier fluid was chosen to allow a higher percentage of solid content to be added and still retain a lower viscosity when not energized. The main properties of the carrier fluid are contained in Table 4-2.

Table 4-2 ISO 32 Hydraulic Fluid Properties

Property	Limit	Test Method
Specific Gravity @15.6 °C	0.8631	ASTM D4052
Viscosity @ 40 °C cSt	32.11	ASTM D445
Viscosity @ 100 °C cSt	5.55	ASTM D455
Viscosity Index	110	ASTM D2270

To create the magnetorheological fluid samples, approximately 300 mL of the carrier fluid was poured into individual containers and weighed using a model 211 My Weigh iBalance, which has readability of 0.001 g [111]. Next, a corresponding amount of CIP was weighed and mixed in with the carrier fluid to create the desired mixtures of 2%, 5%, 10%, 15%, 25%, 50% and 75% solid content by mass. This provided a wide range of percent solid content MR fluids to evaluate; however, the corresponding amount of white lithium grease to prevent particle settling still had to be determined.

An iterative trial and error process was used to determine the amount of white lithium grease to add to each fluid sample. A small amount of grease, on the order of 3 to 6 grams, was sequentially added to each fluid sample until particle settling was effectively eliminated over a 24 hour monitoring period. The final compositions for each fluid sample are shown in Table 4-3.

Table 4-3 Magnetorheological Fluid Sample Compositions

Solid Content Target (% Mass)	Solid Content (% Mass)	Grease Content (% Mass)
2%	1.91%	5.94%
5%	4.73%	4.13%
10%	9.23%	8.03%
15%	13.81%	7.40%
25%	22.70%	9.30%
50%	43.90%	12.03%
75%	62.59%	15.90%

4.2.2 Magnetorheological Fluid Sample Property Measurements

The viscosity of each fluid sample was measured at 40 ^{o}C and 80 ^{o}C for a range of magnetic fields; using a Lab-Line Model 4537 rotary viscometer, which has an accuracy of +/-1 cP [112]. The samples were poured into a beaker and submerged into a constant temperature water bath, while the magnetic field was applied to the fluid by an electromagnetic cradle as shown in Figure 4-4 below.

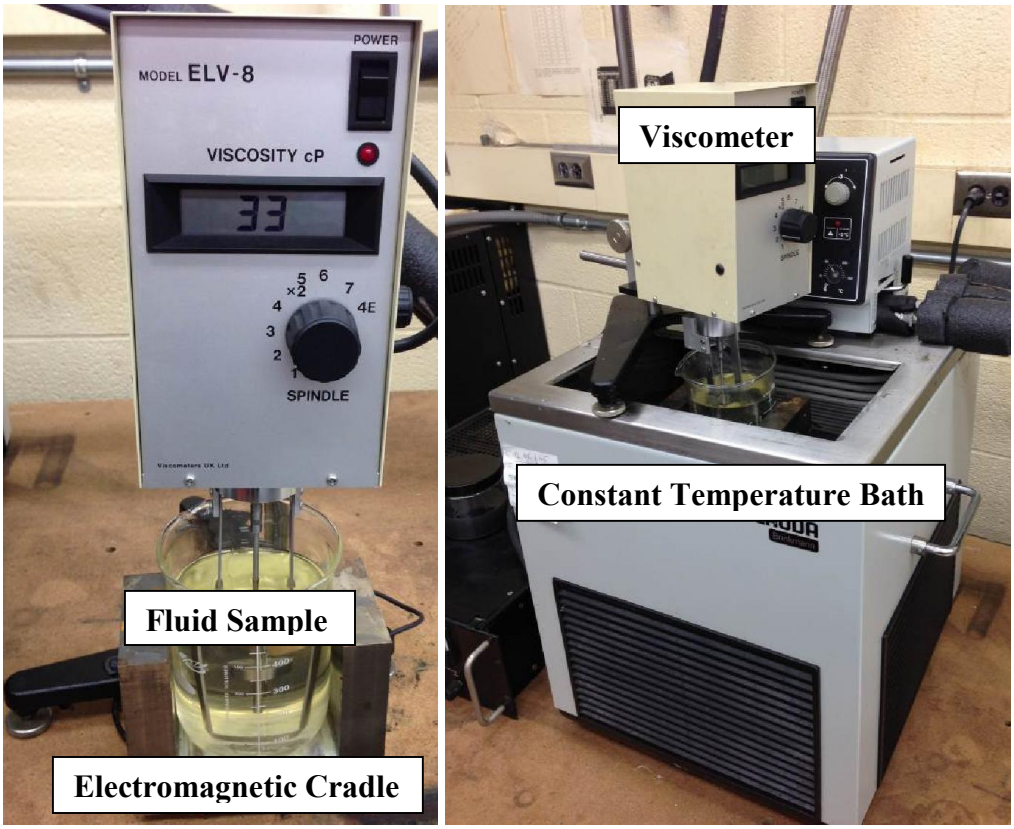

Figure 4-4 Viscosity Measurement and Electromagnetic Cradle Setup

As can be seen in Figure 4-5, the magnetic field applied to the MR fluid samples, travels across the fluid from the magnetic north pole to the magnetic south pole of the electromagnetic cradle. The resulting chain like structures formed by the magnetic particles, are perpendicular to the rotary motion of the viscometer along one axis, and parallel to the opposing axis. This creates two viscosity measurement regions within the fluid; one where the viscous force is due to apparent increased viscosity of the magnetized MR fluid, and a second where the viscous force results from only the un-magnetized fluid viscosity. This means that the dynamic viscosity of the MR fluid could be directly measured when the magnetic field was not applied; while the viscosity of the fluid had to be calculated when the magnetic field was applied.

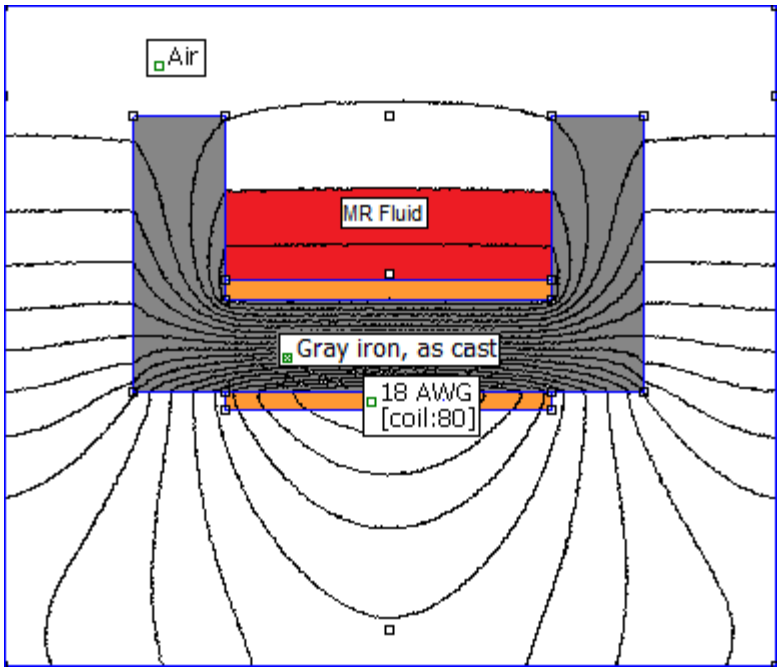

Figure 4-5 Electromagnetic Cradle Cross Section with Magnetic Field Applied

Both the dynamic viscosity and yield stress of the energized MR fluid had to be calculated from the viscosity measurements generated by the rotary viscometer. The dynamic viscosity of the MR fluid when the magnetic field was applied was calculated by doubling the increase in viscosity and adding it to the unmagnetized fluid viscosity.

$$\mu_{apparent} = 2 \cdot \left(\mu_{measured} - \mu_{unmagnitized}\right) + \mu_{unmagnitized} \qquad \text{Equation 4-1}$$

The yield stress could then be calculated from the difference between the shear stress of the fluid when the magnetic field was applied and not applied.

$$\tau_{yield} = \tau_{apparent} - \tau_{unmagnitized} \qquad \text{Equation 4-2}$$

Details regarding the calculation of the dynamic viscosity and yield stress of the MR fluid can be found in Appendix F.

The magnetic field was generated by applying a range of currents from a SRL 49-25 model Sornsen power supply to an 80 turn solenoid made of 18 AWG copper wire. Since the magnetic field is dependent on the magnetic permeability of the medium it travels through, in this case the fluid sample, the applied current was fixed at increments from 5 Amps up to 20 Amps. The corresponding magnetic induction was measured using an AlphaLab GM 1-ST Gauss meter which has an accuracy of +/-1% at 16 to 20 ^{o}C and +/-2% at -4 to 65 ^{o}C [113]. The increase in solid particle content increased the overall magnetic permeability of each fluid sample which creates a higher magnetic field within the fluid sample as can be seen in Figure 4-6. The resulting magnetic induction measurements were found to be independent of temperature, while the increase in magnetic field appears to approach an asymptotic saturation point beyond 25% solid content by mass.

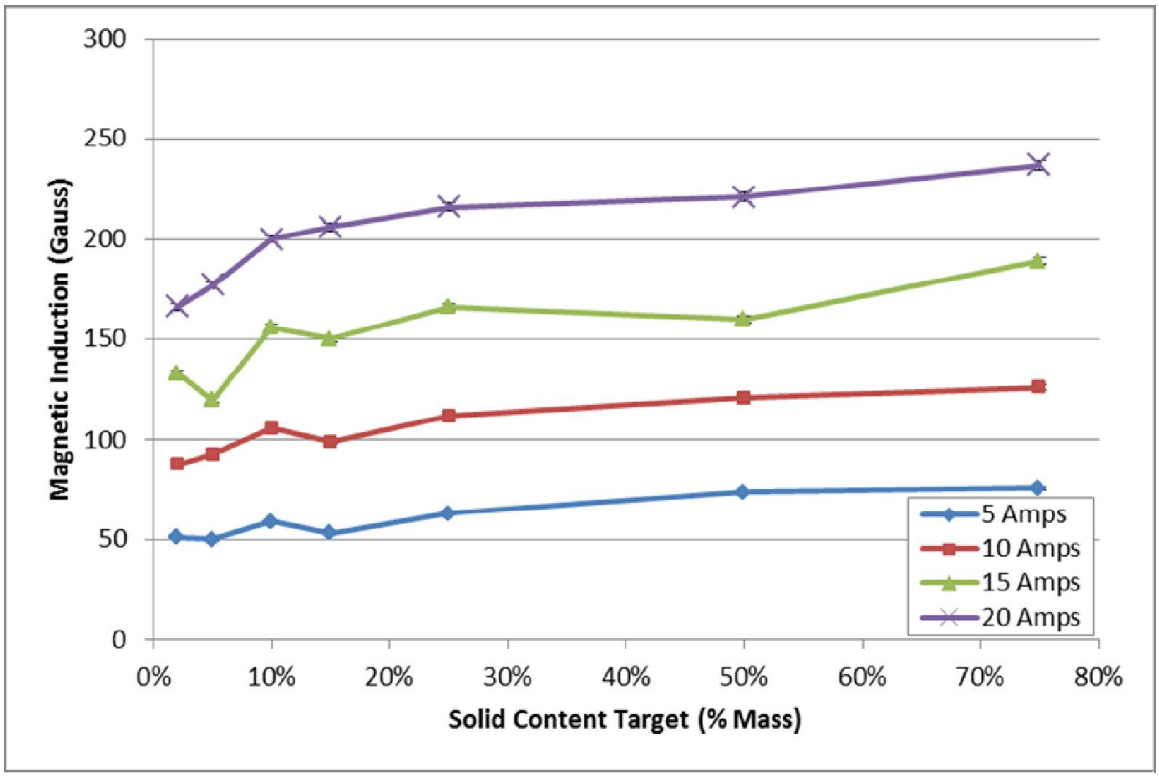

Figure 4-6 Magnetic Field Inside Fluid Samples at Various Applied Currents

The specific gravity of each fluid sample was measured at 15.6ºC using hydrometers as specified in the ASTM E-100 procedure. The specific gravity was then used to determine the density at 15.6 ºC; while more direct, albeit less accurate, method was utilized to determine the density at elevated temperatures. For fluid temperatures of 40 ºC, 80 ºC and room temperature (approximately 24 ºC), a 10 ml graduated cylinder and 211 My Weigh iBalance were used. A transfer pipette was used to add 9 ml of each sample fluid into the 10 ml graduated cylinder which was weighed before and after the fluid sample was added. The fluid samples were then heated using a constant temperature bath and the fluid volume was recorded. The fluid densities were then determined by

dividing the original fluid mass by the fluid volume at each temperature which is shown in Figure 4-7.

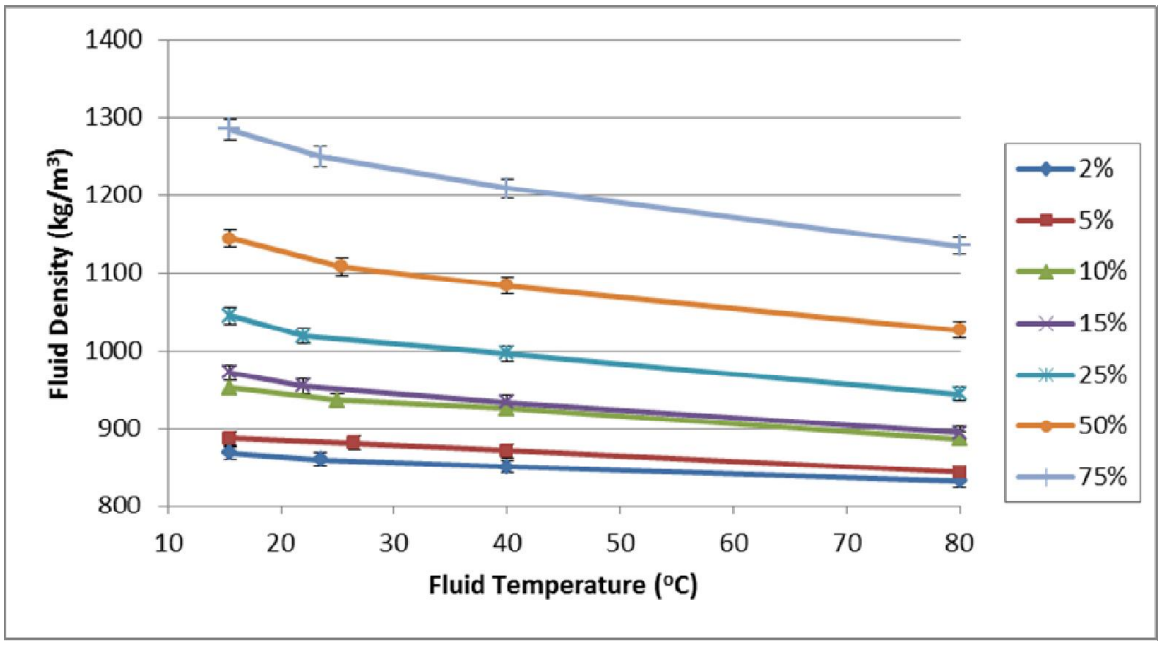

Figure 4-7 Density of Fluid Samples at Various Temperatures

4.3 Hydrodynamic Journal Bearing Assembly Design

The key geometric parameter of a bearing is the radial internal clearance; which is the difference in the radii of the bearing and the journal. Typical bearing diametric clearances range between 25-50 μm per 25 mm diameter. The clearance for this design was chosen to be at the upper limit of acceptable values to increase fluid flow and lower operating temperatures. This also allows for better resolution in the measurement of the relative positions of the journal and bearing centers. The radial internal clearance and other defining dimensions are listed below.

- Bearing Radial Clearance: 0.120 mm
- Journal Diameter: 50 mm

- Bearing Length: 60 mm

4.3.1 Journal and Bearing Design

The construction of the journal bearing (Figure 4-8) consisted of a grey iron journal and a 304 stainless steel bearing. The relevant characteristics of both materials are provided in Table 4-4 below. These materials were carefully chosen to allow a consistent magnetic field across the fluid film, perpendicular to the shearing forces. The paramagnetic bearing design allowed the magnetic field to pass through the bearing cross section at one magnetic pole and along the length of the high magnetic permeability ferromagnetic journal and return to the opposite magnetic pole.

Table 4-4 Journal and Bearing Material Properties

	Journal	**Bearing**
Material Name	Cast Grey Iron	304 Stainless Steel
Density (kg/m^3)	7,150	8,030
Heat Capacity (J/g-C)	0.45	0.5
Thermal Coefficient (μm/C)	12	17
Relative Permeability	5,000 max	1.0

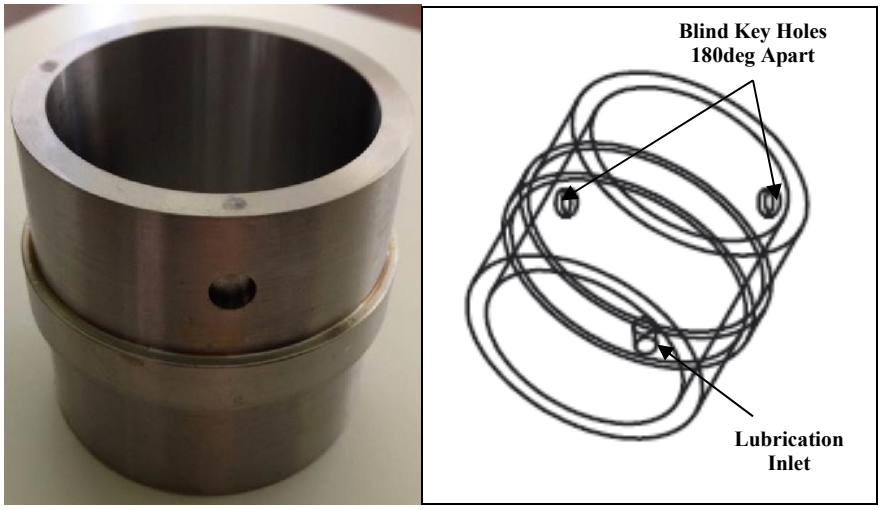

Figure 4-8 Journal Bearing Design

Figure 4-9 below provides an overview, and additional dimensions, of the bearing design. As can been seen in Figure 4-9, the bearing cross section is 2 mm thick with a small step in the center which aides in aligning the U-shaped electromagnets. The lubrication inlet feed is a 5 mm diameter through bore located at the center of the bearing, which leads to a 100 mm long section of flexible tubing. This lubrication feed was specifically designed to accommodate the electromagnet arrangement. Two blind bore holes can also be seen in Figure 4-9, which are 180 degrees apart and on one axial end of the bearing. These blind holes were designed to accommodate two small grey iron pins that fit into similar holes in two of the electromagnets. This prevents the complement of electromagnets from rotating along the outer circumference of the bearing.

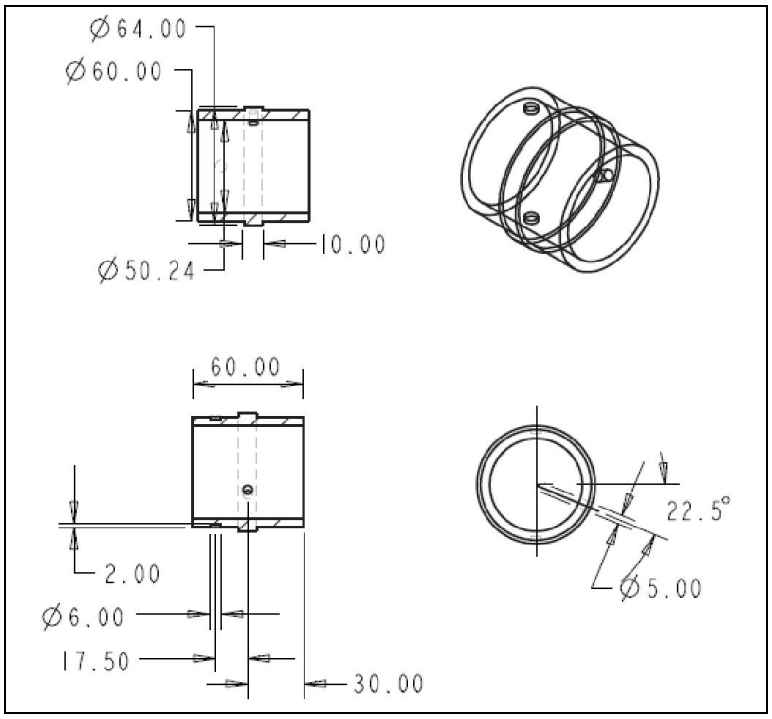

Figure 4-9 Bearing Dimensions

Figure 4-10 below provides an overview and additional dimensions of the journal design. The journal is a 152 mm long cylinder that is coupled to a drive motor on one axial end and coupled to a 21 channel electrical slip ring on the opposite axial end (couplings not shown in Figure 4-10). Three 1 mm diameter pressure ports extend approximately half the length of the journal to allow pressure readings to be recorded at the surface of the journal during operation. One pressure port is located at the center of the bearing location, while the other two are located 15 mm from each axial end of the bearing location. The axial portals are located 60 degrees apart for assembly purposes; however, a pressure profile of the entire bearing at three axial locations could be generated for each revolution of the journal.

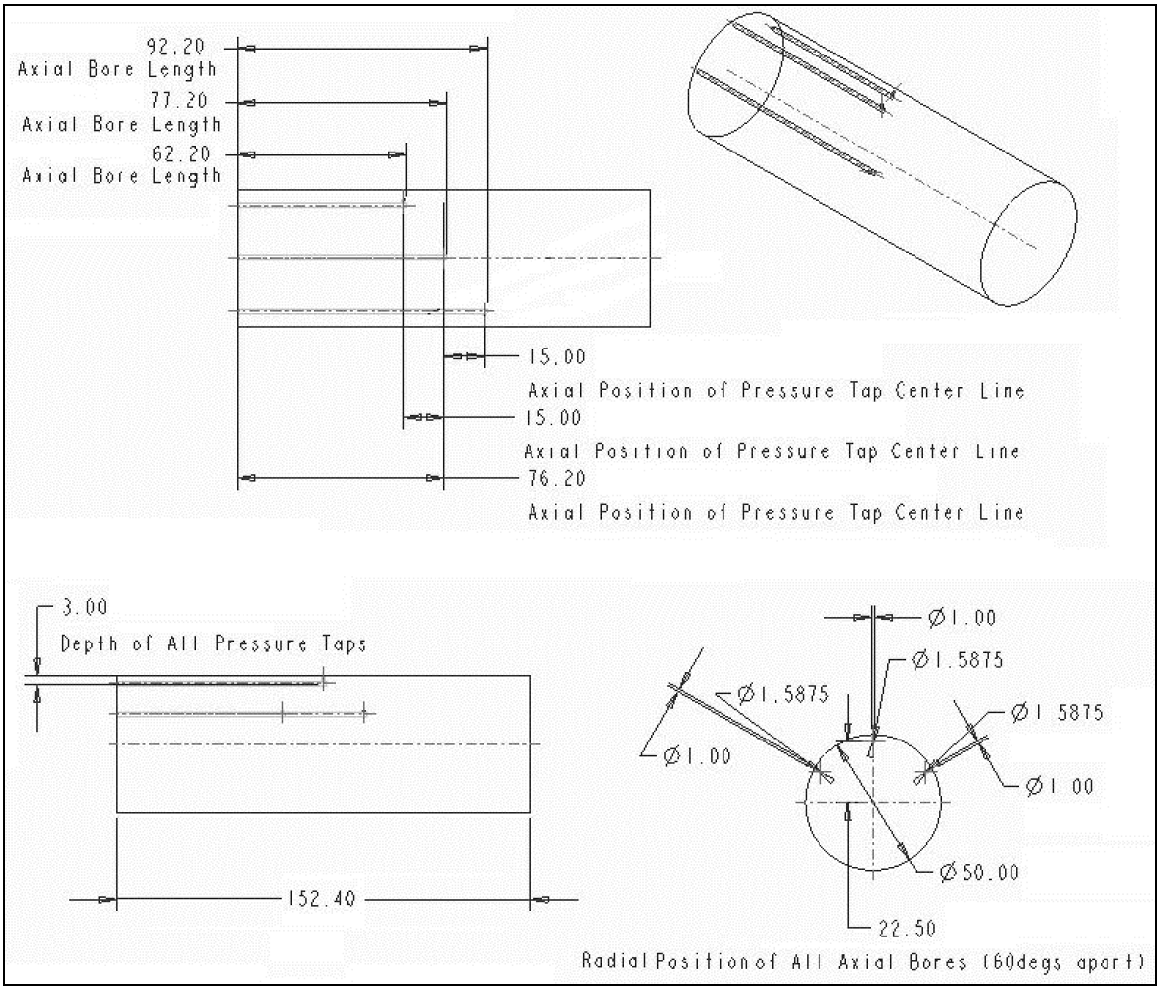

Figure 4-10 Journal Dimensions

The use of dissimilar materials for the bearing and journal was necessary to facilitate the magnetic field; however, it introduces an additional design consideration. The rate of thermal expansion for the stainless steel bearing is significantly greater than that of the grey iron journal. Thus, as the operating temperature increases, the radial internal clearance in the bearing will increase at a rate of approximately 1% for every 10 ^{o}C above ambient conditions. The dimensional increase in the bearing radial internal clearance verses the increase in operating temperature is provided in Figure 4-11 below.

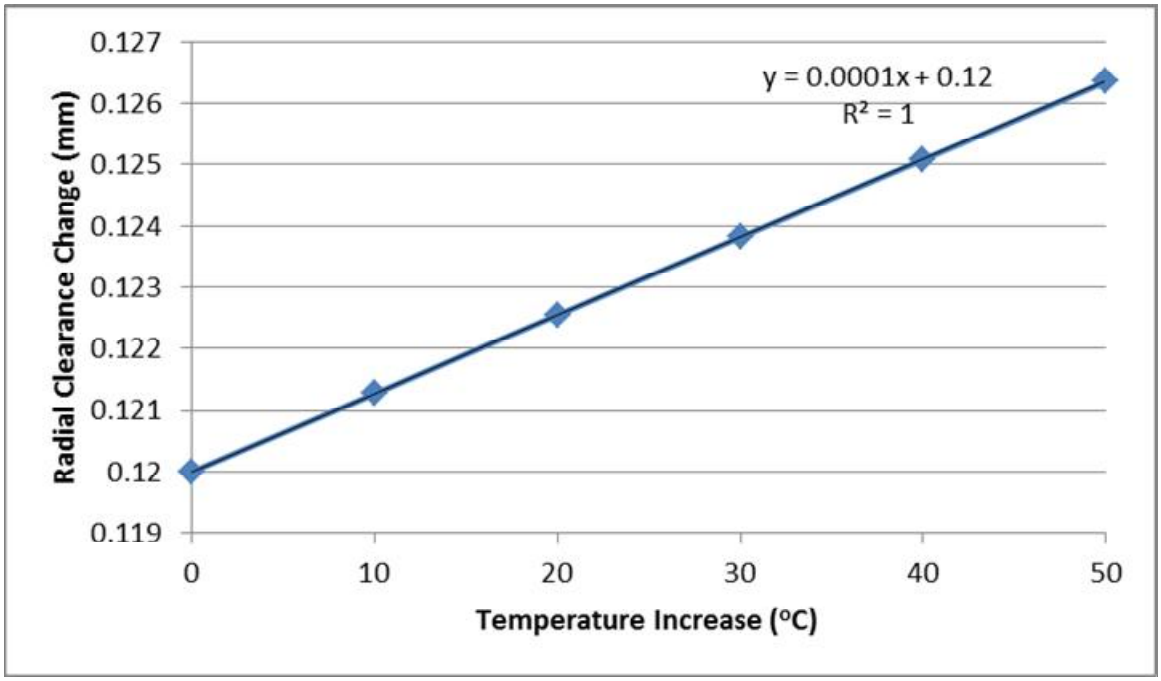

Figure 4-11 Bearing Clearance Relative to Increasing Temperature

4.3.2 Electromagnet Design

The magnetic field was applied by eight nearly identical electromagnets arranged around the circumference of the bearing. The electromagnets were designed such that the complement of electromagnets was fixed to the bearing to create a single assembled piece, as was shown in Figure 4-1. Each electromagnet was comprised of a 40 turn coil solenoid, of 18AWG copper wire, surrounding a grey iron U-shaped core (Figure 4-12). The relevant material properties of the electromagnets are provided in Table 4-5 below.

Table 4-5 Electromagnet Material Properties

	Solenoid	Magnetic Core
Material Name	18 AWG Copper Wire	Cast Grey Iron
Density (kg/m^3)	8960	7150
Heat Capacity (J/g-C)	0.385	0.45
Thermal Coefficient (μm/C)	17	12
Resistance (Ω/m)	0.02095	N/A
Relative Permeability	1.0	5,000 max

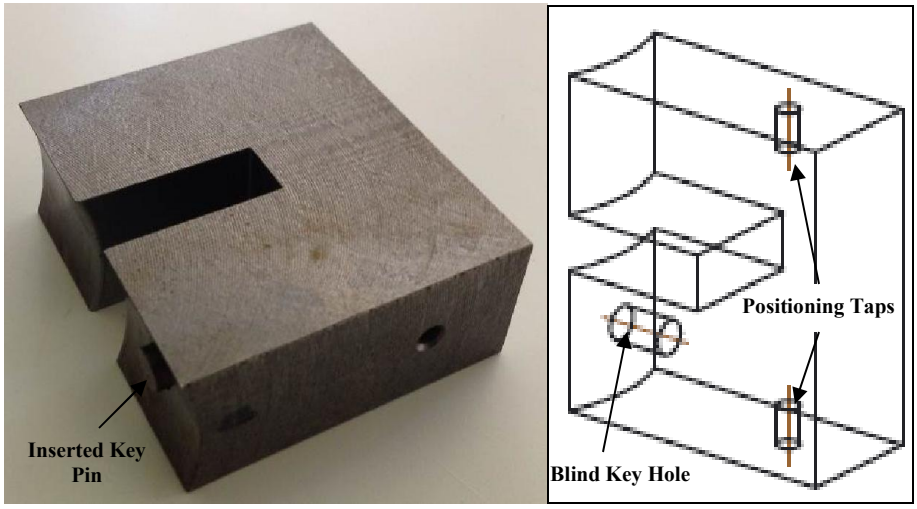

Figure 4-12 Electromagnetic Core Design

Figure 4-13 below provides an overview and dimensions of the electromagnetic core design. As can been seen in Figure 4-13, the electromagnet core is essentially a 50 x 60 x 23 mm block with a 30 mm radius cut into the base to fit against the outer circumference of the bearing and a 10 mm wide slot to accommodate the 40 turn solenoid. Three blind bore holes can also be seen in Figure 4-13, one on each axial end of the electromagnet and the third on one end of the magnetic poles. These blind holes were designed to affix the complement of electromagnets to the bearing as a single assembled piece. Each electromagnet is fastened to a positioning ring with machine screws on each

axial end to keep each electromagnet evenly spaced 45 degrees apart. The third blind hole accommodates a small grey iron pin, which fits into two similar holes in the bearing, which prevents the complement of electromagnets from rotating along the outer circumference of the bearing.

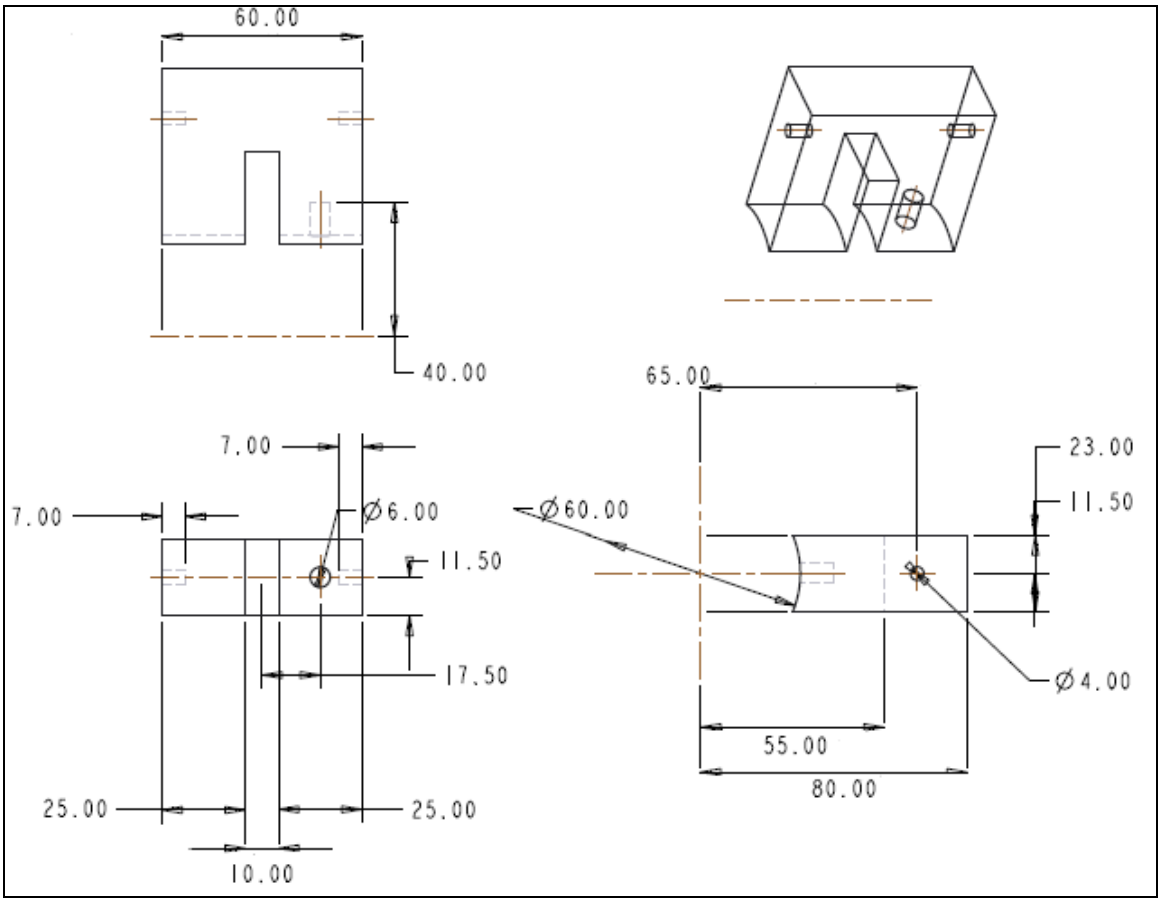

Figure 4-13 Electromagnet Core Dimensions

Solenoids act like resistors which convert electrical energy into heat. The amount of heat generated can have a significant impact in the bearing performance as the fluid viscosity, electrical resistance across the solenoids and the bearing clearance (due to the dissimilar materials used) are all temperature dependent. Using Ohm's law and Joule's first law, the rate of heat generation can be calculated for a given applied current. Using

the properties of the 18AWG copper wire (provided in Table 4-5), the rate of temperature increase can be calculated. The worst case scenario, in which the heat dissipation is neglected, is shown in Figure 4-14 below. While a more complex heat sink was not required, the operating temperature should be closely monitored at higher applied currents during continued operation.

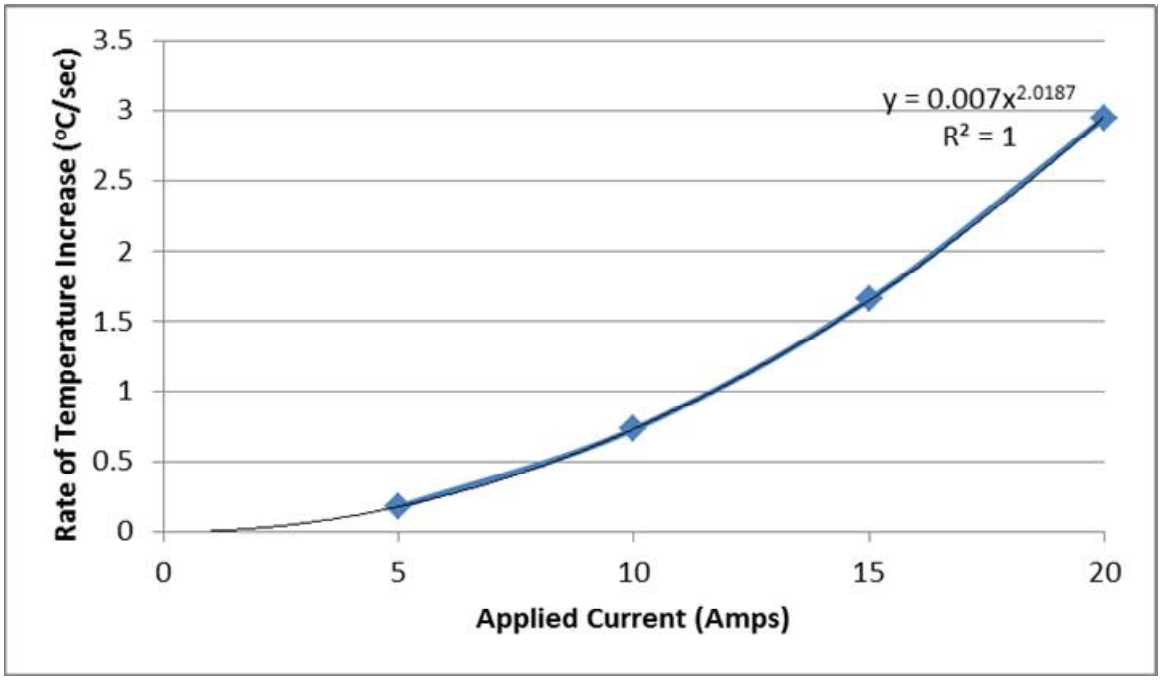

Figure 4-14 Rate of Temperature Increase for Each Solenoid

4.3.3 Bearing Assembly Method

The bearing assembly consists of 30 separate components: 1 journal, 1 bearing, 8 electromagnets, 2 positioning pins and 2 positioning rings with 16 set screws to attach to the electromagnets on each side. This allows the entire bearing assembly to function as a single unit, while still allowing for complete disassembly, as shown in the exploded view

in Figure 4-15 below (with the exception of the solenoids which are permanently fixed to the magnetic cores).

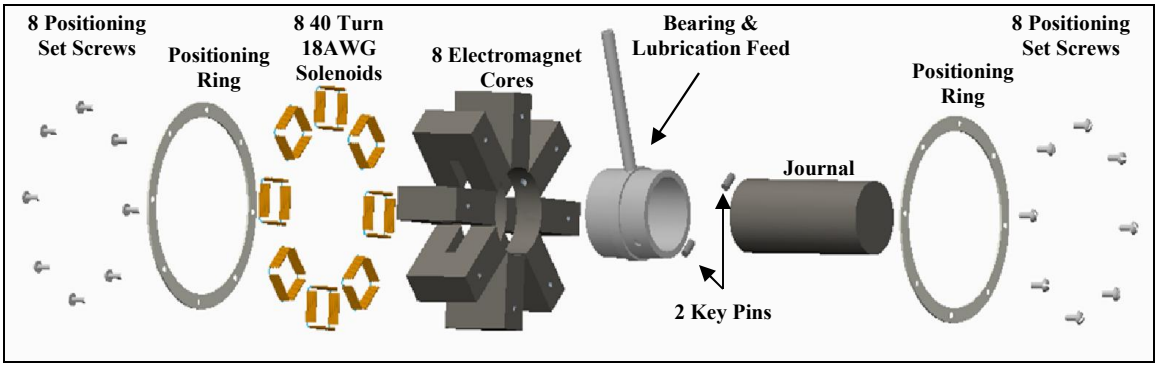

Figure 4-15 Exploded View of Bearing Components

4.4 Bench Test Setup

An available test bench at the University of Akron was used to provide a proof of concept for the bearing design. The bearing assembly was assembled on the journal which was connected a 15hp Inverter drive motor and connected to an array of measurement devices. A section of clear PVC pipe was used as an enclosure with sealed end caps at each axial end. Access ports for the load application, lubrication and various instrumentation and wiring were located around the circumference of the enclosure. The other main components of the test bench were the lubrication circuit, load application, power supply and the drive motor, each of which are identified by unique colors in Figure 4-16. Additional detail on each of the subcomponents and as well as the data acquisition system are discussed in the following subsections. Calibration data for each measurement device can be found in Appendix H.

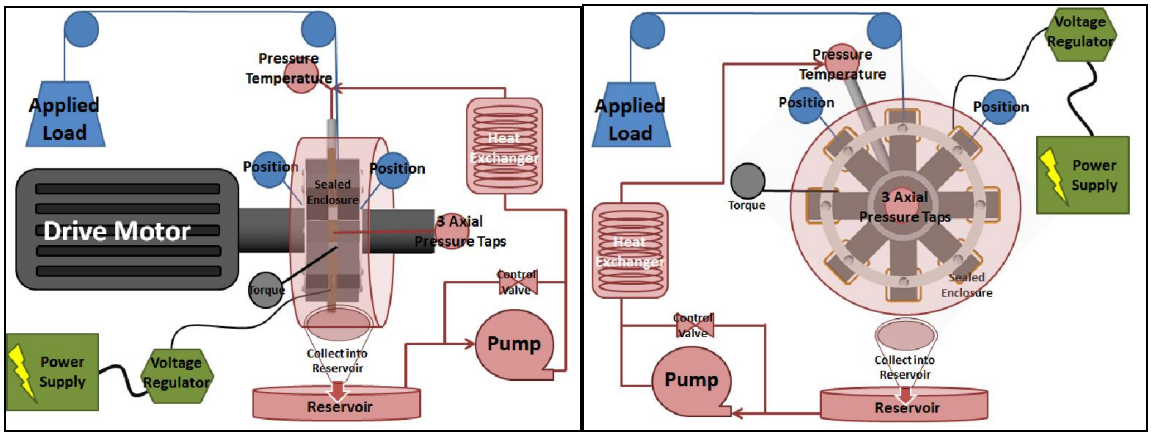

Figure 4-16 Bench Test Setup Overview (Side and End View of Bearing Assembly)

4.4.1 Bearing Load Application System

The load was applied to the bearing assembly by a hanging weight system. A bracket was attached to the center of the top electromagnet on the bearing assembly. A cable was attached to the bracket and run through an access portal in the enclosure up to a pair of overhead pulleys and back down to a weight hanger on one side of the bearing assembly. The total bearing assembly weighed 4.768 kg and an equivalent weight was added to the weight hanger to balance the system. Weight added subsequently to the hanger provided the load to the bearing in the vertical upwards direction, effectively loading the bearing in the same manner as applying a load on the journal in the downward vertical direction.

Two 3300 XL 8 mm Bently Nevada proximity transducers, which have a +/-5% measurement error capability, were used to measure the position of the bearing center relative to the center of the journal. The transducers were placed 90 degrees apart and held in place by a support that was isolated from the test bench to eliminate any vibration translating from the test bench to the proximity sensors. A small section of threaded steel

bar was used as a position indicator button for the sensors. The steel indicator button was attached to the bearing assembly, and insulated from the electromagnetic field generated from the electromagnets, by a 1 inch section of threaded stainless steel extending from the electromagnet to just outside of the bearing enclosure where it then was attached to the indicator button using a stainless steel nut.

The rotational torque of the bearing assembly was measured by a load cell created by a temperature compensated quarter-bridge strain gauge circuit. The strain gauges were placed on a load arm made of a piece of spring steel that was extended from the load cell inside the bearing enclosure through an access port located on the side of the enclosure. The load arm rested at a single point on the top side of one of the electromagnets 50 mm from the centerline of the bearing, such that the rotational torque transmitted from the journal to the bearing assembly was resisted by the load cell arm.

4.4.2 Lubrication Circuit

The lubrication circuit consisted of a 4 liter lubrication sump feeding a ½ horsepower rotary pump which supplied the lubrication to the single lubrication inlet port in the bearing. Once the lubrication exited the axial ends of the bearing, it was collected in the bearing enclosure and gravity fed back into the sump located just below the enclosure. The lubrication supply pressure to the bearing was controlled by a manual recirculation valve spanning the pump; while the temperature of the bearing lubrication supply was controlled by a 5x12 inch tube and shell heat exchanger utilizing city water supply as the control fluid.

The lubrication supply pressure and temperature were measured at a t-fitting located 100 mm upstream from the bearing inlet port and controlled to the desired set points by manual control valves to the pump and heat exchanger respectively. A ¼ NPT pipe plug type K thermocouple was used to measure the inlet temperature with a specified error limit of 0.4% or at least 1.1 ºC. To measure the lubrication inlet pressure, a 100 psi pressure transducer made by PartsSquare with an accuracy of 1% full scale was used.

To allow pressure readings to be recorded during operation, three 1 mm diameter pressure ports located at one axial end of the journal were connected to three 100 psig EPI-050/5 pressure transducers made by Entran Devices Inc., with an accuracy of +/- 0.25% full scale. One pressure port measured at the center of the bearing location, while the other two are located 15 mm from each axial end of the bearing location. The symmetry of the pressure ports on each axial end would provide a means for determining if the bearing was centered on the pressure ports during operation.

4.4.3 Electromagnet Power Supply

The magnetic field was generated by applying varying currents generated from a SRL 49-25 model Sornsen power supply to the eight electromagnets. Each of the eight electromagnets was comprised of a 40 turn, 18AWG copper wire solenoid, surrounding a grey iron U-shaped core. The electromagnets were wired in series and arranged around the circumference of the bearing. Due to the symmetry of the design, the magnetic field was applied uniformly across the fluid gap for a given current and the corresponding magnetic field was measured using an AlphaLab GM 1-ST Gauss meter.

In the cavitated region of the bearing, it was presumed that the application of the magnetic field would have little to no impact on the bearing performance. Thus, disconnecting the power supply to the electromagnets in the cavitated region could reduce the overall power consumption. A single pole double throw relay was wired in, as shown in Figure 4-17, to allow for one or more series of electromagnets located in the low pressure region to be selectively turned off through the use of a toggle switch. Similarly, additional relays could be added such that each of the eight electromagnets could be controlled individually. Moving forward, potentiometers could be used to add an analog control for the applied current to each electromagnet and thus a controllable variable magnetic field around the circumference of the bearing.

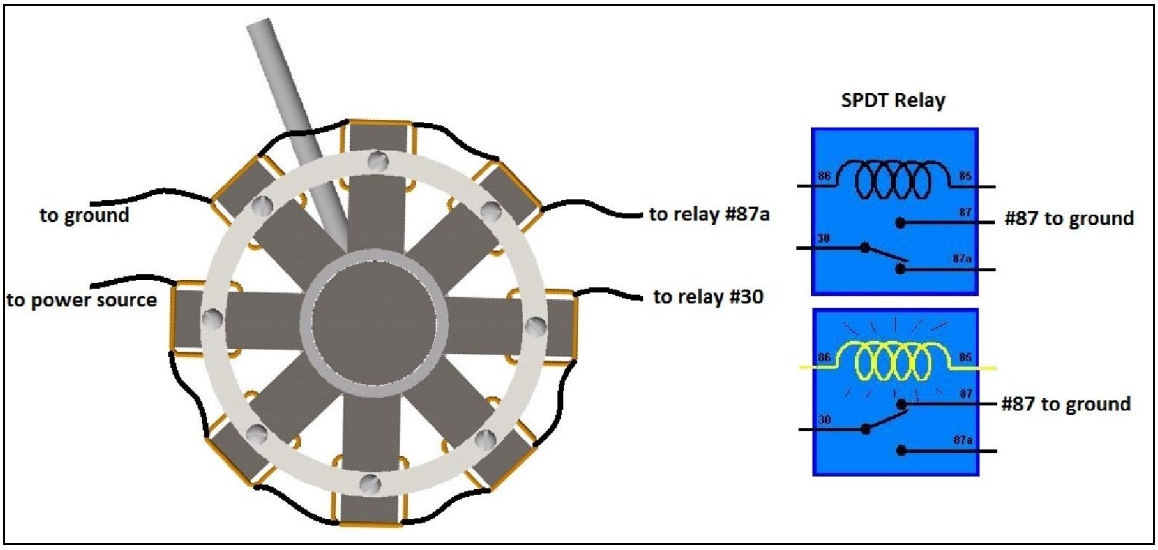

Figure 4-17 Electromagnet Wiring Diagram

4.4.4 Data Acquisition

The data acquisition system used for the bench test was a LabJack model U6 multifunction DAQ unit connected to a laptop computer equipped with LabVIEW. The

U6 is a high function data acquisition system with 14 analog inputs capable of up to 50 kHz high speed streaming input with a resolution of 16 bits as well as 20 digital I/O that were not used for this specific application [114]. The input signals from each of the four pressure transducers, two position sensors, load cell, speed encoder and thermocouple, as described in the previous sections, were recorded at 200 Hz speed. The signal voltage was recorded and then converted to physical units through post processing in Microsoft Excel using the calibration data found in Appendix H.

4.4.5 Testing Procedure

The initial test procedure involved setting up the test stand for a single operating condition with all controlled parameters established prior to recording the data for that given set of conditions. However, after analysis of the data collected, it was noted that with every shutdown of the stand and subsequent restart at the next set of operating conditions, variability was introduced. This was particularly true of the position measurement, where small axial movements of the bearing assembly relative to the proximity sensors at each restart of the test condition, resulted in significant shifts in the resulting measurements.

The subsequent test procedure was altered such that the range of operating conditions were all executed while the stand was in continuous operation and the data was recorded throughout. A marker was added to the data set, to indicate when each set of final operating conditions were met. This allowed the variability introduced by a shutdown to be eliminated from the data and also permitted easy identification of each set of operation conditions within the continuously recorded data.

In order to accommodate various devices utilized on the bench test, some limitations on operational conditions in regards to load and speed were required. The journal was unsupported at one axial end resulting in an overhung loading of the journal. To minimize the impact of shaft deflection and misalignment during operation the maximum applied load to the bearing assembly was 158 N. In order to accommodate the response time of some of the data acquisition equipment and the durability of the seals on the enclosure, the maximum operating speed was limited to 2500 rpm.

The final test procedure had a constant applied load of 158 N and speeds ranging from 500 – 2500 rpms in 500 rpm increments. Currents of 10 and 20 Amps were applied at each speed resulting in a measured magnetic field of 290 and 500 Gauss respectively across the fluid film gap. The data acquisition was initialized at the start of the test procedure at 500 rpm and no applied current. A marker was activated for 10 seconds to indicate that steady state testing conditions were achieved. The marker was then deactivated while the applied current was adjusted to 10 Amps. The marker was then activated for 10 seconds to indicate the next test condition was achieved. Subsequent testing conditions proceeded in a similar fashion with speed and current incrementally increased as shown in Table 4-6.

Table 4-6 Test Operating Conditions

Speed (rpm)	Current (Amps)	Applied Load (N)	Inlet Pressure (kPa)	Fluid Temperature (°C)
500	0, 10, 20	158	310	21
1000	0, 10, 21	158	310	21
1500	0, 10, 22	158	310	21
2000	0, 10, 23	158	310	21
2500	0, 10, 24	158	310	21

In order to evaluate the bearing performance when half of the electromagnets on the low pressure side of the bearing assembly were removed from the power supply circuit, the data acquisition started recording while the speed was set to 1000 rpm with a 158 N load applied. The marker was then activated for 10 seconds to set the baseline performance. Next, the current was increased to 20 Amps and the toggle switch connected to a relay was switched on. This removed the power supply from 4 of the 8 electromagnets on the top side of the bearing assembly and the marker was reactivated for an additional 10 seconds. Lastly, the toggle switch was turned back off such that all the magnets were connected in series while the applied current remained at 20 Amps and the marked was reactivated for 10 seconds.

The final experimental procedure was used to evaluate the dynamic response of the bearing. To accomplish this, the data acquisition began recording while the speed was set to 1000 rpm with a 136 N load applied. A 2.2 kg weight was dropped from 50 mm on top of the hanging weights to create an impact load. The 2.2 kg weight was then removed from the hanging weights and the applied current was increase to 20 Amps. The 2.2 kg weight was again dropped from 50 mm on to the hanging weights.

CHAPTER V

RESULTS

5.1 Introduction

The following chapter reviews the results for the numerical and experimental analyses whose procedures were outlined in Chapters 3 and 4 respectively. Solutions regarding the magnetorheological fluid lubricated journal bearing are presented with a varied range of speeds, loads and applied magnetic field strengths. The first section, Section 5.2, reviews the proposed bearing design and evaluates the bearing performance through numerical methods. The proof of concept is then reviewed in the subsequent section, Section 5.3, which is validated through experimental methods. The final section, Section 5.4, compares the results between the numerical and experimental investigations.

5.2 Numerical Results

The numerical study of the performance of the magnetorheological fluids consisted of a grey iron journal with a 304 stainless steel bearing surrounded by eight electromagnets comprised of a 40 turn coil using 18AWG copper wire surrounding a grey iron core. The selected fluid was MRF-140CG, which was the highest yield strength and solid particle content fluid offered by the Lord Corporation. The fluid film was divided into 10,800 subdomains with 60 in the axial direction and 180 in the circumferential

direction. The bearing is assumed to be operating in ideal conditions having perfect alignment with isothermal and laminar fluid flow. The main dimensions of the bearing and fluid properties are listed below.

- Journal Diameter: 50 mm
- Bearing Radial Clearance: 0.120 mm
- Bearing Length: 60 mm
- Inlet Feed Line Length: 100 mm
- Fluid Viscosity: 0.28 kg/m-s @ 40^{o}C
- Fluid Density: 3640 kg/m^3
- Solids Content by Weight: 85.44%
- Ambient Pressure: 101,325 N/m^2

The bearing performance was analyzed for speeds of 250, 500, 1000, 2000 and 5000 rpm, with eccentricity ratios ranging from 0.1 to 0.7, while the magnetic field was varied from 0 to 60,000 A/m. With all combinations of speeds, eccentricities and magnetic field strengths, a total of 290 unique steady state conditions were studied. The following subsections review the results of these conditions; beginning with the bearing performance with no magnetic field applied, then the electromagnets performance is discussed, followed by the bearing performance with a magnetic field applied and finally the dynamic analysis results are presented.

5.2.1 Baseline Journal Bearing Performance

The first numerical analysis performed was a baseline evaluation of the standard hydrodynamic journal bearing design. This was done by using a steady state model for

the bearing design, without applying any magnetic field to vary the rheological properties of the working fluid. Without an applied field, the yield strength of the magnetorheological fluid was set to zero. The bearing performance was analyzed for 250, 500, 1000, 2000 and 5000 rpm, with eccentricities ranging from 0.1 to 0.7 and the cavitation pressure set to zero. A representative profile of the pressure distribution and velocity profiles are shown in Figure 5-1 to Figure 5-3 below.

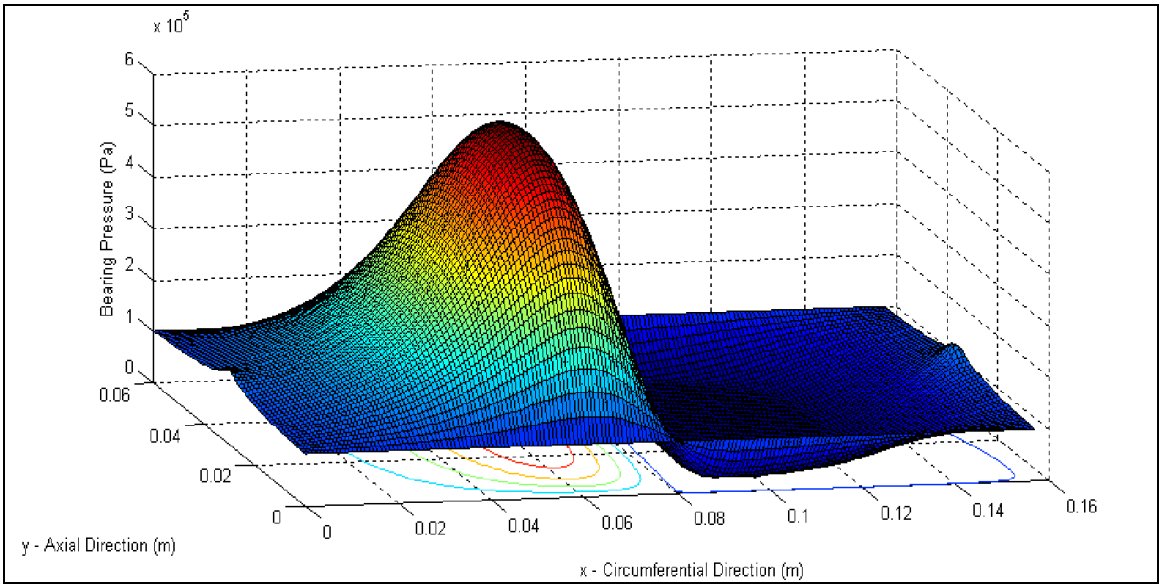

Figure 5-1 Numerical Pressure Distribution for Steady State Solution (500rpm, 0.5 Eccentricity Ratio, 0 A/m Magnetic Field)

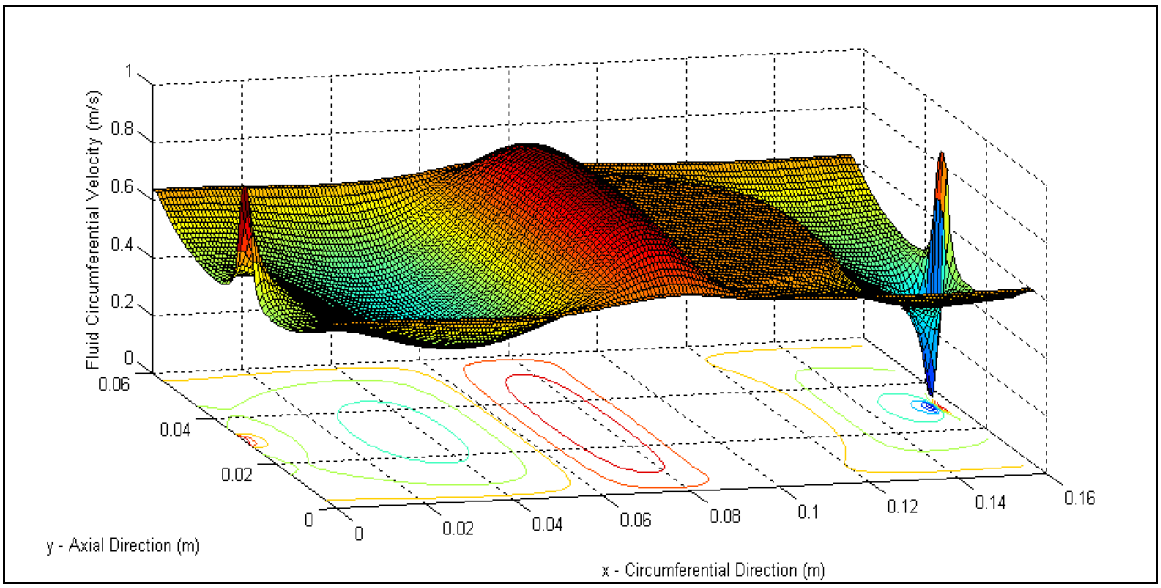

Figure 5-2 Numerical Circumferential Velocity Profile for Steady State Solution (500rpm, 0.5 Eccentricity Ratio, 0 A/m Magnetic Field)

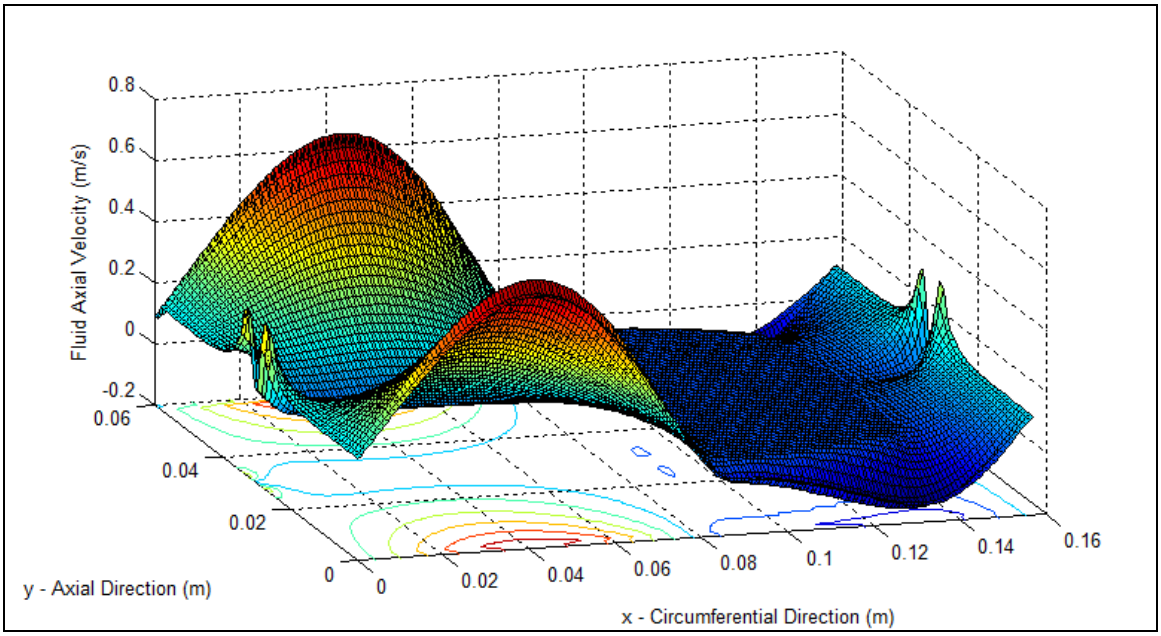

Figure 5-3 Numerical Axial Velocity Profile for Steady State Solution (500rpm, 0.5 Eccentricity Ratio, 0 A/m Magnetic Field)

The pressure distribution in Figure 5-1 shows the expected characteristics of a typical hydrodynamic journal bearing, starting with a high pressure build up in the

converging section of the bearing and followed by a sharp drop in pressure moving in to the diverging section. Figure 5-1 also highlights two key features of the numerical model. The first being the flat profile of the cavitated region located in the low pressure region of diverging section of the bearing. The second is a small pressure spike correlating to the inlet feed, which nearly aligns with the line of centers for the 500 rpm and 0.5 eccentricity ratio conditions used in this specific example.

Figure 5-2 and Figure 5-3 show the fluid velocities at the midpoint of the clearance for the circumferential and axial directions respectively. The direction of rotation defines the positive direction for the circumferential velocity, while the positive direction for the axial velocity begins in the center of the bearing and extends outward towards both axial ends. As with the pressure distribution, the cavitation and inlet feed models give rise to some unique features in the velocity profiles. For both velocity profiles, the cavitation region is represented by a flat region in the diverging section of the bearing. For the circumferential velocity, the cavitation region is a constant value due to the component of the flow driven by shearing the force. The pressure gradient within the cavitation region is zero, removing the flow contribution driven by pressure; however, some fluid is still being pulled though the cavitation region due to the journal rotation. The axial velocity in the cavitated region is zero since there is no shearing force in the axial direction. The unique profile features around the inlet feed warrant comment as well. Due to the choice of positive directions for both the circumferential and axial velocities, moving towards the higher pressure inlet impedes the fluid motion, while moving away from the higher pressure increases the fluid motion. Therefore at the inlet

location discontinuities in the velocity profiles occur as the fluid switches from moving towards the localized higher pressure to moving away.

The pressure distribution was solved for 250, 500, 1000, 2000 and 5000 rpm, with eccentricities ranging from 0.1 to 0.7 during steady state operation. By integrating the pressure distribution the load capacity of the bearing for each operating condition was solved. Using the load components normal and tangent to the line of centers, the attitude angle was also determined for each operating condition. The results of the load capacity and attitude angle for the range of operating conditions under steady state operation without the application of a magnetic field are given in Figure 5-4 and Figure 5-5 respectively. These results provide baseline data to be used in comparison with the bearing performance when a variable magnetic field is applied.

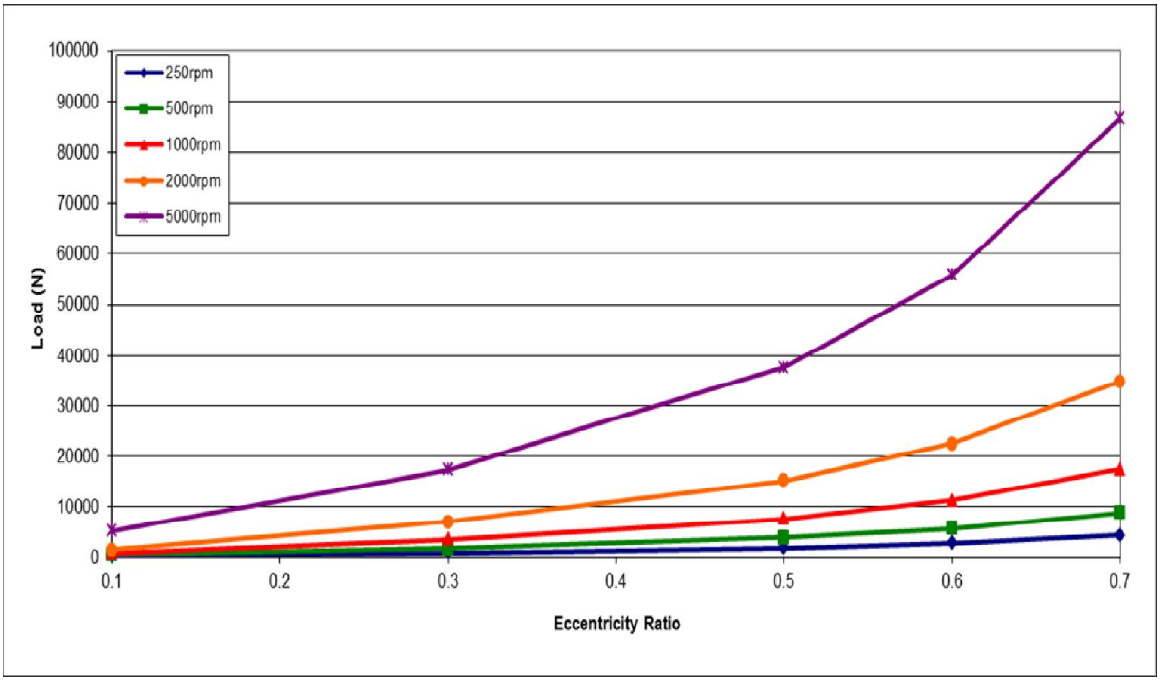

Figure 5-4 Numerical Bearing Load Capacity Relative to the Eccentricity Ratio

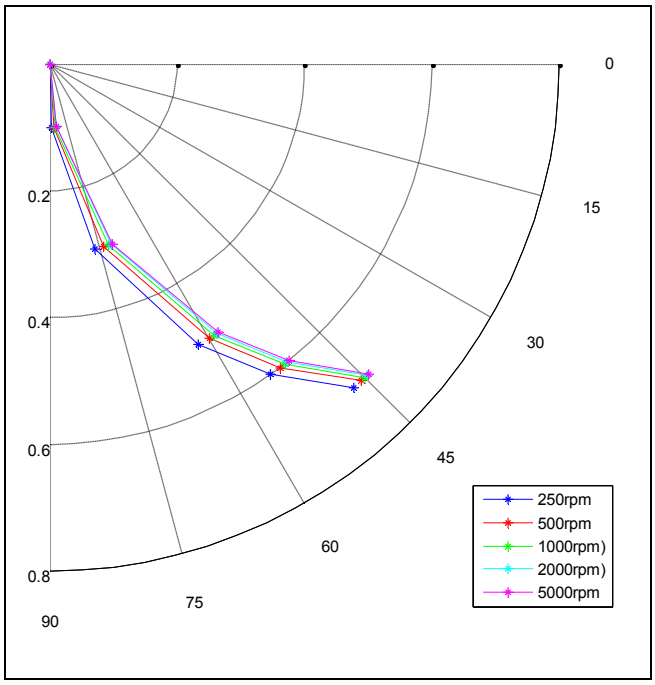

Figure 5-5 Numerical Bearing Attitude Angle Relative to the Eccentricity Ratio

5.2.2 Electromagnet Results

Before reviewing the results of the electromagnets, the determination of the operating range should be discussed. Once the design and configuration of the electromagnets was determined (based on achieving a strong and uniform magnetic field across the fluid film), two important pieces of information were needed to determine the operating range of the electromagnets. The first being the change in the fluids yield strength relative to the magnetic field strength. For the numerical analysis, data provided by the manufacturer, shown in Figure 5-6, was used. The second piece of information was the magnitude of the shearing forces applied to the fluid film during operation to ensure the yield strength of the fluid is not excessive. Based on this information a maximum magnetic field strength of 60,000 A/m was necessary.

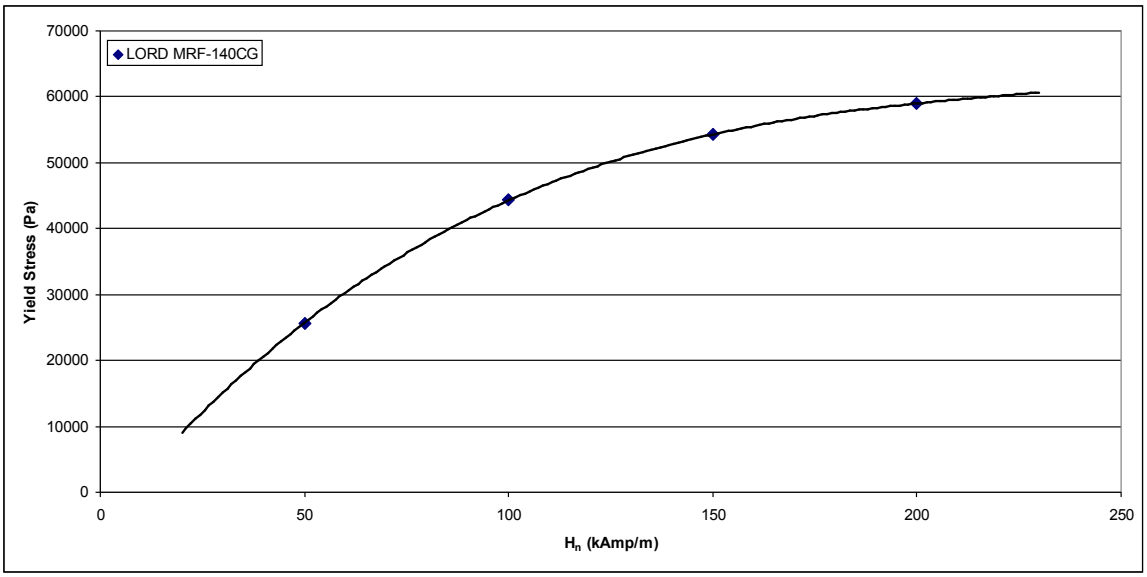

Figure 5-6 Yield Stress vs. Magnetic Field Strength for Lord MRF-140CG

The poles of each electromagnet are aligned with the axial ends of the bearing such that the magnetic field travels from one pole through the bearing and into the journal. The field then travels along the axis of the journal bearing back into to the opposing pole of each electromagnet. The magnetic field lines, generated by the FEMM software, can be seen in the cross section diagram in Figure 5-7 below. The magnetic field lines pass through the fluid film, which is highlighted in red in Figure 5-7, such that the field, at the pole locations, is normal to the shearing forces generated from the journal rotation. These lines represent the direction and magnitude of the gradient of the magnetic field strength and thus Figure 5-7 is representative of any condition where the electromagnets are activated.

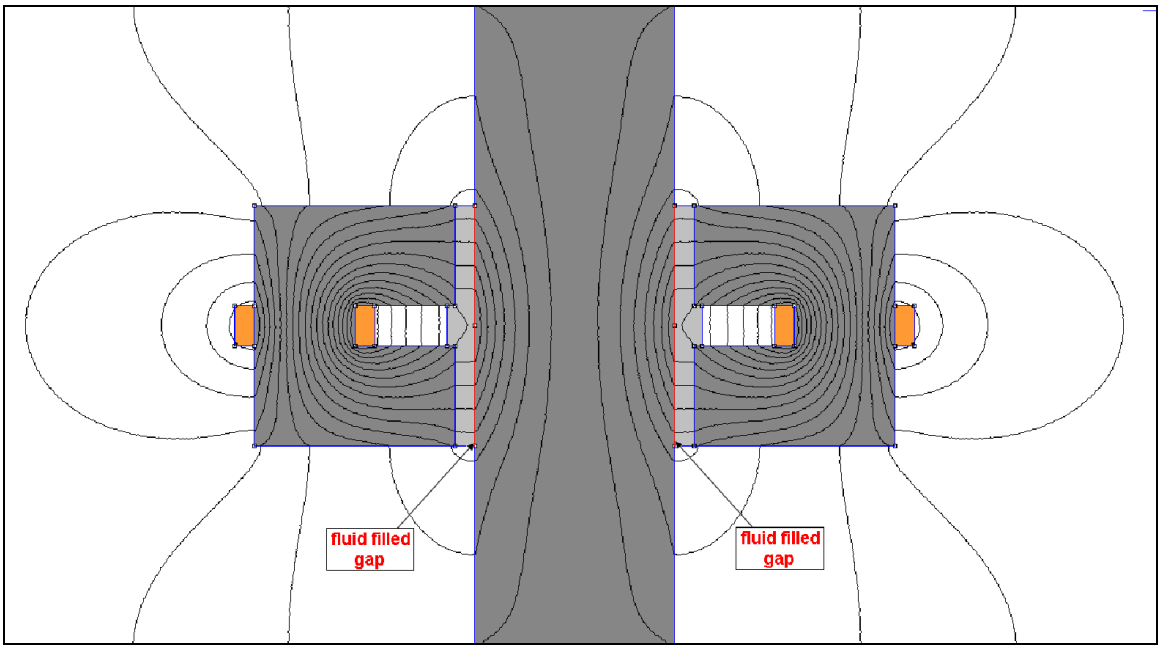

Figure 5-7 Full Bearing Cross Section Showing Magnetic Field Lines

The magnetic field lines are important to confirm that the field is passing through the fluid film normal to the shearing forces; however, the information needed for the numerical analysis is the magnitude of the magnetic field strength within the fluid film and normal to the shearing forces. This data was generated by the FEMM software for a range of applied currents, which is shown in Figure 5-8. As expected, the magnetic field strength tapers off at the axial ends of each of the poles. At the axial ends of the bearing this results in a difference of less than fifteen percent from the average value at the center of the pole.

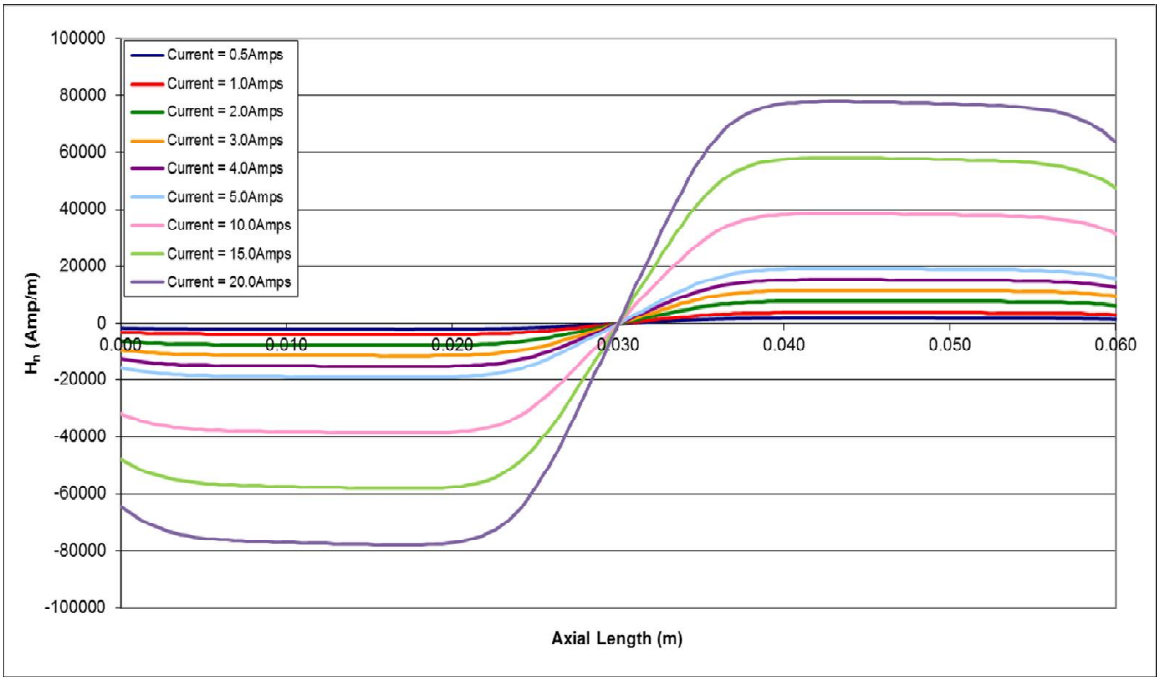

Figure 5-8 Numerical Magnetic Field Strength Inside Fluid Film and Normal to the Clearance for Range of Applied Currents

The magnetic field strength along the axial length of the bearing is symmetric about the center and appears to be linearly proportional to the applied current at any point along the bearings length. Figure 5-9 confirms that the average magnetic field strength at the pole location is in fact linearly proportional to the applied current. This trend also holds true at the opposing pole location and at the axial ends of each pole. The information in Figure 5-8 and Figure 5-9 can be used to determine the magnetic field strength applied to the fluid film normal to the shearing forces, which eliminates the need for additional runs of the FEMM software analysis for any applied current within the operable range. This means that the magnetic field strength could be solved by a subroutine inside the source code for the pressure distribution without requiring data from an external source.

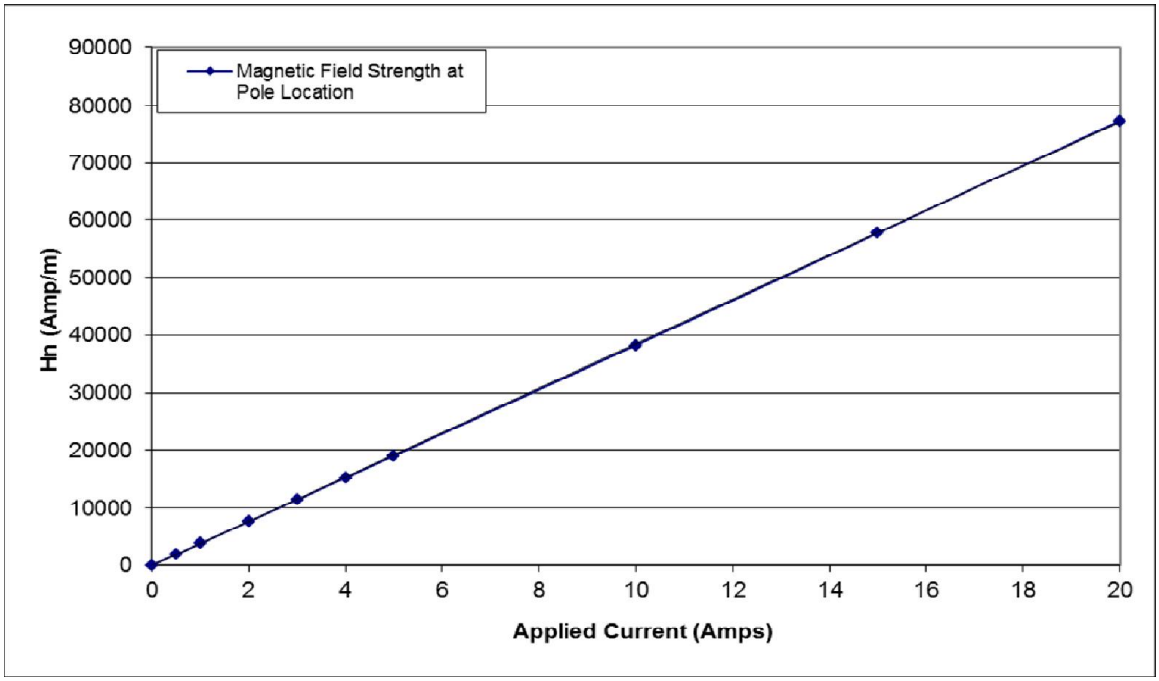

Figure 5-9 Numerical Magnetic Field Strength Normal to the Clearance at Pole Location

The results of the magnetic field produced by the electromagnets presented in this section were produced using the FEMM software. Based on these results, the necessary information to determine the yield strength of the fluid for can be calculated without the use of the FEMM software. This allows the calculation of the pressure distribution of the bearing to be performed in a self-contained source code. With the magnetic field strength and the resulting yield strength of the fluid known, the bearing performance utilizing the magnetorheological fluids controllable shear stress can be analyzed.

5.2.3 Journal Bearing Performance with Applied Magnetic Field

The application of a magnetic field to the magnetorheological fluid causes the fluid to behave as a Bingham plastic with a yield strength dependent on the magnitude of the magnetic field strength. The viscoelastic behavior of the fluid results in a core

formation where the shear forces are below the yield strength of the fluid. This core formation is highlighted in red in Figure 5-10, where the velocity gradient in the z-direction is zero. The velocity profile on the left hand side of Figure 5-10 represents a velocity profile that would be found near the minimum bearing clearance. The shear force is broken into two components, shear due to the moving boundary and shear due to the pressure gradient. These two shear components combine into the total shear profile shown in the right hand side of Figure 5-10. As can be seen, there is a section of the fluid where the shear forces are below the yield strength of the fluid resulting in the formation of a viscoelastic core.

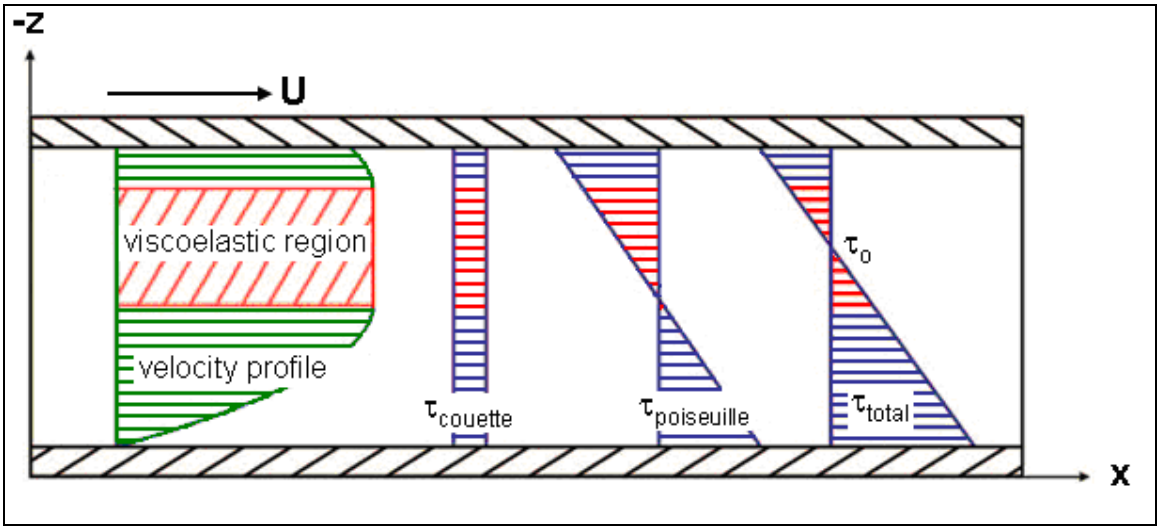

Figure 5-10 Velocity Profile Showing Viscoelastic Region

The result of this core formation within the fluid film is a change in the bearing performance, which includes an increase in the load capacity and damping characteristics of the bearing. The bearing performance was numerically analyzed for the same range of speeds and eccentricity ratios as before, while the magnetic field was varied from 0 to 60,000 A/m. With all different speeds, eccentricities and magnetic field combinations; a

total of 290 unique steady state conditions were studied. A representative profile of the pressure distribution and velocity profiles are shown in Figure 5-11 to Figure 5-13 below.

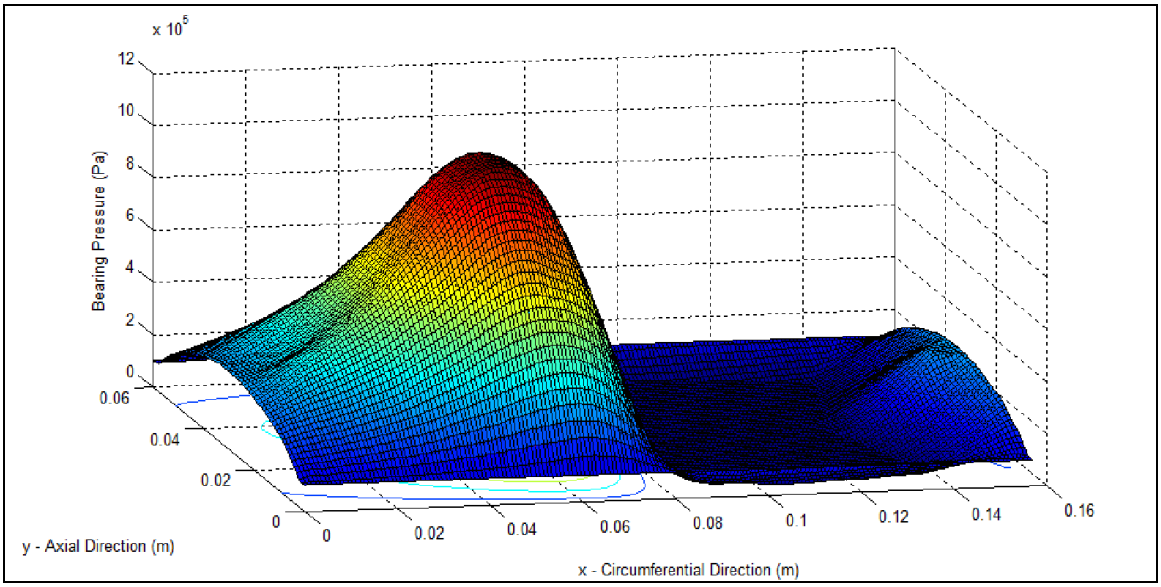

Figure 5-11 Numerical Pressure Distribution for Steady State Solution (500rpm, 0.5 Eccentricity Ratio, 4800 A/m Magnetic Field)

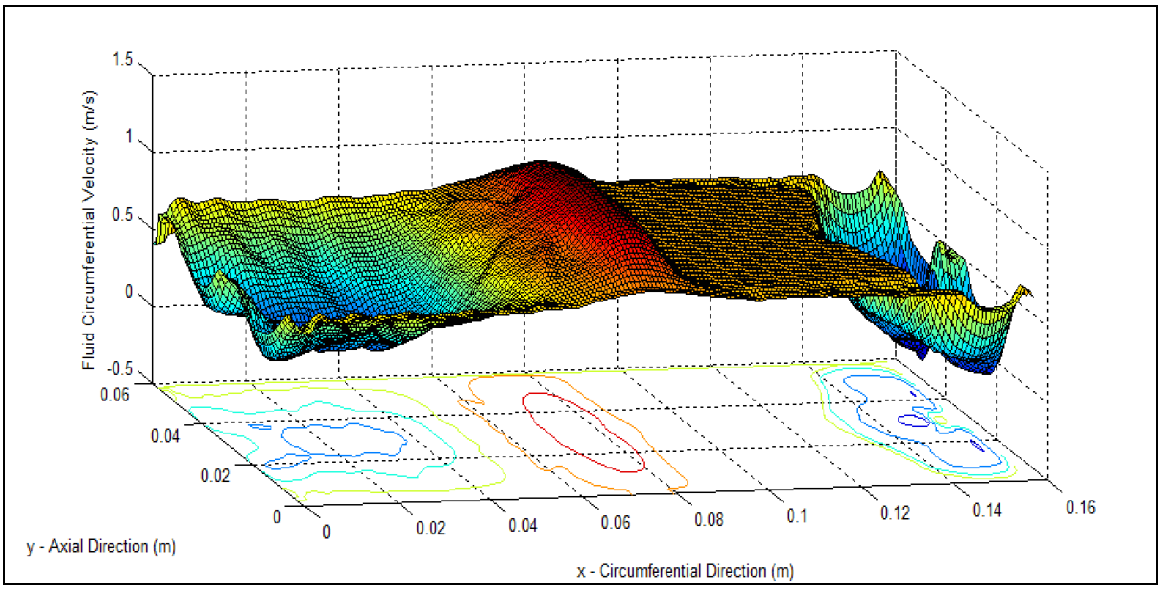

Figure 5-12 Numerical Circumferential Velocity Profile for Steady State Solution (500rpm, 0.5 Eccentricity Ratio, 4800 A/m Magnetic Field)

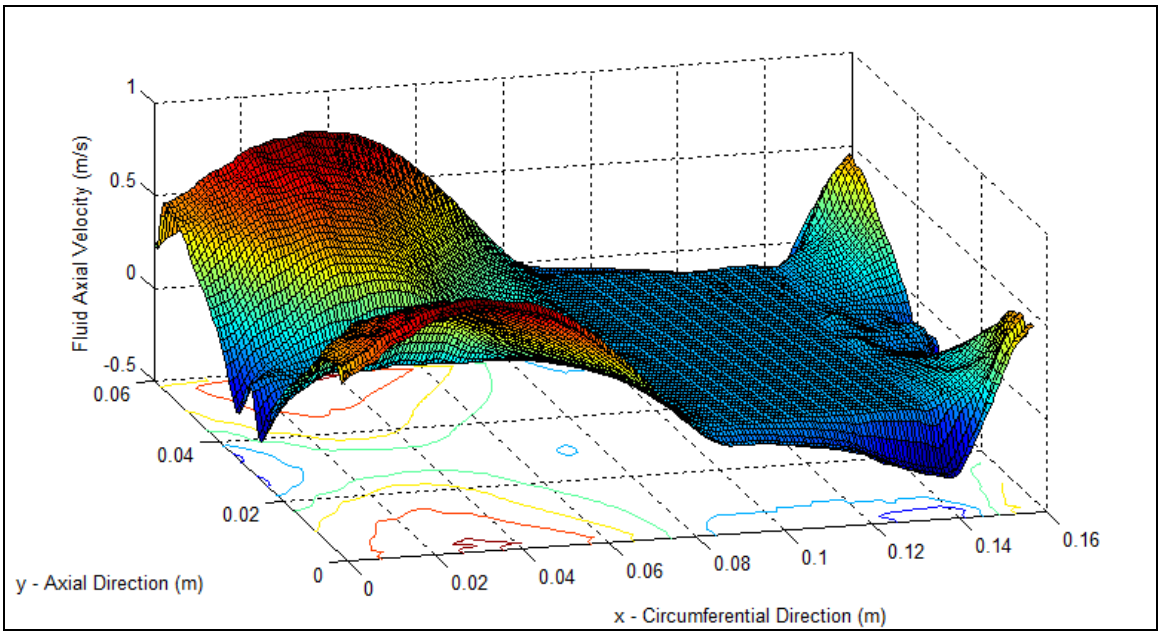

Figure 5-13 Numerical Axial Velocity Profile for Steady State Solution (500rpm, 0.5 Eccentricity Ratio, 4800 A/m Magnetic Field)

The pressure distribution in Figure 5-11 largely shows the same characteristics of a typical hydrodynamic journal bearing, as was seen in Figure 5-1; starting with a high pressure build up in the converging section of the bearing, followed by a sharp drop in pressure moving in to the diverging section. Figure 5-11 also shows the flat profile of the cavitated region located in the low pressure region of diverging section of the bearing and a small pressure spike correlating to the inlet feed. Two key differences are visible in comparing Figure 5-1, where no magnetic field is applied, and Figure 5-11, where a magnetic field is applied, are the increase in the magnitude of the pressure profile and change in the gradient of the pressure profile in the axial direction at the centerline where there is a break in the applied magnetic field.

The overall increase in the magnitude of the pressure profile and change in the gradient of the pressure profile near the centerline highlights the resulting impact on the

operating conditions when the magnetic field is properly applied. The application of the magnetic field increases the yield strength of the fluid, which effectively increases the fluid viscosity resulting in an increase in the magnitude of the pressure profile, provided the rotational speed and eccentricity ratio are kept constant. This effect is also highlighted at the axial centerline where, due to the configuration of the electromagnets, almost no magnetic field is applied normal to the direction of the shearing forces. This is observed in Figure 5-11 as the pressure profile gradient leveling off at the axial centerline as the fluid yield strength goes to zero.

Figure 5-12 and Figure 5-13 show the fluid velocities at the mid-point of the clearance for the circumferential and axial directions respectively. The direction of rotation defines the positive direction for the circumferential velocity, while the positive direction for the axial velocity begins in the center of the bearing and extends outward towards both axial ends. For the circumferential velocity, the cavitation region is a constant value due to the fluid being pulled though the cavitation region by the journal rotation. The axial velocity in the cavitated region is zero since there is no shearing force in the axial direction.

The velocity profiles with the magnetic field applied, shown in Figure 5-12 and Figure 5-13, have relatively higher magnitudes when compared to the velocity profiles without the magnetic field applied shown in Figure 5-2 and Figure 5-3. The increase in the magnitude of the velocity is the result of the proper application of the magnetic field, which increases the yield strength of the fluid. The increase in the yield strength effectively increases the fluid viscosity and also, as previously discussed, increases the magnitude of the pressure profile of the bearing. This results in an increase in the

contributions of both the Couette and Poiseuille flow components to the local velocity provided the rotational speed and eccentricity ratio are kept constant.

The pressure distribution was solved for 250, 500, 1000, 2000 and 5000 rpm, with eccentricities ranging from 0.1 to 0.7, while the magnetic field was varied from 0 up to 60,000 A/m during steady state operation. By integrating the pressure distribution, the load capacity of the bearing for each operating condition was solved. Using the load components normal and tangent to the line of centers, the attitude angle was also determined for each operating condition. The calculated load capacity of the bearing for a range of steady state operating conditions is shown in Figure 5-14 through Figure 5-18 below.

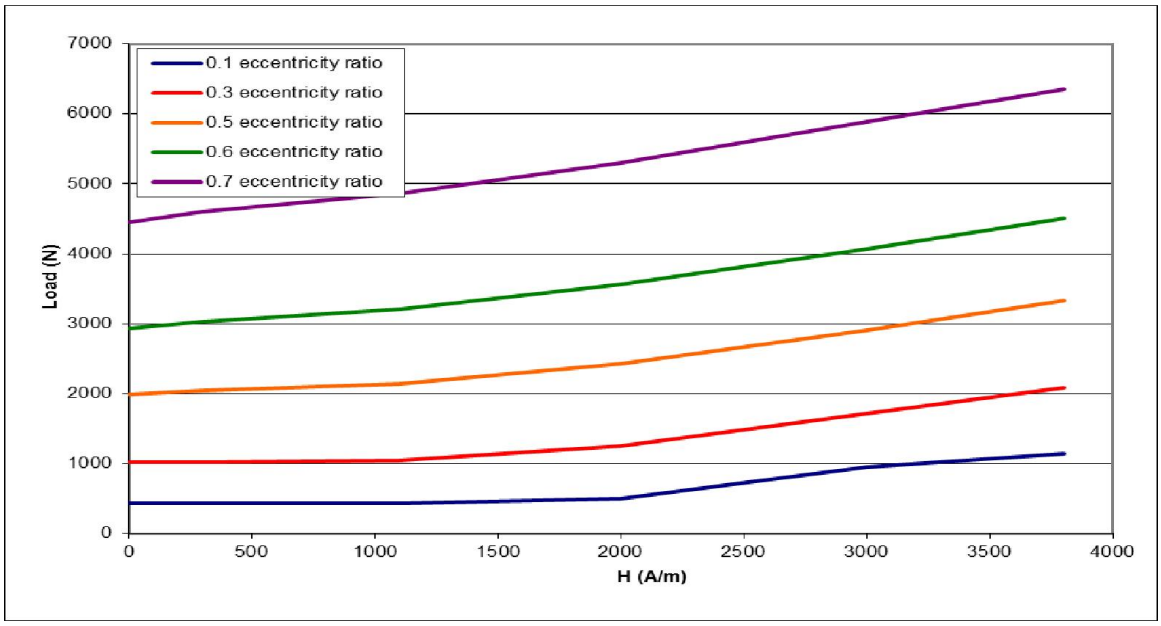

Figure 5-14 Numerical Bearing Load Capacity Relative to the Eccentricity Ratio for a Range of Applied Magnetic Fields at 250rpm

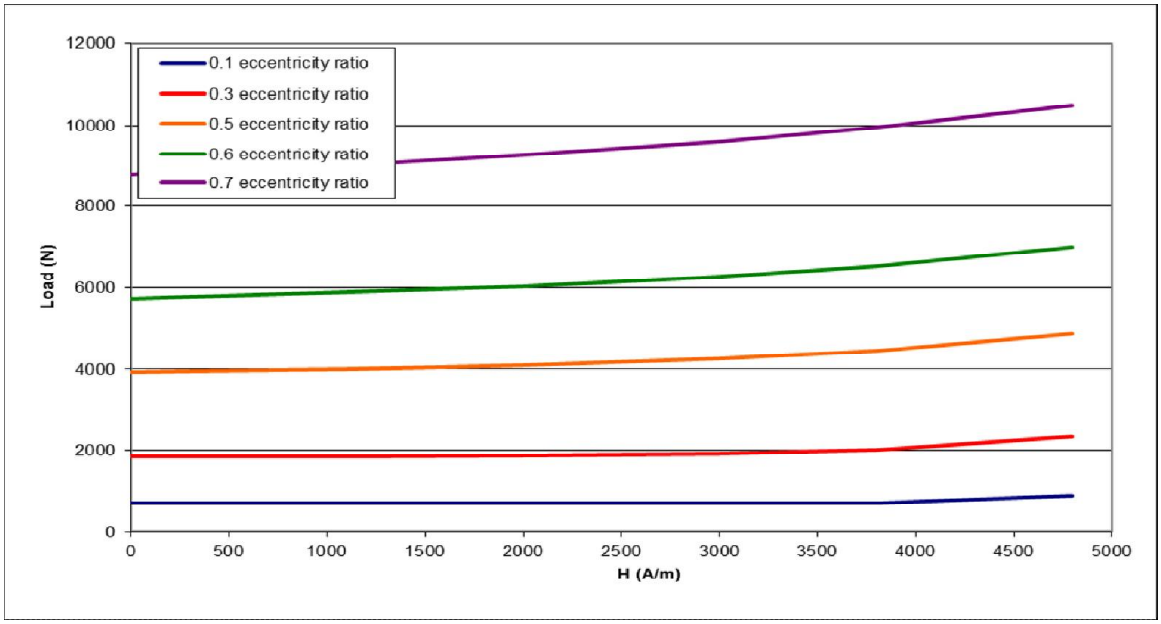

Figure 5-15 Numerical Bearing Load Capacity Relative to the Eccentricity Ratio for a Range of Applied Magnetic Fields at 500rpm

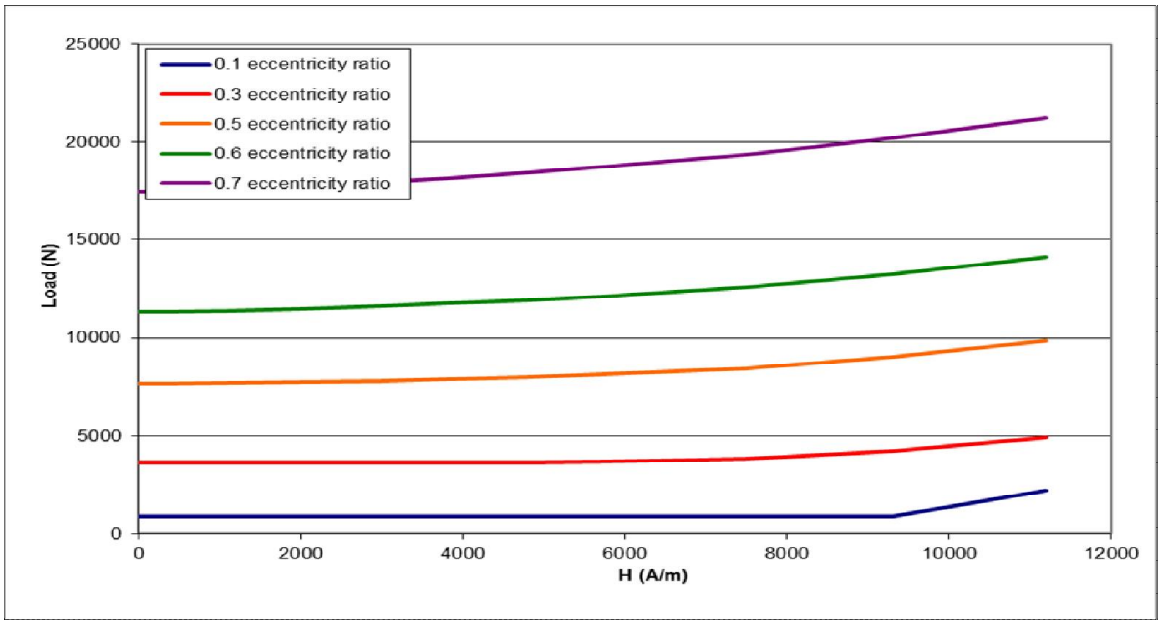

Figure 5-16 Numerical Bearing Load Capacity Relative to the Eccentricity Ratio for a Range of Applied Magnetic Fields at 1000rpm

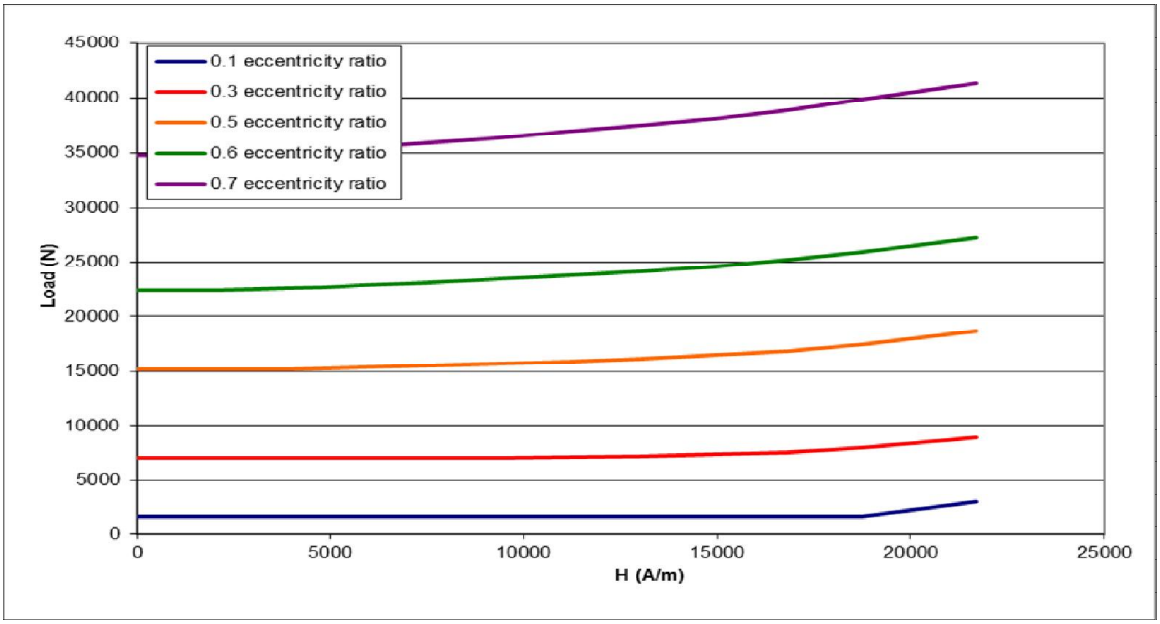

Figure 5-17 Numerical Bearing Load Capacity Relative to the Eccentricity Ratio for a Range of Applied Magnetic Fields at 2000rpm

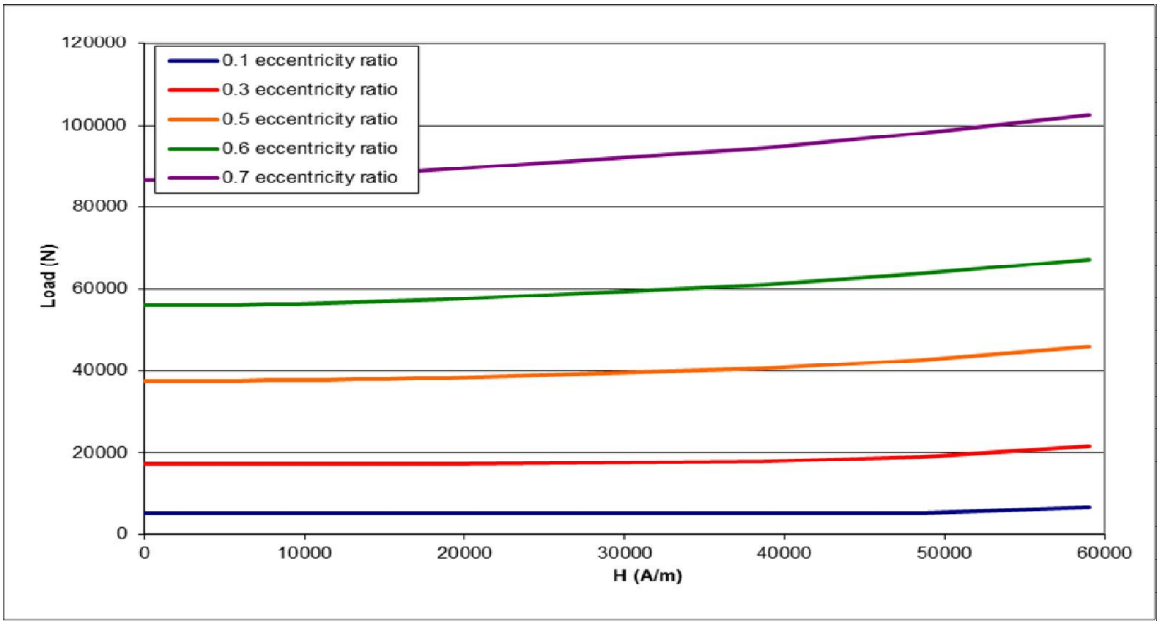

Figure 5-18 Numerical Bearing Load Capacity Relative to the Eccentricity Ratio for a Range of Applied Magnetic Fields at 5000rpm

The bearing load capacities in the figures above show that the application of the magnetic field resulted in an increase in the load capacity. However, the relationship in the load capacity relative to the applied magnetic field strength was not straight forward. As the rotational speed and eccentricity ratio was increased, a greater magnetic field was required to achieve the same relative increase in load capacity. For some of the highest speed and eccentricity ratio combinations, only a nominal increase in the load capacity was achieved. Though, for most speed and eccentricity ratio combinations, an increase of 20% in the load capacity was achieved relative to the baseline load capacity. The percent increase in the load capacity for the maximum applied magnetic field strength over the baseline load capacity, is shown in Table 5-1 below, for the range of speed and eccentricity ratios analyzed.

Table 5-1 Relative Increase in Bearing Load Capacity Due to Applied Magnetic Field

Speed	Magnetic Field Strength	Applied Current	Eccentricity Ratio	Percent Increase in Load Capacity	Increase in Load Capacity (N)
250rpm	3800 A/m	1.00 Amp	0.1	62.44%	712
			0.3	50.94%	1066
			0.5	40.10%	1337
			0.6	34.84%	1570
			0.7	29.90%	1901
500rpm	4800 A/m	1.26 A	0.1	22.67%	204
			0.3	20.41%	477
			0.5	18.99%	922
			0.6	17.97%	1254
			0.7	16.19%	1698
1000rpm	11200 A/m	2.94 A	0.1	60.97%	1349
			0.3	26.05%	1279
			0.5	21.97%	2163
			0.6	20.09%	2838
			0.7	17.93%	3811
2000rpm	21700 A/m	5.7 A	0.1	46.34%	1388
			0.3	20.98%	1871
			0.5	18.63%	3473
			0.6	17.65%	4801
			0.7	15.91%	6575
5000rpm	59000 A/m	15.5 A	0.1	21.15%	1407
			0.3	19.72%	4248
			0.5	17.77%	8132
			0.6	17.08%	11482
			0.7	15.44%	15821

The calculated attitude angle of the bearing for the 290 steady state operating conditions are shown in Figure 5-19 through Figure 5-23 below. By studying the attitude angle, the impact of the magnetic field on the steady state position can be observed. As can be seen in the figures below, the result of an increase in the magnetic field strength is generally an increase in the attitude angle. Although this effect is small, the application of

the magnetic field does alter the steady state position of the journal, particularly at higher eccentricity ratios.

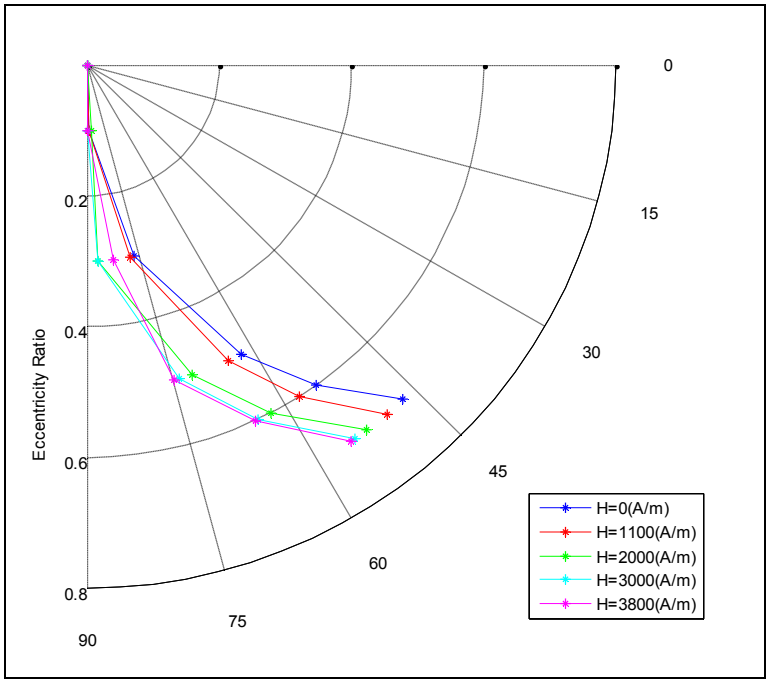

Figure 5-19 Numerical Bearing Attitude Angle Relative to the Eccentricity Ratio for a Range of Applied Magnetic Fields at 250rpm

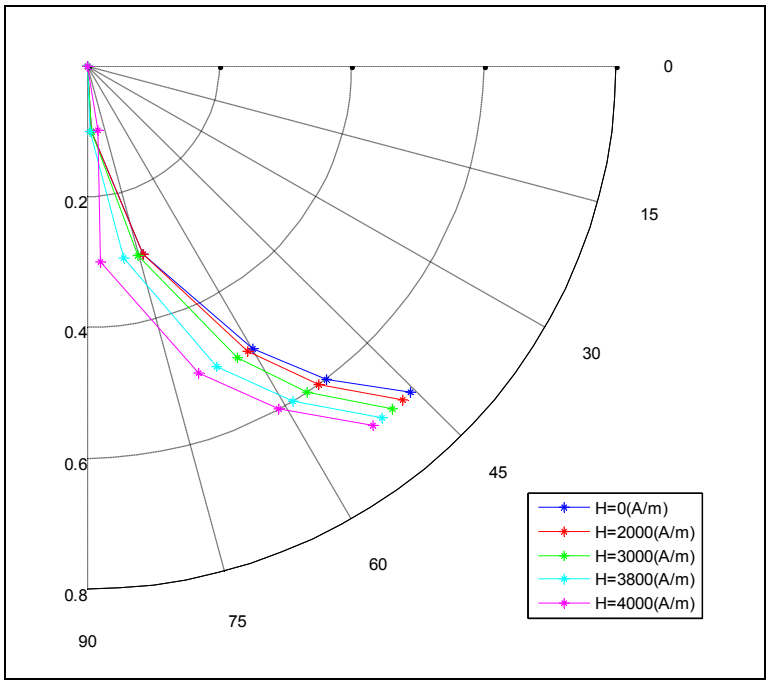

Figure 5-20 Numerical Bearing Attitude Angle Relative to the Eccentricity Ratio for a Range of Applied Magnetic Fields at 500rpm

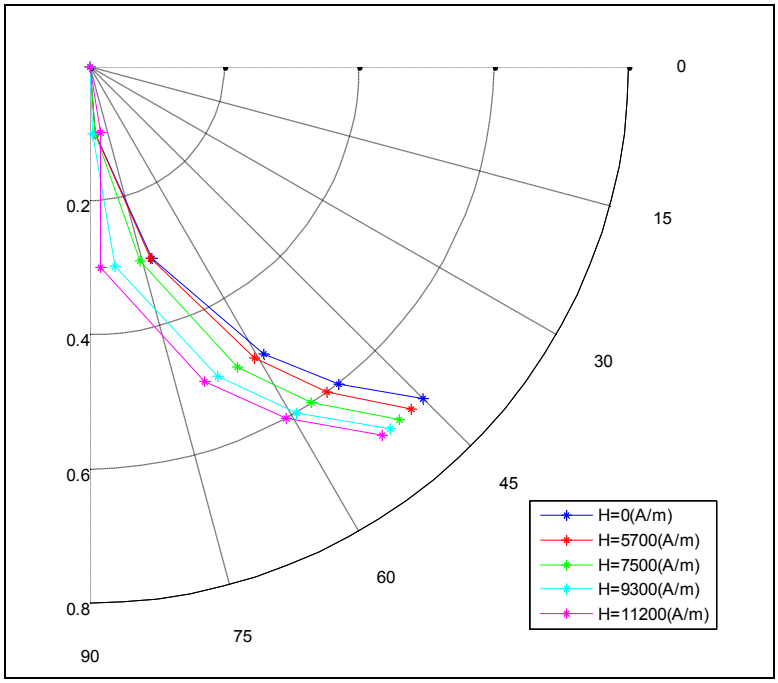

Figure 5-21 Numerical Bearing Attitude Angle Relative to the Eccentricity Ratio for a Range of Applied Magnetic Fields at 1000rpm

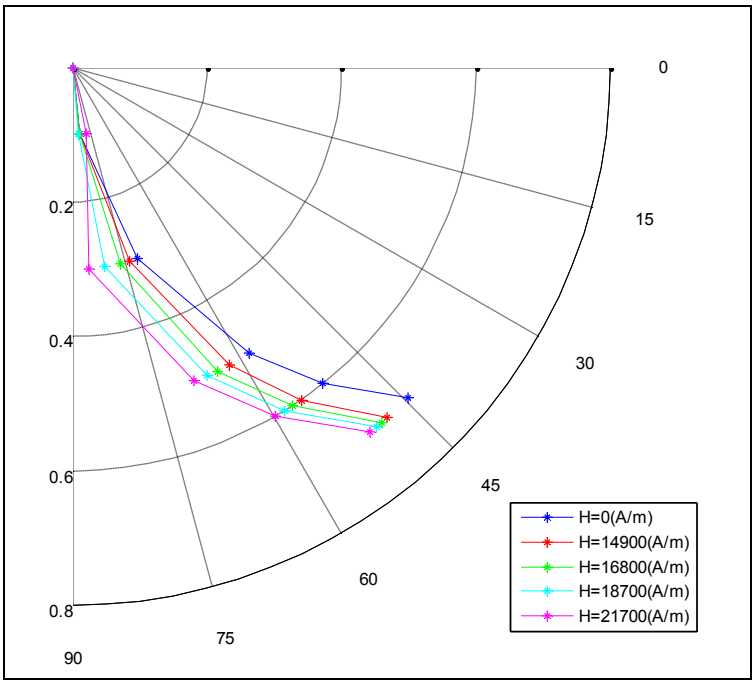

Figure 5-22 Numerical Bearing Attitude Angle Relative to the Eccentricity Ratio for a Range of Applied Magnetic Fields at 2000rpm

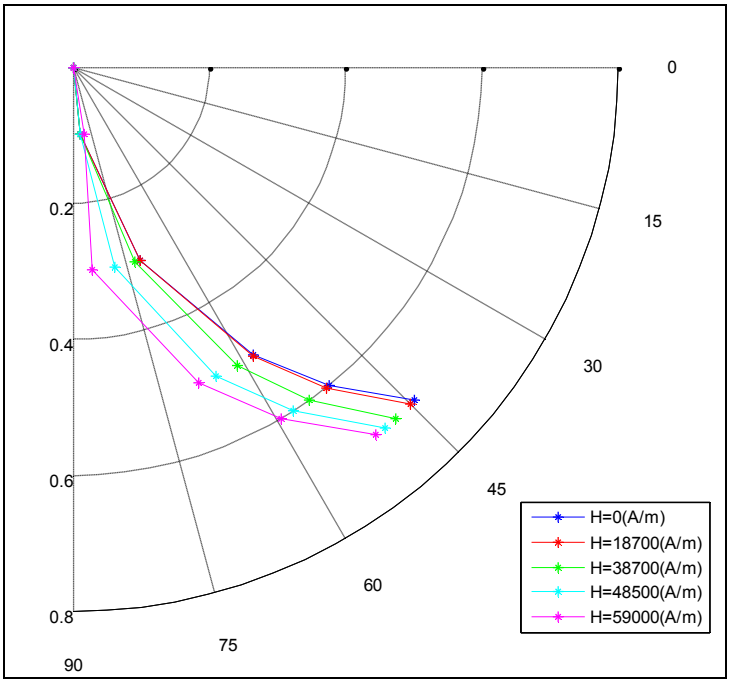

Figure 5-23 Numerical Bearing Attitude Angle Relative to the Eccentricity Ratio for a Range of Applied Magnetic Fields at 5000rpm

The results presented in this section showed the effects that increasing the yield strength of the magnetorheological fluid, due to an applied magnetic field, has on the journal bearing performance. Two key characteristics of the bearing, load capacity and attitude angle, were used to highlight the changes observed when a variable magnetic field was applied. Obviously, many other parameters were also affected by the application of the magnetic field, such as the pressure distribution and the fluid flow. While these other parameters can help provide insight to the changes occurring when the magnetic field is introduced, only a single detailed case, with and without a magnetic field applied, was presented for brevity.

5.2.4 Journal Bearing Dynamics Results

The previous subsections were focused on numerical results during steady state operation, where the loads and speeds of the self-acting journal bearing were constant. However, many bearing applications are dynamically loaded and are not inherently stable; under certain operating conditions, a self-exciting whirl orbit can increase until the journal comes into contact with the bearing. The following subsection covers the numerical results for dynamic response of the bearing due to a small perturbation.

The bearing performance was analyzed for speeds of 250, 500, 1000, 2000 and 5000 rpm, with eccentricities ranging from 0.1 to 0.7, with and without a magnetic field applied. Unlike the steady state analyses, where a range of magnetic field strengths were applied, only the maximum applied magnetic field was analyzed due to the time intensive nature of the dynamic analysis. With all combinations of speeds, eccentricities and magnetic field applications, a total of 50 unique dynamic conditions were studied.

The results of the numerical analysis of dynamic response are stiffness and damping coefficients that represent the load dependent response of the bearing to a small perturbation. These coefficients can then be used to calculate the dynamic response of the bearing for a specific set of conditions. The calculated stiffness and damping coefficients for all operating conditions with and without the magnetic field applied are given in Appendix G. An example of the dynamic response with and without a magnetic field applied is shown Figure 5-24 below for a speed of 500 rpm with an eccentricity ratio of 0.5 and a perturbation provided by the application of 2% load increase.

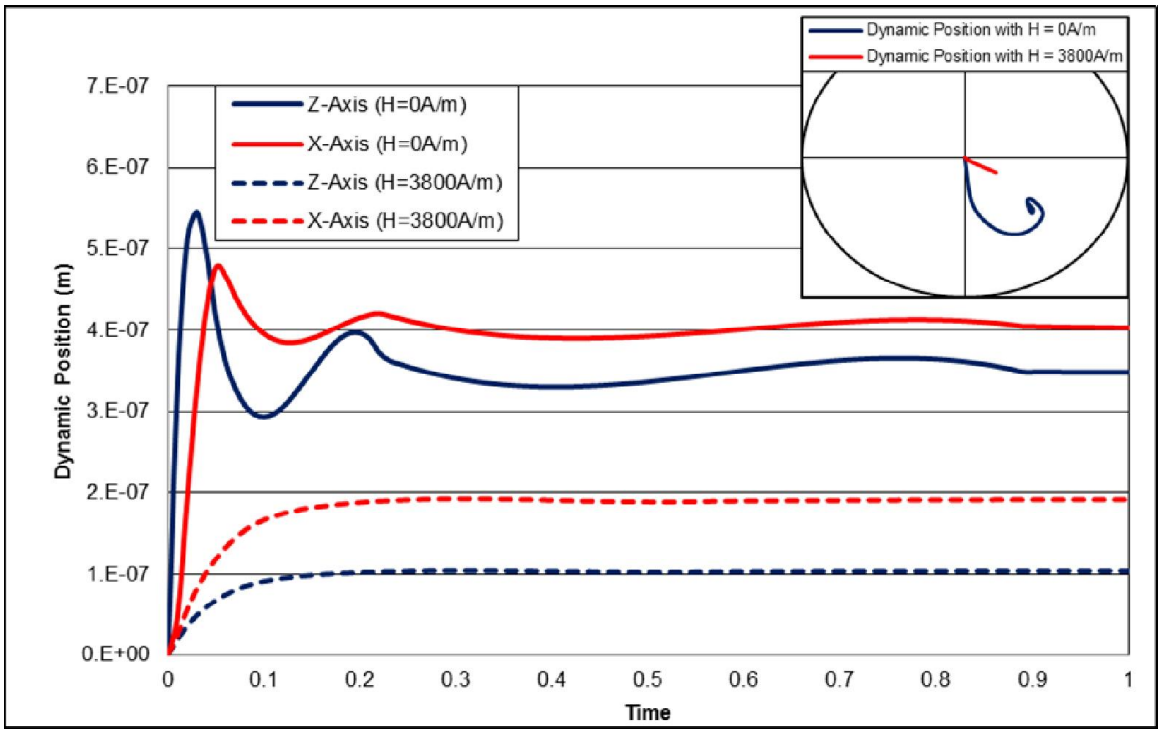

Figure 5-24 Numerical Comparison of Dynamic Response to Small Perturbation With and Without Applied Magnetic Field (500rpm, 0.5 Eccentricity Ratio)

Figure 5-24 provides a visual representation of the impact that the application of a magnetic field has on the damping and spring rate properties of the bearing. As can be seen in Figure 5-24, a perturbation of the bearing without an applied magnetic field, due

to the sudden application of an increase in load; results in a slight overshoot, followed by an oscillation, before settling into a new steady state position. The same perturbation load applied to the bearing while a magnetic field is applied, virtually eliminates any overshoot or oscillation in the position and also significantly reduces the total deflection of the new steady state position.

The data presented in Figure 5-24 is a good representation of the effects of the magnetic field; however, it is a time intensive process to produce the data and only represents a specific set of operating conditions and perturbation. Another way to demonstrate the effects of the magnetic field is the critical mass which represents the mass the bearing can support and maintain stable operation. Since the critical mass is constant for a given set of steady state operating conditions, this dimensionless critical mass can be used to create a stability map for a range of rotational speeds and bearing loads as shown in Figure 5-25 and Figure 5-26 respectively.

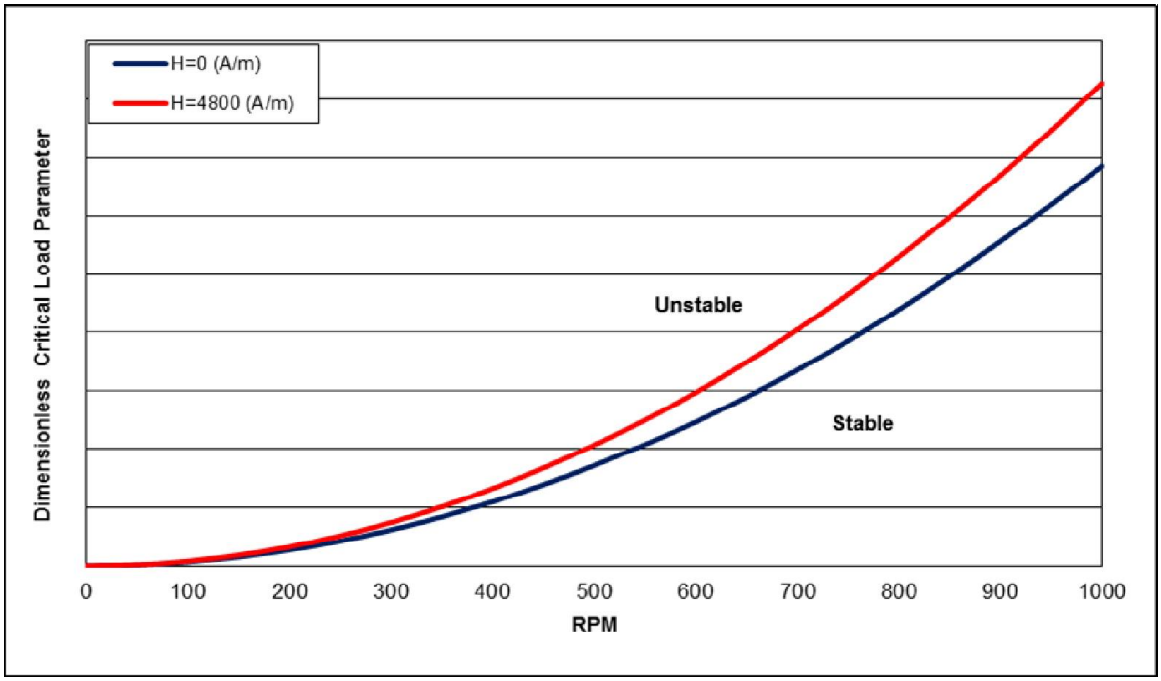

Figure 5-25 Numerical Speed Stability Map for Dynamic Response to Small Perturbation With and Without Applied Magnetic Field (500rpm, 0.5 Eccentricity Ratio)

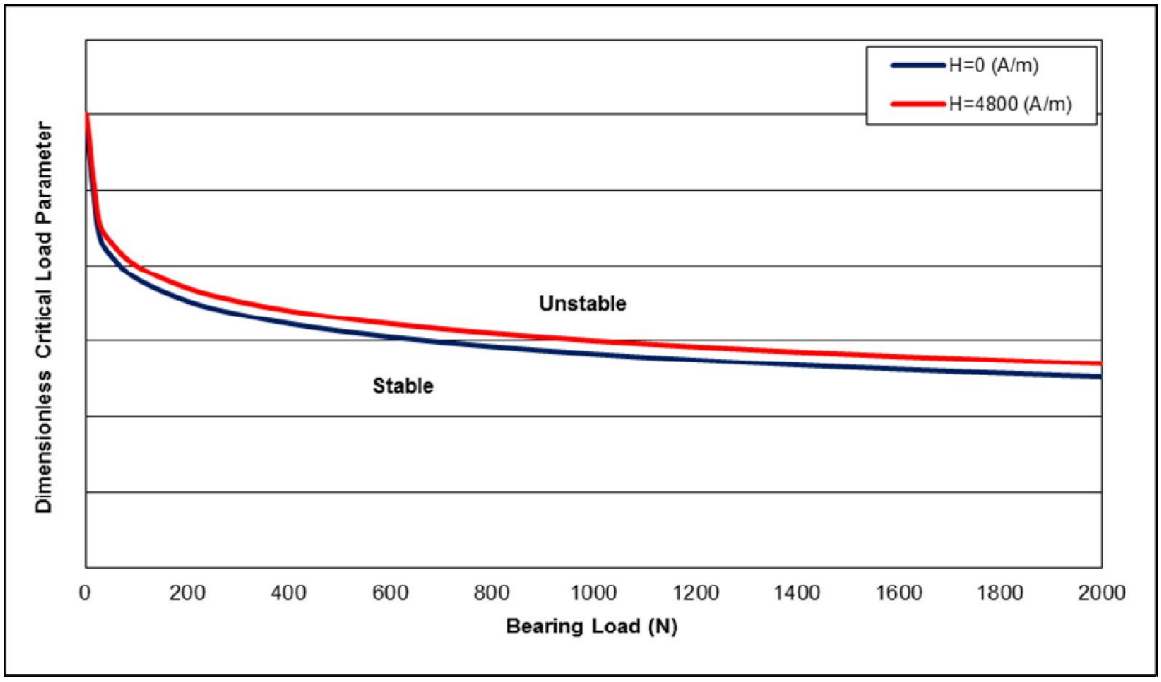

Figure 5-26 Load Stability Map for Dynamic Response to Small Perturbation With and Without Applied Magnetic Field (500rpm, 0.5 Eccentricity Ratio)

Figure 5-25 and Figure 5-26 show that a substantial increase in the stable operating range of the bearing with the application of the magnetic field. Like the dynamic position in Figure 5-24, the dimensionless critical mass provides a good representation of the effects of the magnetic field application on bearing stability; however, one hundred figures, like Figure 5-25 and Figure 5-26, would be necessary to present results for all the conditions that were analyzed. A more concise way to present the data was needed; thus, the percent increase in the critical mass, for the maximum applied magnetic field strength, relative to the baseline without an applied field, is given in Table 5-2 below, for the range of speed and eccentricity ratios analyzed.

Table 5-2 Increase in Dimensionless Critical Mass Due to Applied Magnetic Field

Speed	Magnetic Field Strength	Applied Current	Eccentricity Ratio	Percent Increase in Critical Load
250rpm	3,800 A/m	1.00 Amp	0.1	80.45%
			0.3	63.05%
			0.5	64.39%
			0.6	64.69%
			0.7	65.04%
500rpm	4,800 A/m	1.26 Amp	0.1	36.07%
			0.3	38.95%
			0.5	32.80%
			0.6	39.32%
			0.7	43.84%
1000rpm	11,200 A/m	2.94 Amp	0.1	74.51%
			0.3	39.86%
			0.5	41.21%
			0.6	45.82%
			0.7	49.92%
2000rpm	21,700 A/m	5.70 Amp	0.1	32.04%
			0.3	30.10%
			0.5	35.15%
			0.6	41.19%
			0.7	45.36%
5000rpm	59,000 A/m	15.50 Amp	0.1	38.94%
			0.3	31.96%
			0.5	32.43%
			0.6	39.78%
			0.7	43.89%

5.2.5 Journal Bearing Performance Using Half the Electromagnets

The previous range of operating conditions that were numerically analyzed produced a large cavitation region through most of the diverging section of the bearing. Due to the minimal amount of fluid contained within the cavitated region, the effects of applying the magnetic field are minimal. Thus, the electromagnets could be removed from the diverging section of the bearing design with minimal impact on performance,

and reduce the electrical energy requirements. Figure 5-27, shows the bearing design with the electromagnets covering half of the circumference of the bearing.

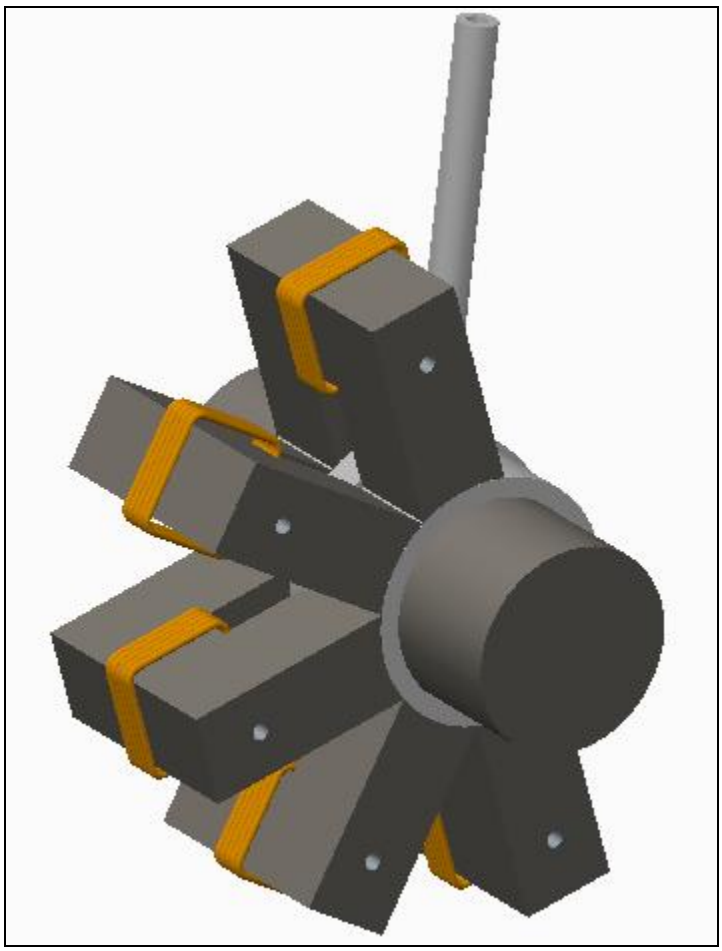

Figure 5-27 Removal of Electromagnets in Diverging Section of the Bearing

The bearing performance was numerically analyzed for the new arrangement of the electromagnets, by aligning the electromagnets with the attitude angle of the bearing such that the magnetic field was applied only in converging section of the bearing. The pressure distribution was again solved for 250, 500, 1000, 2000 and 5000 rpm, with eccentricities ranging from 0.1 to 0.7, while the magnetic field was varied from 0 up to 60,000 A/m during steady state operation. By integrating the pressure distribution, the

load capacity of the bearing for each operating condition was solved. The calculated load capacity of the bearing was compared to the original design, having the full complement of electromagnets, for a range of steady state operating conditions which is shown in Figure 5-28 through Figure 5-32.

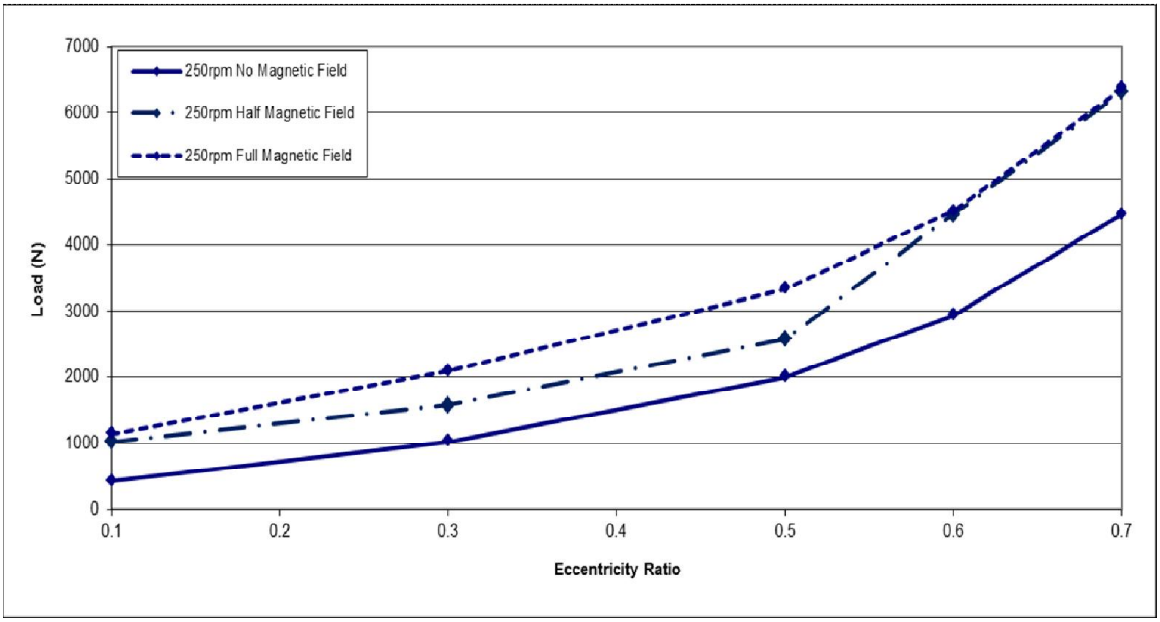

Figure 5-28 Comparison of Numerical Bearing Load Capacity for Zero, Half and Full Magnetic Field Application at 250rpm

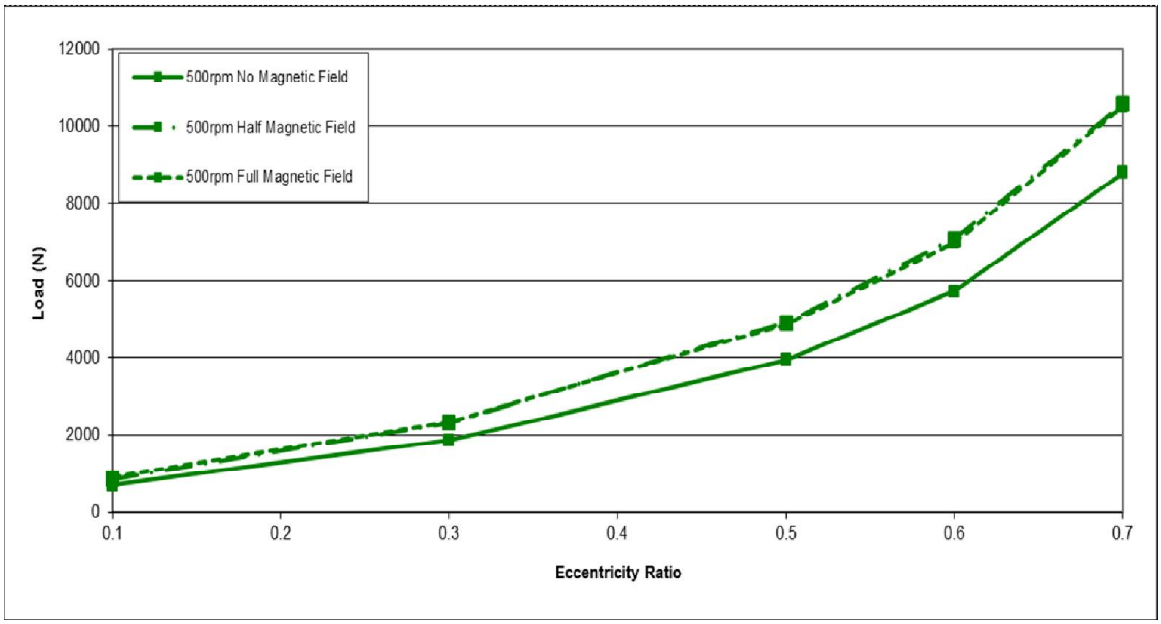

Figure 5-29 Comparison of Numerical Bearing Load Capacity for Zero, Half and Full Magnetic Field Application at 500rpm

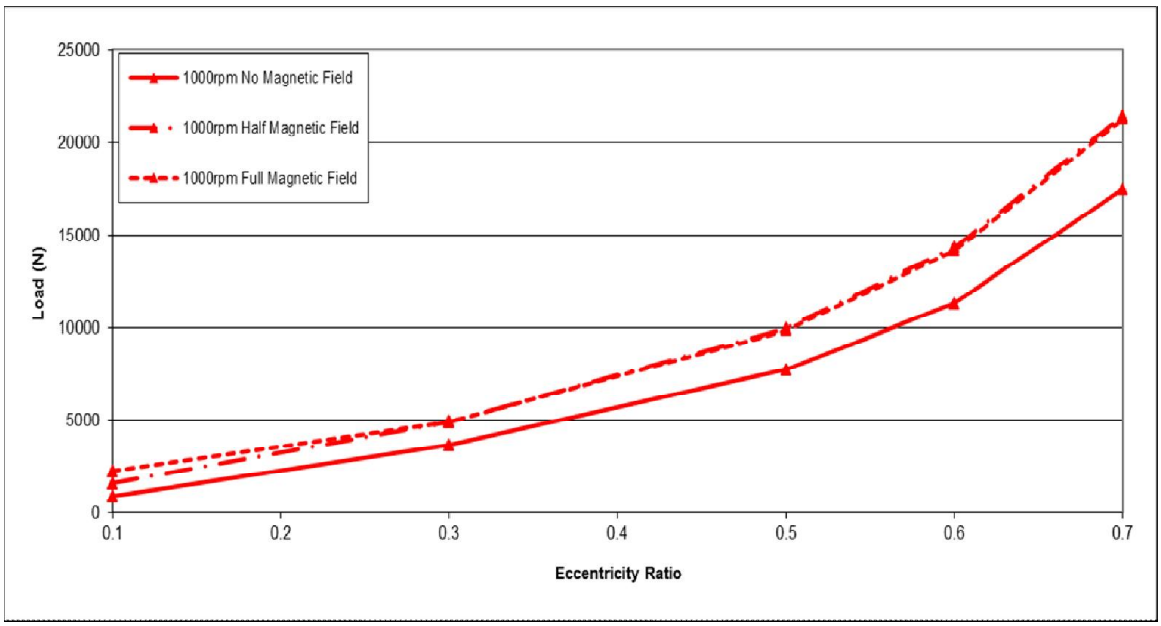

Figure 5-30 Comparison of Numerical Bearing Load Capacity for Zero, Half and Full Magnetic Field Application at 1000rpm

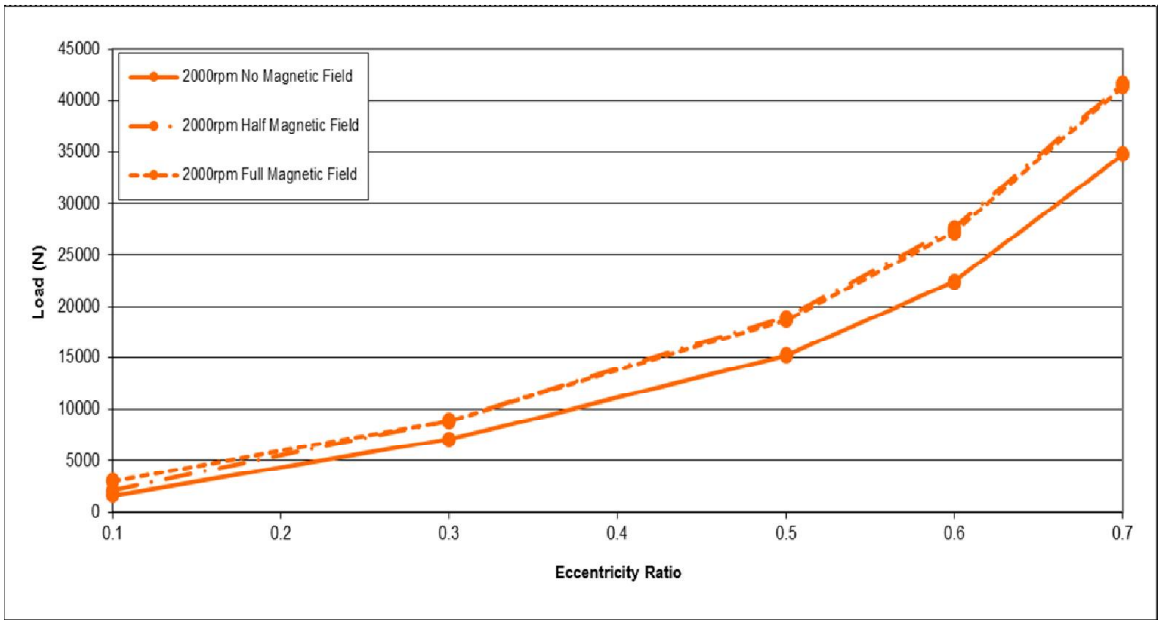

Figure 5-31 Comparison of Numerical Bearing Load Capacity for Zero, Half and Full Magnetic Field Application at 2000rpm

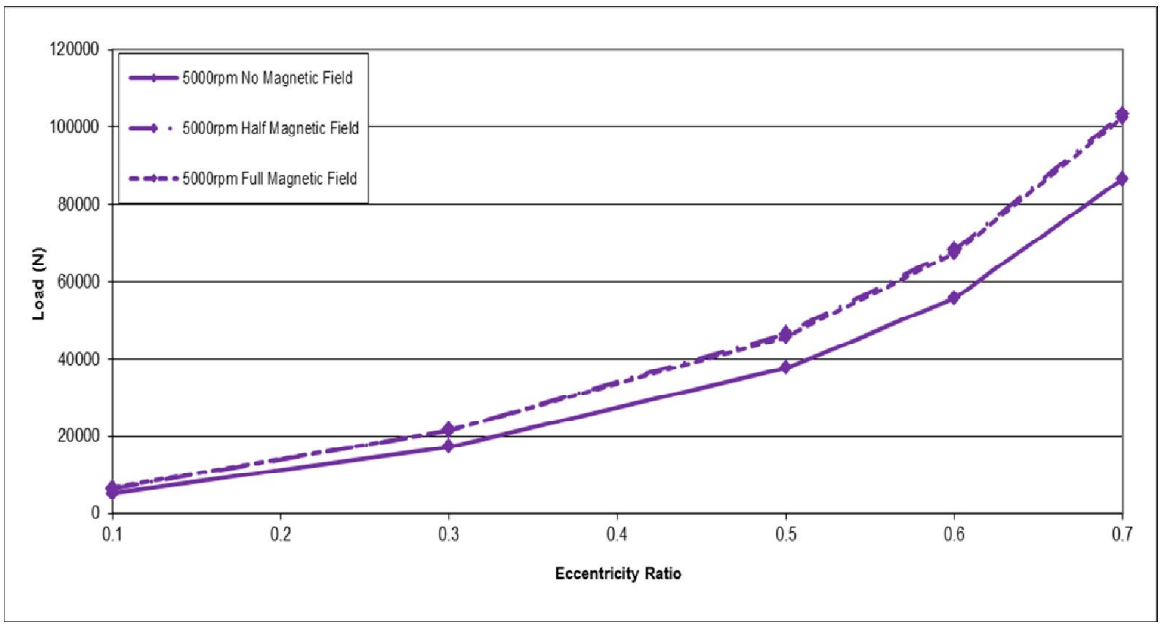

Figure 5-32 Comparison of Numerical Bearing Load Capacity for Zero, Half and Full Magnetic Field Application at 5000rpm

Figure 5-28 through Figure 5-32 show that removing the magnetic field on the diverging section of the bearing has minimal impact on the improved load capacity of the bearing for most of the operating conditions; the exceptions being the 250rpm operating speed and the lowest eccentricity ratio of 0.1, where the cavitated region is significantly smaller. Removing the electromagnets from the diverging section of the bearing had minimal impact on other parameters, such as attitude angle, pressure distribution and fluid flow rate, relative to the full complement of electromagnets.

The removal of half the electromagnets has the benefit of reducing the electrical energy demands in half. However, physically removing the electromagnets would be impractical; because in order to retain the equivalent performance, limits to how the altered design could be applied would be necessary. Since the attitude angle and eccentricity ratio depend on the operating conditions, the more practical way to reduce electrical energy demands would be to remove the electrical current supplied to the electromagnets covering the diverging section of the bearing. This would allow cutting the electrical energy demands by half, while still retaining the equivalent performance as the full complement of electromagnets, for any set of operating conditions including bi-directional rotation.

5.3 Experimental Results

The previous subsections discussed the numerical results of bearing design utilizing published data on a commercially available magnetorheological fluid MRF-140CG, which was the highest yield strength and solid particle content fluid offered by the Lord Corporation. The following subsections review the experimental results for the

bearing design using a bulk magnetorheological fluid created and quantified as part of this research.

Seven different magnetorheological fluid samples, consisting of a range solid content of carbonyl iron powder from approximately 2% to 75%., were created and evaluated. The viscosity and specific gravity at 40 ºC and 80 ºC for a range of applied magnetic fields was measured prior to selecting the final bulk fluid composition. The final magnetorheological fluid used for testing consisted of 9.24% by mass of carbonyl iron powder and 8.01% by mass of white lithium grease mixed into to an ISO 32 viscosity grade hydraulic carrier fluid. The measured viscosity and calculated yield stress for the bulk test fluid can be found in Appendix F.

The experimental evaluation of the performance of the bearing assembly design consisted of 15 steady state conditions with operational parameters of speed and applied magnetic field as the key variables. A constant load of 158 N was applied while speed was varied, in 500 rpm increments, ranging from 500 – 2500 rpms. Currents of 10 and 20 Amps were applied at each speed resulting in a measured magnetic field of 290 and 500 Gauss respectively across the fluid film gap.

The bearing assembly consisted of a cast grey iron journal with a 304 stainless steel bearing. Surrounding the bearing, were eight electromagnets comprised of a 40 turn coil using 18AWG copper wire surrounding a cast grey iron core. The main dimensions of the bearing and fluid properties are listed below.

- Journal Diameter: 50 mm
- Bearing Radial Clearance: 0.120 mm
- Bearing Length: 60 mm

- Inlet Feed Line Length: 100 mm
- Fluid Viscosity: 0.17 kg/m-s @ 40ºC
- Fluid Density: 934 kg/m^3
- Solids Content by Weight: 9.24%

For the 15 steady state operation conditions, the bearing performance was analyzed by measuring eccentricity, torque and fluid pressure. The following subsections review the results of these experiments; beginning with the results of the magnetorheological fluid properties, followed by the bearing performance with no magnetic field applied, then the bearing performance with a magnetic field applied and finally the comparison of the experimental results relative to the numerical results are presented.

5.3.1 Magnetorheological Fluid Properties

The magnetorheological fluid was created by adding carbonyl iron powder to an ISO 32 viscosity grade hydraulic carrier fluid with white lithium grease mixed into the fluid to act as a surfactant dispersing agent. Seven different samples of approximately 400ml were evaluated which consisted of a range solid content by mass of carbonyl iron powder from approximately 2% to 75%. The viscosity and specific gravity at 40 ºC and 80 ºC for a range of magnetic fields was measured using the method outlined in Section 4.2.2.

Figure 5-33 and Figure 5-34 below, shows the increase in measured viscosity at 40 ºC and 80 ºC for a range of magnetic fields generated by applying a specified current to the electromagnetic cradle for each fluid sample. As the applied current is increased

from 0 to 20 Amps, the measured viscosity also increases due to the formation of chainlike structures by the suspended CIP particles. For the lowest percent solid content fluid sample of 2%, significant increase in viscosities were achieved only at the highest applied currents. For the higher percent solid content samples, measured viscosities increased more the twice the un-energized fluid viscosity. It can also be seen that the percent increase in viscosity for each fluid sample is greater at the higher temperature. This is due to the decrease in the base fluid viscosity, reducing the hydrodynamic force that resists the particles magnetic moments trying to align and form chainlike structures. The actual values for the measured viscosity are included in Table 5-3 below.

Table 5-3 Measured Viscosity for Various Solid Particle Content Sample MR Fluids

Current (Amps)	Magnetic Field (Gauss) *Error +/-1%*	Viscosity (cP) @ 40°C *Error +/-1cP*						
		2% Solid Content	5% Solid Content	10% Solid Content	15% Solid Content	25% Solid Content	50% Solid Content	75% Solid Content
0	0	125	73	172	185	310	330	740
5	51-76	141	105	229	245	520	510	1040
10	88-126	163	134	319	356	610	800	1560
15	133-189	194	168	408	495	830	1120	2010
20	166-237	225	203	494	611	1000	1250	2790
Current (Amps)	**Magnetic Field (Gauss)** *Error +/-1%*	**Viscosity (cP) @ 80°C** *Error +/-1cP*						
		2% Solid Content	**5% Solid Content**	**10% Solid Content**	**15% Solid Content**	**25% Solid Content**	**50% Solid Content**	**75% Solid Content**
0	0	47	27	78	98	230	200	430
5	51-76	55	43	126	137	270	300	830
10	88-126	73	66	190	213	420	460	1120
15	133-189	101	100	255	276	610	720	1520
20	166-237	136	121	360	359	900	1140	2080

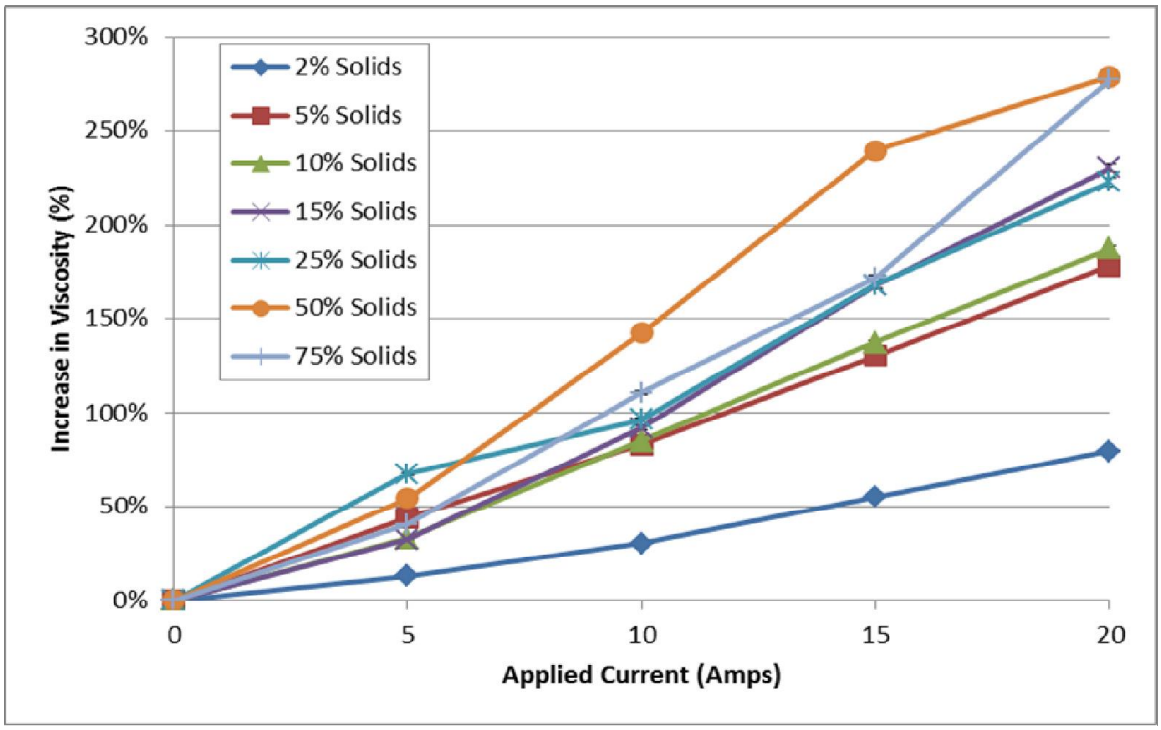

Figure 5-33 Measured Viscosity vs. Applied Current at 40ºC for MR Fluid Samples

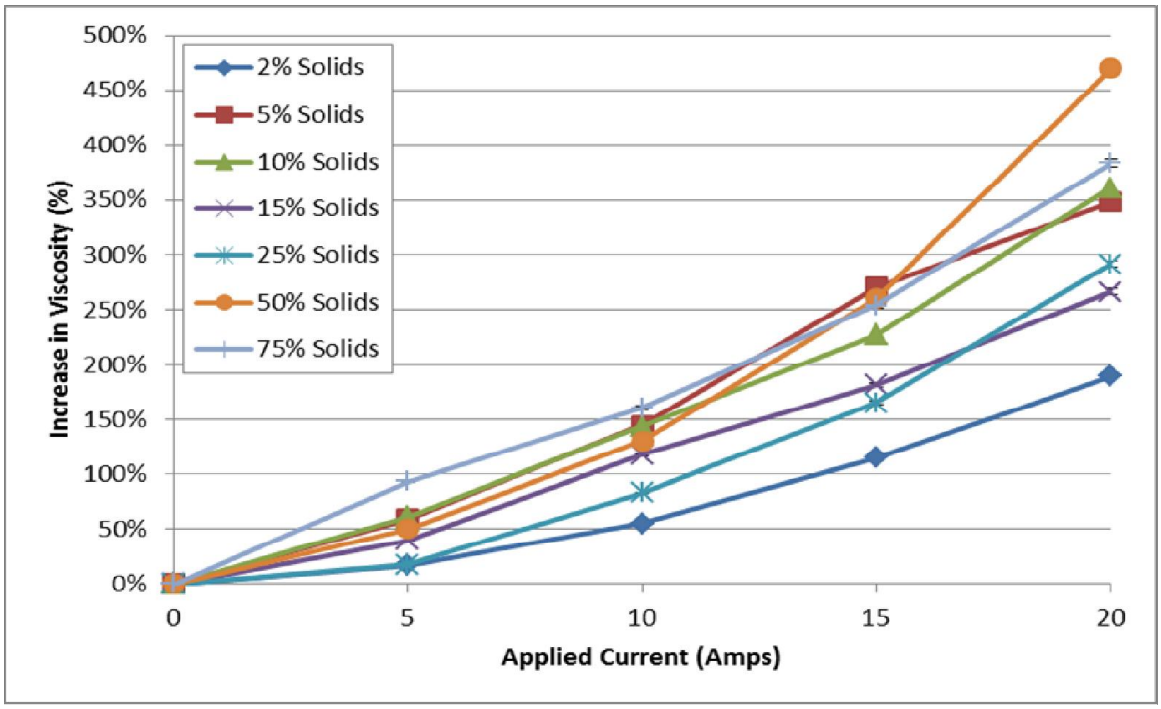

Figure 5-34 Measured Viscosity vs. Applied Current at 80ºC for MR Fluid Samples

Both the dynamic viscosity and yield stress of the energized MR fluid had to be calculated from the viscosity measurements generated by the rotary viscometer. The dynamic viscosity of the MR fluid when the magnetic field was applied was calculated by doubling the increase in viscosity and adding it to the unmagnetized fluid viscosity. The yield stress could then be calculated from the difference between the shear stress of the fluid when the magnetic field was applied and not applied. Figure 5-35 and Figure 5-36 below, show the increase in calculated yield stress at 40 ºC and 80 ºC for a range of magnetic fields generated by applying a specified current to the electromagnetic cradle. As was seen in the viscosity measurements, as the applied current is increased from 0 to 20 Amps, the calculated yield stress also increases due to the formation of chainlike structures by the suspended CIP particles.

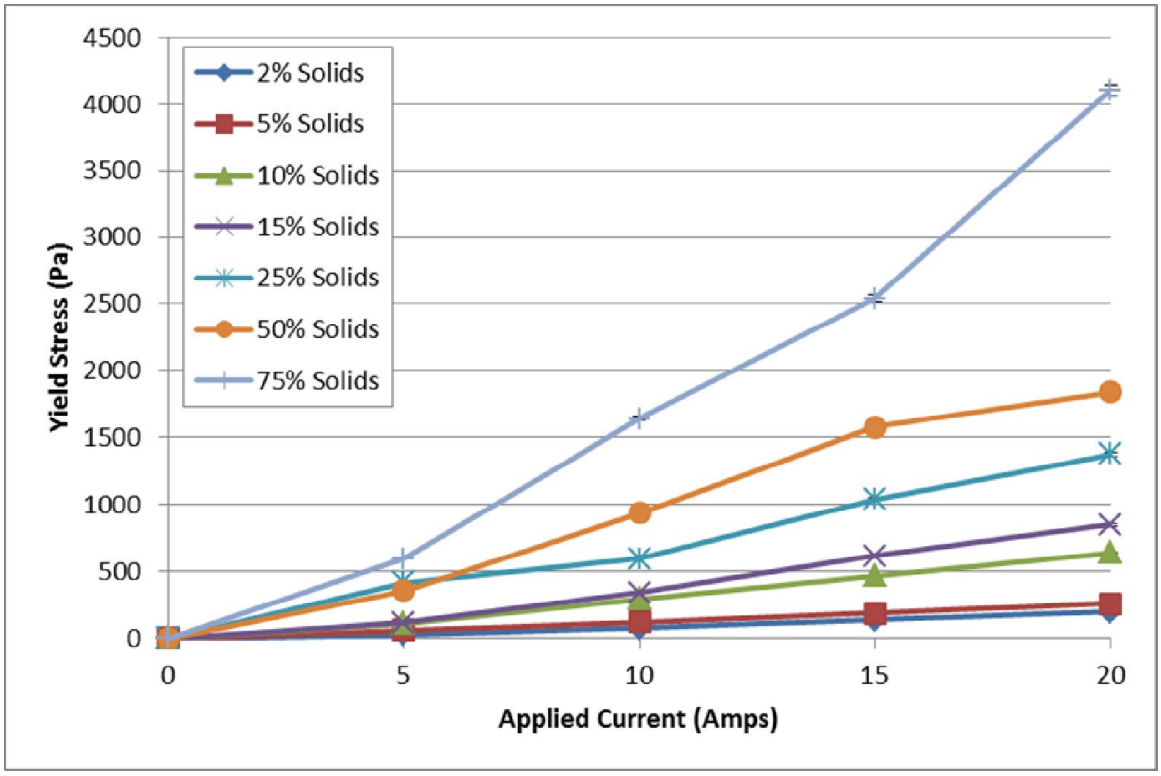

Figure 5-35 Yield Stress vs. Applied Current at 40ºC for MR Fluid Samples

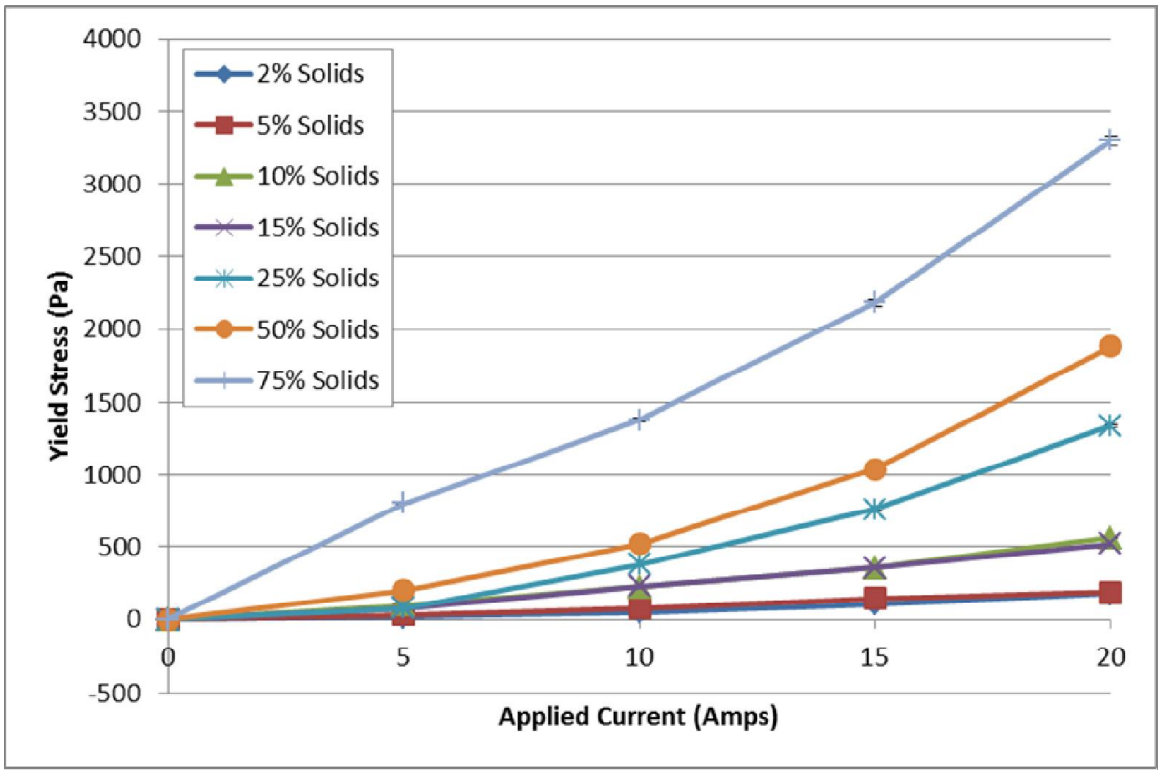

Figure 5-36 Yield Stress vs. Applied Current at 80°C for MR Fluid Samples

The increase in solid particle content of each fluid sample increased the overall magnetic permeability, which creates a higher magnetic field within the fluid sample for a given applied current. Figure 5-37 shows the measured magnetic field within the fluid samples as the applied current is increased from 0 to 20 Amps. It can be seen, as the applied current increases, the magnetic field also increases in a linear fashion. As the solid content of each sample increases the slope of the linear relationship also increases which corresponds to the increase in relative magnetic permeability. Unlike the viscosity measurements, the magnetic field did not vary with temperature and therefore only a single temperature data set is presented.

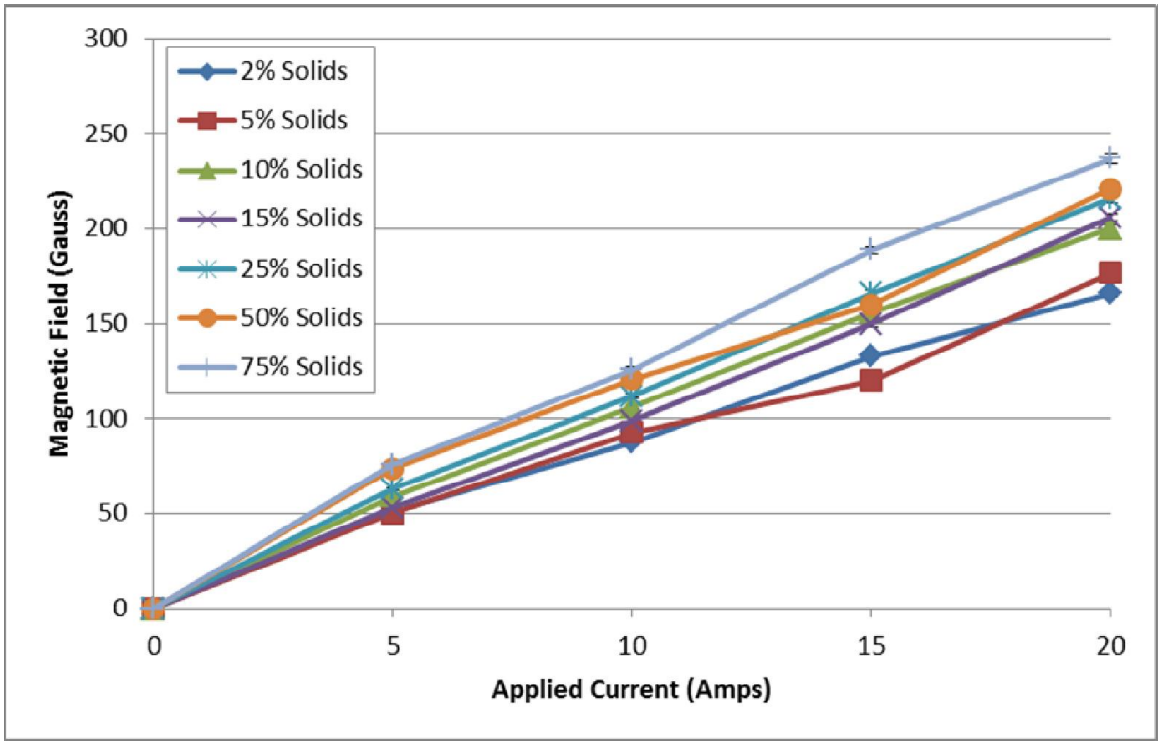

Figure 5-37 Magnetic Field Inside Fluid Samples at Various Applied Currents

Rheological properties of magnetorheological fluids are typically given at a single temperature and to the authors knowledge; this is the first time that these properties at multiple temperatures has been published. The results of the measurements showed that for a given applied magnetic field, the percent increase in viscosity for each fluid sample is greater at the higher temperature; while the measured viscosity and calculated yield strength is lower at higher temperatures for the same applied magnetic field. Thus, the lower base oil viscosity at higher temperatures shows a greater relative increase in measured viscosity; however, the apparent yield strength of the fluid still decreases as temperature increases. The measured viscosity and calculated yield stress for the bulk test fluid can be found in Appendix F.

The fluid used for the numerical analysis was MRF-140CG, which was the highest yield strength and solid particle content fluid offered by the Lord Corporation. This fluid had a solid content by percent mass of 85.44%, whereas the bulk test fluid contains only 9.23% solid content by percent mass. Figure 5-38 shows the numerical load capacity for the bearing design using both the MRF-140CG fluid and the bulk test fluid with and without 10 Amps of applied current. As expected the MRF-140CG has a larger overall load capacity due to the higher base viscosity and also greater increase in load capacity when the magnetic field is applied due to the higher solid particle content.

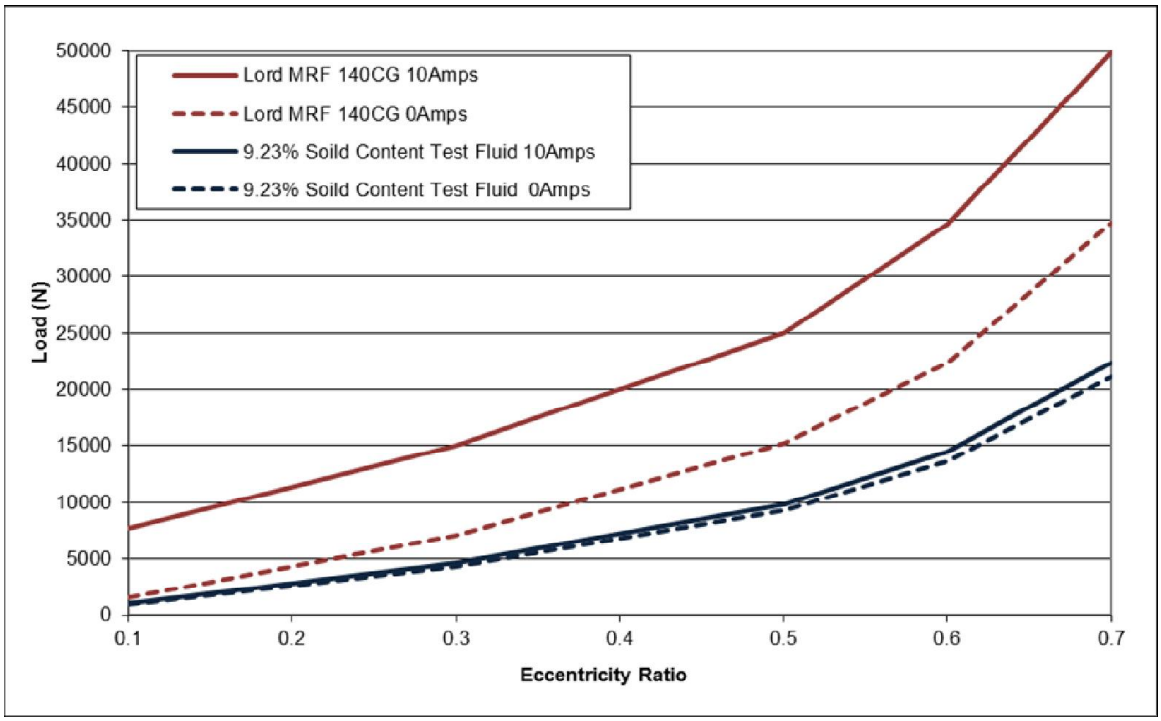

Figure 5-38 Numerical Load Capacity for Commercial MR Fluid vs. Test MR Fluid at 2000rpm for a Range of Eccentricity Ratios

5.3.2 Baseline Journal Bearing Performance

The first analysis performed on the experimental results was a baseline evaluation of the hydrodynamic journal bearing design. This initial analysis not only showed that the

bearing assembly was functioning properly, but also provided validation that the various measurement devices were configured in the correct manner. The bearing performance was analyzed for 500, 1000, 1500, 2000 and 2500 rpm by taking the average of the 10 second data collected at each speed, with no magnetic field applied to vary the rheological properties of the working fluid.

The eccentricity ratio was calculated by using the measured position of the bearing assembly during operation relative to the measured bearing position at rest. Knowing the radial internal clearance, the eccentricity ratio could be calculated. The average of three repeat runs for the test procedure was used to calculate the eccentricity ratio. Given the applied load of 158 N, the eccentricity ratio was very small (less than 0.05); however, as can be seen in Figure 5-39 the measured eccentricity ratio decreases as the speed increases as expected.

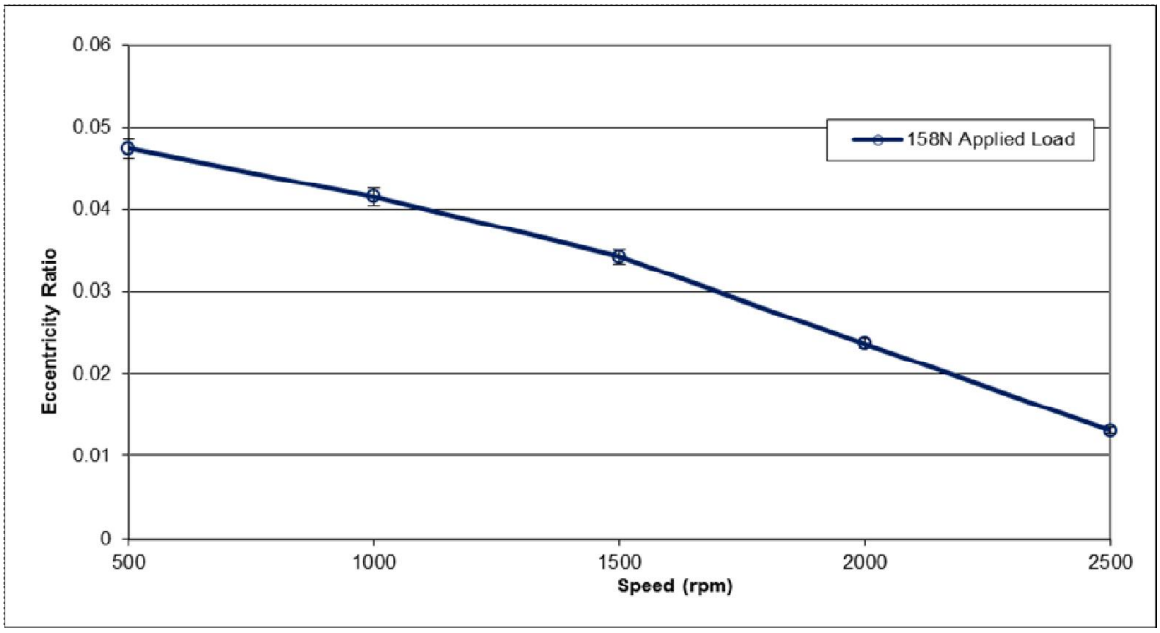

Figure 5-39 Measured Eccentricity Ratio vs. Speed with No Magnetic Field Applied

The torque generated by the journal rotation on the bearing assembly was calculated by measuring the load applied on the torque arm and multiplying it by the distance from the center of the journal to the point of contact by the load arm. The amount of torque measured was relatively small; however, as can be seen in Figure 5-40 the torque increases with speed as expected.

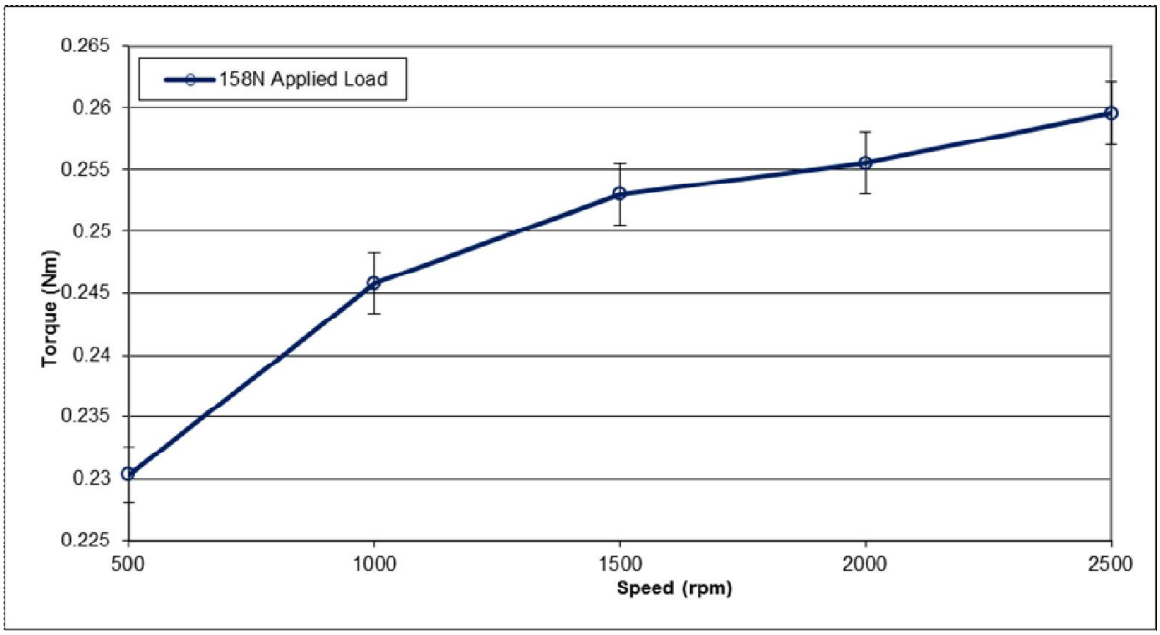

Figure 5-40 Measured Torque vs. Speed with No Magnetic Field Applied

The pressure measurement from the three axial ports was expected to provide a pressure profile as the journal rotated at the center of the bearing and at each axial end; however, the speed of the data acquisition equipment was not fast enough to provide an accurate measurement of the pressure profile and thus only the maximum pressure data is shown in Figure 5-41. The minimum pressure for both positions was equivalent to atmospheric conditions and was not included in the plot. Additionally, the third pressure transducers signal to noise ratio prevented any valid data to be retrieved. Figure 5-41

shows that the center pressure is significantly higher than the pressure reading at the axial end of the bearing, although losing the third pressure transducer makes it impossible to determine how well the center pressure tap aligned with the center of the bearing assembly. Figure 5-41 also shows that both pressure readings increase as the speed increases as expected.

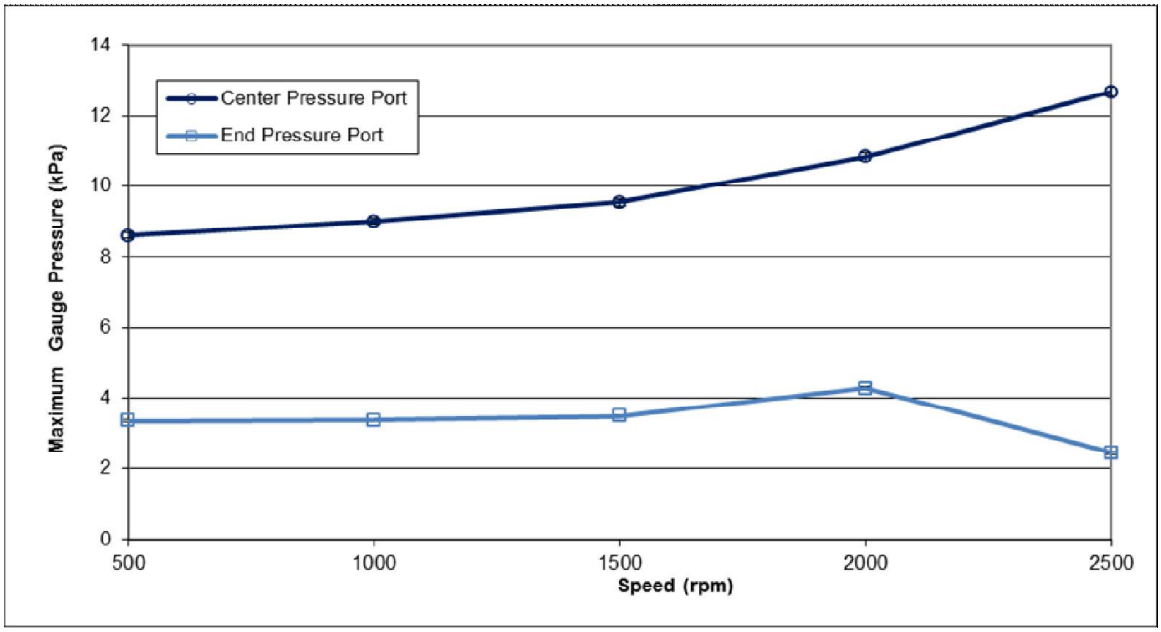

Figure 5-41 Measured Pressure vs. Speed with No Magnetic Field Applied

5.3.3 Journal Bearing Performance with Applied Magnetic Field

The application of a magnetic field to the magnetorheological fluid causes the suspended particles in the fluid become magnetized and form chain like structures, which align with the applied magnetic field lines. The particle chains restrict the movement of the fluid which produces an apparent increase in yield strength fluid and the fluid behaves as a Bingham plastic with a yield strength dependent on the magnitude of the magnetic field strength. The increase in yield strength within the fluid film results in a change in

the bearing performance, which includes an increase in the load capacity and friction losses. The bearing performance was experimentally evaluated for the same range of speeds as the baseline, while the magnetic field was varied from 0 to 500,000 A/m (0 – 20 Amps of applied current). With all different combinations of speeds and magnetic fields, a total of 15 unique steady state conditions were analyzed.

Figure 5-42 shows the measured eccentricity ratio relative to the operating speed with and without the magnetic field applied. The results shown represent an average of three repeated runs of the test procedure. The application of the magnetic field resulted in a decrease in the eccentricity ratio across all speeds. Given the applied load remained constant at 158 N, a decrease in eccentricity correlates to an increase in load capacity with the application of the magnetic field.

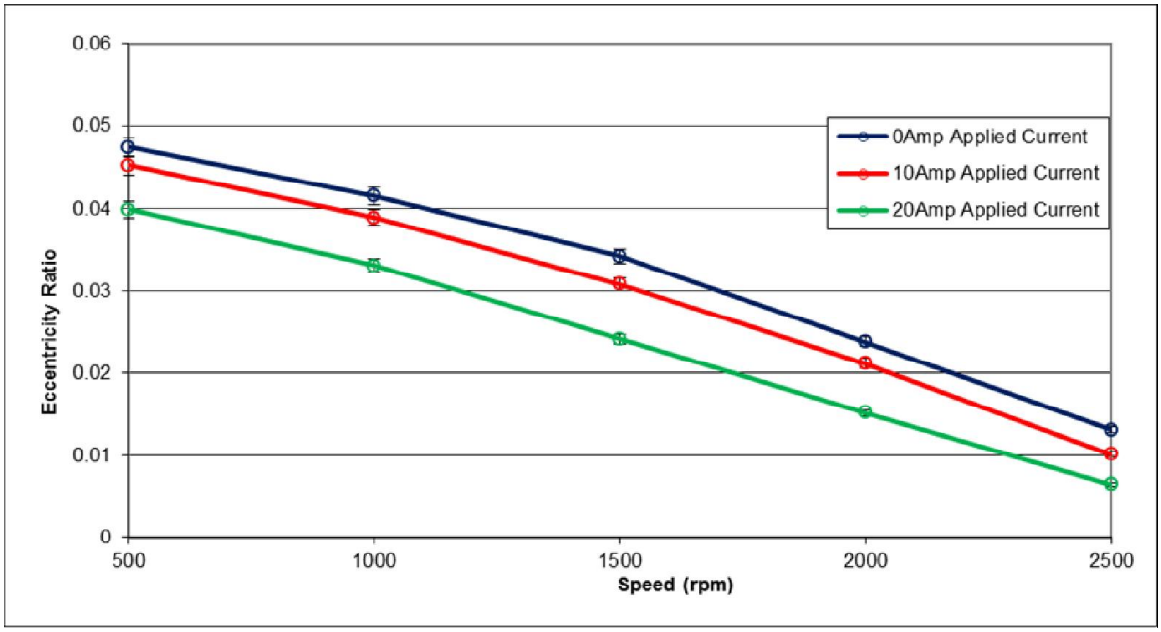

Figure 5-42 Measured Eccentricity Ratio vs. Speed with Magnetic Field Applied

The relationship in the decrease in eccentricity ratio relative to the applied magnetic field strength is not as direct as it may appear in Figure 5-42. Table 5-4 shows the percent decrease in the eccentricity ratio relative to the eccentricity ratio of the baseline run with no magnetic field applied. As can be seen, as the rotational speed increases, the relative decrease in the eccentricity ratio is greater. This indicates that a lower magnetic field would be required to achieve the same relative decrease in the eccentricity ratio.

Table 5-4 Percent Decrease in Eccentricity Ratio Relative to Baseline

	500rpm	1000rpm	1500rpm	2000rpm	2500rpm
10Amp	4.61%	6.34%	9.93%	10.93%	22.58%
20Amp	15.81%	20.33%	29.59%	36.08%	50.35%

Figure 5-43 shows the results of the measured torque for all speeds with and without the magnetic field applied. As can be seen, there is a minimal increase in torque at the lowest applied magnetic field; however, there is a significant increase in measured torque when the applied current is increased from 10 to 20 Amps. Table 5-5 shows the corresponding percent increase in measured torque at each applied current relative to no magnetic field. Table 5-5 highlights this relative jump in measured torque between 10 and 20 Amps of applied current going from less than 1% at 10 Amps to a 3-4% increase at 20 Amps.

Table 5-5 Percent Increase in Torque Relative to Baseline Torque

	500rpm	1000rpm	1500rpm	2000rpm	2500rpm
10Amp	-0.21%	0.27%	0.60%	0.28%	0.21%
20Amp	4.59%	3.83%	4.40%	3.65%	2.99%

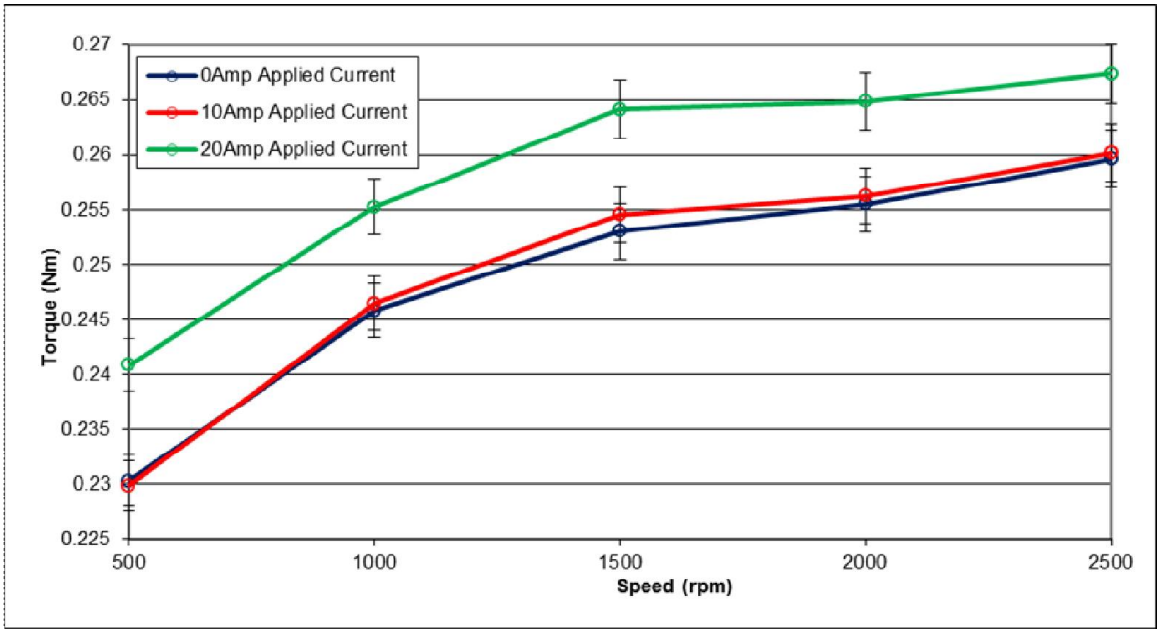

Figure 5-43 Measured Torque vs. Speed with Magnetic Field Applied

Figure 5-44 shows the maximum pressure measured at the approximate center and 15 mm from one axial end of the bearing with and without the magnetic field applied. When the magnetic field was applied the maximum pressure increased for all measured speeds. Table 5-6 provides the percent increase in the maximum measured pressure for each applied current relative to the baseline run with no magnetic field applied. As with the torque measurement, the pressure increase at 10 Amps is minimal at approximately 5% for most speeds; while increases of 30% occur at 20 Amps for most speeds. Data collected at 2500 rpm does not adhere to this trend and appears to be anomalous. This result was attributed to a small axial shift in the bearing assembly relative to the pressure ports located on the journal at this speed.

Table 5-6 Percent Increase in Maximum Pressure Relative to Baseline

End Pressure Tap					
	500rpm	**1000rpm**	**1500rpm**	**2000rpm**	**2500rpm**
10Amp	4.78%	4.74%	8.66%	7.40%	105.41%
20Amp	40.50%	27.97%	33.69%	32.99%	86.13%
Center Pressure Tap					
	500rpm	**1000rpm**	**1500rpm**	**2000rpm**	**2500rpm**
10Amp	4.06%	2.66%	10.07%	6.13%	14.55%
20Amp	35.78%	24.28%	31.06%	27.83%	12.87%

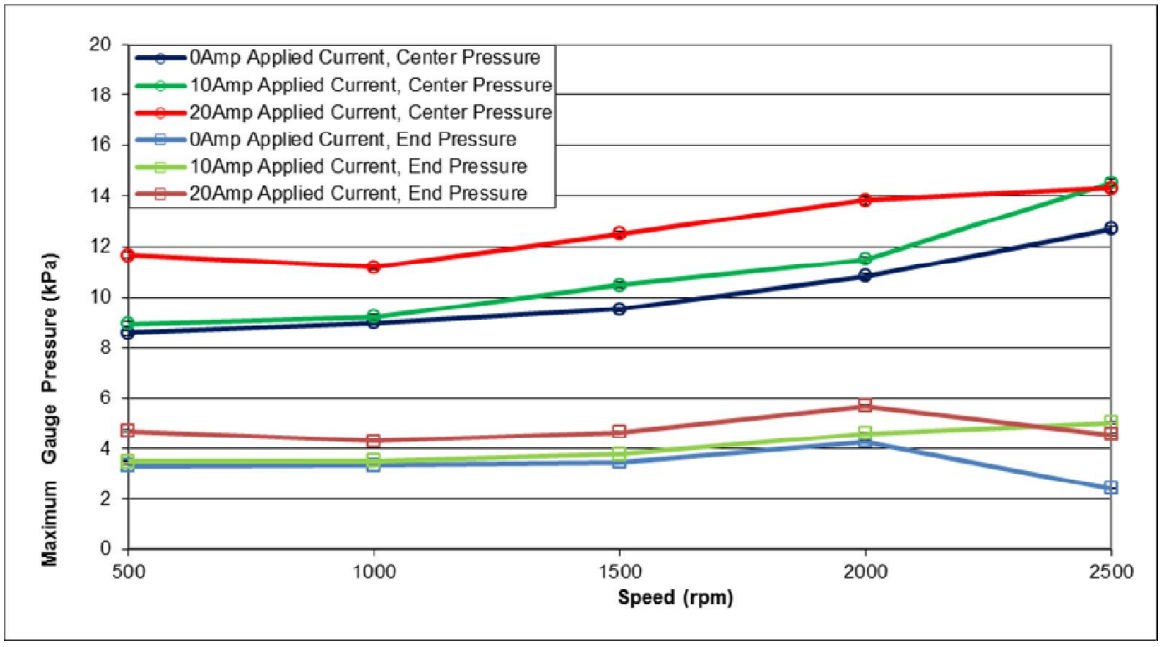

Figure 5-44 Measured Pressure vs. Speed with Magnetic Field Applied

The experimental results presented in this section showed the effects that increasing the yield strength of the magnetorheological fluid, due to an applied magnetic field, has on the journal bearing performance. Three key characteristics of the bearing, eccentricity ratio, pressure and torque, were used to quantify the changes observed when a variable magnetic field was applied. The results indicated that, a decrease of 15% in the

eccentricity ratio was achievable relative to the baseline eccentricity ratio for all speeds. Given the applied load remained constant, a decrease in eccentricity correlates to an increase in load capacity with the application of the magnetic field. It is interesting to note that the numerical results showed a diminishing impact on the load capacity for a given applied current as the rotational speed was increased; whereas, the experimental results showed an opposite trend for the decrease in eccentricity ratio. The results validate and confirm both the advantages and disadvantages of this bearing design; having the expected positive impact on eccentricity and load capacity, but paying a penalty in increased heat generation and torque, as well as power consumption from the electromagnets.

5.3.4 Results Using Half the Electromagnets and Dynamic Response

The previous subsections were focused on experimental results during steady state operation, where the load and speed of the journal bearing were held constant and the full complement of electromagnets were utilized. Additional testing to evaluate the bearing performance included evaluating the bearing performance when half of the electromagnets on the low pressure side of the bearing assembly were removed from the power supply circuit and evaluating the dynamic response of the bearing.

Table 5-7 shows the results of the eccentricity measurements for the baseline with no magnetic field applied and with 20 Amps of applied current to half and the full complement of electromagnets at 1000 rpm. The reduction in eccentricity ratio approximately remained the same when removing the power supply to the low pressure side of the bearing as compared to the full complement of electromagnets. Although it

should be noted, that the variability in the bearing position measurement was noticeably higher when only half the electromagnets where active. This may indicate that the discontinuous magnetic field introduced instability in the bearing operation.

Table 5-7 Measured Eccentricity Ratio Using Half the Electromagnets

	Eccentricity Ratio
0 Amp Applied Current	0.0402
20 Amps Half Electromagnets	0.0306
20 Amps Full Electromagnets	0.0331

Figure 5-45 shows the dynamic results of the measured eccentricity ratio verses time, with and without the magnetic field applied at 1000 rpm. The bearing was operating at steady state conditions for just over 3 seconds with a 136 N load applied until a 2.2 kg weight was dropped from 50 mm on top of the hanging weights to create an impact load. In both cases, the eccentricity ratio measurement returns to a new steady state position in approximately 1 second; although, it appears that small oscillations may still be present in the baseline run for an additional 0.5 second. The magnitude of the initial oscillation in eccentricity ratio clearly shows that the baseline run with no magnetic field applied is significantly greater than that of the run with the magnetic field applied. The maximum eccentricity for the baseline run reaches 0.14, whereas the run with the magnetic field applied stays below 0.10.

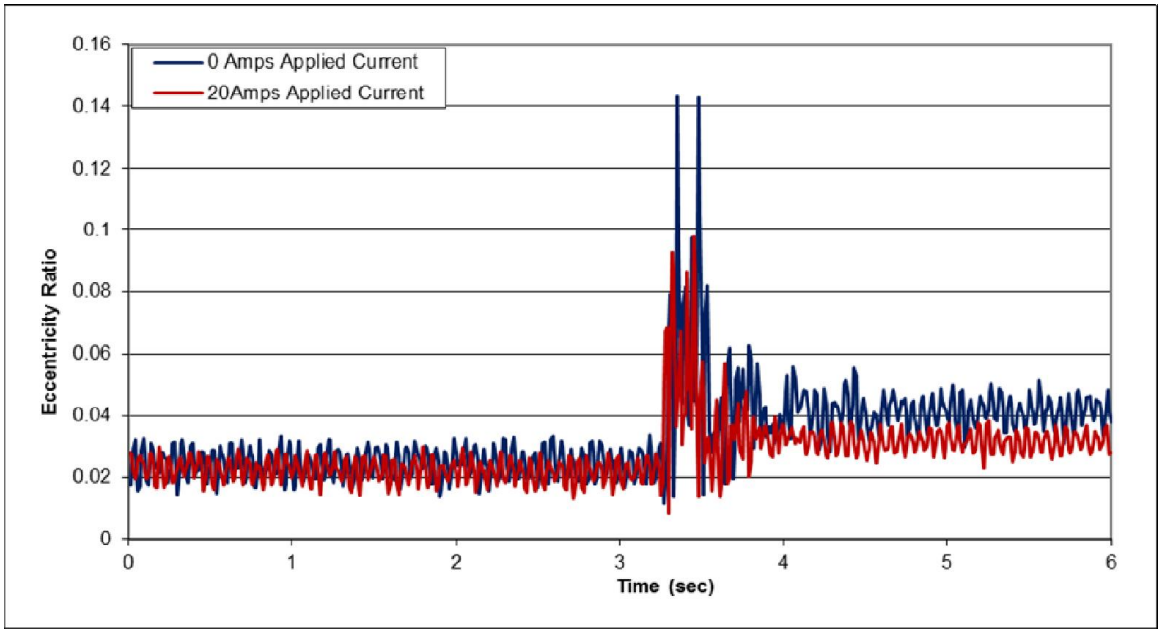

Figure 5-45 Comparison of Dynamic Response With and Without Magnetic Field

The experimental results of the steady state loading along with the dynamic response show that not only does the application of the magnetic field increase load capacity, but it also improves the orbital control through increasing the bearings stiffness and dampening capabilities. Furthermore, the ability of the bearing to maintain the same eccentricity ratio when the power supply is removed from half of the electromagnets indicates that there is an opportunity to optimize the efficiency of the bearing design by selectively deactivating the electromagnets located in the cavitation region of the bearing for a specified set of operating conditions.

5.4 Numerical and Experimental Results Comparison

The comparison of the numerical results to the experimental results was limited to the parameters that were evaluated for both cases which include bearing position and bearing pressure with and without the magnetic field applied. However, only the lower of

the two magnetic fields applied during the experimental testing could be used. This is because, the magnetic field generated at 20 Amps of applied current exceeded the capability of the electromagnetic cradle used to quantify the fluid properties.

Figure 5-46 compares the results of numerical models eccentricity ratio to the experimentally measured eccentricity ratio for speeds ranging from 500-2500 rpm. The correlation between the experimental and numerical eccentricity ratio is very good at 500 and 2500 rpm while there is some separation between the results at 1000, 1500 and 2000 rpm. It should be noted that a difference in the eccentricity ratio of 0.01 represents a dimensional difference of 0.0012 mm.

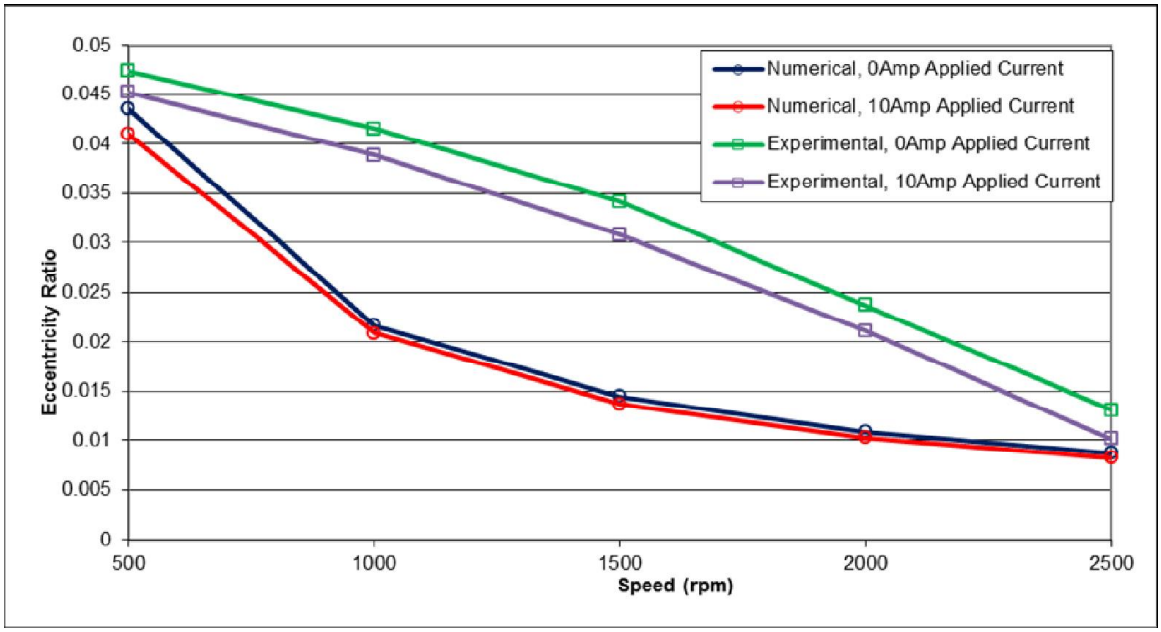

Figure 5-46 Numerical vs. Experimental Eccentricity Ratio

While the eccentricity ratio shows good correlation between the numerical and experimental results, the decrease in the eccentricity ratio when the magnetic field is applied is in less agreement. Table 5-8 shows the percent decrease in eccentricity ratio

relative to the baseline when the magnetic field is applied for both the numerical and experimental methods. As can be seen in Table 5-8, the percent decrease in the eccentricity ratio for the numerical method is relatively constant at approximately 5.75%, while the percent decrease for the experimental results is greater as the speed increases and ranges from approximately 4.5% up to 22.5%.

Table 5-8 Numerical vs. Experimental Percent Decrease in Eccentricity Ratio

	500rpm	1000rpm	1500rpm	2000rpm	2500rpm
Numerical Results	5.75%	5.53%	5.52%	5.96%	5.75%
Experimental Results	4.61%	6.34%	9.93%	10.93%	22.58%

Figure 5-47 compares the results of numerical models maximum pressure to the experimentally measured maximum pressure for speeds ranging from 500-2500 rpm. Figure 5-47 shows, the maximum pressure for the numerical method is relatively constant at approximately 150 kPa, while the maximum pressure for the experimental results starts at approximately 160 kPa and increases as the speed increases up to nearly 200 kPa. Similarly, the increase in the maximum pressure for the numerical method is barely visible at less than 0.5%, while the increase in maximum pressure for the experimental method starts at approximately 4% and increases to 14.5% as the speed increases.

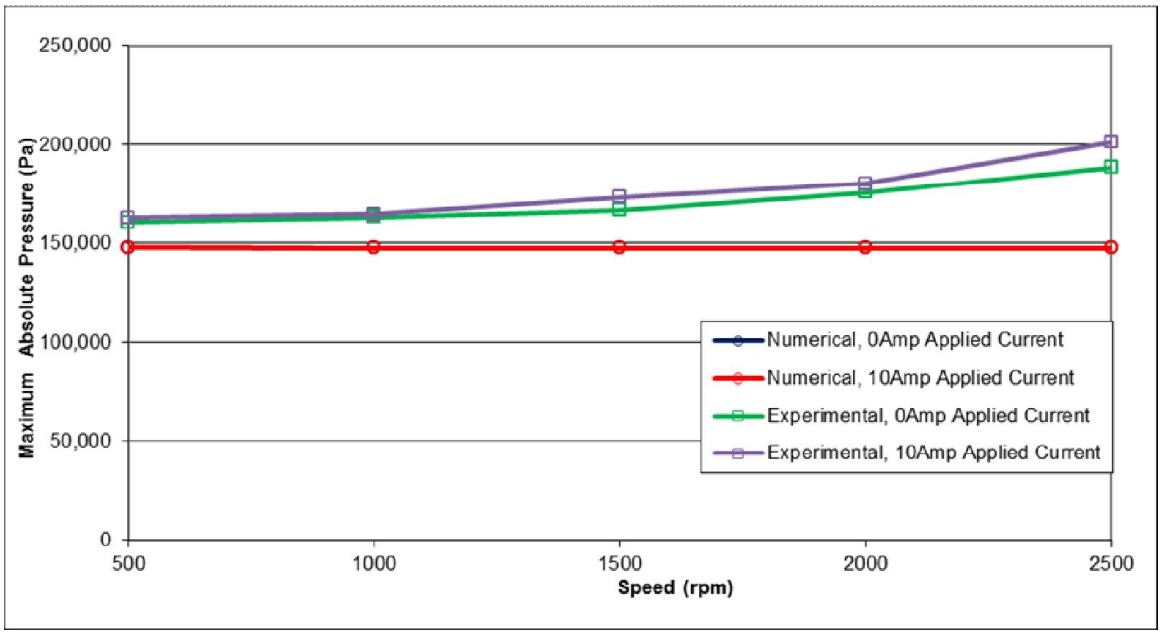

Figure 5-47 Numerical vs. Experimental Maximum Bearing Pressure

Comparing the numerical results to the experimental results showed that the numerical model provides a good approximation for predicting actual bearing performance. Considering the operating conditions that were tested were at the low end of the eccentricity ratio spectrum, the level of correlation between the two results was surprisingly good. Although a wider range of eccentricities would provide a much clearer evaluation of the accuracy of the numerical model; this was not possible utilizing the existing test bench set up.

CHAPTER VI

CONCLUSIONS AND RECOMMENDATIONS

6.1 Conclusions

This research comprised of several stages in an effort to create a hydrodynamic journal bearing design that had capability to be actively controlled through the use of magnetorheological fluids. The initial stage was to design an arrangement of electromagnets such that the magnetic field lines generated by those magnets were perpendicular to the shearing forces across the fluid filled gap of the bearing. This required the magnetic field to be applied in the radial direction around the circumference of the bearing. Utilizing FEMM programs to evaluate various designs, the final design was accomplished by placing eight electromagnetic dipoles circumferentially around the bearing. The eight dipoles covered the entire circumference of the bearing and directed the field perpendicular to the fluid filled gap such that the normal magnetic field strength was nearly uniform within the fluid at the pole locations.

The second stage in this research was to create a numerical model to evaluate the performance of a hydrodynamic journal bearing using a fluid that had variable rheological properties relative to the magnetic field strength. To accomplish this, a modified Reynolds equation was derived where the fluid was modeled as a Bingham plastic, whose yield strength is proportional to the strength of the applied magnetic field.

This was achieved by replacing the Newtonian shear stress terms, in the derivation of the Reynolds equation, with a shear stress representative of a Bingham plastic that was dependent on the strain rate and the yield strength of the magnetorheological fluid. The subdomain method or the control-volume formulation was then utilized as the discretization method.

The results of the numerical model indicated that, for most speed and eccentricity ratio combinations, an increase of 20% in the load capacity was achievable relative to the baseline load capacity while utilizing the fluid properties of a commercially available magnetorheological fluid MRF-140CG by the Lord Corporation. The analysis also showed that an increase of 30% in the critical mass, which represents the mass the bearing can support and maintain stable operation, was achievable relative to the baseline with no magnetic field applied. These results highlight the potential advantages of this bearing design in combination with a magnetorheological fluid.

The third stage in this effort was to create a more complete quantification of the rheological properties of magnetorheological fluids. To accomplish this seven different samples, which consisted of a range solid content by mass of carbonyl iron powder from approximately 2% to 75%, were analyzed. The viscosity and specific gravity for a range of magnetic fields was measured at multiple temperatures for each sample. Although it is unlikely that this level of information regarding magnetorheological fluids is not available, to the authors knowledge, this is the first time that it has been made publically available.

The fourth and final stage in this research was to create a bench test to provide a proof of performance for the bearing design. To accomplish this, the bearing assembly

components were machined and assembled on a test bench. The evaluation of the performance of the bearing design consisted of 15 steady state conditions with operational parameters of speed and applied magnetic field as the key variables, while the bearing performance was analyzed by measuring eccentricity, torque and fluid pressure.

The results of the experimental testing indicated that, a decrease of 15% in the eccentricity ratio was achievable relative to the baseline eccentricity ratio for all speeds. Given the applied load remained constant, a decrease in eccentricity correlates to an increase in load capacity with the application of the magnetic field. The analysis also showed that an increase of up to 4.5% in the bearing torque, which represents reduction in operating efficiency when a magnetic field is applied. These results validate both the advantages and disadvantages of this bearing design. This proves the bearing design gives the ability to control the bearing performance with the expected consequence of increased heat generation and power consumption from the electromagnets as well as the bearing torque.

Comparing the numerical results to the experimental results showed that the numerical model provides a good approximation for predicting actual bearing performance. Considering the operating conditions that were tested were at the low end of the eccentricity ratio spectrum, the level of correlation between the two results was surprisingly good. Although a wider range of eccentricities would provide a much clearer evaluation of the accuracy of the numerical model; this was not possible utilizing the existing test bench set up.

6.2 Recommendations

The magnetorheological fluid created for testing was selected from seven samples with varying levels of carbonyl iron powder. To keep the particles in suspension, an iterative process of adding incremental amounts white lithium grease was used, until particle settling was not observed for a period of 24 hours. However, particle settling over extended periods of time still occurred. Although it may not be feasible to eliminate long term settling with the particle size needed for magnetorheological fluids, there is still room for improvement. It may be possible to increase settling time by mixing the carbonyl iron powder with a chelating agent such as ethylene diamine tetra acidic acid or more oil soluble fatty acids such as oleic acid or linoleic acid prior to mixing with the bulk carrier fluid. Whereas the white lithium grease currently used, could not easily be mixed with the carbonyl iron powder prior to blending into the bulk fluid. The author recognizes that settling issues have presumably already been resolved in commercially available magnetorheological fluids.

The bearing design created for this research was shown to function as intended through both numerical and experimental analyses. The correlation between the numerical models predicted performance and the experimental results were satisfactory as well. The next logical steps are to further refine the bearing design and continue to quantify the bearing performance through additional experimental efforts. Prior to running further experimental efforts, additional features to enhance the test stand capabilities are recommended. To increase the acceptable load capacity of the stand, an additional support should be added to the axial end of the journal such that an overhung load is not created by the bearing assembly. Additionally, a reduction in vibration

measured by the position sensors may be possible by supporting the indicator button with a bracket rather than a section of threaded stainless steel.

One of the key features of the bearing design was the eight electromagnets placed around the circumference of the bearing. Although, the experimental efforts in this study were focused on a proof of performance where the electromagnets were wired in series; this design feature allows each magnet to be controlled individually. In Section 4.4.3 it was shown that a relay was added to the electromagnets power supply such that one or a series of electromagnets could be isolated and turned off by a toggle switch. Additional relays could be added in a similar fashion to provide the same control for each of the electromagnets. Furthermore, potentiometers could be used to add an analog control for the applied current to each electromagnet and thus a controllable variable magnetic field around the circumference of the bearing.

Through additional testing, utilizing a more complex experimental evaluation, one could combine a more complete understanding of the bearing performance with the variable magnetic field around the circumference of the bearing, to develop a programmable strategy and control the bearing performance for a given set of operating conditions. The number of magnets used to cover the circumference of the bearing could be increase to improve the resolution of the magnetic field as well. This would be the ultimate fulfillment of this bearing design.

BIBLIOGRAPHY

1. Rosensweig, R.E. “Ferrohydrodynamics.” Mineola, New York: Dover, 1997.

2. Winslow, Willis M. “Method and Means for Translating Electrical Impulses into Mechanical Force.” US Patent 2,417,850. March 25, 1947.

3. Wen, Weijia, Zheng, D.W., and Tu, K.N. “Fractal-Chain Transition of Field-Induced Colloid Structure.” Physical Review E, Vol. 58, Issue: 6, December 01, 1998. pp. 7682-7685.

4. Wen, Weijia, Zheng, D.W., and Tu, K.N. “Chain/Column Evolution and Corresponding Electrorheological Effect.” Journal of Applied Physics, Vol. 85, Issue: 1, January 01, 1999. pp. 530-533.

5. Conrad, Hans, and Sprecher, Arnold F. “Characteristics and Mechanisms of Electrorheological Fluids.” Journal of Statistical Physics, Vol. 64, Issue: 5-6, September 1991. pp. 1073 – 1091.

6. Agafonov, A.V., and Zakharov, A.G. “Electrorheological Fluids.” Russian Journal of General Chemistry, Vol. 80, Issue: 3, March 2010. pp. 567 – 575.

7. Stangroom, J.E. “Electrorheological Fluids.” Physics in Technology, Vol. 14, Issue: 6, November 01, 1983. pp. 290-296.

8. See, H., Tamura, H., and Doi, M. “The Role of Water Capillary Forces in Electro-Rheological Fluids.” Journal of Physics D: Applied Physics, Vol. 26, Issue: 5, May 14, 1993. pp. 746-752.

9. Chena, T.Y., and Luckham, P.F. “Effect of Frequency on a Water-Activated Electrorheological Fluid in an A.C. Electric Field.” Colloids and Surfaces A: Physicochemical and Engineering Aspects Volume 78, 15 October 1993. Pages 167-175.

10. Che, T.Y., Brisco, B.J., and Luckha, P.F. “Microstructural Studies of Electro-rheological Fluids Under Shear.” Journal of the Chemical Society, Faraday Transactions, Vol. 91, Issue: 12, 1995. pp. 1787-1794.

11. Stangroom, James E. “Basic Considerations in Flowing Electrorheological Fluids.” Journal of Statistical Physics, Vol. 64, Issue: 5-6, September 1991. pp. 1059 – 1072.

12. Phulé, Pradeep P. “Magnetorheological (MR) Fluids: Principles and Applications.” Smart Materials Bulletin, Vol. 2001, Issue: 2, February 2001. pp. 7 – 10.

13. Olabi, A.G., and Grunwald, A. “Design and Application of Magneto-Rheological Fluid.” Materials and Design, Vol. 28, Issue: 10, 2007. pp. 2658-2664.

14. Jacob, Rabinov “Magnetic Fluid Torque and Force Transmitting Device.” US Patent 2,575,360. November 20, 1951.

15. Lord Corporation. “Magneto-Rheological Fluid Technology.” August 2010 <www.lord.com>.

16. “Magnetorheological fluid Devices: Principles, Characteristics and Applications in Mechanical Engineering.” Proceedings of the Institution of Mechanical Engineers, Part L: Journal of Materials: Design and Applications, Vol. 215, Issue: 3, 2001. pp. 165-174.

17. Jolly, M.R., Bender, J.W., and Carlson, J.D. “Properties and Application of Magnetorheological Fluids.” SPIE 5th Annual Int. Symposium on Smart Structures and Materials, March 15, 1998.

18. Simon, T.M., Reitich, F., Jolly, M.R., Ito, K., and Banks, H.T. “The Effective Magnetic Properties of Magnetorheological Fluids.” Mathematical and Computer Modeling, Vol. 33, Issue: 1-3, January - February, 2001. pp. 273-284.

19. Jolly, M.R., Carlson, J.D., and Munoz, B.C. “A Model of the Behaviour of Magnetorheological Materials.” Smart Materials and Structures, Vol. 5, Issue: 5, October 01, 1996. pp. 607-614.

20. Odenbach, S. “Recent Progress in Magnetic Fluid Research.” Journal of Physics: Condensed Matter, Vol. 16, Issue: 32, August 18, 2004. pp. R1135-R1150.

21. Olabi, A.G., and Grunwald, A. “Design and Application of Magneto-Rheological Fluid.” Materials and Design, Vol. 28, Issue: 10, 2007. pp. 2658-2664.

22. Rinaldi, Carlos, Chaves, Arlex, Elborai, Shihab, He, Xiaowei (Tony), and Zahn, Markus “Magnetic Fluid Rheology and Flows.” Current Opinion in Colloid and Interface Science, Vol. 10, Issue: 3-4, October, 2005. pp. 141-157.

23. Jolly, M.R., Bender, J.W., and Carlson, J.D. “Properties and Applications of Commercial Magnetorheological Fluids.” SPIE 5th Annual Int. Symposium on Smart Structures and Materials, March 15, 1998.

24. Einstein, A. “Eine neue Bestimmung der Molekuldimensionen.” [AdP 19, 289 (1906)]; Annalen der Physik, Vol. 14, Issue: S1, February 2005. pp. 229 – 247.

25. Odenbach, S. “Ferrofluids: Magnetically Controllable Liquids.” PAMM, Vol. 1, Issue: 1, March 2002. pp. 28 – 32.

26. Vekas, Ladislau “Ferrofluids and Magnetorheological Fluids.” Advances in Science and Technology, Vol. 54, September, 2008. pp. 127-136.

27. Yang, J., Chen, S., Zhang, Q., and Liu, Z. “Transient Dynamic Analysis of Ferro-Fluid Bearing Spindle Motor.” Microsystem Technologies, Vol. 8, Issue: 4-5, August, 2002. pp. 282 – 288.

28. Hang, Q. Chen, S. Winoto, S.H., Ong, E. “Design of High-Speed Magnetic Fluid Bearing Spindle Motor.” IEEE Transactions on Magnetics, Vol. 37 Issue: 4, July, 2001. pp. 2647 – 2650.

29. Han-dan, L., Wei, X., Shi-gang, W., Zun-ji, K. “Hydrodynamic Modeling of Ferrofluid Flow in Magnetic Targeting Drug Delivery Applied Mathematics and Mechanics.” Vol. 29, Issue: 10, October 2008. pp. 1341 – 1349.

30. “Designing with MR Fluids.” Lord Corporation Engineering Note, December 1999.

31. Agrawal, Ashish, Ciocanel, Constantin, Martinez, Tony, Vieira, Sheila L., Naganathan, Nagi G., Robb, Scott, and Duggan, Jim “A Bearing Application Using Magnetorheological Fluids.” Journal of Intelligent Material Systems and Structures, Vol. 13, Issue: 10, October 2002. pp. 667-673.

32. Broge, Jean L. “Valveless Damping Suspension System.” Automotive Engineering International, December 1999. pp. 50-52.

33. McTague, John P. “Magnetoviscosity of Magnetic Colloids.” The Journal of Chemical Physics, Vol. 51, Issue: 1, July 01, 1969. pp. 133-136.

34. Hall, W.F., and Busenberg, S.N. “Viscosity of Magnetic Suspensions.” The Journal of Chemical Physics, Vol. 51, Issue: 1, July 01, 1969. pp. 137-144.

35. Patel, Rajesh, Upadhyay, R.V., and Mehta, R.V. “Viscosity Measurements of a Ferrofluid: Comparison with Various Hydrodynamic Equations.” Journal of Colloid and Interface Science, Vol. 263, Issue: 2, July 15, 2003. pp. 661-664.

36. Buscher, K., Helm, C.A., Gross, C., Glockl, G., Romanus, E., and Weitschies, W. “Nanoparticle Composition of a Ferrofluid and its Effects on the Magnetic Properties.” Langmuir, Vol. 20, Issue: 6, March 16, 2004. pp. 2435-2444.

37. Zubarev, A.Yu., Odenbach, S., and Fleischer, J. “Rheological Properties of Dense Ferrofluids, Effects of Chain-Like Aggregates.” Journal of Magnetism and Magnetic Materials, Vol. 252, November, 2002. pp. 241-243.

38. Bossis, G., Lacis, S., Meunier, A., and Volkova, O. “Magnetorheological Fluids.” Journal of Magnetism and Magnetic Materials, Vol. 252, November, 2002. pp. 224-228.

39. Conrad, Hans “An Analytical Model for Magnetorheological Fluids.” Journal of Physics D: Applied Physics, Vol. 33, Issue: 23, December 07, 2000. pp. 3026-3032.

40. Bingham, Eugene C. "An Investigation of the Laws of Plastic Flow." US Bureau of Standards Bulletin, 1916. pp. 309-353.

41. Herschel, Winslow H., and Bulkley, Ronald, "Konsistenzmessungen von Gummi-Benzollösungen." Colloid and Polymer Science, Vol. 39, pp. 291–300.

42. Wereley, Norman M. “Nondimensional Herschel-Bulkley Analysis of Magnetorheological and Electrorheological Dampers.” Journal of Intelligent Material Systems and Structures, Vol. 19, Issue: 3, March 2008. pp. 257-268.

43. Bassani, R., and Piccigallo, B. “Hydrostatic Lubrication.” Amsterdam: Elsevier Science, 1992.

44. Pinkus, O., and Sternlicht, B. “Theory of Hydrodynamic Lubrication.” New York: McGraw-Hill, 1961.

45. Martin, J.K. “Design Guidelines for Hydrostatic Journal Bearings.” Industrial Lubrication and Tribology, Vol. 58, Issue: 3, 2006. pp. 135-139.

46. Hesselbach, J., and Abel-Keilhack, C. “Active Hydrostatic Bearing with Magnetorheological Fluid.” Journal of Applied Physics, Vol. 93, Issue: 10, May 15, 2003. pp. 8441-8443.

47. Guldbakke, J.M., and Hesselbach, J. “Development of Bearings and a Damper Based on Magnetically Controllable Fluids.” Journal of Physics: Condensed Matter, Vol. 18, Issue: 38, September 27, 2006. pp. S2959-S2972.

48. Hamrock, B. “Fundamentals of Fluid Film Lubrication.” New York: McGraw-Hill, 1994.

49. Elsharkawy, A.A., and Nassar, M.M. “Hydrodynamic Lubrication of Squeeze-Film Porous Bearings.” Acta Mechanica, Vol. 118, Issue: 1-4, March 1996. pp. 121 – 134.

50. Prajapati, B.L. “Magnetic-Fluid-Based Porous Squeeze Films.” Journal of Magnetism and Magnetic Materials, Vol. 149, Issue: 1-2, August, 1995. pp. 97-100.

51. Shah, Rajesh C. “Ferrofluid Lubrication in Step Bearing with Two Steps.” Industrial Lubrication and Tribology, Vol. 55, Issue: 6, 2003. pp. 265-267.

52. Patel, Rakesh M., and Deheri, G.M. “Magnetic Fluid Based Squeeze Film Between Porous Conical Plates.” Industrial Lubrication and Tribology, Vol. 59, Issue: 3, 2007. pp. 143-147.

53. C. Shah, Rajesh., and Bhat, M.V. “Squeeze Film Based on Magnetic Fluid in Curved Porous Rotating Circular Plates.” Journal of Magnetism and Magnetic Materials, Vol. 208, Issue: 1-2, January, 2000. pp. 115-119.

54. Vora, K.H. and Bhat, M.V., “The Load Capacity of a Squeeze Film Between Curved Porous Rotating Circular Plates.” Wear, Vol. 65, Issue: 1, December 1980. pp. 39-46.

55. Bhat, M.V., and Deheria, G.M., “Magnetic-Fluid-Based Squeeze Film in Curved Porous Circular Discs.” Journal of Magnetism and Magnetic Materials, Vol. 127, Issues: 1-2, October 1993 pp. 159-162.

56. Agrawala, V.K. "Magnetic-Fluid-Based Porous Inclined Slider Bearing." Wear, Vol. 107, Issue 2, 15 January 1986, pp. 133-139.

57. Shah, Rajesh C., and Bhat, M.V. “Ferrofluid Based Secant Shaped Slider Bearing.” Industrial Lubrication and Tribology, Vol. 55, Issue: 3, 2003, pp.113-115.

58. Shah, Rajesh C., and Bhat, M.V. “Ferrofluid Lubrication of a Porous Slider Bearing with a Convex Pad Surface Considering Slip Velocity.” International Journal of Applied Electromagnetics and Mechanics, Vol. 20, Issue 1/2004, August 19, 2004, pp. 1-9.

59. Shah, Rajesh C., and Bhat, M.V. “Ferrofluid Lubrication in Porous Inclined Slider Bearing with Velocity Slip.” International Journal of Mechanical Sciences, Vol. 44, Issue: 12, December, 2002. pp. 2495-2502.

60. Shah, Rajesh C., and Bhat, M.V. “Lubrication of Porous Parallel Plate Slider Bearing with Slip Velocity, Material Parameter and Magnetic Fluid.” Industrial Lubrication and Tribology, Vol. 57, Issue: 3, 2005. pp. 103-106.

61. Shah, Rajesh C., and Bhat, M.V. “Porous Secant Shaped Slider Bearing with Slip Velocity Lubricated by Ferrofluid.” Industrial Lubrication and Tribology, Vol. 55, Issue: 3, 2003. pp. 113-115.

62. Ahmad, N., and Singh, J.P. “Magnetic Fluid Lubrication of Porous-Pivoted Slider Bearings with Slip Velocity.” Journal of Engineering Tribology, Vol. 221, Issue: J, April, 2007. pp. 609-613.

63. Ochonski, W. “Sliding Bearings Lubricated with Magnetic Fluids.” Industrial Lubrication and Tribology, Vol. 59, Issue: 6, 2007. pp. 252-265.

64. Miwa, M., Harita, H., Nishigami, T., Kaneko, R., and Unozawa, H. “Frequency Characteristics of Stiffness and Damping Effect of a Ferrofluid Bearing.” Tribology Letters, Vol. 15, Issue: 2, August 2003. pp. 97-105.

65. Huang, S.Y., Jiang, L.M., Qian, H.X., Shen, X.M., and Sun, D.C. “On the Magnetic Sealing Capability of Ferrofluid-Lubricated Journal Bearings.” Proceedings of the Royal Society of London. Series A, Mathematical and Physical Sciences, Vol. 404, 1986. pp. 69-88.

66. Osman, T.A., Nada, G.S., and Safar, Z.S. “Static and Dynamic Characteristics of Magnetized Journal Bearings Lubricated with Ferrofluid.” Tribology International, Vol. 34, Issue: 6, June, 2001. pp. 369-380.

67. Osman, T.A., Nada, G.S., and Safar, Z.S. “Effect of Using Current-Carrying-Wire Models in the Design of Hydrodynamic Journal Bearings Lubricated with Ferrofluids.” Tribology Letters, Vol. 11, Issue: 1, July 2001. pp. 61-70.

68. Osman, T.A., Nada, G.S., and Safar, Z.S. “Different Magnetic Models in the Design of Hydrodynamic Journal Bearings Lubricated with Non-Newtonian Ferrofluid.” Tribology Letters, Vol. 14, Issue: 3, April 2003. pp. 211-223.

69. Batra, R. L. “Rheodynamic Lubrication of a Journal Bearing.” Applied Scientific Research, Vol. 15, Issue: 1, January 1966. pp. 331 – 344.

70. Tichy, John A. “Hydrodynamic Lubrication Theory for the Bingham Plastic Flow Model.” Journal of Rheology, Vol. 35, Issue: 4, May 1991. pp. 477-496.

71. Gertzos, K.P., Nikolakopoulos, P.G., and Papadopoulos, C.A. “CFD Analysis of Journal Bearing Hydrodynamic Lubrication by Bingham Lubricant.” Tribology International, Vol. 41, Issue: 12, December 2008. pp. 1190-1204.

72. Bompos, D.A., and Nikolakopoulos, P.G. “CFD Simulation of Magnetorheological Fluid Journal Bearings.” Simulation Modeling Practice and Theory, Vol. 19, January 2011. pp. 1035-1060.

73. Forte, P., Paterno, M., and Rustighi, E. “A Magnetorheological Fluid Damper for Rotor Applications.” International Journal of Rotating Machinery, Vol. 10, Issue: 3, 2004. pp. 175-182.

74. Urreta, H., Leicht, Z., Sanchez, A., Agirre, A., Kuzhir, P., and Magnac, G. "Hydrodynamic Bearing Lubricated with Magnetic Fluids." Journal of Physics: Conference Series, Vol. 149, 2009. pp. 1-4.

75. Urreta, H., Leicht, Z., Sanchez, A., Agirre, A., Kuzhir, P., and Magnac, G. "Hydrodynamic Bearing Lubricated with Magnetic Fluids." Journal of Intelligent Material Systems and Structures, Vol. 21, October, 2010. 1491-1499.

76. Reynolds, O. "The Theory of Lubrication and its Application to Mr. Beauchamp Tower's Experiments, Including an Experimental Determination of the Viscosity of Olive Oil." Philosophical Transactions of the Royal Society, Part 1, 1886. pp. 228-310.

77. Towers, B. "First Report on Friction Experiments (Friction of Lubricated Bearings)." Proceedings of the Institution of Mechanical Engineers, 1883. pp. 632-659.

78. Cope, W.F. "The Hydrodynamical Theory of Film Lubrication." Proceedings of the Royal Society of London. Series A, Mathematical and Physical Sciences, Vol. 197, Issue: 1049, June 7, 1949. pp. 201-217.

79. Dowson, D. "A Generalized Reynolds Equation for Fluid-Film Lubrication." International Journal of Mechanical Sciences, Vol. 4, 1962. pp. 159-170.

80. Constantinescu, V.N., Nica, A., Pascovici, M.D., Ceptureanu, G., and Nedelcu, S. "Sliding Bearings." New York: Allerton Press, 1985.

81. Santos, I.F., and Russo, F.H. "Tilting-Pad Journal Bearings with Electronic Radial Oil Injection." Journal of Tribology, Vol. 120, Issue: 3, July, 1998. pp. 583-595.

82. Floberg, L. "On Journal Bearing Lubrication Considering the Tensile Strength of the Liquid Lubricant." Transactions of Machine Elements Division, Lund Technical University, Lund, Sweden, 1973. pp. 1-27.

83. Braun, M.J., and Hannon, W.M. "Cavitation Formation and Modeling for Fluid Film Bearings: A Review." Journal Engineering Tribology, Vol. 224, Part J, 2010. pp. 839-863.

84. Gumbel, L. "Das Problem der Lagerreibung." Monatsblatter, Berliner Bezirks Verein Deutscher Ingenieure, 1914, Vol. 5, pp. 87-104 and 109-120.

85. Swift, H.W. "The Stability of Lubricating Films in Journal Bearings." Proceedings: Institution of Civil Engineers, 1932, Vol. 233, pp. 267-288.

86. Stieber, W. "Das Schwimmlager: Hydrodynamische Theorie des Gleitlagers." Verein Deutscher Ingenieure Verlag, Berlin, 1933, pp. 106.

87. Brewe, D.E., Ball, J.H., and Khonsari, M.M. “Introduction. Part 2: Current Research in Cavitating Fluid Films.” Proceedings of the Cavitation Symposium, STLE Annual Meeting, NASA TM-103184, 1988, pp. 25-26.

88. Jakobsson, B., and Floberg, L. “The Finite Journal Bearing Considering Vaporization.” Chalmers Tekniska Hoegskolas Handlingar, Goteborg, Sweden, Vol. 190, 1957, pp. 1-116.

89. Olsson, K.O. “Cavitation in Dynamically Loaded Journal Bearings.” Chalmers University of Technology, Goteborg, Sweden, 1965, Vol. 308.

90. Etsion, I., and Ludwig, L.P. “Observation of Pressure Variation in the Cavitation Region of Submerged Journal Bearings.” ASME Journal of Lubrication Technology, Vol. 104, No. 2, April, 1982, pp. 157-163.

91. Elrod, H.G., and Adams, M.L. “A Computer Program for Cavitation and Starvation Problems.” Cavitation and Related Phenomena in Lubrication, Mechanical Engineering Publication, New York, 1974, pp. 37-41.

92. Elrod, H.G. “A Cavitation Algorithm.” ASME Journal of Lubrication Technology, Vol. 103, No. 3, July, 1981, pp. 350-354. Tribology Transcripts, 1989, Vol. 32, No. 2, pp. 225-233.

93. Keith, T.G., and Vijayaraghavan, D. “Development and Evaluation of a Cavitation Algorithm.”

94. Jiles, D. "Introduction to Magnetic Materials." New York: Chapman and Hall, 1990.

95. Oersted, H.C. “Experimenta circa Effectum Conflictus Electriciti in Acum Magneticam.” July 1820.

96. "Epistola Petri Peregrini de Maricourt ad Sygerum de Foucaucourt, militem, de magnete." Encyclopædia Britannica. 2010. Encyclopædia Britannica Online. 29 Nov. 2010 <http://www.britannica.com/EBchecked/topic/190321/Epistola-Petri-Peregrini-de-Maricourt-ad-Sygerum-de-Foucaucourt-militem-de-magnete>.

97. Binns, K., and Lawrenson, P. “Analysis and Computation of Electric and Magnetic Field Problems.” New York: Pergamon Press, 1973.

98. Corson, D., and Lorrain, P. "Introduction to Electromagnetic Fields and Waves." San Francisco: W.H. Freeman and Company, 1962.

99. Espinosa, O., and Slusarenko, V. “The Magnetic Field of an Infinite Solenoid.” American Journal of Physics, Vol. 71, Issue: 9, September 2003. pp. 953-954.

100. Kraus, J.D. “Electromagnetics.” New York: McGraw-Hill Book Company, 1953.

101. McHarris, O., and Signell, P. “The Ampere-Laplace-Biot-Savart Law.” Physnet, MISN-0-125, February 1, 2000.

102. Trowbridge, C.W. “Electromagnetic Computing: The Way Ahead?” IEEE Transaction on Magnetics, Vol. 24, Issue: 1, January, 1988, pp. 13-18.

103. Meeker, D.C. “Finite Element Method Magnetics.” Version 4.2, October 2010. <http://www.femm.info>.

104. Patankar, S.V. “Numerical Heat Transfer and Fluid Flow.” Hemisphere Publishing Corporation, 1980.

105. Tannehill, J.C., Anderson, D.A., and Pletcher, R.H. “Computational Fluid Mechanics and Heat Transfer.” Philadelphia: Taylor and Francis, 1997.

106. Lund, J.W. “Self-Excited Stationary Whirl Orbits of a Journal in a Sleeve Bearing.” Doctoral Thesis, Rensselaer Polytechnic Institute, April, 1966.

107. Lund, J.W. “Calculation of Stiffness and Damping Properties of Gas Bearings.” Journal of Lubrication Technology, October, 1968, pp. 793-803.

108. Choy, F.K., Braun, M.J., and Hu, Y. “Nonlinear Effects in a Plain Journal Bearing: Part 1 – Analytical Study.” Journal of Tribology, Vol. 113, July, 1991, pp. 555-561.

109. Choy, F.K., Braun, M.J., and Hu, Y. “Nonlinear Effects in a Plain Journal Bearing: Part 2 – Results.” Journal of Tribology, Vol. 113, July, 1991, pp. 563-570.

110. “CIP Product Overview.” BASF Publication, March 2012. <http://www.carbonylironpowder.com>

111. “High Precision Balances iBalance 211.” My Weigh Product Manual, 2013. <http://www.myweigh.com/product/ibalance-211/>

112. “Lab-Line Viscometers Operation Manual.” Melrose Park: Lab-Line Instruments, Inc., 1990.

113. “DC Gaussmeter Model GM1-ST.” DC Gaussmeter Model GM1-ST Instructions, 2011. <http://www.trifield.com/content/dc-guassmeter-model-gm1-st/>

114. U6 User’s Guide, 2012. < http://www.labjack.com/u6>

APPENDICES

APPENDIX A

ORDER OF MAGNITUDE ANALYSIS

In 1886, Osborne Reynolds proposed the first mathematical model to solve the pressure within a journal bearing that respected the continuity of mass and momentum. Reynolds used the dominating pressure and viscous terms to reduce the Navier-Stokes and mass continuity equations to the classical Reynolds equation. Several dimensionless quantities can be used to validate those simplifying assumptions, by demonstrating the inertial and body forces are negligibly small for a given bearing design and set of operating conditions. The necessary information, for the bearing design discussed in this paper, is provided below.

$c = 0.00012m$	$O(10^{-4})$
$g = 9.81\ m/s^2$	$O(10^{1})$
$p = 10^5\ to\ 10^7\ N/m^2$	$O(10^5\ to\ 10^7)$
$R_b = 0.025m$	$O(10^{-2})$
$U = 2\pi \mathrm{R_b} \cdot \mathrm{rpm}/60\ \mathrm{m/s}$	$O(10^{-1}\ to\ 10^{1})$
$\mu = 0.28\mathrm{kg/m \cdot s}$	$O(10^{-1})$
$\rho = 3640\mathrm{kg/m^3}$	$O(10^{3})$

The first assumption that can be validated is the assumption of laminar flow. In 1923, Taylor found that vortices developed in concentric cylinders for Reynolds numbers higher than

$$\mathrm{Re} > 41.3\sqrt{R_b/c}$$

Thus, the Taylor number can be used to determine when laminar flow breaks down into turbulence which is defined as

$$Ta = \frac{\rho U^2 c^3}{R_b \mu^2} > 1705$$

Which for the bearing design discussed in this paper is equal to

$$Ta = \frac{3640 \cdot 13.1^2 \cdot 0.00012^3}{0.025 \cdot 0.28^2} = 5.51 \cdot 10^{-4}$$

This indicates that laminar flow conditions exist and the Reynolds assumption holds true.

The relative significance of the inertia and viscous terms can be determined from the Reynolds number

$$\mathrm{Re} = \frac{\rho U c}{\mu}$$

If the Navier-Stokes equations are non-dimensionalized, a modified Reynolds number is multiplied by the dominant viscous term (in the direction of rotation across the fluid film) and is often used for fluid film lubrication

$$\mathrm{Re} = \frac{\rho U c^2}{2\pi R_b \mu}$$

Which for the bearing design discussed in this paper is equal to

$$\mathrm{Re} = \frac{3640 \cdot 13.1 \cdot 0.00012^2}{2\pi \cdot 0.025 \cdot 0.28} = 1.6 \cdot 10^{-2}$$

This indicates that viscous terms dominate and the simplifying Reynolds assumption to neglect the inertia terms can be applied.

The only body forces on the lubrication are gravity and magnetic forces. The magnetic forces were discussed in the body of the text and are not repeated here. For the

gravitational forces, the Froude number provides a relative comparison to the inertial forces, which can then be compared to the Reynolds number for comparison to the dominant viscous forces.

$$Fr = \frac{U^2}{2\pi R_b g}$$

The Froude number for the bearing design discussed in this paper is equal to

$$Fr = \frac{13.1^2}{2\pi \cdot 0.025 \cdot 9.81} = 1.1 \cdot 10^3$$

This indicates that inertia terms, which were shown to be negligibly small, dominate the gravitational forces. Using the Froude number and the Reynolds number, the simplifying Reynolds assumption to neglect the body forces is proven valid.

The final term in the Navier-Stokes equations to be evaluated for significance is the pressure term. The relative importance of the pressure term can be evaluated using the Euler number which compares the pressure to the inertia, which can then be compared to the Reynolds number.

$$Eu = \frac{p}{\rho U^2}$$

The Euler number for the bearing design discussed in this paper is equal to

$$Eu = \frac{10^7}{3640 \cdot 13.1^2} = 1.6 \cdot 10^2$$

This indicates that pressure term is more significant than the inertia terms. By comparing the Euler number to the Reynolds number, it can be seen that the pressure term and viscous terms are on the same order of magnitude relative to the inertia terms. While the

viscous term is larger, the difference is not significant enough to neglect the pressure term and both terms should be included in the final equation.

Using the Taylor, Reynolds, Froude and Euler numbers, an order of magnitude analysis showed, that for the bearing design discussed in this paper, the flow in the bearing is laminar and the viscous and pressure terms dominate. Thus demonstrating the simplifying Reynolds assumptions are applicable in reducing the Navier-Stokes equations to the classical Reynolds equation.

APPENDIX B

DERIVATION OF MODIFIED REYNOLDS EQUATION

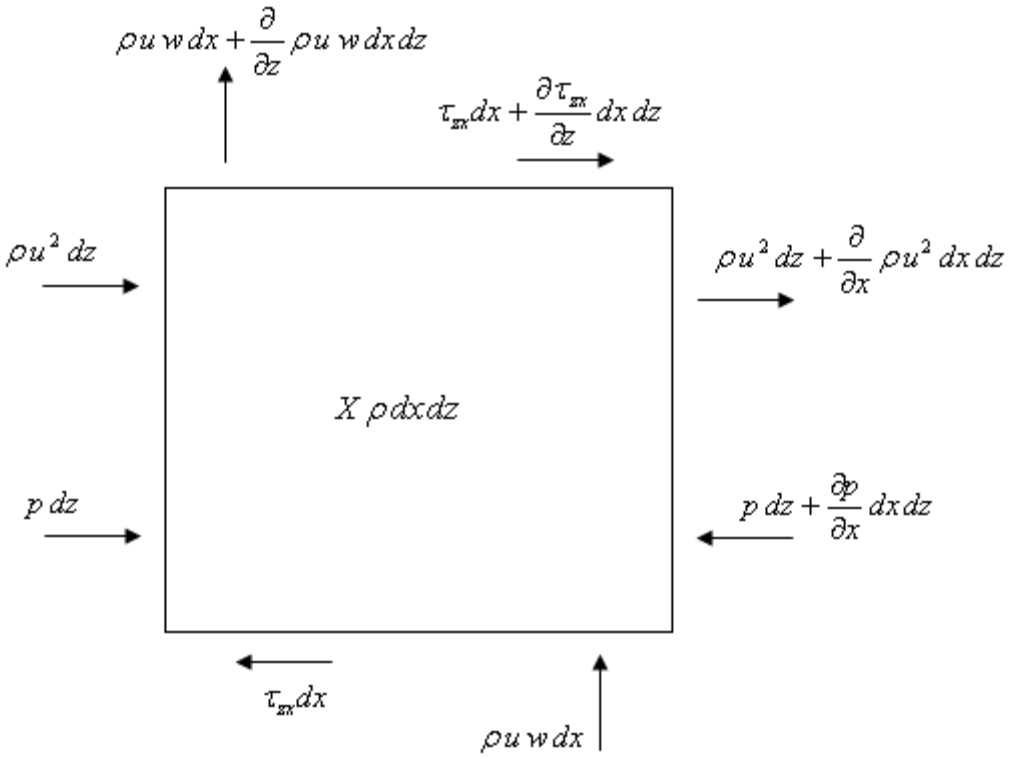

Figure B-1 Control Element for X-Direction

Starting with control element:

$$-\rho u^2\, dz + \rho u^2\, dz + \frac{\partial}{\partial x}\rho u^2\, dx\, dz - \rho u\, w\, dx + \rho u\, w\, dx + \frac{\partial}{\partial z}\rho u\, w\, dx\, dz =$$

$$X\, \rho\, dx\, dz + p\, dz - p\, dz - \frac{\partial p}{\partial x} dx\, dz - \tau_{zx} dx + \tau_{zx} dx + \frac{\partial \tau_{zx}}{\partial z} dx\, dz$$

which reduces to:

$$\rho\left(u\frac{\partial u}{\partial x}+w\frac{\partial u}{\partial z}\right)=\rho X-\frac{\partial p}{\partial x}+\frac{\partial \tau_{zx}}{\partial z}$$

Applying Reynolds assumptions the viscous and body force terms are eliminated:

$$\frac{\partial p}{\partial x}=\frac{\partial \tau_{zx}}{\partial z}$$

where for an MR fluid,

$$\tau_{zx}=H\left(|\dot{\gamma}|\right)\left(\mu\frac{\partial u}{\partial z}+\operatorname{sgn}\left(\dot{\gamma}\right)\tau_o\right)$$

$$\tau_o=f\left(x\right)$$

The expanded equation becomes:

$$\frac{\partial p}{\partial x}=\frac{\partial}{\partial z}\left[H\left(|\dot{\gamma}|\right)\left(\mu\frac{\partial u}{\partial z}+\operatorname{sgn}\left(\dot{\gamma}\right)\tau_o\right)\right]$$

Integrating across the gap twice yields:

$$\frac{\partial p}{\partial x}\frac{z^2}{2}+\left(C_1+H\left(|\dot{\gamma}|\right)\cdot\operatorname{sgn}\left(\dot{\gamma}\right)\cdot\tau_o\right)\cdot z=H\left(|\dot{\gamma}|\right)\cdot\mu\cdot u+C_2$$

Applying the boundary conditions:

$$\begin{array}{lllll} BC: & z=0 & u=U_1 & v=0 \\ & z=h & u=U_2 & v=0 \end{array}$$

$$C_1=\frac{\mu\cdot H\left(|\dot{\gamma}|\right)}{h}\left(U_2-U_1\right)+H\left(|\dot{\gamma}|\right)\cdot\operatorname{sgn}\left(\dot{\gamma}\right)\cdot\tau_o-\frac{\partial p}{\partial x}\frac{h}{2}$$

$$C_2=-\mu\cdot H\left(|\dot{\gamma}|\right)\cdot U_1$$

The final velocity equation is:

$$u=\frac{1}{2\mu\cdot H\left(|\dot{\gamma}|\right)}\frac{\partial p}{\partial x}\left(z^2-hz\right)+\frac{z}{h}\left(U_2-U_1\right)+U_1$$

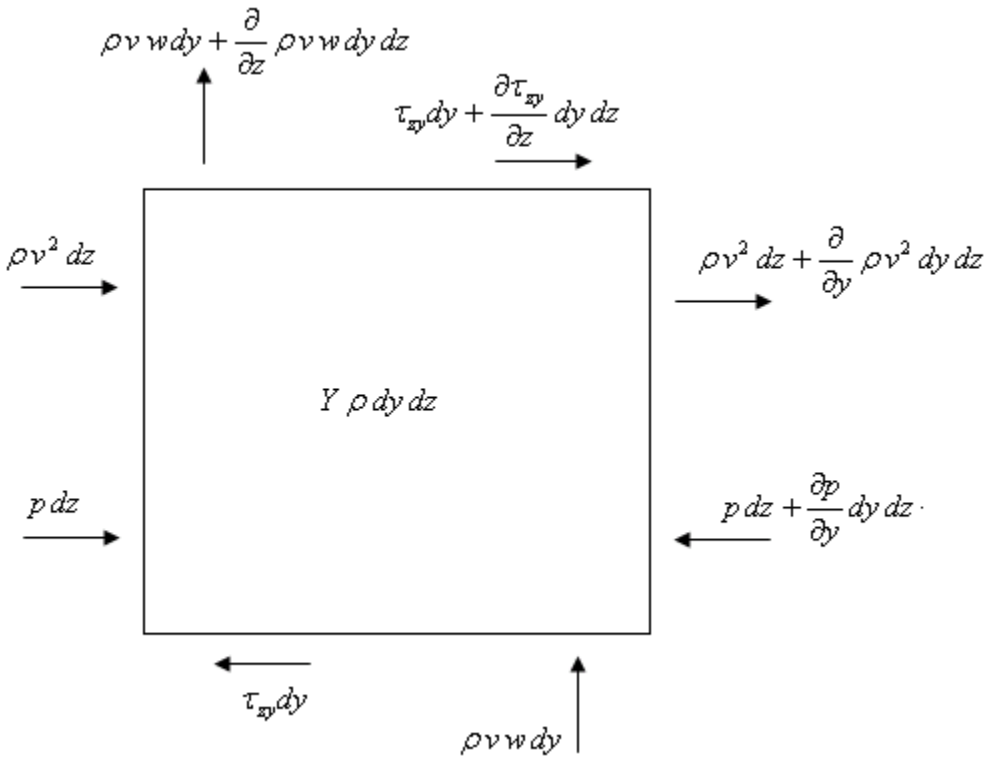

Figure B-2 Control Element for Y-Direction

Starting with control element:

$$-\rho v^2 dz + \rho v^2 dz + \frac{\partial}{\partial y} \rho v^2 dy dz - \rho v w dy + \rho v w dy + \frac{\partial}{\partial z} \rho v w dy dz =$$

$$Y \rho dy dz + p dz - p dz - \frac{\partial p}{\partial y} dy dz - \tau_{zy} dy + \tau_{zy} dy + \frac{\partial \tau_{zy}}{\partial z} dy dz$$

which reduces to:

$$\rho \left(v \frac{\partial v}{\partial y} + w \frac{\partial v}{\partial z} \right) = \rho Y - \frac{\partial p}{\partial y} + \frac{\partial \tau_{zy}}{\partial z}$$

Applying Reynolds assumptions the viscous and body force terms are eliminated:

$$\frac{\partial p}{\partial y} = \frac{\partial \tau_{zy}}{\partial z}$$

where for an MR fluid,

$$\tau_{zy} = H\left(|\dot{\gamma}|\right)\left(\mu\frac{\partial v}{\partial z} + \text{sgn}\left(\dot{\gamma}\right)\tau_o\right)$$

$$\tau_o = f\left(x\right)$$

The expanded equation becomes:

$$\frac{\partial p}{\partial y} = \frac{\partial}{\partial z}\left[H\left(|\dot{\gamma}|\right)\left(\mu\frac{\partial v}{\partial z} + \text{sgn}\left(\dot{\gamma}\right)\tau_o\right)\right]$$

Integrating across the gap twice yields:

$$\frac{\partial p}{\partial y}\frac{z^2}{2} + \left(C_3 + H\left(|\dot{\gamma}|\right)\cdot\text{sgn}\left(\dot{\gamma}\right)\cdot\tau_o\right)\cdot z = H\left(|\dot{\gamma}|\right)\cdot\mu\cdot v + C_4$$

Applying the boundary conditions:

$$\begin{array}{lllll} BC: & z = 0 & u = U_1 & v = 0 \\ & z = h & u = U_2 & v = 0 \end{array}$$

$$C_3 = H\left(|\dot{\gamma}|\right)\cdot\text{sgn}\left(\dot{\gamma}\right)\cdot\tau_o - \frac{\partial p}{\partial y}\frac{h}{2}$$

$$C_4 = 0$$

The final velocity equation is:

$$v = \frac{1}{2\mu\cdot H\left(|\dot{\gamma}|\right)}\frac{\partial p}{\partial y}\left(z^2 - hz\right)$$

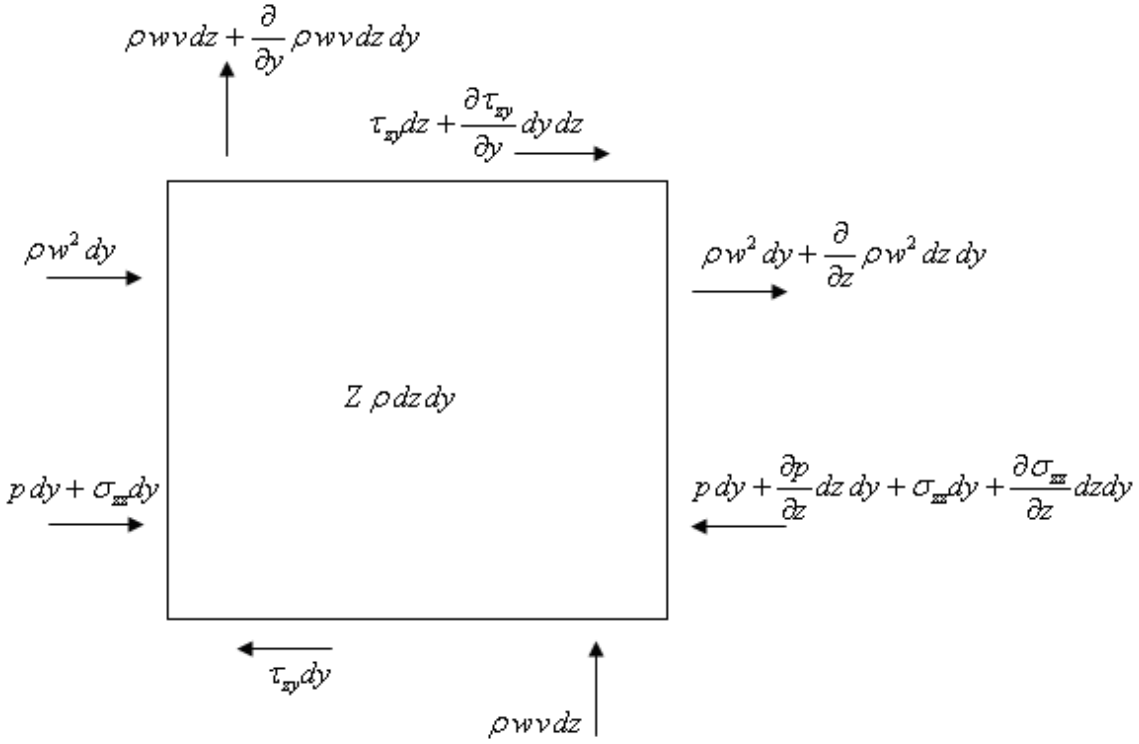

Figure B-3 Control Element for Z-Direction

Starting with an expanded control element for the lubrication inlet:

$$-\rho w^2\,dy + \rho w^2\,dy + \frac{\partial}{\partial z}\rho w^2\,dz\,dy - \rho w v\,dz + \rho w v\,dz + \frac{\partial}{\partial y}\rho w v\,dz\,dy =$$

$$Z\,\rho\,dz\,dy + p\,dy - \sigma_{zz}dy - p\,dy - \frac{\partial p}{\partial z}dz\,dy + \sigma_{zz}dy + \frac{\partial \sigma_{zz}}{\partial z}dzdy - \tau_{zy}dz + \tau_{zy}dy + \frac{\partial \tau_{zy}}{\partial y}dy\,dz$$

which reduces to:

$$\frac{\partial \rho w^2}{\partial z} + \frac{\partial \rho w v}{\partial y} = \rho Z - \frac{\partial p}{\partial z} + \frac{\partial \sigma_{zz}}{\partial z} + \frac{\partial \tau_{zy}}{\partial y}$$

Applying Reynolds assumptions the viscous and body force terms are eliminated:

$$0 = \frac{\partial}{\partial z}\left(2\mu\frac{\partial w}{\partial z}\right)$$

Integrating across the gap twice yields:

$$\mu w = C_5 \cdot z + C_6$$

Applying the boundary conditions:

$$BC: \quad z = 0 \qquad w = \frac{\partial h}{\partial t} = w$$

$$z = h \qquad w = w_{inj}(x,y) = -\frac{1}{4\mu}\frac{\partial p}{\partial z}\left(\frac{d_o^2}{4} - (x - x_i)^2 - (y - y_i)^2\right)$$

$$\left(w_{inj} = 0, \textit{ outside orifice}\right)$$

where, x_i and y_i are the circumferential and axial location of the lubrication inlet

$$C_6 = \mu w$$

$$C_5 = \frac{\mu}{h}\left(w_{inj} - w\right)$$

The final velocity equation is:

$$w = \frac{h - z}{h} w + \frac{z}{h} w_{inj}$$

Starting with the continuity equation:

$$0 = \frac{\partial \rho u}{\partial x} + \frac{\partial \rho v}{\partial y} + \frac{\partial \rho w}{\partial z}$$

Integrating across the gap:

$$\int_0^h \frac{\partial \rho w}{\partial z} = \rho w\Big|^h - \rho w\Big|_0 = \rho w_{inj} - \rho w$$

since h = f(x), use Leibniz rule for u and v:

$$\int_{A(x)}^{B(x)} \frac{\partial}{\partial x} u(x,z)dz = \frac{d}{dx}\int_{A(x)}^{B(x)} u(x,z)dz - u(x,B)\frac{dB}{dx} + u(x,A)\frac{dA}{dx}$$

$$A(x) = 0$$

$$B(x) = h(x)$$

$$\int_0^h \frac{\partial}{\partial x} \rho u dz = \frac{d}{dx}\int_0^h \rho u dz - u(x,h)\frac{d\rho h}{dx} + u(x,0)\frac{d\rho 0}{dx}$$

$$= \frac{d}{dx}\int_0^h \rho u dz - U_2$$

$$\int_0^h \frac{\partial}{\partial y} \rho v dz = \frac{d}{dy}\int_0^h \rho v dz - v(y,h)\frac{d\rho h}{dy} + v(y,0)\frac{d\rho 0}{dy}$$

$$= \frac{d}{dy}\int_0^h \rho v dz$$

Replacing back into the continuity equation yields:

$$0 = \rho w_{inj} - \rho w + \frac{d}{dx}\int_0^h \rho u dz - U_2 + \frac{d}{dy}\int_0^h \rho v dz$$

Inserting previously solved u and v velocities:

$$0 = \rho w_{inj} - \rho w + \frac{d}{dx}\int_0^h \rho\left(\frac{1}{2\mu \cdot H\left(|\dot{\gamma}|\right)}\frac{\partial p}{\partial x}\left(z^2 - hz\right) + \frac{z}{h}\left(U_2 - U_1\right) + U_1\right)dz - U_2$$
$$+ \frac{d}{dy}\int_0^h \rho\left(\frac{1}{2\mu \cdot H\left(|\dot{\gamma}|\right)}\frac{\partial p}{\partial y}\left(z^2 - hz\right)\right)dz$$

which reduces to:

$$\frac{\partial}{\partial x}\left(\frac{h^3}{\mu \cdot H\left(|\dot{\gamma}|\right)}\frac{\partial p}{\partial x}\right) + \frac{\partial}{\partial y}\left(\frac{h^3}{\mu \cdot H\left(|\dot{\gamma}|\right)}\frac{\partial p}{\partial y}\right) - \frac{3}{\mu l_o}p\left(\Im\right) = 6U_1\frac{\partial h}{\partial x} - 12\frac{\partial h}{\partial t} - \frac{3}{\mu l_o}p_{inj}\left(\Im\right)$$

Introducing a switch function for the lubrication inlet:

$$\Im(x,y) = \begin{cases} \frac{d_o^2}{4} - \left(x - x_i\right)^2 - \left(y - y_i\right)^2, & if\ \left(x - x_i\right)^2 - \left(y - y_i\right)^2 < \frac{d_o^2}{4} \\ 0, & if\ \left(x - x_i\right)^2 - \left(y - y_i\right)^2 \geq d_o^2 \end{cases}$$

APPENDIX C

SOURCE CODE

Abridged Steady State Source Code:

```
clear
format long
%%inputs%%
xi = #NUMBER#; %injection x circumferential location (m)
e_r = #NUMBER#; %eccentricity ratio
rpm = #NUMBER#; %rotational speed (rev/sec)
k_max = #NUMBER#; %max z-directional nodes
i_max = #NUMBER#; %max y-directional nodes
Pinj = #NUMBER#; %injection pressure (N/m^2)
Hn(1:i_max) = #NUMBER#; %normal magnetic field strength (A/m)
relax = #NUMBER#; %relaxation coefficient
%dimensional data
Rj = 0.025; %journal radius (m)
Rb = 0.02512; %bearing radius (m)
L = 0.060; %bearing length (m)
c = Rb - Rj; %bearing clearance (m)
e_a = e_r * c; %absolute eccentricity (m)
lo = 0.10; %feed length (m)
do = 0.005; %feed diameter (m)
yi = L/2; %injection y axial location (m)
%fluid data
mu = 0.28; %viscosity @ 40C (kg/m-s)
rho = 3640; %density (kg/m^3)
Pa = 101325; %atmospheric pressure (N/m^2)
Pc = 1; %cavitation pressure (N/m^2)
%speed data
U = 2*pi*Rj*rpm/60; %journal wall boundary velocity (m/s)
Re = rho * U * c / mu; %Reynolds number
%grid data
scaler = round(2*pi*Rj/L)*i_max;
j_max = scaler; %max x-directional nodes
dy = L/(i_max-1); %y-direction step size (m)
dx = 2*pi*Rj/(j_max-1); %x-direction step size (m)
dtheta = dx/Rj; %angular step size (rad)
%magnetic field distribution
for i = 29:33 %field between poles
    Hn(i) = abs((Hn(1)/5) * (31 - i));
end
%yield stress distribution (Pa)
if max(Hn) == 0
```

```
    To(1:i_max,1:j_max) = 0;
else
for j=1:j_max
for i=1:i_max
    To(i,j) = -0.000000000002474*Hn(i)^3 - 0.000000977670287*Hn(i)^2 +
0.561953109679834*Hn(i) + 355.824281459907;
end
end
end
%create y array (m)
y(1) = 0;
y(i_max) = L;
for i=2:i_max-1
    y(i) = y(i-1) + dy;
end
%create x array (m)
x(1) = 0;
x(j_max) = 2*pi*Rj;
for j=2:j_max-1
    x(j) = x(j-1) + dx;
end
%create angle array (rad)
theta = x/Rj;
%create h array (m)
for j=1:j_max
    h(j) = c * (1 + e_r * cos(x(j)/Rj));
end
h(j_max) = h(1);
%%%numerical solution%%%
P(1:i_max,1:j_max) = Pa; %initial pressure
Pnew(1:i_max,1:j_max) = Pa; %initial replacement pressure
u(1:i_max,1:j_max,1:k_max) = 0; %initial x velocity
u(1:i_max,1:j_max,1) = U; %initial x velocity at boundary
v(1:i_max,1:j_max,1:k_max) = 0; %initial y velocity
g(1:i_max,1:j_max) = 1.0; %initial cavitation switch function
H(1:i_max,1:j_max) = 1.0; %initial shear switch function
Hold(1:i_max,1:j_max,1:old) = 1.0; %initial shear switch function
error_max = 100; %initial error
counter = 0; %initial iteration counter
while (error_max > 0.2) || (counter < 1000) %iteration until max error
reached
    %%%Calculate pressures
    for i=2:i_max-1 %solve pressure at boundary (x = 0 = 2*pi*Rj)
        j = 1;
      %boundary at feed
      circle = (x(j)-xi)^2 + (y(i)-yi)^2;
        if circle <= do^2/4
            F(i,j) = do^2/4 - (x(j)-xi)^2 - (y(i)-yi)^2;
        else
            F(i,j)=0;
        end
        if circle >= do^2
            F(i,j) = 0;
        end
        g_sum = g(i+1,j) + g(i-1,j) + g(i,j+1) + g(i,j_max-1);
```

```
        if g_sum < 1
            Pnew(i,j) = 1.0;
        else
        An(i,j)= H(i+1,j) * g(i+1,j) * dx / mu / dy * h(j)^3;
        As(i,j)= H(i-1,j) * g(i-1,j) * dx / mu / dy * h(j)^3;
        Ae(i,j)= H(i,j+1) * g(i,j+1) * dy / mu / dx * ((h(j) + h(j+1))
/ 2)^3;
        Aw(i,j)= H(i,j_max-1) * g(i,j_max-1) * dy / mu / dx * ((h(j) +
h(j_max-1)) / 2)^3;
        Af(i,j)= 3 * F(i,j) * dx * dy / mu / lo;
        Bs(i,j) = 6 * U * dy * (h(j+1) - h(j_max-1)) - 3 * F(i,j) *
Pinj * dx * dy / mu / lo;
        Ap(i,j) = An(i,j) + As(i,j) + Ae(i,j) + Aw(i,j) + Af(i,j);
        Pnew(i,j) = (An(i,j)*Pnew(i+1,j) + As(i,j)*Pnew(i-1,j) +
Ae(i,j)*Pnew(i,j+1) + Aw(i,j)*Pnew(i,j_max-1) - Bs(i,j)) / (Ap(i,j));
        end
        if Pnew(i,j) < 1.0
            Pnew(i,j) = 1.0;
        end
        %BC x = 0 & 2*pi*R
        Pnew(i,j_max) = Pnew(i,1);
    end
    for j=2:j_max-1 %solve pressure circumferential direction
    for i=2:i_max-1 %solve pressure axial direction
      %boundary at feed
      circle = (x(j)-xi)^2 + (y(i)-yi)^2;
        if circle <= do^2/4
            F(i,j) = do^2/4 - (x(j)-xi)^2 - (y(i)-yi)^2;
        else
            F(i,j)=0;
        end
        if circle >= do^2
            F(i,j) = 0;
        end
        g_sum = g(i+1,j) + g(i-1,j) + g(i,j+1) + g(i,j-1);
        if g_sum < 1
            Pnew(i,j) = 1.0;
        else
        An(i,j)= H(i+1,j) * g(i+1,j) * dx / mu / dy * h(j)^3;
        As(i,j)= H(i-1,j) * g(i-1,j) * dx / mu / dy * h(j)^3;
        Ae(i,j)= H(i,j+1) * g(i,j+1) * dy / mu / dx * ((h(j) + h(j+1))
/ 2)^3;
        Aw(i,j)= H(i,j-1) * g(i,j-1) * dy / mu / dx * ((h(j) + h(j-1))
/ 2)^3;
        Af(i,j)= 3 * F(i,j) * dx * dy / mu / lo;
        Bs(i,j) = 6 * U * dy * (h(j+1) - h(j-1)) - 3 * F(i,j) * Pinj *
dx * dy / mu / lo;
        Ap(i,j) = An(i,j) + As(i,j) + Ae(i,j) + Aw(i,j) + Af(i,j);
        Pnew(i,j) = (An(i,j)*Pnew(i+1,j) + As(i,j)*Pnew(i-1,j) +
Ae(i,j)*Pnew(i,j+1) + Aw(i,j)*Pnew(i,j-1) - Bs(i,j)) / (Ap(i,j));
        end
        if Pnew(i,j) < 1.0
            Pnew(i,j) = 1.0;
        end
    end
```

```
    end
    %%%reset for next iteration step
    for j=1:j_max
    for i=1:i_max
        if Pnew(i,j) <= 1
            g(i,j) = 0;
        else
            g(i,j) = 1;
        end
    end
    end
    P = P + relax * (Pnew - P);
    %%%calculate error
    error_a = max(max(Pnew - P)); %abs error
    Pnew = P;
    %%%calculate velocities
    for i=2:i_max-1 %solve velocity at boundary (x = 0 = 2*pi*Rj)
    for k=2:k_max-1 %solve velocity at boundary (x = 0 = 2*pi*Rj)
        j=1;
        z = (h(j) / (k_max-1)) * (k-1);
        u(i,j,k) = U * (1 - z / h(j)) + 1 / 4 / mu * (z^2 - h(j) * z) *
(Pnew(i,j+1) - Pnew(i,j_max-1)) / dx;
        v(i,j,k) = sign(L/2 - y(i) + dy*0.001) * 1 / 4 / mu * (z^2 -
h(j) * z) * (Pnew(i+1,j) - Pnew(i-1,j)) / dy;
        u(i,j_max,k) = u(i,1,k);
        v(i,j_max,k) = v(i,1,k);
    end
    end
    for j=2:j_max-1 %solve velocity circumferential direction
    for i=2:i_max-1 %solve velocity axial direction
    for k=2:k_max-1 %solve velocity radial direction
        z = (h(j) / (k_max-1)) * (k-1);
        u(i,j,k) = U * (1 - z / h(j)) + 1 / 4 / mu * (z^2 - h(j) * z) *
(Pnew(i,j+1) - Pnew(i,j-1)) / dx;
        v(i,j,k) = sign(L/2 - y(i) + dy*0.001) * 1 / 4 / mu * (z^2 -
h(j) * z) * (Pnew(i+1,j) - Pnew(i-1,j)) / dy;
    end
    end
    end
    %%%calculate velocity gradients
    for j=1:j_max
    for i=1:i_max
    for k=2:k_max-1
        dz = (h(j) / (k_max-1));
        du(i,j,k) = (u(i,j,k+1) - u(i,j,k-1)) / dz / 2;
        dv(i,j,k) = (v(i,j,k+1) - v(i,j,k-1)) / dz / 2;
        Tau(i,j,k) = mu * sqrt(du(i,j,k)^2 + dv(i,j,k)^2);
    end
    end
    end
    Tau(1,1:j_max,2:k_max-1) = Tau(2,1:j_max,2:k_max-1);
    Tau(i_max,1:j_max,2:k_max-1) = Tau(i_max-1,1:j_max,2:k_max-1);
%%%calculate shear switch function
    Hold(:,:,1) = H; %previous shear switch function
    if counter > 10
```

```
    %determine if yield stress is met
    for j=1:j_max
    for i=2:i_max-1
    for k = 2:k_max-1
      ...
    end
    end
    end
    %fraction across gap that yield stress is met
    for j=1:j_max
    for i=2:i_max-1
      ...
    end
    end
    end
counter = counter + 1 %display number of iterations
end
%%%calculate load
for j=1:j_max-1 %sum axial pressure
    Py(j) = (sum(Pnew(:,j)) - 2*Pa);
end
for j=1:j_max-1 %sum circumferential pressure
    Pxsin(j) = Py(j) * sin(theta(j));
    Pxcos(j) = Py(j) * cos(theta(j));
end
Ft = -sum(Pxcos) * Rj * dy * dtheta %tangential force
Fn = sum(Pxsin) * Rj * dy * dtheta %normal force
W = sqrt(Fn^2 + Ft^2) %Load (N)
Phi = asin(Fn/W) * 180 / pi %attitude angle (deg)
```

Abridged Dynamic Response Source Code:

```
clear
format long
%%inputs%%
xi = #NUMBER#; %injection x circumferential location (m)
e_r = #NUMBER#; %eccentricity ratio
rpm = #NUMBER#; %rotational speed (rev/sec)
k_max = #NUMBER#; %max z-directional nodes
i_max = #NUMBER#; %max y-directional nodes
Pinj = #NUMBER#; %injection pressure (N/m^2)
Hn(1:i_max) = #NUMBER#; %normal magnetic field strength (A/m)
relax = #NUMBER#; %relaxation coefficient
%dimensional data
Rj = 0.025; %journal radius (m)
Rb = 0.02512; %bearing radius (m)
L = 0.060; %bearing length (m)
c = Rb - Rj; %bearing clearance (m)
e_a = e_r * c; %absolute eccentricity (m)
lo = 0.10; %feed length (m)
do = 0.005; %feed diameter (m)
yi = L/2; %injection y axial location (m)
%fluid data
mu = 0.28; %viscosity @ 40C (kg/m-s)
rho = 3640; %density (kg/m^3)
Pa = 101325; %atmospheric pressure (N/m^2)
Pc = 1; %cavitation pressure (N/m^2)
%speed data
U = 2*pi*Rj*rpm/60; %journal wall boundary velocity (m/s)
Re = rho * U * c / mu; %Reynolds number
%grid data
scaler = round(2*pi*Rj/L)*i_max;
j_max = scaler; %max x-directional nodes
dy = L/(i_max-1); %y-direction step size (m)
dx = 2*pi*Rj/(j_max-1); %x-direction step size (m)
dtheta = dx/Rj; %angular step size (rad)
%magnetic field distribution
for i = 29:33 %field between poles
    Hn(i) = abs((Hn(1)/5) * (31 - i));
end
%yield stress distribution (Pa)
if max(Hn) == 0
    To(1:i_max,1:j_max) = 0;
else
for j=1:j_max
for i=1:i_max
    To(i,j) = -0.000000000002474*Hn(i)^3 - 0.000000977670287*Hn(i)^2 +
0.561953109679834*Hn(i) + 355.824281459907;
end
end
end
%create y array (m)
y(1) = 0;
y(i_max) = L;
```

```
for i=2:i_max-1
    y(i) = y(i-1) + dy;
end
%create x array (m)
x(1) = 0;
x(j_max) = 2*pi*Rj;
for j=2:j_max-1
    x(j) = x(j-1) + dx;
end
%create angle array (rad)
theta = x/Rj;
%create h array (m)
for j=1:j_max
    h(j) = c * (1 + e_r * cos(x(j)/Rj));
end
h(j_max) = h(1);
%%%numerical solution%%%
%%initial solution to
Po(1:i_max,1:j_max) = Pa; %initial pressure
Ponew(1:i_max,1:j_max) = Pa; %initial replacement pressure
u(1:i_max,1:j_max,1:k_max) = 0; %initial x velocity
u(1:i_max,1:j_max,1) = U; %initial x velocity at boundary
v(1:i_max,1:j_max,1:k_max) = 0; %initial y velocity
g(1:i_max,1:j_max) = 1.0; %initial cavitation switch function
H(1:i_max,1:j_max) = 1.0; %initial shear switch function
Hold(1:i_max,1:j_max,1:old) = 1.0; %initial shear switch function
error_max = 100; %initial error
counter = 0; %initial iteration counter
while (error_max > 0.2) || (counter < 1000) %iteration until max error
reached
    %%%Calculate pressures
    for i=2:i_max-1 %solve pressure at boundary (x = 0 = 2*pi*Rj)
        j = 1;
      %boundary at feed
      circle = (x(j)-xi)^2 + (y(i)-yi)^2;
        if circle <= do^2/4
            F(i,j) = do^2/4 - (x(j)-xi)^2 - (y(i)-yi)^2;
        else
            F(i,j)=0;
        end
        if circle >= do^2
            F(i,j) = 0;
        end
        g_sum = g(i+1,j) + g(i-1,j) + g(i,j+1) + g(i,j_max-1);
        if g_sum < 1
            Ponew(i,j) = 1.0;
        else
        An(i,j)= H(i+1,j) * g(i+1,j) * dx / mu / dy * h(j)^3;
        As(i,j)= H(i-1,j) * g(i-1,j) * dx / mu / dy * h(j)^3;
        Ae(i,j)= H(i,j+1) * g(i,j+1) * dy / mu / dx * ((h(j) + h(j+1))
/ 2)^3;
        Aw(i,j)= H(i,j_max-1) * g(i,j_max-1) * dy / mu / dx * ((h(j) +
h(j_max-1)) / 2)^3;
        Af(i,j)= 3 * F(i,j) * dx * dy / mu / lo;
```

```
        Bs(i,j) = 6 * U * dy * (h(j+1) - h(j_max-1)) - 3 * F(i,j) *
Pinj * dx * dy / mu / lo;
        Ap(i,j) = An(i,j) + As(i,j) + Ae(i,j) + Aw(i,j) + Af(i,j);
        Ponew(i,j) = (An(i,j)*Ponew(i+1,j) + As(i,j)*Ponew(i-1,j) +
Ae(i,j)*Ponew(i,j+1) + Aw(i,j)*Ponew(i,j_max-1) - Bs(i,j)) / (Ap(i,j));
        end
        if Ponew(i,j) < 1.0
            Ponew(i,j) = 1.0;
        end
        %BC x = 0 & 2*pi*R
        Ponew(i,j_max) = Ponew(i,1);
    end
    for j=2:j_max-1 %solve pressure circumferential direction
    for i=2:i_max-1 %solve pressure axial direction
      %boundary at feed
      circle = (x(j)-xi)^2 + (y(i)-yi)^2;
        if circle <= do^2/4
            F(i,j) = do^2/4 - (x(j)-xi)^2 - (y(i)-yi)^2;
        else
            F(i,j)=0;
        end
        if circle >= do^2
            F(i,j) = 0;
        end
        g_sum = g(i+1,j) + g(i-1,j) + g(i,j+1) + g(i,j-1);
        if g_sum < 1
            Ponew(i,j) = 1.0;
        else
        An(i,j)= H(i+1,j) * g(i+1,j) * dx / mu / dy * h(j)^3;
        As(i,j)= H(i-1,j) * g(i-1,j) * dx / mu / dy * h(j)^3;
        Ae(i,j)= H(i,j+1) * g(i,j+1) * dy / mu / dx * ((h(j) + h(j+1))
/ 2)^3;
        Aw(i,j)= H(i,j-1) * g(i,j-1) * dy / mu / dx * ((h(j) + h(j-1))
/ 2)^3;
        Af(i,j)= 3 * F(i,j) * dx * dy / mu / lo;
        Bs(i,j) = 6 * U * dy * (h(j+1) - h(j-1)) - 3 * F(i,j) * Pinj *
dx * dy / mu / lo;
        Ap(i,j) = An(i,j) + As(i,j) + Ae(i,j) + Aw(i,j) + Af(i,j);
        Ponew(i,j) = (An(i,j)*Ponew(i+1,j) + As(i,j)*Ponew(i-1,j) +
Ae(i,j)*Ponew(i,j+1) + Aw(i,j)*Ponew(i,j-1) - Bs(i,j)) / (Ap(i,j));
        end
        if Ponew(i,j) < 1.0
            Ponew(i,j) = 1.0;
        end
    end
    end
    %%%reset for next iteration step
    for j=1:j_max
    for i=1:i_max
        if Ponew(i,j) <= 1
            g(i,j) = 0;
        else
            g(i,j) = 1;
        end
    end
```

```
    end
    Po = Po + relax * (Ponew - Po);
    %%%calculate error
    error_a = max(max(Ponew - Po)); %abs error
    Ponew = Po;
    %%%calculate velocities
    for i=2:i_max-1 %solve velocity at boundary (x = 0 = 2*pi*Rj)
    for k=2:k_max-1 %solve velocity at boundary (x = 0 = 2*pi*Rj)
        j=1;
        z = (h(j) / (k_max-1)) * (k-1);
        u(i,j,k) = U * (1 - z / h(j)) + 1 / 4 / mu * (z^2 - h(j) * z) *
(Ponew(i,j+1) - Ponew(i,j_max-1)) / dx;
        v(i,j,k) = sign(L/2 - y(i) + dy*0.001) * 1 / 4 / mu * (z^2 -
h(j) * z) * (Ponew(i+1,j) - Ponew(i-1,j)) / dy;
        u(i,j_max,k) = u(i,1,k);
        v(i,j_max,k) = v(i,1,k);
    end
    end
    for j=2:j_max-1 %solve velocity circumferential direction
    for i=2:i_max-1 %solve velocity axial direction
    for k=2:k_max-1 %solve velocity radial direction
        z = (h(j) / (k_max-1)) * (k-1);
        u(i,j,k) = U * (1 - z / h(j)) + 1 / 4 / mu * (z^2 - h(j) * z) *
(Ponew(i,j+1) - Ponew(i,j-1)) / dx;
        v(i,j,k) = sign(L/2 - y(i) + dy*0.001) * 1 / 4 / mu * (z^2 -
h(j) * z) * (Ponew(i+1,j) - Ponew(i-1,j)) / dy;
    end
    end
    end
    %%%calculate velocity gradients
    for j=1:j_max
    for i=1:i_max
    for k=2:k_max-1
        dz = (h(j) / (k_max-1));
        du(i,j,k) = (u(i,j,k+1) - u(i,j,k-1)) / dz / 2;
        dv(i,j,k) = (v(i,j,k+1) - v(i,j,k-1)) / dz / 2;
        Tau(i,j,k) = mu * sqrt(du(i,j,k)^2 + dv(i,j,k)^2);
    end
    end
    end
    Tau(1,1:j_max,2:k_max-1) = Tau(2,1:j_max,2:k_max-1);
    Tau(i_max,1:j_max,2:k_max-1) = Tau(i_max-1,1:j_max,2:k_max-1);
%%%calculate shear switch function
    Hold(:,:,1) = H; %previous shear switch function
    if counter > 10
    %determine if yield stress is met
    for j=1:j_max
    for i=2:i_max-1
    for k = 2:k_max-1
      ...
    end
    end
    end
    %fraction across gap that yield stress is met
    for j=1:j_max
```

```
    for i=2:i_max-1
      ...
    end
    end
    end
counter = counter + 1; %display number of iterations
end%end pressure while

%%solution dx
Px(1:i_max,1:j_max) = 0; %initial pressure
Pxnew(1:i_max,1:j_max) = 0; %initial replacement pressure
u(1:i_max,1:j_max,1:k_max) = 0; %initial x velocity
u(1:i_max,1:j_max,1) = U; %initial x velocity at boundary
v(1:i_max,1:j_max,1:k_max) = 0; %initial y velocity
g(1:i_max,1:j_max) = 1.0; %initial cavitation switch function
H(1:i_max,1:j_max) = 1.0; %initial shear switch function
Hold(1:i_max,1:j_max,1:old) = 1.0; %initial shear switch function
error_max = 100; %initial error
counter = 0; %initial iteration counter
while (error_max > 0.2) || (counter < 1000) %iteration until max error
reached
    %%%Calculate pressures
    for i=2:i_max-1 %solve pressure at boundary (x = 0 = 2*pi*Rj)
        j = 1;
      %boundary at feed
      circle = (x(j)-xi)^2 + (y(i)-yi)^2;
        if circle <= do^2/4
            F(i,j) = do^2/4 - (x(j)-xi)^2 - (y(i)-yi)^2;
        else
            F(i,j)=0;
        end
        if circle >= do^2
            F(i,j) = 0;
        end
        g_sum = g(i+1,j) + g(i-1,j) + g(i,j+1) + g(i,j_max-1);
        if g_sum < 1
            Pxnew(i,j) = 1.0;
        else
        An(i,j)= H(i+1,j) * g(i+1,j) * dx / mu / dy * h(j)^3;
        As(i,j)= H(i-1,j) * g(i-1,j) * dx / mu / dy * h(j)^3;
        Ae(i,j)= H(i,j+1) * g(i,j+1) * dy / mu / dx * ((h(j) + h(j+1))
/ 2)^3;
        Aw(i,j)= H(i,j_max-1) * g(i,j_max-1) * dy / mu / dx * ((h(j) +
h(j_max-1)) / 2)^3;
        Af(i,j)= 3 * F(i,j) * dx * dy / mu / lo;
        Bs(i,j) = 6 * U * dy * (cos(x(j+1)/Rj) - cos(x(j_max-1)/Rj)) -
3 * Ae(i,j) / ((h(j) + h(j+1)) / 2) * cos(x(j+1)/Rj) * (Ponew(i,j+1) -
Ponew(i,j)) + 3 * Aw(i,j) / ((h(j) + h(j_max-1)) / 2) * cos(x(j_max-
1)/Rj) * (Ponew(i,j) - Ponew(i,j_max-1)) - 3 * An(i,j) / h(j) *
cos(x(j)/Rj) * (Ponew(i+1,j) - Ponew(i,j)) + 3 * As(i,j) / h(j) *
cos(x(j)/Rj) * (Ponew(i,j) - Ponew(i-1,j));
        Ap(i,j) = An(i,j) + As(i,j) + Ae(i,j) + Aw(i,j) + Af(i,j);
        Pxnew(i,j) = (An(i,j)*Pxnew(i+1,j) + As(i,j)*Pxnew(i-1,j) +
Ae(i,j)*Pxnew(i,j+1) + Aw(i,j)*Pxnew(i,j_max-1) - Bs(i,j)) / (Ap(i,j));
        end
```

```
        if Pxnew(i,j) < 1.0
            Pxnew(i,j) = 0;
        end
        %BC x = 0 & 2*pi*R
        Pxnew(i,j_max) = Pxnew(i,1);
    end
    for j=2:j_max-1 %solve pressure circumferential direction
    for i=2:i_max-1 %solve pressure axial direction
      %boundary at feed
      circle = (x(j)-xi)^2 + (y(i)-yi)^2;
        if circle <= do^2/4
            F(i,j) = do^2/4 - (x(j)-xi)^2 - (y(i)-yi)^2;
        else
            F(i,j)=0;
        end
        if circle >= do^2
            F(i,j) = 0;
        end
        g_sum = g(i+1,j) + g(i-1,j) + g(i,j+1) + g(i,j-1);
        if g_sum < 1
            Pxnew(i,j) = 1.0;
        else
        An(i,j)= H(i+1,j) * g(i+1,j) * dx / mu / dy * h(j)^3;
        As(i,j)= H(i-1,j) * g(i-1,j) * dx / mu / dy * h(j)^3;
        Ae(i,j)= H(i,j+1) * g(i,j+1) * dy / mu / dx * ((h(j) + h(j+1))
/ 2)^3;
        Aw(i,j)= H(i,j-1) * g(i,j-1) * dy / mu / dx * ((h(j) + h(j-1))
/ 2)^3;
        Af(i,j)= 3 * F(i,j) * dx * dy / mu / lo;
        Bs(i,j) = 6 * U * dy * (cos(x(j+1)/Rj) - cos(x(j-1)/Rj)) - 3 *
Ae(i,j) / ((h(j) + h(j+1)) / 2) * cos(x(j+1)/Rj) * (Ponew(i,j+1) -
Ponew(i,j)) + 3 * Aw(i,j) / ((h(j) + h(j-1)) / 2) * cos(x(j-1)/Rj) *
(Ponew(i,j) - Ponew(i,j-1)) - 3 * An(i,j) / h(j) * cos(x(j)/Rj) *
(Ponew(i+1,j) - Ponew(i,j)) + 3 * As(i,j) / h(j) * cos(x(j)/Rj) *
(Ponew(i,j) - Ponew(i-1,j));
        Ap(i,j) = An(i,j) + As(i,j) + Ae(i,j) + Aw(i,j) + Af(i,j);
        Pxnew(i,j) = (An(i,j)*Pxnew(i+1,j) + As(i,j)*Pxnew(i-1,j) +
Ae(i,j)*Pxnew(i,j+1) + Aw(i,j)*Pxnew(i,j-1) - Bs(i,j)) / (Ap(i,j));
        end
        if Pxnew(i,j) < 1.0
            Pxnew(i,j) = 0;
        end
    end
    end
    %%%reset for next iteration step
    for j=1:j_max
    for i=1:i_max
        if (0.1 * e_a * Pxnew(i,j) + Ponew(i,j)) < 0
            g(i,j) = 0;
        else
            g(i,j) = 1;
        end
    end
    end
    Px = Px + relax * (Pxnew - Px);
```

```
    %%%calculate error
    error_a = max(max(Pxnew - Px)); %abs error
    Pxnew = Px;
    %%%calculate velocities
    for i=2:i_max-1 %solve velocity at boundary (x = 0 = 2*pi*Rj)
    for k=2:k_max-1 %solve velocity at boundary (x = 0 = 2*pi*Rj)
        j=1;
        z = (h(j) / (k_max-1)) * (k-1);
        u(i,j,k) = U * (1 - z / h(j)) + 1 / 4 / mu * (z^2 - h(j) * z) *
(Pxnew(i,j+1) - Pxnew(i,j_max-1)) / dx;
        v(i,j,k) = sign(L/2 - y(i) + dy*0.001) * 1 / 4 / mu * (z^2 -
h(j) * z) * (Pxnew(i+1,j) - Pxnew(i-1,j)) / dy;
        u(i,j_max,k) = u(i,1,k);
        v(i,j_max,k) = v(i,1,k);
    end
    end
    for j=2:j_max-1 %solve velocity circumferential direction
    for i=2:i_max-1 %solve velocity axial direction
    for k=2:k_max-1 %solve velocity radial direction
        z = (h(j) / (k_max-1)) * (k-1);
        u(i,j,k) = U * (1 - z / h(j)) + 1 / 4 / mu * (z^2 - h(j) * z) *
(Pxnew(i,j+1) - Pxnew(i,j-1)) / dx;
        v(i,j,k) = sign(L/2 - y(i) + dy*0.001) * 1 / 4 / mu * (z^2 -
h(j) * z) * (Pxnew(i+1,j) - Pxnew(i-1,j)) / dy;
    end
    end
    end
    %%%calculate velocity gradients
    for j=1:j_max
    for i=1:i_max
    for k=2:k_max-1
        dz = (h(j) / (k_max-1));
        du(i,j,k) = (u(i,j,k+1) - u(i,j,k-1)) / dz / 2;
        dv(i,j,k) = (v(i,j,k+1) - v(i,j,k-1)) / dz / 2;
        Tau(i,j,k) = mu * sqrt(du(i,j,k)^2 + dv(i,j,k)^2);
    end
    end
    end
    Tau(1,1:j_max,2:k_max-1) = Tau(2,1:j_max,2:k_max-1);
    Tau(i_max,1:j_max,2:k_max-1) = Tau(i_max-1,1:j_max,2:k_max-1);
%%%calculate shear switch function
Hold(:,:,1) = H; %previous shear switch function
    if counter > 10
    %determine if yield stress is met
    for j=1:j_max
    for i=2:i_max-1
    for k = 2:k_max-1
      ...
    end
    end
    end
    %fraction across gap that yield stress is met
    for j=1:j_max
    for i=2:i_max-1
      ...
```

```
    end
    end
    end
counter = counter + 1; %display number of iterations
end %%end pressure while

%%solution dz
Pz(1:i_max,1:j_max) = 0; %initial presssure
Pznew(1:i_max,1:j_max) = 0; %initial replacement presssure
u(1:i_max,1:j_max,1:k_max) = 0; %initial x velocity
u(1:i_max,1:j_max,1) = U; %initial x velocity at boundary
v(1:i_max,1:j_max,1:k_max) = 0; %initial y velocity
g(1:i_max,1:j_max) = 1.0; %initial cavitation switch function
H(1:i_max,1:j_max) = 1.0; %initial shear switch function
Hold(1:i_max,1:j_max,1:old) = 1.0; %initial shear switch function
error_max = 100; %initial error
counter = 0; %initial iteration counter
while (error_max > 0.2) || (counter < 1000) %iteration until max error
reached
    %%%Calculate pressures
    for i=2:i_max-1 %solve pressure at boundary (x = 0 = 2*pi*Rj)
        j = 1;
      %boundary at feed
      circle = (x(j)-xi)^2 + (y(i)-yi)^2;
        if circle <= do^2/4
            F(i,j) = do^2/4 - (x(j)-xi)^2 - (y(i)-yi)^2;
        else
            F(i,j)=0;
        end
        if circle >= do^2
            F(i,j) = 0;
        end
        g_sum = g(i+1,j) + g(i-1,j) + g(i,j+1) + g(i,j_max-1);
        if g_sum < 1
            Pznew(i,j) = 1.0;
        else
        An(i,j)= H(i+1,j) * g(i+1,j) * dx / mu / dy * h(j)^3;
        As(i,j)= H(i-1,j) * g(i-1,j) * dx / mu / dy * h(j)^3;
        Ae(i,j)= H(i,j+1) * g(i,j+1) * dy / mu / dx * ((h(j) + h(j+1))
/ 2)^3;
        Aw(i,j)= H(i,j_max-1) * g(i,j_max-1) * dy / mu / dx * ((h(j) +
h(j_max-1)) / 2)^3;
        Af(i,j)= 3 * F(i,j) * dx * dy / mu / lo;
        Bs(i,j) = 6 * U * dy * (sin(x(j+1)/Rj) - sin(x(j_max-1)/Rj)) -
3 * Ae(i,j) / ((h(j) + h(j+1)) / 2) * sin(x(j+1)/Rj) * (Ponew(i,j+1) -
Ponew(i,j)) + 3 * Aw(i,j) / ((h(j) + h(j_max-1)) / 2) * sin(x(j_max-
1)/Rj) * (Ponew(i,j) - Ponew(i,j_max-1)) - 3 * An(i,j) / h(j) *
sin(x(j)/Rj) * (Ponew(i+1,j) - Ponew(i,j)) + 3 * As(i,j) / h(j) *
sin(x(j)/Rj) * (Ponew(i,j) - Ponew(i-1,j));
        Ap(i,j) = An(i,j) + As(i,j) + Ae(i,j) + Aw(i,j) + Af(i,j);
        Pznew(i,j) = (An(i,j)*Pznew(i+1,j) + As(i,j)*Pznew(i-1,j) +
Ae(i,j)*Pznew(i,j+1) + Aw(i,j)*Pznew(i,j_max-1) - Bs(i,j)) / (Ap(i,j));
        end
        if Pznew(i,j) < 1.0
            Pznew(i,j) = 0;
```

```
        end
        %BC x = 0 & 2*pi*R
        Pznew(i,j_max) = Pznew(i,1);
    end
    for j=2:j_max-1 %solve pressure circumferential direction
    for i=2:i_max-1 %solve pressure axial direction
      %boundary at feed
      circle = (x(j)-xi)^2 + (y(i)-yi)^2;
        if circle <= do^2/4
            F(i,j) = do^2/4 - (x(j)-xi)^2 - (y(i)-yi)^2;
        else
            F(i,j)=0;
        end
        if circle >= do^2
            F(i,j) = 0;
        end
        g_sum = g(i+1,j) + g(i-1,j) + g(i,j+1) + g(i,j-1);
        if g_sum < 1
            Pznew(i,j) = 1.0;
        else
        An(i,j)= H(i+1,j) * g(i+1,j) * dx / mu / dy * h(j)^3;
        As(i,j)= H(i-1,j) * g(i-1,j) * dx / mu / dy * h(j)^3;
        Ae(i,j)= H(i,j+1) * g(i,j+1) * dy / mu / dx * ((h(j) + h(j+1))
/ 2)^3;
        Aw(i,j)= H(i,j-1) * g(i,j-1) * dy / mu / dx * ((h(j) + h(j-1))
/ 2)^3;
        Af(i,j)= 3 * F(i,j) * dx * dy / mu / lo;
        Bs(i,j) = 6 * U * dy * (sin(x(j+1)/Rj) - sin(x(j-1)/Rj)) - 3 *
Ae(i,j) / ((h(j) + h(j+1)) / 2) * sin(x(j+1)/Rj) * (Ponew(i,j+1) -
Ponew(i,j)) + 3 * Aw(i,j) / ((h(j) + h(j-1)) / 2) * sin(x(j-1)/Rj) *
(Ponew(i,j) - Ponew(i,j-1)) - 3 * An(i,j) / h(j) * sin(x(j)/Rj) *
(Ponew(i+1,j) - Ponew(i,j)) + 3 * As(i,j) / h(j) * sin(x(j)/Rj) *
(Ponew(i,j) - Ponew(i-1,j));
        Ap(i,j) = An(i,j) + As(i,j) + Ae(i,j) + Aw(i,j) + Af(i,j);
        Pznew(i,j) = (An(i,j)*Pznew(i+1,j) + As(i,j)*Pznew(i-1,j) +
Ae(i,j)*Pznew(i,j+1) + Aw(i,j)*Pznew(i,j-1) - Bs(i,j)) / (Ap(i,j));
        end
        if Pznew(i,j) < 1.0
            Pznew(i,j) = 0;
        end
    end
    end
    %%%reset for next iteration step
    for j=1:j_max
    for i=1:i_max
        if (0.1 * e_a * Pznew(i,j) + Ponew(i,j)) < 0
            g(i,j) = 0;
        else
            g(i,j) = 1;
        end
    end
    end
    Pz = Pz + relax * (Pznew - Pz);
    %%%calculate error
    error_a = max(max(Pznew - Pz)); %abs error
```

```
    Pznew = Pz;
    %%%calculate velocities
    for i=2:i_max-1 %solve velocity at boundary (x = 0 = 2*pi*Rj)
    for k=2:k_max-1 %solve velocity at boundary (x = 0 = 2*pi*Rj)
        j=1;
        z = (h(j) / (k_max-1)) * (k-1);
        u(i,j,k) = U * (1 - z / h(j)) + 1 / 4 / mu * (z^2 - h(j) * z) *
(Pznew(i,j+1) - Pznew(i,j_max-1)) / dx;
        v(i,j,k) = sign(L/2 - y(i) + dy*0.001) * 1 / 4 / mu * (z^2 -
h(j) * z) * (Pznew(i+1,j) - Pznew(i-1,j)) / dy;
        u(i,j_max,k) = u(i,1,k);
        v(i,j_max,k) = v(i,1,k);
    end
    end
    for j=2:j_max-1 %solve velocity circumferential direction
    for i=2:i_max-1 %solve velocity axial direction
    for k=2:k_max-1 %solve velocity radial direction
        z = (h(j) / (k_max-1)) * (k-1);
        u(i,j,k) = U * (1 - z / h(j)) + 1 / 4 / mu * (z^2 - h(j) * z) *
(Pznew(i,j+1) - Pznew(i,j-1)) / dx;
        v(i,j,k) = sign(L/2 - y(i) + dy*0.001) * 1 / 4 / mu * (z^2 -
h(j) * z) * (Pznew(i+1,j) - Pznew(i-1,j)) / dy;
    end
    end
    end
    %%%calculate velocity gradients
    for j=1:j_max
    for i=1:i_max
    for k=2:k_max-1
        dz = (h(j) / (k_max-1));
        du(i,j,k) = (u(i,j,k+1) - u(i,j,k-1)) / dz / 2;
        dv(i,j,k) = (v(i,j,k+1) - v(i,j,k-1)) / dz / 2;
        Tau(i,j,k) = mu * sqrt(du(i,j,k)^2 + dv(i,j,k)^2);
    end
    end
    end
    Tau(1,1:j_max,2:k_max-1) = Tau(2,1:j_max,2:k_max-1);
    Tau(i_max,1:j_max,2:k_max-1) = Tau(i_max-1,1:j_max,2:k_max-1);
%%%calculate shear switch function
Hold(:,:,1) = H; %previous shear switch function
    if counter > 10
    %determine if yield stress is met
    for j=1:j_max
    for i=2:i_max-1
    for k = 2:k_max-1
      ...
    end
    end
    end
    %fraction across gap that yield stress is met
    for j=1:j_max
    for i=2:i_max-1
      ...
    end
    end
```

```
    end
counter = counter + 1; %display number of iterations
end %%end pressure while

%%solution dxt
Pxt(1:i_max,1:j_max) = 0; %initial presssure
Pxtnew(1:i_max,1:j_max) = 0; %initial replacement presssure
u(1:i_max,1:j_max,1:k_max) = 0; %initial x velocity
u(1:i_max,1:j_max,1) = U; %initial x velocity at boundary
v(1:i_max,1:j_max,1:k_max) = 0; %initial y velocity
g(1:i_max,1:j_max) = 1.0; %initial cavitation switch function
H(1:i_max,1:j_max) = 1.0; %initial shear switch function
Hold(1:i_max,1:j_max,1:old) = 1.0; %initial shear switch function
error_max = 100; %initial error
counter = 0; %initial iteration counter
while (error_max > 0.2) || (counter < 1000) %iteration until max error
reached
    %%%Calculate pressures
    for i=2:i_max-1 %solve pressure at boundary (x = 0 = 2*pi*Rj)
        j = 1;
      %boundary at feed
      circle = (x(j)-xi)^2 + (y(i)-yi)^2;
        if circle <= do^2/4
            F(i,j) = do^2/4 - (x(j)-xi)^2 - (y(i)-yi)^2;
        else
            F(i,j)=0;
        end
        if circle >= do^2
            F(i,j) = 0;
        end
        g_sum = g(i+1,j) + g(i-1,j) + g(i,j+1) + g(i,j_max-1);
        if g_sum < 1
            Pxtnew(i,j) = 1.0;
        else
        An(i,j)= H(i+1,j) * g(i+1,j) * dx / mu / dy * h(j)^3;
        As(i,j)= H(i-1,j) * g(i-1,j) * dx / mu / dy * h(j)^3;
        Ae(i,j)= H(i,j+1) * g(i,j+1) * dy / mu / dx * ((h(j) + h(j+1))
/ 2)^3;
        Aw(i,j)= H(i,j_max-1) * g(i,j_max-1) * dy / mu / dx * ((h(j) +
h(j_max-1)) / 2)^3;
        Af(i,j)= 3 * F(i,j) * dx * dy / mu / lo;
        Bs(i,j) = 12 * dy * (sin(x(j+1)/Rj) - sin(x(j_max-1)/Rj));
        Ap(i,j) = An(i,j) + As(i,j) + Ae(i,j) + Aw(i,j) + Af(i,j);
        Pxtnew(i,j) = (An(i,j)*Pxtnew(i+1,j) + As(i,j)*Pxtnew(i-1,j) +
Ae(i,j)*Pxtnew(i,j+1) + Aw(i,j)*Pxtnew(i,j_max-1) - Bs(i,j)) /
(Ap(i,j));
        end
        if Pxtnew(i,j) < 1.0
            Pxtnew(i,j) = 0;
        end
        %BC x = 0 & 2*pi*R
        Pxtnew(i,j_max) = Pxtnew(i,1);
    end
    for j=2:j_max-1 %solve pressure circumferential direction
    for i=2:i_max-1 %solve pressure axial direction
```

```
      %boundary at feed
      circle = (x(j)-xi)^2 + (y(i)-yi)^2;
        if circle <= do^2/4
            F(i,j) = do^2/4 - (x(j)-xi)^2 - (y(i)-yi)^2;
        else
            F(i,j)=0;
        end
        if circle >= do^2
            F(i,j) = 0;
        end
        g_sum = g(i+1,j) + g(i-1,j) + g(i,j+1) + g(i,j-1);
        if g_sum < 1
            Pxtnew(i,j) = 1.0;
        else
        An(i,j)= H(i+1,j) * g(i+1,j) * dx / mu / dy * h(j)^3;
        As(i,j)= H(i-1,j) * g(i-1,j) * dx / mu / dy * h(j)^3;
        Ae(i,j)= H(i,j+1) * g(i,j+1) * dy / mu / dx * ((h(j) + h(j+1))
/ 2)^3;
        Aw(i,j)= H(i,j-1) * g(i,j-1) * dy / mu / dx * ((h(j) + h(j-1))
/ 2)^3;
        Af(i,j)= 3 * F(i,j) * dx * dy / mu / lo;
        Bs(i,j) = 12 * dy * (sin(x(j+1)/Rj) - sin(x(j-1)/Rj));
        Ap(i,j) = An(i,j) + As(i,j) + Ae(i,j) + Aw(i,j) + Af(i,j);
        Pxtnew(i,j) = (An(i,j)*Pxtnew(i+1,j) + As(i,j)*Pxtnew(i-1,j) +
Ae(i,j)*Pxtnew(i,j+1) + Aw(i,j)*Pxtnew(i,j-1) - Bs(i,j)) / (Ap(i,j));
        end
        if Pxtnew(i,j) < 1.0
            Pxtnew(i,j) = 0;
        end
    end
    end
    %%%reset for next iteration step
    for j=1:j_max
    for i=1:i_max
        if (0.1 * e_a * Pxtnew(i,j) + Ponew(i,j)) < 0
            g(i,j) = 0;
        else
            g(i,j) = 1;
        end
    end
    end
    Pxt = Pxt + relax * (Pxtnew - Pxt);
    %%%calculate error
    error_a = max(max(Pxtnew - Pxt)); %abs error
    Pxtnew = Pxt;
    %%%calculate velocities
    for i=2:i_max-1 %solve velocity at boundary (x = 0 = 2*pi*Rj)
    for k=2:k_max-1 %solve velocity at boundary (x = 0 = 2*pi*Rj)
        j=1;
        z = (h(j) / (k_max-1)) * (k-1);
        u(i,j,k) = U * (1 - z / h(j)) + 1 / 4 / mu * (z^2 - h(j) * z) *
(Pxtnew(i,j+1) - Pxtnew(i,j_max-1)) / dx;
        v(i,j,k) = sign(L/2 - y(i) + dy*0.001) * 1 / 4 / mu * (z^2 -
h(j) * z) * (Pxtnew(i+1,j) - Pxtnew(i-1,j)) / dy;
        u(i,j_max,k) = u(i,1,k);
```

```
        v(i,j_max,k) = v(i,1,k);
    end
    end
    for j=2:j_max-1 %solve velocity circumferential direction
    for i=2:i_max-1 %solve velocity axial direction
    for k=2:k_max-1 %solve velocity radial direction
        z = (h(j) / (k_max-1)) * (k-1);
        u(i,j,k) = U * (1 - z / h(j)) + 1 / 4 / mu * (z^2 - h(j) * z) *
(Pxtnew(i,j+1) - Pxtnew(i,j-1)) / dx;
        v(i,j,k) = sign(L/2 - y(i) + dy*0.001) * 1 / 4 / mu * (z^2 -
h(j) * z) * (Pxtnew(i+1,j) - Pxtnew(i-1,j)) / dy;
    end
    end
    end
    %%%calculate velocity gradients
    for j=1:j_max
    for i=1:i_max
    for k=2:k_max-1
        dz = (h(j) / (k_max-1));
        du(i,j,k) = (u(i,j,k+1) - u(i,j,k-1)) / dz / 2;
        dv(i,j,k) = (v(i,j,k+1) - v(i,j,k-1)) / dz / 2;
        Tau(i,j,k) = mu * sqrt(du(i,j,k)^2 + dv(i,j,k)^2);
    end
    end
    end
    Tau(1,1:j_max,2:k_max-1) = Tau(2,1:j_max,2:k_max-1);
    Tau(i_max,1:j_max,2:k_max-1) = Tau(i_max-1,1:j_max,2:k_max-1);
%%%calculate shear switch function
Hold(:,:,1) = H; %previous shear switch function
    if counter > 10
    %determine if yield stress is met
    for j=1:j_max
    for i=2:i_max-1
    for k = 2:k_max-1
      ...
    end
    end
    end
    %fraction across gap that yield stress is met
    for j=1:j_max
    for i=2:i_max-1
      ...
    end
    end
    end
counter = counter + 1; %display number of iterations
end %%end pressure while

%%solution dzt
Pzt(1:i_max,1:j_max) = 0; %initial presssure
Pztnew(1:i_max,1:j_max) = 0; %initial replacement presssure
u(1:i_max,1:j_max,1:k_max) = 0; %initial x velocity
u(1:i_max,1:j_max,1) = U; %initial x velocity at boundary
v(1:i_max,1:j_max,1:k_max) = 0; %initial y velocity
g(1:i_max,1:j_max) = 1.0; %initial cavitation switch function
```

```
H(1:i_max,1:j_max) = 1.0; %initial shear switch function
Hold(1:i_max,1:j_max,1:old) = 1.0; %initial shear switch function
error_max = 100; %initial error
counter = 0; %initial iteration counter
while (error_max > 0.2) || (counter < 1000) %iteration until max error
reached
    %%%Calculate pressures
    for i=2:i_max-1 %solve pressure at boundary (x = 0 = 2*pi*Rj)
        j = 1;
      %boundary at feed
      circle = (x(j)-xi)^2 + (y(i)-yi)^2;
        if circle <= do^2/4
            F(i,j) = do^2/4 - (x(j)-xi)^2 - (y(i)-yi)^2;
        else
            F(i,j)=0;
        end
        if circle >= do^2
            F(i,j) = 0;
        end
        g_sum = g(i+1,j) + g(i-1,j) + g(i,j+1) + g(i,j_max-1);
        if g_sum < 1
            Pztnew(i,j) = 1.0;
        else
        An(i,j)= H(i+1,j) * g(i+1,j) * dx / mu / dy * h(j)^3;
        As(i,j)= H(i-1,j) * g(i-1,j) * dx / mu / dy * h(j)^3;
        Ae(i,j)= H(i,j+1) * g(i,j+1) * dy / mu / dx * ((h(j) + h(j+1))
/ 2)^3;
        Aw(i,j)= H(i,j_max-1) * g(i,j_max-1) * dy / mu / dx * ((h(j) +
h(j_max-1)) / 2)^3;
        Af(i,j)= 3 * F(i,j) * dx * dy / mu / lo;
        Bs(i,j) = -12 * dy * (cos(x(j+1)/Rj) - cos(x(j_max-1)/Rj));
        Ap(i,j) = An(i,j) + As(i,j) + Ae(i,j) + Aw(i,j) + Af(i,j);
        Pztnew(i,j) = (An(i,j)*Pztnew(i+1,j) + As(i,j)*Pztnew(i-1,j) +
Ae(i,j)*Pztnew(i,j+1) + Aw(i,j)*Pztnew(i,j_max-1) - Bs(i,j)) /
(Ap(i,j));
        end
        if Pztnew(i,j) < 1.0
            Pztnew(i,j) = 0;
        end
        %BC x = 0 & 2*pi*R
        Pztnew(i,j_max) = Pztnew(i,1);
    end
    for j=2:j_max-1 %solve pressure circumferential direction
    for i=2:i_max-1 %solve pressure axial direction
      %boundary at feed
      circle = (x(j)-xi)^2 + (y(i)-yi)^2;
        if circle <= do^2/4
            F(i,j) = do^2/4 - (x(j)-xi)^2 - (y(i)-yi)^2;
        else
            F(i,j)=0;
        end
        if circle >= do^2
            F(i,j) = 0;
        end
        g_sum = g(i+1,j) + g(i-1,j) + g(i,j+1) + g(i,j-1);
```

```
        if g_sum < 1
            Pztnew(i,j) = 1.0;
        else
        An(i,j)= H(i+1,j) * g(i+1,j) * dx / mu / dy * h(j)^3;
        As(i,j)= H(i-1,j) * g(i-1,j) * dx / mu / dy * h(j)^3;
        Ae(i,j)= H(i,j+1) * g(i,j+1) * dy / mu / dx * ((h(j) + h(j+1))
/ 2)^3;
        Aw(i,j)= H(i,j-1) * g(i,j-1) * dy / mu / dx * ((h(j) + h(j-1))
/ 2)^3;
        Af(i,j)= 3 * F(i,j) * dx * dy / mu / lo;
        Bs(i,j) = -12 * dy * (cos(x(j+1)/Rj) - cos(x(j-1)/Rj));
        Ap(i,j) = An(i,j) + As(i,j) + Ae(i,j) + Aw(i,j) + Af(i,j);
        Pztnew(i,j) = (An(i,j)*Pztnew(i+1,j) + As(i,j)*Pztnew(i-1,j) +
Ae(i,j)*Pztnew(i,j+1) + Aw(i,j)*Pztnew(i,j-1) - Bs(i,j)) / (Ap(i,j));
        end
        if Pztnew(i,j) < 1.0
            Pztnew(i,j) = 0;
        end
    end
    end
    %%%reset for next iteration step
    for j=1:j_max
    for i=1:i_max
        if (0.1 * e_a * Pztnew(i,j) + Ponew(i,j)) < 0
            g(i,j) = 0;
        else
            g(i,j) = 1;
        end
    end
    end
    Pzt = Pzt + relax * (Pztnew - Pzt);
    %%%calculate error
    error_a = max(max(Pztnew - Pzt)); %abs error
    Pztnew = Pzt;
    %%%calculate velocities
    for i=2:i_max-1 %solve velocity at boundary (x = 0 = 2*pi*Rj)
    for k=2:k_max-1 %solve velocity at boundary (x = 0 = 2*pi*Rj)
        j=1;
        z = (h(j) / (k_max-1)) * (k-1);
        u(i,j,k) = U * (1 - z / h(j)) + 1 / 4 / mu * (z^2 - h(j) * z) *
(Pztnew(i,j+1) - Pztnew(i,j_max-1)) / dx;
        v(i,j,k) = sign(L/2 - y(i) + dy*0.001) * 1 / 4 / mu * (z^2 -
h(j) * z) * (Pztnew(i+1,j) - Pztnew(i-1,j)) / dy;
        u(i,j_max,k) = u(i,1,k);
        v(i,j_max,k) = v(i,1,k);
    end
    end
    for j=2:j_max-1 %solve velocity circumferential direction
    for i=2:i_max-1 %solve velocity axial direction
    for k=2:k_max-1 %solve velocity radial direction
        z = (h(j) / (k_max-1)) * (k-1);
        u(i,j,k) = U * (1 - z / h(j)) + 1 / 4 / mu * (z^2 - h(j) * z) *
(Pztnew(i,j+1) - Pztnew(i,j-1)) / dx;
        v(i,j,k) = sign(L/2 - y(i) + dy*0.001) * 1 / 4 / mu * (z^2 -
h(j) * z) * (Pztnew(i+1,j) - Pztnew(i-1,j)) / dy;
```

```
    end
    end
    end
    %%%calculate velocity gradients
    for j=1:j_max
    for i=1:i_max
    for k=2:k_max-1
        dz = (h(j) / (k_max-1));
        du(i,j,k) = (u(i,j,k+1) - u(i,j,k-1)) / dz / 2;
        dv(i,j,k) = (v(i,j,k+1) - v(i,j,k-1)) / dz / 2;
        Tau(i,j,k) = mu * sqrt(du(i,j,k)^2 + dv(i,j,k)^2);
    end
    end
    end
    Tau(1,1:j_max,2:k_max-1) = Tau(2,1:j_max,2:k_max-1);
    Tau(i_max,1:j_max,2:k_max-1) = Tau(i_max-1,1:j_max,2:k_max-1);
%%%calculate shear switch function
Hold(:,:,1) = H; %previous shear switch function
    if counter > 10
    %determine if yield stress is met
    for j=1:j_max
    for i=2:i_max-1
    for k = 2:k_max-1
      ...
    end
    end
    end
    %fraction across gap that yield stress is met
    for j=1:j_max
    for i=2:i_max-1
      ...
    end
    end
    end
counter = counter + 1; %display number of iterations
end %%end pressure while

%%%calculate load Po
for j=1:j_max-1
    Poy(j) = (sum(Ponew(:,j)) - 2*Pa);
end
for j=1:j_max-1
    Poxsin(j) = Poy(j) * sin(theta(j));
    Poxcos(j) = Poy(j) * cos(theta(j));
end
Fot = -sum(Poxcos) * Rj * dy * dtheta;
Fon = sum(Poxsin) * Rj * dy * dtheta;
Wo = sqrt(Fon^2 + Fot^2); %Load (N)
Phio = asin(Fon/Wo) * 180 / pi; %attitude angle (deg)
%%%calculate load px
for j=1:j_max-1
    Pxy(j) = sum(Pxnew(:,j));
end
for j=1:j_max-1
    Pxxsin(j) = Pxy(j) * sin(theta(j));
```

```
    Pxxcos(j) = Pxy(j) * cos(theta(j));
end
Fxt = -sum(Pxxcos) * Rj * dy * dtheta;
Fxn = sum(Pxxsin) * Rj * dy * dtheta;
Wx = sqrt(Fxt^2 + Fxn^2); %Load (N)
Phix = asin(Fxn/Wx) * 180 / pi; %attitude angle (deg)
%%%calculate load pz
for j=1:j_max-1
    Pzy(j) = sum(Pznew(:,j));
end
for j=1:j_max-1
    Pzxsin(j) = Pzy(j) * sin(theta(j));
    Pzxcos(j) = Pzy(j) * cos(theta(j));
end
Fzt = -sum(Pzxcos) * Rj * dy * dtheta;
Fzn = sum(Pzxsin) * Rj * dy * dtheta;
Wz = sqrt(Fzt^2 + Fzn^2); %Load (N)
Phiz = asin(Fzn/Wz) * 180 / pi; %attitude angle (deg)
%%%calculate load pxt
for j=1:j_max-1
    Pxty(j) = sum(Pxtnew(:,j));
end
for j=1:j_max-1
    Pxtxsin(j) = Pxty(j) * sin(theta(j));
    Pxtxcos(j) = Pxty(j) * cos(theta(j));
end
Fxtt = -sum(Pxtxcos) * Rj * dy * dtheta;
Fxtn = sum(Pxtxsin) * Rj * dy * dtheta;
Wxt = sqrt(Fxtt^2 + Fxtn^2); %Load (N)
Phixt = asin(Fxtn/Wxt) * 180 / pi; %attitude angle (deg)
%%%calculate load pzt
for j=1:j_max-1
    Pzty(j) = sum(Pztnew(:,j));
end
for j=1:j_max-1
    Pztxsin(j) = Pzty(j) * sin(theta(j));
    Pztxcos(j) = Pzty(j) * cos(theta(j));
end
Fztt = -sum(Pztxcos) * Rj * dy * dtheta;
Fztn = sum(Pztxsin) * Rj * dy * dtheta;
Wzt = sqrt(Fztt^2 + Fztn^2); %Load (N)
Phizt = asin(Fztn/Wzt) * 180 / pi; %attitude angle (deg)

%stiffness coefficients (N/m)
Kxx = (1/c) * ((Fxt*cos((Phio/180*pi)) +
Fxn*sin((Phio/180*pi)))*cos((Phio/180*pi)) - (Fzt*cos((Phio/180*pi)) +
Fzn*sin((Phio/180*pi)))*sin((Phio/180*pi)))
Kxz = (1/c) * ((Fxt*cos((Phio/180*pi)) +
Fxn*sin((Phio/180*pi)))*sin((Phio/180*pi)) + (Fzt*cos((Phio/180*pi)) +
Fzn*sin((Phio/180*pi)))*cos((Phio/180*pi)))
Kzx = (1/c) * ((Fxt*sin((Phio/180*pi)) -
Fxn*cos((Phio/180*pi)))*cos((Phio/180*pi)) - (Fzt*sin((Phio/180*pi)) -
Fzn*cos((Phio/180*pi)))*sin((Phio/180*pi)))
```

```
Kzz = (1/c) * ((Fxt*sin((Phio/180*pi)) -
Fxn*cos((Phio/180*pi)))*sin((Phio/180*pi)) + (Fzt*sin((Phio/180*pi)) -
Fzn*cos((Phio/180*pi)))*cos((Phio/180*pi)))
%damping coefficients (N.s/m)
Bxx = (1/c) * ((Fxtt*cos((Phio/180*pi)) +
Fxtn*sin((Phio/180*pi)))*cos((Phio/180*pi)) - (Fztt*cos((Phio/180*pi))
+ Fztn*sin((Phio/180*pi)))*sin((Phio/180*pi)))
Bxz = (1/c) * ((Fxtt*cos((Phio/180*pi)) +
Fxtn*sin((Phio/180*pi)))*sin((Phio/180*pi)) + (Fztt*cos((Phio/180*pi))
+ Fztn*sin((Phio/180*pi)))*cos((Phio/180*pi)))
Bzx = (1/c) * ((Fxtt*sin((Phio/180*pi)) -
Fxtn*cos((Phio/180*pi)))*cos((Phio/180*pi)) - (Fztt*sin((Phio/180*pi))
- Fztn*cos((Phio/180*pi)))*sin((Phio/180*pi)))
Bzz = (1/c) * ((Fxtt*sin((Phio/180*pi)) -
Fxtn*cos((Phio/180*pi)))*sin((Phio/180*pi)) + (Fztt*sin((Phio/180*pi))
- Fztn*cos((Phio/180*pi)))*cos((Phio/180*pi)))
```

APPENDIX D

DYNAMIC RESPONSE CALCULATIONS

The response of a hydrodynamic journal bearing displays a spring like resistance, however; the displacement of the journal relative to the bearing is not linearly related to the applied load as with a typical spring. The hydrodynamic fluid film separating the journal and bearing also exhibits damping effects which are important to the bearing stability. Figure D-1 below depicts the reaction of bearing lubrication film, with bearing stiffness represented by springs and the bearing dampening represented by dashpots.

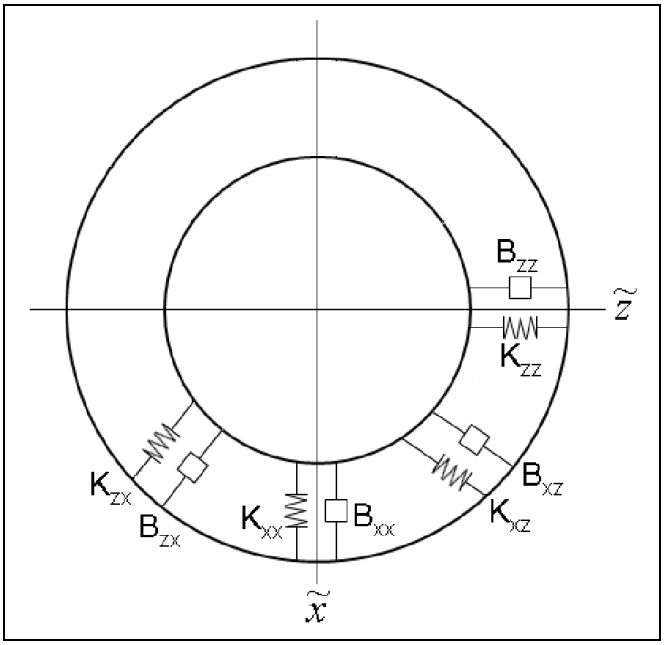

Figure D-1 Journal Bearing Spring and Damping Coefficient Schematic

Solving the bearings dynamic response to a small perturbation, the journal motion is assumed to take place in the form of small perturbations around some steady state equilibrium position such that the instantaneous journal location can be given by:

$$\widetilde{x} = \widetilde{x}_o + \Delta\widetilde{x}$$
$$\widetilde{z} = \widetilde{z}_o + \Delta\widetilde{z}$$

where the subscript *o* indicates steady state variable and the delta prefix indicates a perturbation term, which represents a relatively small displacement of the journal from the steady state position. By performing a first order Taylor series expansion on the pressure, letting p_o be the steady state pressure distribution, we get the following:

$$\begin{aligned} p &= p\big|_o + \left.\frac{\partial p}{\partial \widetilde{x}}\right|_o \cdot \Delta\widetilde{x} + \left.\frac{\partial p}{\partial \widetilde{z}}\right|_o \cdot \Delta\widetilde{z} + \left.\frac{\partial p}{\partial \dot{\widetilde{x}}}\right|_o \cdot \Delta\dot{\widetilde{x}} + \left.\frac{\partial p}{\partial \dot{\widetilde{z}}}\right|_o \cdot \Delta\dot{\widetilde{z}} \\ &= p_o + p_{\widetilde{x}} \cdot \Delta\widetilde{x} + p_{\widetilde{z}} \cdot \Delta\widetilde{z} + p_{\dot{\widetilde{x}}} \cdot \Delta\dot{\widetilde{x}} + p_{\dot{\widetilde{z}}} \cdot \Delta\dot{\widetilde{z}} \end{aligned}$$

The fluid film thickness can be written as:

$$h = c + e\cos(\theta - \Delta\Phi) \approx c + e_o\cos(\theta) + \Delta\widetilde{x}\cos(\theta) + \Delta\widetilde{z}\sin(\theta)$$

such that,

$$h_0 = c + e_o\cos(\theta)$$

$$h = h_o + \cos(\theta)\cdot\Delta\widetilde{x} + \sin(\theta)\cdot\Delta\widetilde{z}$$
$$\frac{\partial h}{\partial t} = \cos(\theta)\cdot\Delta\dot{\widetilde{x}} + \sin(\theta)\cdot\Delta\dot{\widetilde{z}}$$

Starting with the modified Reynolds equation:

$$g\cdot\frac{\partial}{\partial x}\left(\frac{h^3}{\mu\cdot H\left(|\dot{\gamma}|\right)}\frac{\partial p}{\partial x}\right) + g\cdot\frac{\partial}{\partial y}\left(\frac{h^3}{\mu\cdot H\left(|\dot{\gamma}|\right)}\frac{\partial p}{\partial y}\right) - g\cdot\frac{3}{\mu l_o}p\cdot\Im = 6U\frac{\partial h}{\partial x} - 12\frac{\partial h}{\partial t} - \frac{3}{\mu l_o}p_{inj}\cdot\Im$$

Replace expanded pressure and film thickness terms in modified Reynolds equation:

$$g \cdot \frac{\partial}{\partial \tilde{x}} \left(\frac{\left(h_o + \cos(\theta) \cdot \Delta\tilde{x} + \sin(\theta) \cdot \Delta\tilde{z}\right)^3}{\mu \cdot H\left(\left|\dot{\gamma}\right|\right)} \frac{\partial\left(p_o + p_{\tilde{x}} \cdot \Delta\tilde{x} + p_{\tilde{z}} \cdot \Delta\tilde{z} + p_{\dot{\tilde{x}}} \cdot \Delta\dot{\tilde{x}} + p_{\dot{\tilde{z}}} \cdot \Delta\dot{\tilde{z}}\right)}{\partial \tilde{x}} \right) + \ldots$$

$$+ g \cdot \frac{\partial}{\partial \tilde{y}} \left(\frac{\left(h_o + \cos(\theta') \cdot \Delta\tilde{x} + \sin(\theta) \cdot \Delta\tilde{z}\right)^3}{\mu \cdot H\left(\left|\dot{\gamma}\right|\right)} \frac{\partial\left(p_o + p_{\tilde{x}} \cdot \Delta\tilde{x} + p_{\tilde{z}} \cdot \Delta\tilde{z} + p_{\dot{\tilde{x}}} \cdot \Delta\dot{\tilde{x}} + p_{\dot{\tilde{z}}} \cdot \Delta\dot{\tilde{z}}\right)}{\partial \tilde{y}} \right) - \ldots$$

$$- g \cdot \frac{3}{\mu l_o} \left(p_o + p_{\tilde{x}} \cdot \Delta\tilde{x} + p_{\tilde{z}} \cdot \Delta\tilde{z} + p_{\dot{\tilde{x}}} \cdot \Delta\dot{\tilde{x}} + p_{\dot{\tilde{z}}} \cdot \Delta\dot{\tilde{z}}\right) \cdot \Im =$$

$$= 6U \frac{\partial\left(h_o + \cos(\theta) \cdot \Delta\tilde{x} + \sin(\theta) \cdot \Delta\tilde{z}\right)}{\partial \tilde{x}} - 12\left(\cos(\theta) \cdot \Delta\dot{\tilde{x}} + \sin(\theta) \cdot \Delta\dot{\tilde{z}}\right) - \ldots$$

$$- \frac{3}{\mu l_o} p_{inj} \cdot \Im$$

Retaining the terms of the same order of magnitude, the following system of differential equations is obtained:

$$\mathrm{O}(1)$$

$$\frac{\partial}{\partial \tilde{x}}\left(\frac{(h_o)^3}{\mu \cdot H(|\dot{\gamma}|)}\frac{\partial(p_o)}{\partial \tilde{x}}\right)+\frac{\partial}{\partial \tilde{y}}\left(\frac{(h_o)^3}{\mu \cdot H(|\dot{\gamma}|)}\frac{\partial(p_o)}{\partial \tilde{y}}\right)-\frac{3}{\mu l_o}(p_o)\cdot \Im = 6U\frac{\partial(h_o)}{\partial \tilde{x}}-\frac{3}{\mu l_o}(p_{inj})\cdot \Im$$

$$\mathrm{O}(\tilde{x})$$

$$\frac{\partial}{\partial \tilde{x}}\left(\frac{(h_o)^3}{\mu \cdot H(|\dot{\gamma}|)}\frac{\partial(p_{\tilde{x}})}{\partial \tilde{x}}\right)+\frac{\partial}{\partial \tilde{y}}\left(\frac{(h_o)^3}{\mu \cdot H(|\dot{\gamma}|)}\frac{\partial(p_{\tilde{x}})}{\partial \tilde{y}}\right)-\frac{3}{\mu l_o}(p_{\tilde{x}})\cdot \Im =$$

$$=-6U\sin(\theta)-\frac{\partial}{\partial \tilde{x}}\left(\frac{3(h_o)^2}{\mu \cdot H(|\dot{\gamma}|)}\cos(\theta)\frac{\partial(p_o)}{\partial \tilde{x}}\right)-\frac{\partial}{\partial \tilde{y}}\left(\frac{3(h_o)^2}{\mu \cdot H(|\dot{\gamma}|)}\cos(\theta)\frac{\partial(p_o)}{\partial \tilde{y}}\right)$$

$$\mathrm{O}(\tilde{z})$$

$$\frac{\partial}{\partial \tilde{x}}\left(\frac{(h_o)^3}{\mu \cdot H(|\dot{\gamma}|)}\frac{\partial(p_{\tilde{z}})}{\partial \tilde{x}}\right)+\frac{\partial}{\partial \tilde{y}}\left(\frac{(h_o)^3}{\mu \cdot H(|\dot{\gamma}|)}\frac{\partial(p_{\tilde{z}})}{\partial \tilde{y}}\right)-\frac{3}{\mu l_o}(p_{\tilde{z}})\cdot \Im$$

$$=6U\cos(\theta)-\frac{\partial}{\partial \tilde{x}}\left(\frac{3(h_o)^2}{\mu \cdot H(|\dot{\gamma}|)}\sin(\theta)\frac{\partial(p_o)}{\partial \tilde{x}}\right)-\frac{\partial}{\partial \tilde{y}}\left(\frac{3(h_o)^2}{\mu \cdot H(|\dot{\gamma}|)}\sin(\theta)\frac{\partial(p_o)}{\partial \tilde{y}}\right)$$

$$\mathrm{O}(\dot{\tilde{x}})$$

$$\frac{\partial}{\partial \tilde{x}}\left(\frac{(h_o)^3}{\mu \cdot H(|\dot{\gamma}|)}\frac{\partial(p_{\dot{\tilde{x}}})}{\partial \tilde{x}}\right)+\frac{\partial}{\partial \tilde{y}}\left(\frac{(h_o)^3}{\mu \cdot H(|\dot{\gamma}|)}\frac{\partial(p_{\dot{\tilde{x}}})}{\partial \tilde{y}}\right)-\frac{3}{\mu l_o}(p_{\dot{\tilde{x}}})\cdot \Im$$

$$=-12(\cos(\theta))$$

$$\mathrm{O}(\dot{\tilde{z}})$$

$$\frac{\partial}{\partial \tilde{x}}\left(\frac{(h_o)^3}{\mu \cdot H(|\dot{\gamma}|)}\frac{\partial(p_{\dot{\tilde{z}}})}{\partial \tilde{x}}\right)+\frac{\partial}{\partial \tilde{y}}\left(\frac{(h_o)^3}{\mu \cdot H(|\dot{\gamma}|)}\frac{\partial(p_{\dot{\tilde{z}}})}{\partial \tilde{y}}\right)-\frac{3}{\mu l_o}(p_{\dot{\tilde{z}}})\cdot \Im$$

$$=-12(\sin(\theta))$$

Expanding the RHS of the 2nd and 3rd equations:

$$\mathrm{O}(\tilde{x})$$

$$-\frac{\partial}{\partial\tilde{x}}\left(\frac{3(h_o)^2}{\mu\cdot H(|\dot{\gamma}|)}\cos(\theta)\frac{\partial(p_o)}{\partial\tilde{x}}\right)-\frac{\partial}{\partial\tilde{y}}\left(\frac{3(h_o)^2}{\mu\cdot H(|\dot{\gamma}|)}\cos(\theta)\frac{\partial(p_o)}{\partial\tilde{y}}\right)=$$

$$=-\frac{3\cos(\theta)}{h_o}\left(\frac{\partial}{\partial\tilde{x}}\left(\frac{(h_o)^3}{\mu\cdot H(|\dot{\gamma}|)}\frac{\partial(p_o)}{\partial\tilde{x}}\right)+\frac{\partial}{\partial\tilde{y}}\left(\frac{(h_o)^3}{\mu\cdot H(|\dot{\gamma}|)}\frac{\partial(p_o)}{\partial\tilde{y}}\right)\right)-\frac{3(h_o)^3}{\mu\cdot H(|\dot{\gamma}|)}\frac{\partial(p_o)}{\partial\tilde{x}}\frac{\partial}{\partial\tilde{x}}\left(\frac{\cos(\theta)}{h_o}\right)$$

$$\mathrm{O}(\tilde{z})$$

$$-\frac{\partial}{\partial\tilde{x}}\left(\frac{3(h_o)^2}{\mu\cdot H(|\dot{\gamma}|)}\sin(\theta)\frac{\partial(p_o)}{\partial\tilde{x}}\right)-\frac{\partial}{\partial\tilde{y}}\left(\frac{3(h_o)^2}{\mu\cdot H(|\dot{\gamma}|)}\sin(\theta)\frac{\partial(p_o)}{\partial\tilde{y}}\right)=$$

$$=-\frac{3\sin(\theta)}{h_o}\left(\frac{\partial}{\partial\tilde{x}}\left(\frac{(h_o)^3}{\mu\cdot H(|\dot{\gamma}|)}\frac{\partial(p_o)}{\partial\tilde{x}}\right)+\frac{\partial}{\partial\tilde{y}}\left(\frac{(h_o)^3}{\mu\cdot H(|\dot{\gamma}|)}\frac{\partial(p_o)}{\partial\tilde{y}}\right)\right)-\frac{3(h_o)^3}{\mu\cdot H(|\dot{\gamma}|)}\frac{\partial(p_o)}{\partial\tilde{x}}\frac{\partial}{\partial\tilde{x}}\left(\frac{\sin(\theta)}{h_o}\right)$$

Thus, we have a system of equations for the unknown pressure functions that only differ by the source term:

$$\left[\frac{\partial}{\partial\tilde{x}}\left(\frac{{h_o}^3}{\mu\cdot H(|\dot{\gamma}|)}\frac{\partial(\ )}{\partial\tilde{x}}\right)+\frac{\partial}{\partial\tilde{y}}\left(\frac{{h_o}^3}{\mu\cdot H(|\dot{\gamma}|)}\frac{\partial(\ )}{\partial\tilde{y}}\right)-\frac{3}{\mu l_o}(\ )\cdot\Im\right]*\begin{bmatrix}p_o\\ p_{\tilde{x}}\\ p_{\tilde{z}}\\ p_{\dot{\tilde{x}}}\\ p_{\dot{\tilde{z}}}\end{bmatrix}=$$

$$\begin{bmatrix}
6U\frac{\partial(h_o)}{\partial\tilde{x}}-\frac{3}{\mu l_o}(p_{inj})\\
-6U\sin(\theta)-\frac{3}{h_o}\cos(\theta')\left(\frac{3\cdot\Im\cdot p_o}{\mu\cdot l_o}+6U\frac{\partial h_o}{\partial\tilde{x}}-\frac{3\cdot\Im\cdot p_{inj}}{\mu\cdot l_o}\right)-\frac{3(h_o)^3}{\mu\cdot H(|\dot{\gamma}|)}\frac{\partial(p_o)}{\partial\tilde{x}}\frac{\partial}{\partial\tilde{x}}\left(\frac{\cos(\theta)}{h_o}\right)\\
6U\cos(\theta)-\frac{3}{h_o}\sin(\theta')\left(\frac{3\cdot\Im\cdot p_o}{\mu\cdot l_o}+6U\frac{\partial h_o}{\partial\tilde{x}}-\frac{3\cdot\Im\cdot p_{inj}}{\mu\cdot l_o}\right)-\frac{3(h_o)^3}{\mu\cdot H(|\dot{\gamma}|)}\frac{\partial(p_o)}{\partial\tilde{x}}\frac{\partial}{\partial\tilde{x}}\left(\frac{\sin(\theta)}{h_o}\right)\\
-12\cos(\theta)\\
-12\sin(\theta)
\end{bmatrix}$$

The steady state pressure distribution can be solved subsequently allowing the same method to be used for perturbation pressures to be solved with updated source terms. The perturbation pressure distributions can then be added to the steady state pressure distribution through the Taylor Series expansion equation.

Once the solutions to the system of differential equations are determined, the resultant reaction load can be calculated by integration of the pressure distribution. Performing a first order Taylor series expansion on the components of the resultant reaction loads gives:

$$W_{\tilde{x}} = W_{\tilde{x},o} + \left.\frac{\partial W_{\tilde{x}}}{\partial \tilde{x}}\right|_o \Delta\tilde{x} + \left.\frac{\partial W_{\tilde{x}}}{\partial \tilde{z}}\right|_o \Delta\tilde{z} + \left.\frac{\partial W_{\tilde{x}}}{\partial \dot{\tilde{x}}}\right|_o \Delta\dot{\tilde{x}} + \left.\frac{\partial W_{\tilde{x}}}{\partial \dot{\tilde{z}}}\right|_o \Delta\dot{\tilde{z}}$$

$$W_{\tilde{z}} = W_{\tilde{z},o} + \left.\frac{\partial W_{\tilde{z}}}{\partial \tilde{x}}\right|_o \Delta\tilde{x} + \left.\frac{\partial W_{\tilde{z}}}{\partial \tilde{z}}\right|_o \Delta\tilde{z} + \left.\frac{\partial W_{\tilde{z}}}{\partial \dot{\tilde{x}}}\right|_o \Delta\dot{\tilde{x}} + \left.\frac{\partial W_{\tilde{z}}}{\partial \dot{\tilde{z}}}\right|_o \Delta\dot{\tilde{z}}$$

The differential terms can be written in terms of the spring and damping coefficients. Using the layout described in Figure D-1 we get:

$$K_{\tilde{x}\tilde{x}} = -\left.\frac{\partial W_{\tilde{x}}}{\partial \tilde{x}}\right|_o \qquad K_{\tilde{x}\tilde{z}} = -\left.\frac{\partial W_{\tilde{x}}}{\partial \tilde{z}}\right|_o \qquad K_{\tilde{z}\tilde{x}} = -\left.\frac{\partial W_{\tilde{z}}}{\partial \tilde{x}}\right|_o \qquad K_{\tilde{z}\tilde{z}} = -\left.\frac{\partial W_{\tilde{z}}}{\partial \tilde{z}}\right|_o$$

$$B_{\tilde{x}\tilde{x}} = -\left.\frac{\partial W_{\tilde{x}}}{\partial \dot{\tilde{x}}}\right|_o \qquad B_{\tilde{x}\tilde{z}} = -\left.\frac{\partial W_{\tilde{x}}}{\partial \dot{\tilde{z}}}\right|_o \qquad B_{\tilde{z}\tilde{x}} = -\left.\frac{\partial W_{\tilde{z}}}{\partial \dot{\tilde{x}}}\right|_o \qquad B_{\tilde{z}\tilde{z}} = -\left.\frac{\partial W_{\tilde{z}}}{\partial \dot{\tilde{z}}}\right|_o$$

Using the Cartesian coordinates shown in Figure D-2, the component loads are:

$$-W_{\tilde{x}} = F_t \cos(\Phi) + F_n \sin(\Phi)$$
$$-W_{\tilde{z}} = F_t \cos(\Phi) - F_n \sin(\Phi)$$

where the subscripts *n* and *t* denote the normal and tangential coordinates relative to the line of centers shown in Figure D-2. The component forces in the normal and tangential

direction can be found by integration of the pressure distribution (atmospheric boundary conditions are not applied to perturbation solutions and should not be subtracted during integration of the pressure distribution when solving for reaction loads).

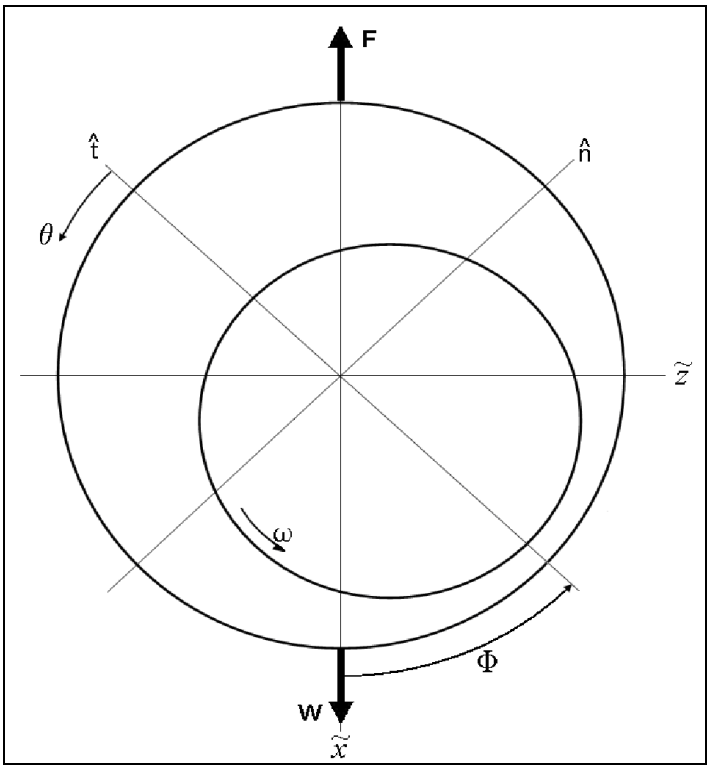

Figure D-2 Journal Bearing System of Coordinates

Using the geometry shown in Figure D-2, the spring and damping coefficients can be written in terms of the normal and tangential component forces calculated from the pressure distributions of the five differential equations. The condensed form of the spring and damping coefficients can be written as:

$$c \cdot K_{\tilde{x}\tilde{x}} = \left(F_{t,\Delta\tilde{x}} \cos(\Phi) + F_{n,\Delta\tilde{x}} \sin(\Phi)\right)\cos(\Phi) - \left(F_{t,\Delta\tilde{z}} \cos(\Phi) + F_{n,\Delta\tilde{z}} \sin(\Phi)\right)\sin(\Phi)$$
$$c \cdot K_{\tilde{x}\tilde{z}} = \left(F_{t,\Delta\tilde{x}} \cos(\Phi) + F_{n,\Delta\tilde{x}} \sin(\Phi)\right)\sin(\Phi) + \left(F_{t,\Delta\tilde{z}} \cos(\Phi) + F_{n,\Delta\tilde{z}} \sin(\Phi)\right)\cos(\Phi)$$
$$c \cdot K_{\tilde{z}\tilde{x}} = \left(F_{t,\Delta\tilde{x}} \sin(\Phi) - F_{n,\Delta\tilde{x}} \cos(\Phi)\right)\cos(\Phi) - \left(F_{t,\Delta\tilde{z}} \sin(\Phi) - F_{n,\Delta\tilde{z}} \cos(\Phi)\right)\sin(\Phi)$$
$$c \cdot K_{\tilde{z}\tilde{z}} = \left(F_{t,\Delta\tilde{x}} \sin(\Phi) - F_{n,\Delta\tilde{x}} \cos(\Phi)\right)\sin(\Phi) + \left(F_{t,\Delta\tilde{z}} \sin(\Phi) - F_{n,\Delta\tilde{z}} \cos(\Phi)\right)\cos(\Phi)$$
$$c \cdot B_{\tilde{x}\dot{\tilde{x}}} = \left(F_{t,\Delta\dot{\tilde{x}}} \cos(\Phi) + F_{n,\Delta\dot{\tilde{x}}} \sin(\Phi)\right)\cos(\Phi) - \left(F_{t,\Delta\dot{\tilde{z}}} \cos(\Phi) + F_{n,\Delta\dot{\tilde{z}}} \sin(\Phi)\right)\sin(\Phi)$$
$$c \cdot B_{\tilde{x}\dot{\tilde{z}}} = \left(F_{t,\Delta\dot{\tilde{x}}} \cos(\Phi) + F_{n,\Delta\dot{\tilde{x}}} \sin(\Phi)\right)\sin(\Phi) + \left(F_{t,\Delta\dot{\tilde{z}}} \cos(\Phi) + F_{n,\Delta\dot{\tilde{z}}} \sin(\Phi)\right)\cos(\Phi)$$
$$c \cdot B_{\tilde{z}\dot{\tilde{x}}} = \left(F_{t,\Delta\dot{\tilde{x}}} \sin(\Phi) - F_{n,\Delta\dot{\tilde{x}}} \cos(\Phi)\right)\cos(\Phi) - \left(F_{t,\Delta\dot{\tilde{z}}} \sin(\Phi) - F_{n,\Delta\dot{\tilde{z}}} \cos(\Phi)\right)\sin(\Phi)$$
$$c \cdot B_{\tilde{z}\dot{\tilde{z}}} = \left(F_{t,\Delta\dot{\tilde{x}}} \sin(\Phi) - F_{n,\Delta\dot{\tilde{x}}} \cos(\Phi)\right)\sin(\Phi) + \left(F_{t,\Delta\dot{\tilde{z}}} \sin(\Phi) - F_{n,\Delta\dot{\tilde{z}}} \cos(\Phi)\right)\cos(\Phi)$$

APPENDIX E

BEARING LOAD CAPACITY CALCULATIONS

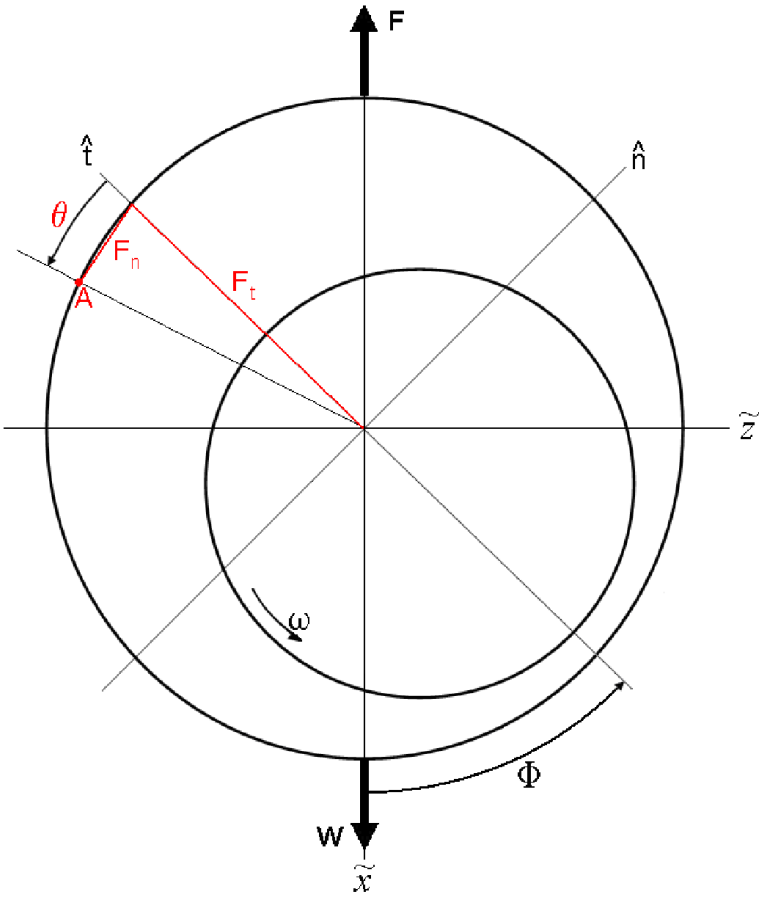

Figure E-1 Journal Bearing System of Coordinates

The load capacity of the bearing can be determined by solving the normal and tangential components of the force the fluid applies to the journal. This can be accomplished by integrating the pressure distribution solved through an iterative

calculation using the modified Reynolds equation. Since the bearing geometry was "unwrapped" starting at the line of centers, the attitude angle does not need to be known to solve the normal and tangential components of the force. Defining the tangential axis at the location of the largest clearance along the line of centers, the bearing geometry is unwrapped, making the tangential axis the boundary for $\theta = 0$ & 2π.

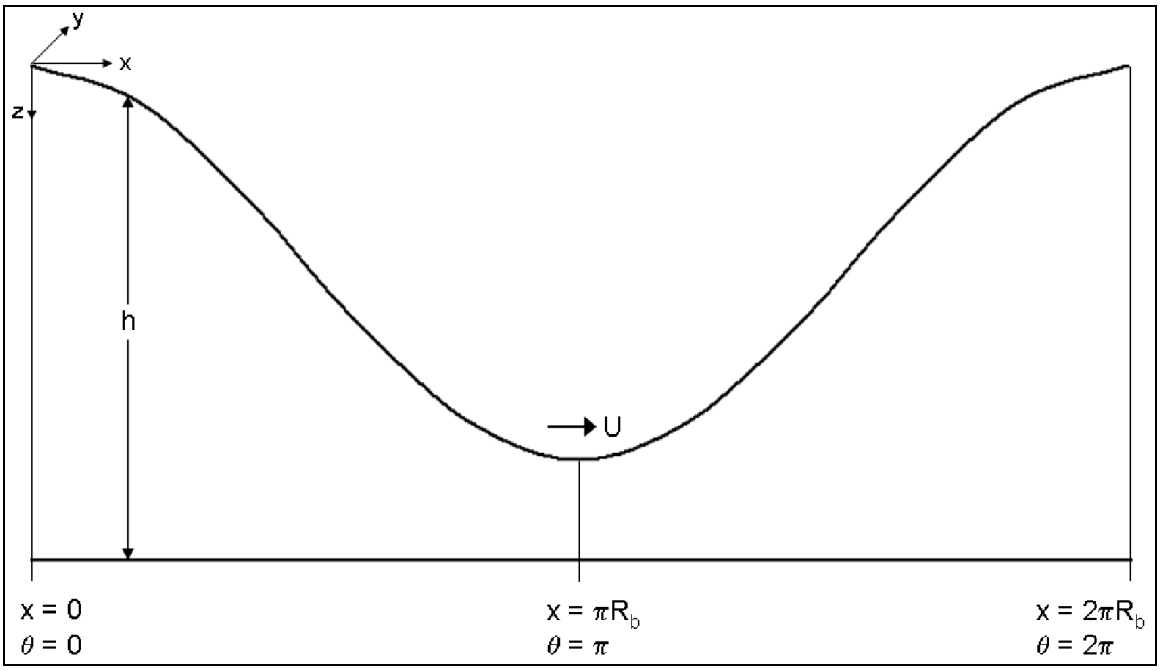

Figure E-2 Unwrapped Fluid Film Cross Section

Defining the positive direction of the angular coordinate θ in the direction of rotation the process of solving the bearing capacity can be formulated. At any arbitrary angle around the bearing, the fluid pressure at that point exerts a force on the journal which can be broken into normal and tangential directions. Looking at a randomly selected point along the bearing circumference labeled 'A' in Figure E-1, those normal and tangential force components can be seen highlighted in red. By integrating the pressure distribution acting on the entire journal surface the normal and tangential

component forces can be found using the two equations below. Note that the pressure applies the force in the opposite direction resulting in a negative sign on the tangential force equation; the normal force component is already in the opposite direction of the normal axis shown in Figure E-1.

$$F_t = \int -p \cdot \cos\theta \cdot dA = -\int_y \int_\theta p \cdot \cos\theta \cdot R_j \cdot d\theta \, dy$$

$$F_n = \int p \cdot \sin\theta \cdot dA = \int_y \int_\theta p \cdot \sin\theta \cdot R_j \cdot d\theta \, dy$$

The attitude angle can then be calculated from the normal and tangential component forces. Finally, the applied load in terms of the fixed global coordinate system can be determined. As can be seen in Figure E-1 and from the equations below, the x-axis is defined opposite of the tangential axis rotated by an angle equal to the attitude angle, while the z-axis is in the same direction as the normal axis and rotated by an angle equal to the attitude angle.

$$\Phi = \sin^{-1}\left(\frac{F_n}{F}\right)$$

$$-W_{\tilde{x}} = F_t \cos(\Phi) + F_n \sin(\Phi)$$

$$-W_{\tilde{z}} = F_t \cos(\Phi) - F_n \sin(\Phi)$$

APPENDIX F

VISCOSITY AND YIELD STRESS CALCULATIONS

The electromagnetic cradle used to apply the magnetic field to the MR fluid to determine the change in viscosity resulted in chain like structures being formed perpendicular to the rotary motion of the viscometer along one axis, and parallel to the opposing axis, as shown in Figure F-1. This creates two viscosity measurement regions within the fluid; one where the viscous force is due to apparent increased viscosity of the magnetized MR fluid, and a second where the viscous force results from only the un-magnetized fluid viscosity.

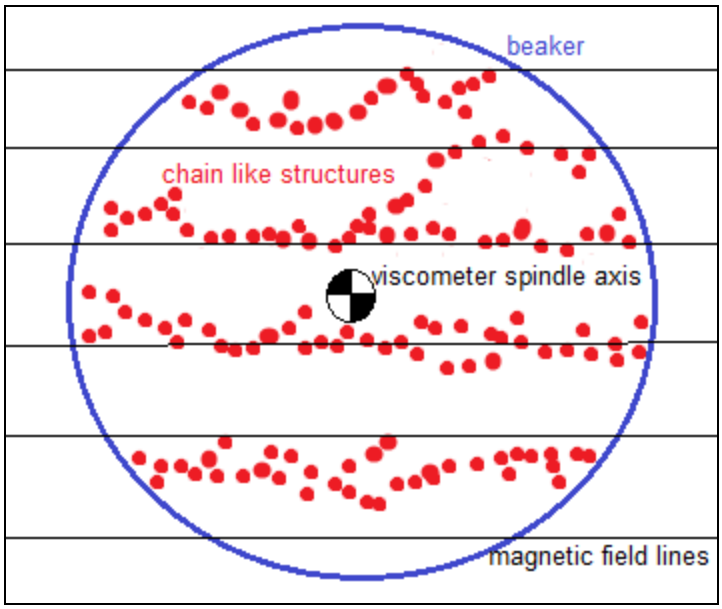

Figure F-1 Top View of Magnetic Field Applied to Fluid Sample in Viscometer

In order to calculate the yeild stress of the MR fluid, the apparent dynamic viscosity needs to be calculated from the viscosity value measured by the rotary viscometer. The Lab-Line Model 4537 rotary viscometer calculates the viscosity of the fluid by measure the viscous torque on a given spindle rotating at a specified speed.

$$F = \mu \cdot Area \cdot \frac{rpm}{60}$$

Ideally, the measured force would result from the sum of the unmagnetized base fluid viscosity and the increase in viscosity due to energizing the MR fluid.

$$F_{ideal} = \left(\mu_o + \mu_{mag}\right) \cdot Area \cdot \frac{rpm}{60}$$

However, the actual force measured is:

$$F_{actual} = \left[\mu_o \cdot \frac{Area}{2} \cdot \frac{rpm}{60}\right] + \left[\left(\mu_o + \mu_{mag}\right) \cdot \frac{Area}{2} \cdot \frac{rpm}{60}\right]$$

It can be shown that the ideal and actual forces are equal if we double the increase in viscosity due to energizing the MR fluid for the measured force.

$$\left(\mu_o + \mu_{mag}\right) \cdot Area \cdot \frac{rpm}{60} = \left[\mu_o \cdot \frac{Area}{2} \cdot \frac{rpm}{60}\right] + \left[\left(\mu_o + 2 \cdot \mu_{mag}\right) \cdot \frac{Area}{2} \cdot \frac{rpm}{60}\right]$$

So, the apparent dynamic viscosity of the magnetized MR fluid can be calculated as such:

$$\mu_{apparent} = 2 \cdot \left(\mu_{measured} - \mu_o\right) + \mu_o$$

To calculate the yeild stress of the fluid, the dynamic viscosity of the base fluid and the apparent dynamic viscosity are used to determine the shear stress of the unmagnetized and magnitzied fluid respectively. The difference between the shear stress of the unmagnitized and magnitzied fluid gives the yield stress of the fluid as shown below.

$$\tau_o = \mu_o \dot{\gamma} \qquad solve\ for\ \tau_o,\ where\ \dot{\gamma} = \frac{rpm}{60}$$

$$\tau_{apparent} = \mu_{apparent} \dot{\gamma} \quad solve\ for\ \tau_{apparent},\ where\ \dot{\gamma} = \frac{rpm}{60}$$

$$\tau_{apparent} = \mu_o \dot{\gamma} + \tau_{yield}$$

$$\tau_{yield} = \tau_{apparent} - \tau_o$$

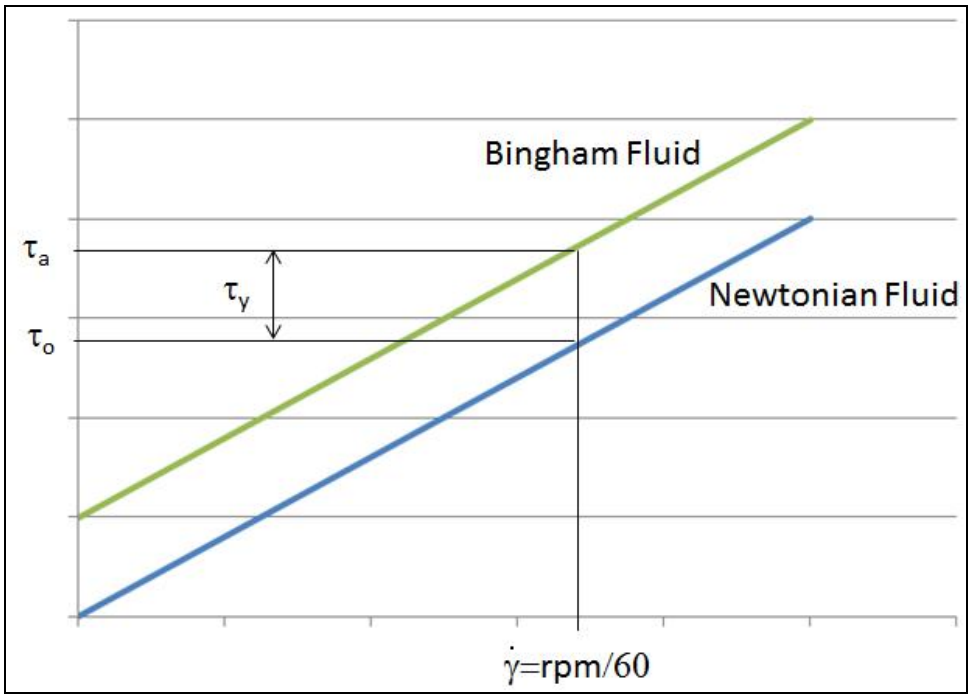

Figure F-2 Yield Stress of Bingham Plastic Fluid

Figure F-3 below, shows the increase in measured viscosity at 40 ºC, 60 ºC and 80 ºC for a range of magnetic fields generated by applying a specified current to the electromagnetic cradle for the bulk test fluid. Figure F-4 below, shows the increase in calculated yield stress at 40 ºC, 60 ºC and 80 ºC for a range of magnetic fields generated by applying a specified current to the electromagnetic cradle for the bulk test fluid.

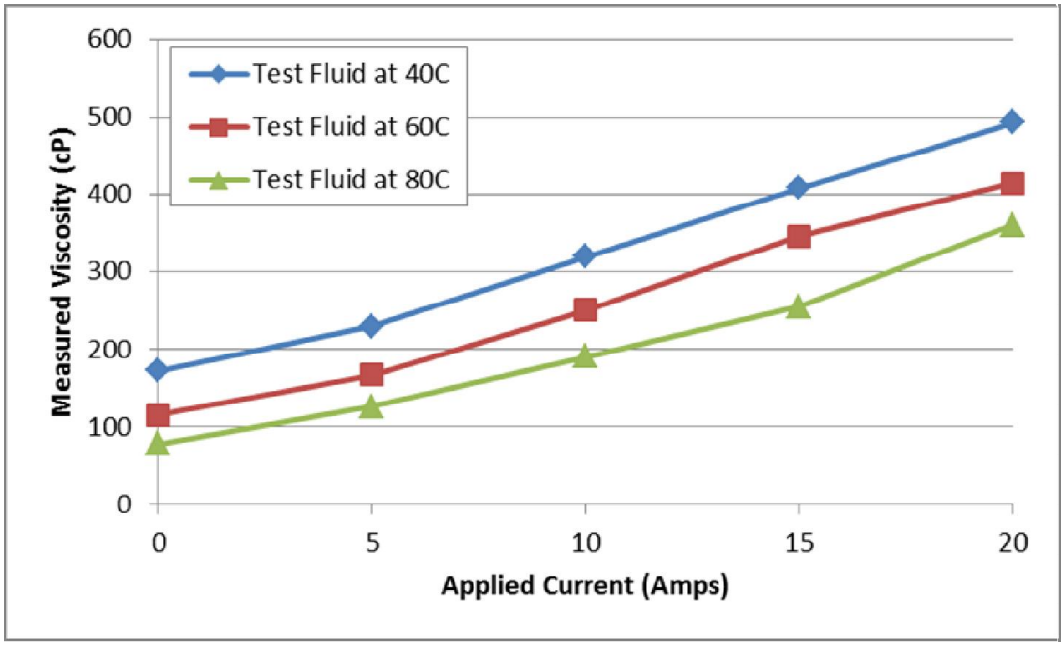

Figure F-3 Measured Viscosity vs. Applied Current for Bulk Test Fluid

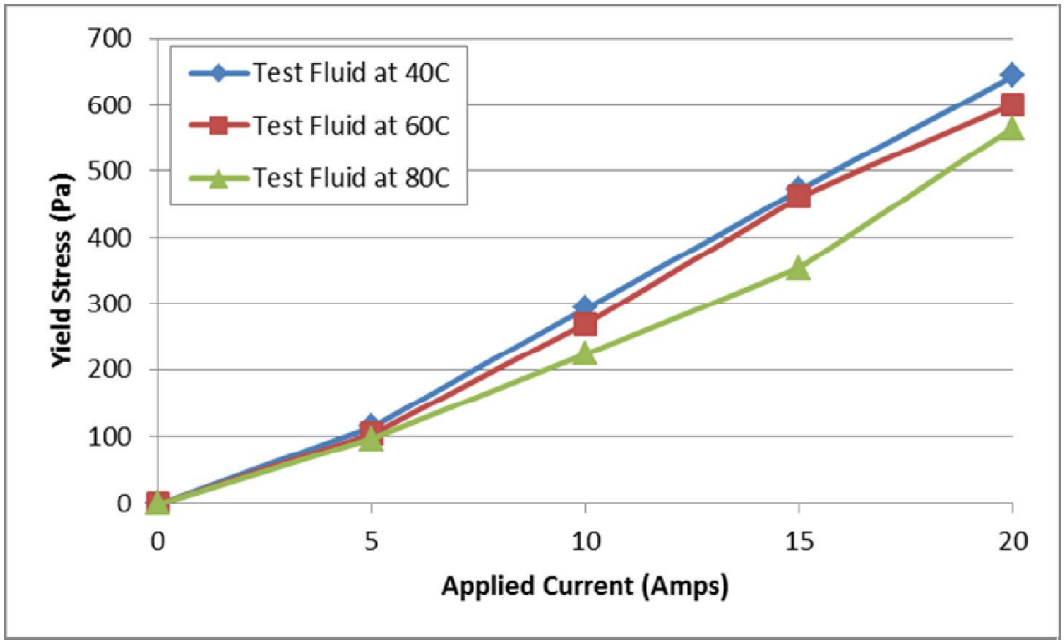

Figure F-4 Yield Stress vs. Applied Current for Bulk Test Fluid

APPENDIX G

STIFFNESS AND DAMPING COEFFICIENTS

Speed	250rpm				
Magnetic Field (A/m)	0				
Eccentricity Ratio	0.1	0.3	0.5	0.6	0.7
Kxx =	2.42E+09	8.43E+09	-1.24E+10	9.29E+09	1.40E+11
Kxz =	2.10E+11	2.54E+11	4.69E+11	7.98E+11	1.52E+12
Kzx =	-2.53E+11	-3.71E+11	-5.21E+11	-6.22E+11	-7.27E+11
Kzz =	4.55E+10	1.84E+11	4.88E+11	7.93E+11	1.32E+12
Bxx =	6.14E+11	6.56E+11	9.24E+11	1.44E+12	2.74E+12
Bxz =	2.84E+09	1.49E+11	7.73E+11	1.47E+12	2.83E+12
Bzx =	-6.11E+10	-6.78E+10	3.28E+11	8.32E+11	1.87E+12
Bzz =	7.76E+11	1.29E+12	2.21E+12	2.94E+12	4.03E+12
Speed	250rpm				
Magnetic Field (A/m)	3800				
Eccentricity Ratio	0.1	0.3	0.5	0.6	0.7
Kxx =	1.40E+11	2.08E+11	3.09E+11	4.00E+11	5.50E+11
Kxz =	8.09E+11	5.99E+11	6.88E+11	9.90E+11	1.69E+12
Kzx =	-1.40E+12	-1.57E+12	-1.13E+12	-1.25E+12	-1.48E+12
Kzz =	1.13E+11	3.30E+11	6.53E+11	1.14E+12	2.01E+12
Bxx =	3.33E+12	2.96E+12	2.51E+12	2.49E+12	3.27E+12
Bxz =	-2.93E+11	-4.74E+11	-2.87E+11	3.99E+11	1.93E+12
Bzx =	-4.24E+11	-3.77E+11	-3.69E+11	1.58E+11	1.49E+12
Bzz =	4.20E+12	4.65E+12	4.18E+12	5.58E+12	7.90E+12

Speed	500rpm				
Magnetic Field (A/m)	0				
Eccentricity Ratio	0.1	0.3	0.5	0.6	0.7
Kxx =	5.17E+09	1.10E+09	2.62E+09	4.12E+10	3.26E+11
Kxz =	4.13E+11	5.20E+11	9.99E+11	1.64E+12	3.08E+12
Kzx =	-5.00E+11	-7.33E+11	-1.02E+12	-1.21E+12	-1.41E+12
Kzz =	7.66E+10	3.34E+11	9.95E+11	1.58E+12	2.61E+12
Bxx =	6.22E+11	6.53E+11	9.71E+11	1.51E+12	2.85E+12
Bxz =	5.29E+09	1.79E+11	8.10E+11	1.52E+12	2.86E+12
Bzx =	-5.91E+10	-3.60E+10	3.63E+11	8.78E+11	1.90E+12
Bzz =	7.73E+11	1.28E+12	2.16E+12	2.86E+12	3.91E+12
Speed	500rpm				

Magnetic Field (A/m)	4800				
Eccentricity Ratio	0.1	0.3	0.5	0.6	0.7
Kxx =	5.33E+10	1.99E+11	2.75E+11	3.42E+11	6.28E+11
Kxz =	5.74E+11	6.93E+11	1.06E+12	1.66E+12	3.08E+12
Kzx =	-5.63E+11	-8.47E+11	-1.34E+12	-1.59E+12	-1.81E+12
Kzz =	1.59E+11	1.88E+11	9.40E+11	1.69E+12	2.99E+12
Bxx =	9.01E+11	1.09E+12	1.30E+12	1.68E+12	2.78E+12
Bxz =	-4.57E+10	-7.64E+10	3.05E+11	9.69E+11	2.37E+12
Bzx =	4.36E+10	-1.02E+11	4.44E+09	4.54E+11	1.52E+12
Bzz =	8.19E+11	1.36E+12	2.59E+12	3.63E+12	5.13E+12

Speed	1000rpm				
Magnetic Field (A/m)	0				
Eccentricity Ratio	0.1	0.3	0.5	0.6	0.7
Kxx =	1.70E+10	5.59E+10	1.76E+10	1.07E+11	6.98E+11
Kxz =	8.29E+11	1.07E+12	2.03E+12	3.31E+12	6.20E+12
Kzx =	-9.97E+11	-1.44E+12	-2.02E+12	-2.38E+12	-2.79E+12
Kzz =	1.52E+11	7.76E+11	2.00E+12	3.16E+12	5.20E+12
Bxx =	6.20E+11	6.58E+11	9.95E+11	1.55E+12	2.91E+12
Bxz =	1.13E+10	1.97E+11	8.33E+11	1.54E+12	2.87E+12
Bzx =	-5.32E+10	-1.81E+10	3.86E+11	8.99E+11	1.91E+12
Bzz =	7.75E+11	1.27E+12	2.14E+12	2.82E+12	3.86E+12
Speed	1000rpm				
Magnetic Field (A/m)	11200				
Eccentricity Ratio	0.1	0.3	0.5	0.6	0.7
Kxx =	1.50E+11	5.01E+11	6.93E+11	8.26E+11	1.42E+12
Kxz =	1.67E+12	1.50E+12	2.19E+12	3.37E+12	6.21E+12
Kzx =	-1.67E+12	-1.82E+12	-2.83E+12	-3.34E+12	-3.84E+12
Kzz =	3.70E+11	3.80E+11	1.95E+12	3.49E+12	6.18E+12
Bxx =	2.00E+12	1.41E+12	1.50E+12	1.83E+12	2.91E+12
Bxz =	-1.65E+11	-1.27E+11	2.00E+11	8.64E+11	2.27E+12
Bzx =	7.70E+10	-4.30E+10	-1.17E+10	4.29E+11	1.51E+12
Bzz =	1.19E+12	1.46E+12	2.74E+12	3.80E+12	5.39E+12

Speed	2000rpm				
Magnetic Field (A/m)	0				
Eccentricity Ratio	0.1	0.3	0.5	0.6	0.7
Kxx =	4.77E+10	1.18E+11	4.88E+10	2.39E+11	1.44E+12
Kxz =	1.66E+12	2.16E+12	4.09E+12	6.66E+12	1.24E+13
Kzx =	-1.99E+12	-2.86E+12	-4.01E+12	-4.72E+12	-5.54E+12
Kzz =	3.15E+11	1.56E+12	4.00E+12	6.31E+12	1.04E+13
Bxx =	6.20E+11	6.60E+11	1.01E+12	1.57E+12	2.94E+12
Bxz =	1.52E+10	2.05E+11	8.44E+11	1.55E+12	2.88E+12
Bzx =	-4.92E+10	-9.91E+09	3.97E+11	9.08E+11	1.91E+12
Bzz =	7.76E+11	1.27E+12	2.13E+12	2.80E+12	3.83E+12

Speed	2000rpm				
Magnetic Field (A/m)	21700				
Eccentricity Ratio	0.1	0.3	0.5	0.6	0.7
Kxx =	3.00E+11	8.45E+11	1.13E+12	1.41E+12	2.60E+12
Kxz =	2.15E+12	2.73E+12	4.25E+12	6.67E+12	1.24E+13
Kzx =	-2.28E+12	-3.41E+12	-5.36E+12	-6.34E+12	-7.23E+12
Kzz =	4.92E+11	7.90E+11	3.82E+12	6.81E+12	1.20E+13
Bxx =	9.76E+11	1.14E+12	1.36E+12	1.76E+12	2.88E+12
Bxz =	-7.51E+10	-7.59E+10	3.08E+11	9.74E+11	2.37E+12
Bzx =	7.26E+10	-7.00E+10	4.38E+10	4.92E+11	1.55E+12
Bzz =	8.08E+11	1.36E+12	2.59E+12	3.61E+12	5.08E+12

Speed	5000rpm				
Magnetic Field (A/m)	0				
Eccentricity Ratio	0.1	0.3	0.5	0.6	0.7
Kxx =	2.34E+11	3.07E+11	1.44E+11	6.35E+11	3.68E+12
Kxz =	4.17E+12	5.41E+12	1.03E+13	1.67E+13	3.12E+13
Kzx =	-4.97E+12	-7.14E+12	-9.98E+12	-1.18E+13	-1.38E+13
Kzz =	9.49E+11	3.92E+12	1.00E+13	1.58E+13	2.59E+13
Bxx =	6.19E+11	6.62E+11	1.01E+12	1.58E+12	2.95E+12
Bxz =	1.62E+10	2.10E+11	8.51E+11	1.55E+12	2.88E+12
Bzx =	-4.83E+10	-5.05E+09	4.04E+11	9.14E+11	1.92E+12
Bzz =	7.76E+11	1.27E+12	2.12E+12	2.79E+12	3.81E+12
Speed	5000rpm				
Magnetic Field (A/m)	59000				
Eccentricity Ratio	0.1	0.3	0.5	0.6	0.7
Kxx =	6.77E+11	1.99E+12	2.61E+12	3.40E+12	6.41E+12
Kxz =	5.23E+12	6.64E+12	1.06E+13	1.67E+13	3.10E+13
Kzx =	-5.35E+12	-8.45E+12	-1.31E+13	-1.56E+13	-1.78E+13
Kzz =	8.80E+11	2.03E+12	9.50E+12	1.69E+13	2.96E+13
Bxx =	8.49E+11	1.08E+12	1.31E+12	1.74E+12	2.88E+12
Bxz =	-4.03E+10	-5.63E+10	3.58E+11	1.01E+12	2.40E+12
Bzx =	3.46E+10	-7.57E+10	6.48E+10	5.12E+11	1.57E+12
Bzz =	7.77E+11	1.34E+12	2.54E+12	3.56E+12	4.99E+12

APPENDIX H

CALIBRATION DATA

Inlet Pressure Transducer:

The inlet pressure transducer was a 100 psi pressure transducer made by PartsSquare with an accuracy of 1% full scale. To generate a calibration curve for the pressure transducers, a calibrated pressure transducer was placed in line with the transducer to be calibrated. Pressure was added to the line and a valve was closed to hold the pressure steady. The signal voltage was recorded at various intervals as the pressure was increased up to 50psig and dropped back down to atmospheric pressure. The resulting calibration curve is given below.

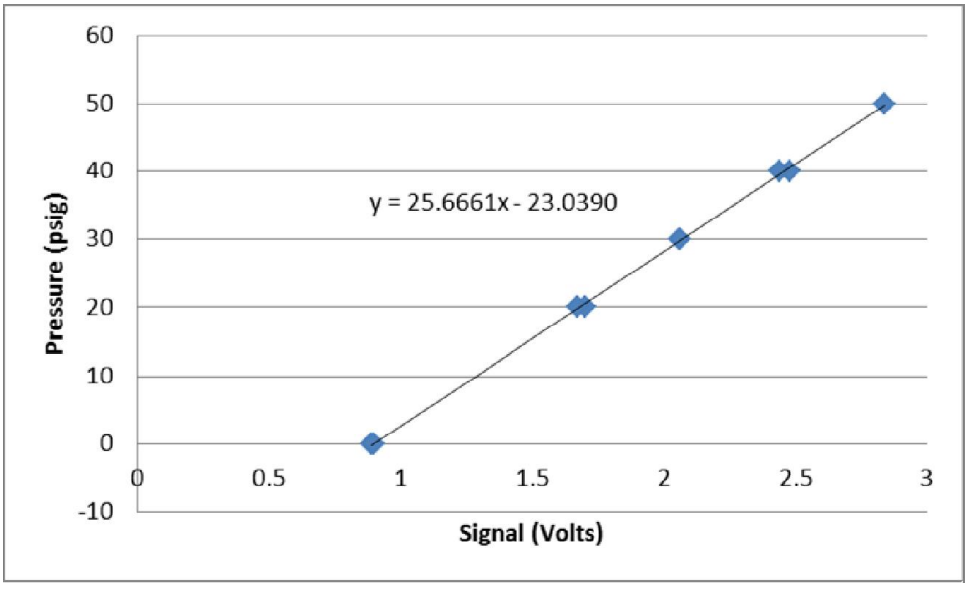

Figure H-1 Inlet Pressure Calibration Curve

Inlet Thermocouple:

A ¼ NPT pipe plug type K thermocouple was used to measure the inlet temperature with a specified error limit of 0.4% or at least 1.1 ºC. To generate a calibration curve for the thermocouple, a calibrated thermocouple was placed in a constant temperature bath with the thermocouple to be calibrated. The temperature was increased incrementally up to 95 ºC as the signal voltage was recorded. The resulting calibration curve is given below (Note: Signal amplification was used).

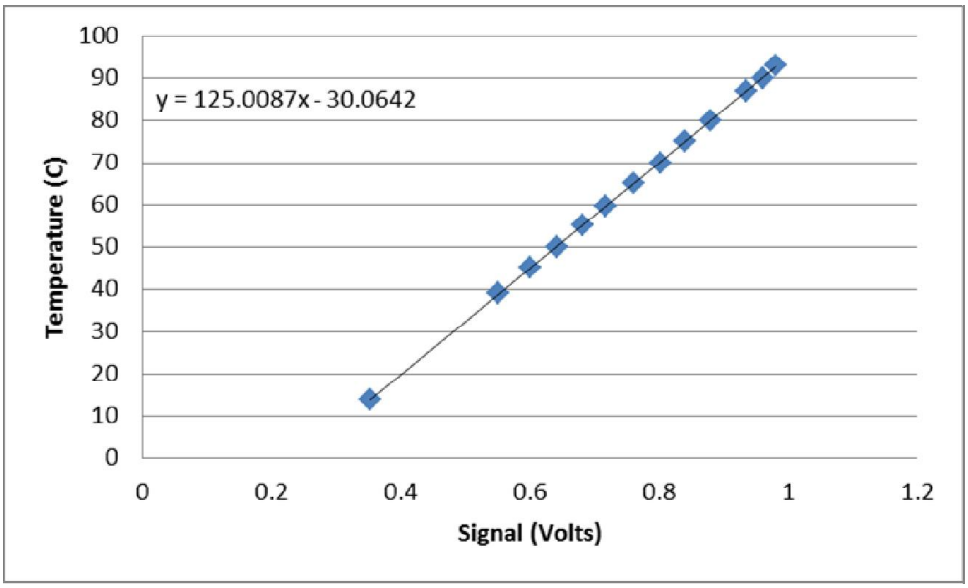

Figure H-2 Inlet Temperature Calibration Curve

Proximity Sensors:

Two 3300 XL 8 mm Bently Nevada proximity transducers, which have a +/-5% measurement capability, were used to measure the position of the bearing center relative to the center of the journal. To generate a calibration curves for the proximity sensors, a calibrated dial gauge with 0.0025" full range was placed on the head of a bolt which was

tightened to butt against the proximity sensor. The bolt was then loosened by 0.0001" increments until the range of the dial gauge was met (approximately 0.0022"). The resulting calibration curves are given below.

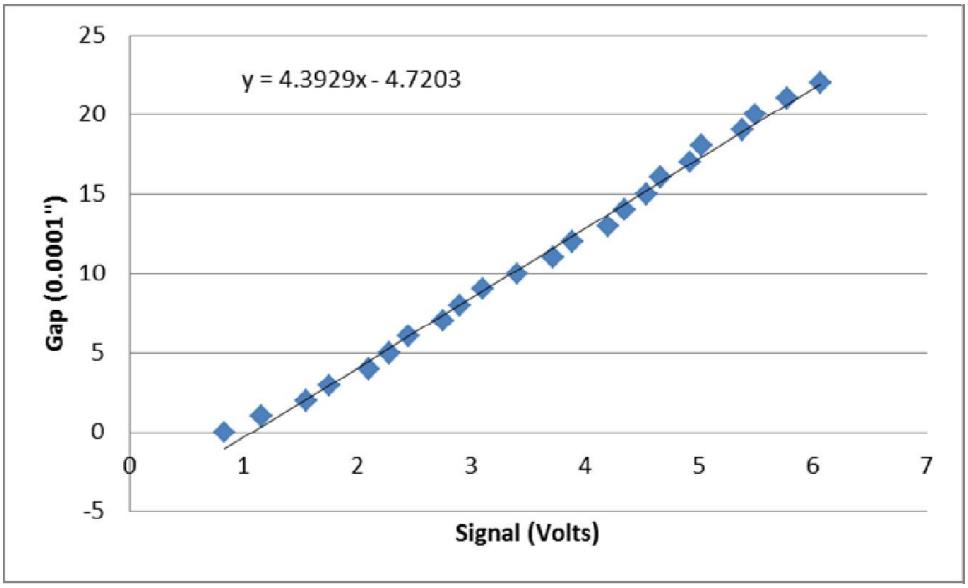

Figure H-3 Proximity Sensor #1 Calibration Curve

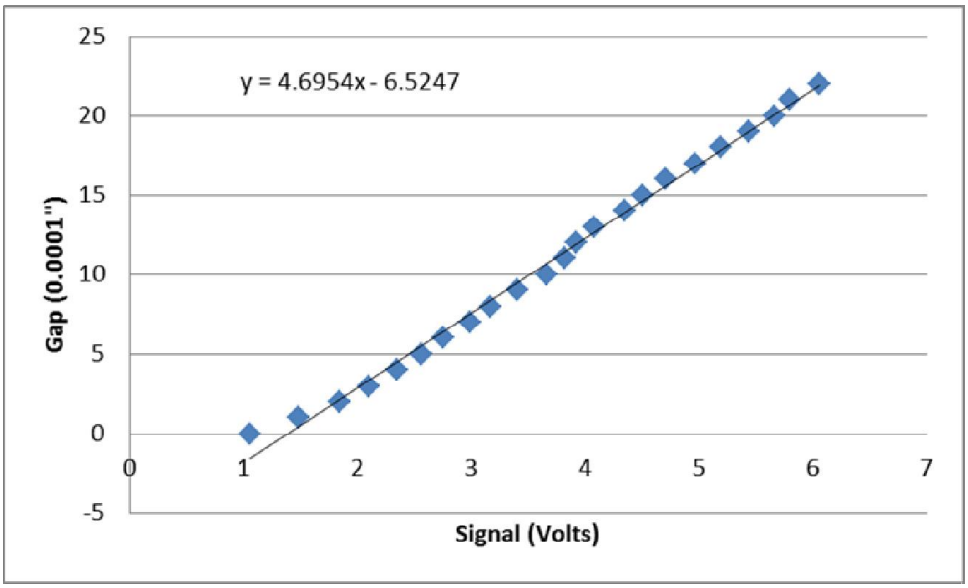

Figure H-4 Proximity Sensor #2 Calibration Curve

Torque Arm:

The rotational torque of the bearing assembly was measured by a load cell created by a temperature compensated quarter-bridge strain gauge circuit. To generate a calibration curve for the torque arm, weights were hung from the load and the voltage signal was recorded. The hanging weights were measured using a model 211 My Weigh iBalance, which has readability of 0.001 g. Measuring the length of the load arm contact point, from the center of the bearing assembly; the torque could then be calculated. The resulting calibration curve is given below (Note: Signal amplification was used).

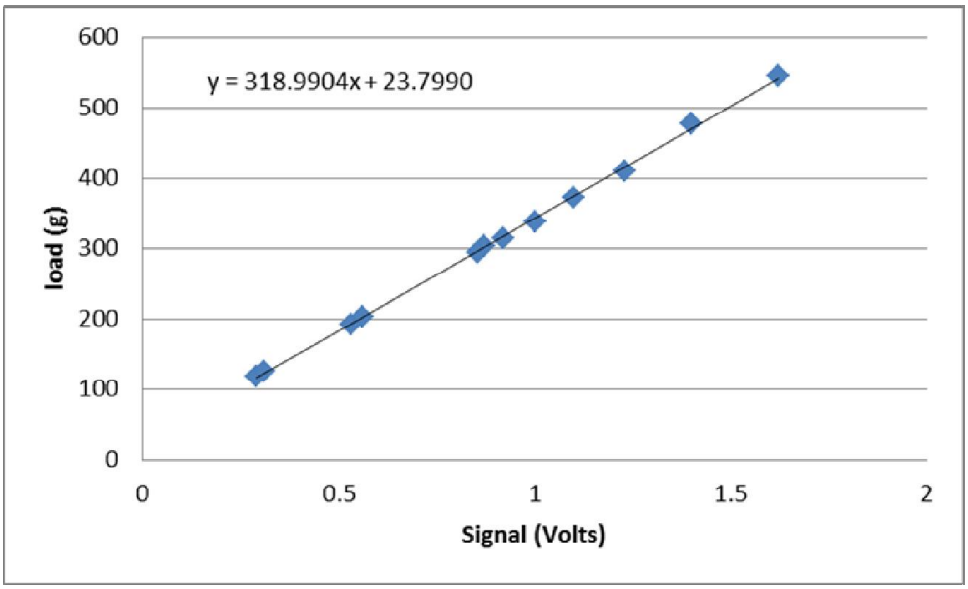

Figure H-5 Torque Arm Calibration Curve

Bearing Pressure Transducers:

Three 100 psig EPI-050/5 pressure transducers made by Entran Devices Inc., with an accuracy of +/- 0.25% full scale were used to measure bearing fluid pressure. To generate the calibration curves for the pressure transducers, a calibrated pressure transducer was placed in line with the transducer to be calibrated. Pressure was added to the line and a

valve was closed to hold the pressure steady. The signal voltage was recorded at various intervals as the pressure was increased up to 50psig and dropped back down to atmospheric pressure. The resulting calibration curves are given below (Note: Signal amplification was used).

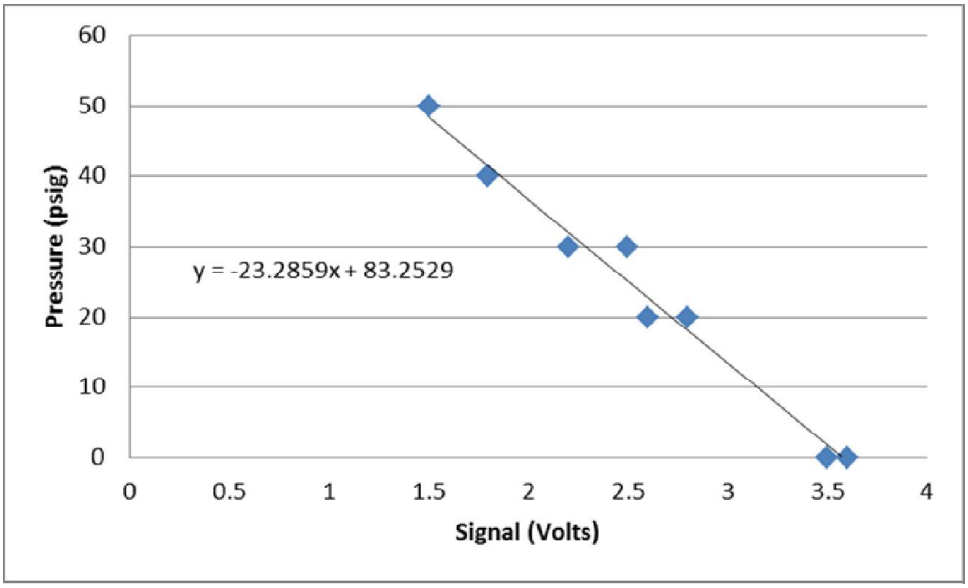

Figure H-6 Bearing Pressure #1 Calibration Curve

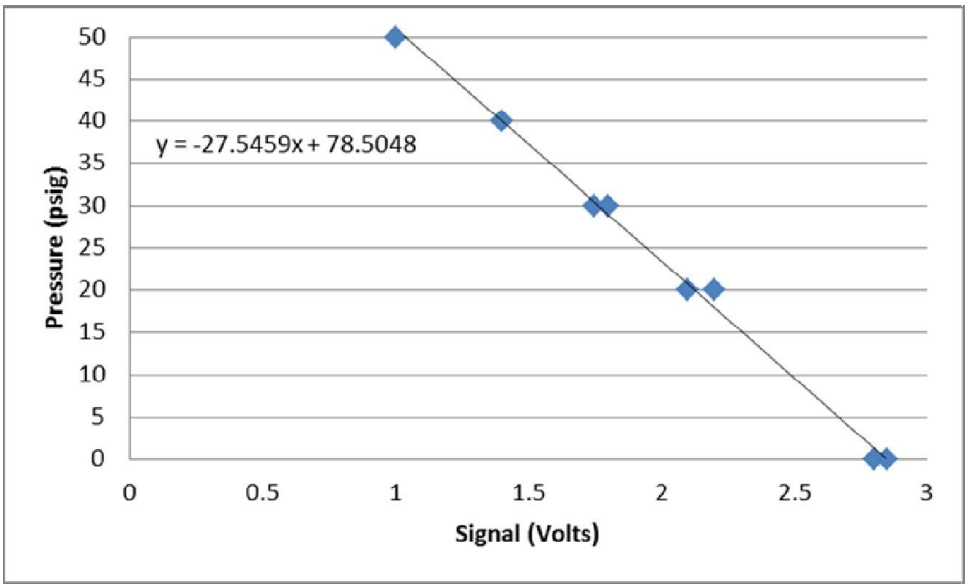

Figure H-7 Bearing Pressure #2 Calibration Curve

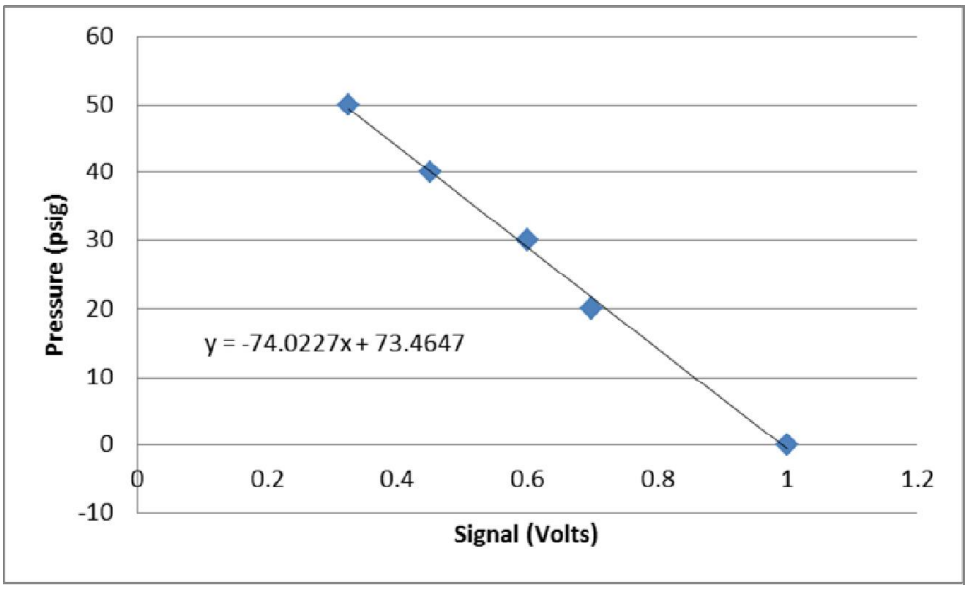

Figure H-8 Bearing Pressure #3 Calibration Curve